2017

Instability in Nonequilibrium and Nonthermal Plasma Discharges

Rajib Mahamud
University of South Carolina

INSTABILITY IN NONEQUILIBRIUM AND NONTHERMAL PLASMA DISCHARGES

by

Rajib Mahamud

Bachelor of Science
Bangladesh University of Engineering & Technology, 2008

Master of Science
University of Nevada Reno, 2011

Submitted in Partial Fulfillment of the Requirements

For the Degree of Doctor of Philosophy in

Mechanical Engineering

College of Engineering and Computing

University of South Carolina

2017

Accepted by:

Tanvir Farouk, Major Professor

Jamil Khan, Committee Member

Sourav Banerjee, Committee Member

Bihter Padak, Committee Member

Cheryl L. Addy, Vice Provost and Dean of the Graduate School

DEDICATION

I would like to dedicate my dissertation to my Parents, brother Rana, and sister Sharna. I would also like to dedicate my work to the taxpayer people of Bangladesh and USA; whose contributions helped provided my education from elementary school to graduate study.

ACKNOWLEDGEMENTS

First and foremost, praise and thanks to the Almighty, for his shower of blessing throughout my research work to complete the research successfully. I would like to thank my parents for their constant encouragement and support during my PhD. I am greatly indebted to my supervisor Dr. Tanvir Farouk for his valuable guidance and suggestions throughout the course of the work. I would also like to thank Dr. Jamil Khan, Dr. Sourav Banerjee, and Dr. Bihter Padak for serving on my committee. I would like to remember my two uncles Late Dr. Mahbubul Haque and Late Mahmudul Haque, school teacher Abdul Khaleque, who owe a special thanks and inspiration in my career. I am grateful to many mentors and colleagues who helped me along the way. I would like to express my gratitude to Dr. Mohammad Ali and Dr. Sheikh Reaz Ahmed at Bangladesh University of Engineering & Technology for introducing me and giving many extra hours of discussion with applied mathematics and CFD analysis during the undergraduate study. I would like to thank few colleagues and friends Dr. Ali Ashraf, Dr. Titan Paul, Dr. Joshua Tarbutton, Dr. Mujibur Khan, Dr. Munsi Basit, Dr. Md. Bhuiya, Dr. Riahi Nezhad, Yousuf, Sharmin, Mayameen, Moinul, Fahd, Ali and Tahiyat for their help and collaboration. Finally, this work would not be possible without the generous financial support from DARPA (ARO Grant No. W911NF1210007) and University of South Carolina.

ABSTRACT

Microplasma, or plasma in micron scale interelectrode separation, is an effective way to attain nonthermal plasma operation at atmospheric and higher pressure. However, the small size causes the effect of other operating parameters to be crucial in stable operation and make the microplasma discharge system to be susceptible to instabilities. The two major instabilities that are commonly observed are the instability in the negative differential resistance (NDR) region and the Striations or the ionization waves. The physics and reaction kinetics of NDR instability for high pressure system is not well understood. This study pursues both experimental characterization and development of mathematical models to understand the physicochemical processes of direct current driven self pulsing non-thermal plasma discharge. The second category of instability that is observed in microplasma discharges is striations, which was previously found in the low pressure discharges. Striations in the positive column is a major efficiency barrier for many potential applications in microplasma discharge system. However, even though there are several investigations, a consistent theoretical framework for describing this phenomenon, especially for diatomic gases, is absent. For this purpose, we propose a detailed mathematical model that considers elaborate vibrational kinetics that is associated with diatomic gases and has shown that for diatomic gases the energy cascades from electrons to vibrational excited states, contributing to the striation formation. We studied a low pressure discharge system for the Striaions modeling due to the availability of experimental data in such conditions.

One of the important applications of plasma discharge is the application in plasma enhanced chemical vapor deposition and micro patterning where the smallest feature size is dictated by smallest discharge current at which stable discharge can be attained. There are no existing method that is aimed at suppressing the instability of atmospheric and high pressure. In this study, a mathematical model was developed to suppress the NDR instability through an external circuit. The mathematical model was validated experimentally and found that the instability in the NDR region can be modulated and suppressed using an external circuit element.

Although microplasma offers significant technical benefits, the small size of the system makes it extremely difficult to perform diagnostics and ion detection. In addition traditional OES, Laser or other spectroscopic measurements are challenging due to the high collisionality of microplasma discharge at elevated pressure. In this study a mathematical model is proposed to predict the ion number density in the microplasma discharges based on the readily available relaxation frequency in the NDR region. The model was validated experimentally and was found to be in a good quantitative agreement with the multiphysics numerical model.

TABLE OF CONTENTS

LIST OF TABLES

LIST OF FIGURES

LIST OF SYMBOLS

A *effective diffusion length*

C capacitance

d inter-electrode separation

D diffusion coefficient

e electron charge

E electric field vector

f *frequency*

f_0 electron energy distribution function

G *gas phase reaction*

h enthalpy

I current

j current density

k thermal conductivity

k_B Boltzmann constant

L inductor

m mass

n number density

N neutral density

p pressure

q charge state

Q rate of enthalpy change

R resistance

R_{im} surface reaction rate

S surface reaction

T temperature

t time

V_d discharge voltage

V_o supply voltage

Greek Symbols

ε permittivity

ε_0 permittivity of free space

ε electron energy

φ electric potential

Γ flux vector

λ mean free path

λ_D Debye length

γ secondary emission coefficient

η reaction rate coefficient

τ *time constant*

μ mobility of charged species

ν electron transport collision frequency

σ plasma conductivity

Subscripts

d discharge

dexcit de-excitation

diss dissociation

e electron

excit excitation

gas species

i ion species

v vibrational

LIST OF ABBREBIATIONS

NDR ..... Negative Differential Resistance

RMS .....Root Mean Square

VI .....Voltage Current

CHAPTER 1

INTRODUCTION

1.1. BACKGROUND

The following sections give a brief background on plasma, microplasma, and plasma instability that is necessary to place the motivation of this research in context.

1.2. PLASMAS

The term ‘plasma’ was first coined by chemist Irving Langmuir in the 1920s while working with argon gas in a vacuum tube to increase the lifetime of the tungsten filaments used for light generation to improve the efficiency of the light bulb. Prior to his study light bulbs did not contain an inert gas, rather it was a vacuum environment with a trace amount of air present in there. His research identified that the addition of an inert gas in the bulb increases its efficiency and it creates an ionized medium under specific electric field condition. However, it was Sir William Crookes, an English physicist, who first identified the ionized state of matter, in 1879, forty one years before Langmuir’s work. Typically plasma is a generalized term for a medium which is comprised of ionized and excited species,

(a) **(b)**

Figure 1.1: a) The Aurora Borealis, or Northern Lights an exemplar non-thermal plasma is generated by the collision of electrons found in the magnetosphere, with atoms in the earth's upper atmosphere. b) the solar core is a classic example of a thermal plasma where temperatures can reach ~ 15,000,000K, sufficient for nuclear fusion reactions. (M. A. Lieberman & Lichtenberg, 2005; Yuri P. Raizer, 1991)

radicals and electrons under external energy sources. Plasma is referred to as the fourth state of matter due to its unique properties that are distinct from those of the other physical states, i.e., solid, liquid and gas. Plasma is the most abandoned state of matter in nature. It is estimated that 99% of the matter in the observable universe is in the plasma state. Plasma systems can be observed over a wide range of physically possible scales in energy/ temperature, density, and space. Based on the energy/temperature of the neutral atoms, ions, and electrons, plasma discharges can be classified as thermal, where the temperature of the neutral gas (T_{gas}) is as high as ~5000K, or non-thermal, where the average temperature of electrons (T_e) is far greater than the netural gas temperature. In a typical non-thermal plasma discharge the average electron temperature is between ~ 1 – 2 eV (1eV = 11,600 K) whereas the neutral gas temperature can maintain ambient room temperature conditions. The widely known example of atmospheric non-thermal plasma is Aurora, shown in Figure 1(a), which is observed in the north pole. Conversely, the most standard

model of thermal plasma is solar core, nature's fusion reactor, and is graphically illustrated in Figure 1(b).

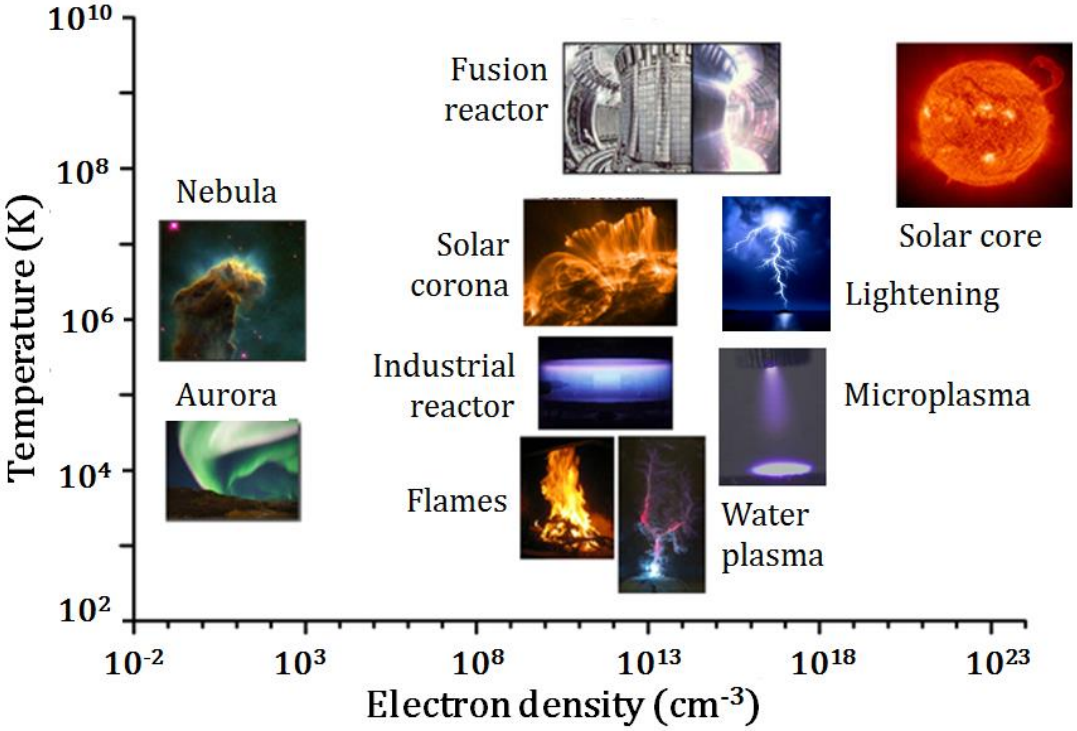

Figure 1.2 Classification of different types of plasma in temperature and electron number density space. [(Pascal Chabert & Braithwaite, 2011)]

Based on the density scale, the tenuous (as well as coldest) form of a plasma is the space nebula and the *Aurora Borealis*, which has a typical electron number density of ~ 10^{-2} cm^{-3} - 10^{2} cm^{-3}. On the other side of the density spectrum is the central core of the sun, which is extremely dense and hot and has an electron density of ~ 10^{23} cm^{-3}. The different type of plasma discharges classified in terms of the electron number density and temperature is depicted in in Figure 1.2. It can also be seen that plasma for all the industrial applications, such as microplasma, water plasma, flames, and fusion reactors, falls in the middle of the density spectrum.

Plasma discharges can be further classified on the basis of the discharge current of the system. Figure 1.3 is an illustrative view graph of voltage versus current for a DC driven plasma discharge that also denotes the different regimes of the discharge in current space.

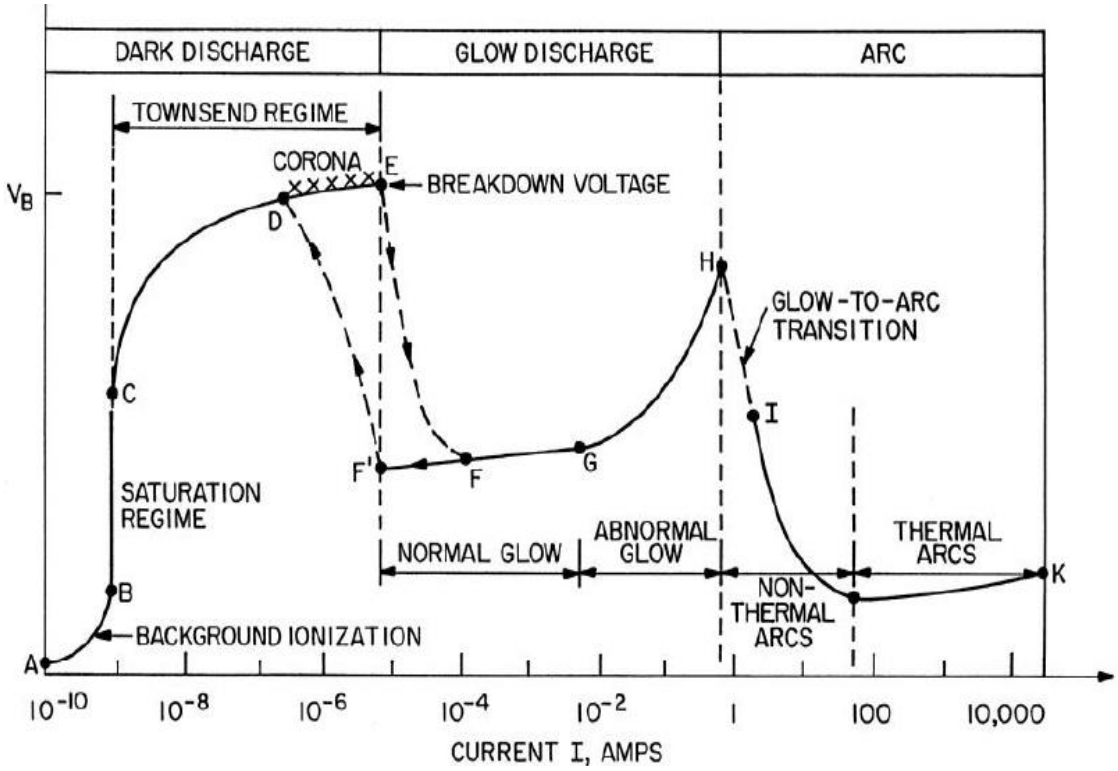

Figure 1.3 Voltage-current characteristics of a DC driven plasma discharge. (Roth, 1995)

As the voltage is initially applied naturally occurring free electrons provide some current (AB in Figure 1.3). As the voltage is increased the electric field becomes sufficient for the electrons to gain energy and ionize some of the gas producing more electrons, but not yet producing a sufficient number to create a self sustained discharge (C-D). In a corona (D-E) a sharp electrode is used to increase the electric field locally, and in the region near the sharp electrode the plasma density is higher, and a glowing region is seen. The shape of C-D-E shown in Figure 1.3 is for a negative corona configuration. In a parallel plate configuration, the C-D-E will actually be a flat line with the voltage at the level of E. The

entire C-D-E region is called the Townsend regime. Low current non-thermal discharges are considered to operate in the Townsend regime.

Eventually, breakdown occurs (E-F) when the discharge becomes self sustaining. Sufficient electron emission from the cathode is one of the requirements for the development of self sustained plasmas. In normal glow discharges, the electron emission occurs because of secondary electron emission due to ion bombardment at the cathode surface. After a breakdown at low currents, the DC *'normal'* glow discharge plasma is observed (F-G). In the *'normal'* glow regime the discharge voltage is constant, and an increase in current causes an increase in the diameter of the discharge.

In the *'normal'* glow regime if the current is increased and the size of the electrodes is limited the current density will increase, and we will have the *'abnormal'* glow discharge (G-H). The *'abnormal'* glow is initially low temperature, but as the current is increased, it can transition to the high temperature arc discharge (H-J). The transition can occur by either 1) the cathode becomes overheated, or thermionically emission greatly increases the current or 2) the gas temperature increases and the dominant mechanism of ionization changes from electron impact ionization to thermal ionization. The higher the density of the gas medium the lower the current at which the transition to an arc occurs. If the size of the electrode is not limited glow to arc transition will also occur but the line G-H will be relatively flat.

Operating pressure hence gas density is known to play a definitive role in plasma formation (Paschen, 1889). This dependence is relayed through the Paschen's law of breakdown which relates the breakdown voltage (i.e., the voltage required to form the

plasma) to the operating pressure and interelectrode separation distance and has the following form:

$$V_B = \frac{Bpd}{\ln(Apd) - \ln[\ln(1+\frac{1}{\gamma})]} \qquad (1.1)$$

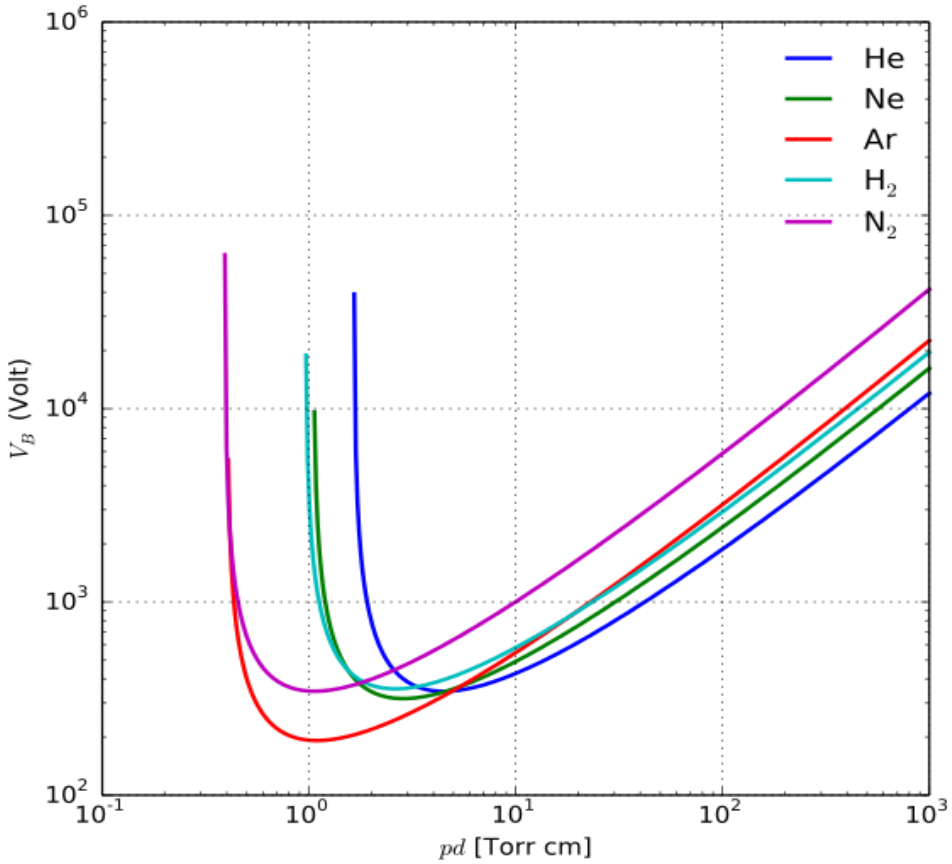

Figure 1.4 Paschen curves for different atomic and molecular gases [(Fridman & Kennedy, 2004a)]

Where V_B is the breakdown voltage, P is the pressure, d is the interelectrode spacing, γ is the secondary electron emission coefficient, A is the saturation ionization in the gas at a particular E/P and B is related to the excitation and ionization energies.

Figure 1.4 shows the Paschen curves (Fridman & Kennedy, 2004a; Yuri P. Raizer, 1991) for different monoatomic and diatomic gases. The parameter *pd* that combines operating pressure and interelectrode separation is simply proportional to the ratio of the discharge length scale to the mean free path or inverse of the Knudsen number. There is a minimum breakdown voltage on the Paschen curve, V_{min} and a corresponding pd_{min} for the different gases and is related to the ionization potential of the specific gas. To the left of the minimum point, either the discharge gap or the pressure is so small that the mean free path in the discharge is insufficient to provide a breakdown/ignition. To the right hand side, required voltage for a possible ignition is higher since the gap or operating pressure is higher and there is a tremendous amount of collisional losses. The Paschen's law, therefore, suggests that one can manipulate either the operating pressure or the inter-electrode separation distance to maintain conditions for the minimum breakdown/ignition energy requirement (Loveless & Garner, 2016). This concept has been successfully utilized in initiating a plasma discharge that maintains non-thermal characteristics at atmospheric or even higher pressure by decreasing the plasma feature size (i.e., the inter-electrode separation distance) to micro levels (Tachibana, 2006) – forming microplasma discharges. However, the stability of such systems is still a concern as the Paschen's law does not convey the necessary information related to the stability of plasma systems .

1.3. MICROPLASMAS

Microplasmas are pressure scaled versions of the common low pressure discharges. The main idea of having micro plasma discharges at atmospheric pressure is based on the Paschen's law (Figure 1.4). The high spatial resolution of micro discharges makes it a topic

of high interest. Various designs of plasma sources have been proposed to generate stable micro plasma discharges. The reported electrode configurations include parallel plates (Yoshiki & Horiike, 2001), cylindrical type (e.g. hollow cathode) (K. H. Schoenbach, Moselhy, Shi, & Bentley, 2003), slot type (Yoshiki & Horiike, 2001) , needle type (Tomoyuki Kikuchi, Hasegawa, & Shirai, 2004), pin plate type (David Staack, Farouk, Gutsol, & Fridman, 2005a) etc. and the applied operation modes vary from direct current (DC) to radio frequency (RF) or microwave. These studies are motivated by numerous potential applications of microplasmas including sensors, integrated MEMS, etching, excimer sources or microreactors and PECVD (Becker, Schoenbach, & Eden, 2006a; Eijkel, Stoeri, & Manz, 2000; Elkholy, Nijdam, van Oijen, & de Goey, 2017; David B Go, Fisher, Garimella, & Bahadur, 2009; R. M. Sankaran & Giapis, 2001)

Microplasma discharges operate in the 10 ~ 1000 μm scale ranges. It requires less power but has high power density due to its small size. As a result, it has higher efficiency and at the same time maintains flexibility in operation than any of the traditional plasma processing systems. The small length scale of microplasma discharges makes it possible to make the residence time (t_R) of the feed gas to be short which inherently can suppress possible thermalization of the system. Also, the discharge is conducive to a pulsed operation where the pulse duration (t_p) of which is shorter than the electron energy relaxation time. As a result, it becomes possible to maintain the nonequilibrium state ($T_e > T_g$).

Atmospheric and high pressure non-thermal plasmas have a significant technical benefit because in contrast to low-pressure plasma no vacuum chamber is needed to ensure proper operating pressure conditions. At the same time, the higher operating pressure

reduces the chemical processing time as a result of higher reaction rates. However, this contributes to the complexity of these systems mainly through increasing the layers of intricacies in the plasma chemical kinetics, higher collisionality, higher charged species (i.e., electrons and ions) concentrations - making these discharges susceptible to instability. One of the main challenges in maintaining the non-thermal mode of plasma at atmospheric and higher pressure is preventing the ionization overheating instability and hence the thermalization of the discharge itself. The ionization overheating instability results in a rapid increase in the gas temperature if not suppressed. At high pressure conditions (i.e., atmospheric pressure and higher), the ionization overheating instability is more prevalent due to the increased rate of collisionality of the systems.

Even though microplasma discharges can suppress the ionization overheating instability at higher pressure due to their small sizes, their small dimensions make them susceptible to instabilities resulting from external parameters. For example, the instability in the NDR (Negative Differential Resistance) region of a nonequilibrium plasma discharge is a norm and is unavoidable. In addition to NDR instability, standing Striations is a common instability in microplasma discharges when a diatomic gas used.

1.4. INSTABILITY IN MICROPLASMAS

Discharge stability is one of the important requirements for the proper functioning of microplasma discharges. The attention on stability and different modes of operation of microplasma discharges were triggered by several observations and their associated studies. These studies included self-pulsing microplasma in a microhollow cathode configuration (Rousseau & Aubert, 2006), instabilities in microplasma jet changing the

mode of operation from continuous to chaotic and bullet like operation (Walsh, Iza, Janson, Law, & Kong, 2010). Since microplasmas are pressure scaled version of the conventional low pressure plasma one can attempt to correlate the findings from low pressure studies. There has been a significant effort in investigating some of this instability in large scale DC driven low pressure plasma discharges, especially self-triggered oscillations and constrictions (Phelps, Petrović, & Jelenković, 1993a). In general, oscillations of gas discharges may be associated with a combination of the physical processes occurring in the discharge itself and the driving power circuit. At extremely low current diffuse regime – Townsend/Dark discharge space charge effects lead to a negative differential resistance (Petrović & Phelps, 1993a) which supports oscillations/instability if the effective round the loop resistance is negative. Phenomenological descriptions using effective circuit elements have been proposed to provide insight into the unstable behavior (Druyvesteyn & Penning, 1940; EMELEUS, 1975). However, in these phenomenological models, the global pulsing behaviors are only attributed to the response time of the different circuit elements. Physics-based models identify the properties of charged particles and their distribution as the source of the instability (Yu. P. Raizer, Gurevich, & Mokrov, 2006). There have only been limited studies (Robert R Arslanbekov & Kolobov, 2003; Tanvir Farouk, Antao, & Farouk, 2014a) that have looked into the interplay of the driving circuit elements and the plasma dynamics on the instability of the system.

For DC driven low pressure plasma discharges numerous operating modes (i.e., oscillatory pattern) in the unstable regime have been identified (Phelps, Petrović, & Jelenković, 1993). Similarities have been drawn between these low pressure plasmas and high pressure microplasma. The different types of oscillations can be of a relaxation type

where the discharge is repeatedly turning itself off through the combined effect of increased current and external circuit. Others may be associated with transitions between different regimes of operation or spatial modes, and some undulations of voltage and current may be due to variable properties on the surface when the discharge is moving (Petrović & Phelps, 1997). This type of behavior has been observed for both the low pressure large scale plasmas and high pressure microplasma discharges. Another common unstable behavior observed is standing or moving waves with smaller undulation in the voltage, current and charged species number density. Specific to microplasmas, different spatial modes are found to exist, and the discharge gets localized to the small area of the electrode due to the small diffusion length scale which results in instability due to the transitions between the different spatial modes. It should be noted that most instabilities are observed in the low current regime of operation (DEFF' region of the voltage-current curve Figure 1.3).

In this low current operation, the unstable behavior can be classified as the negative differential regime and striated regime. A brief description of these two regimes are provided below.

1.4.1 NEGATIVE DIFFERENTIAL RESISTANCE (NDR) UNSTABLE REGIME

In electronics and power circuit a negative resistance or negative differential resistance (NDR) is a property in which an increase in voltage across a device terminal results in a decrease in current through it. This is in contrast to an ordinary resistor in which an increase of applied voltage causes a proportional increase in current due to Ohm's law resulting in a positive resistance. While positive resistance consumes power from current

passing through it, a negative resistance produces powers and under favorable conditions amplify an electrical signal. Furthermore, the simplest considerations concerning power consumption in an electrical circuit also portray that if the circuit contained an element with NDR, it would be possible to create AC power rather than consume it. But such an NDR element will have highly non-linear electrical properties. The NDR regime in the plasma discharge is denoted as the region where the discharge current increases with decreases in voltage as denoted in Figure 1.3 as DEFF' line. However, such a region is not stable and the plasma pulses between different modes of operation; low current and high current - hence the dashed line hysteresis loop of the DEFF' line.

Negative differential resistance can be classified into:

Voltage controlled negative resistance: In this type, the current is single valued, continuous function of the voltage, but the voltage is a multivalued function of the current. In the most common type, there is only one negative resistance region, and the graphical representation of the response resembles the letter 'N' (Figure 1.5 a). As the voltage is increased, the current increases (positive resistance) until it reaches a maximum value, then decreases in the region of negative resistance to a minimum value, then increases again. Exemplary devices include tunnel diode, resonant tunneling diode, and dynatron oscillator.

Current controlled negative resistance: In this type, the voltage is a single valued function of the current, but the current is a multivalued function of the voltage. In the most common type, there is only one negative resistance region, and the graph is a curve shaped like a

letter ‘S’ (Figure 1.5 b). Exemplary devices electric arc, gas discharge tube, fluorescent lamps.

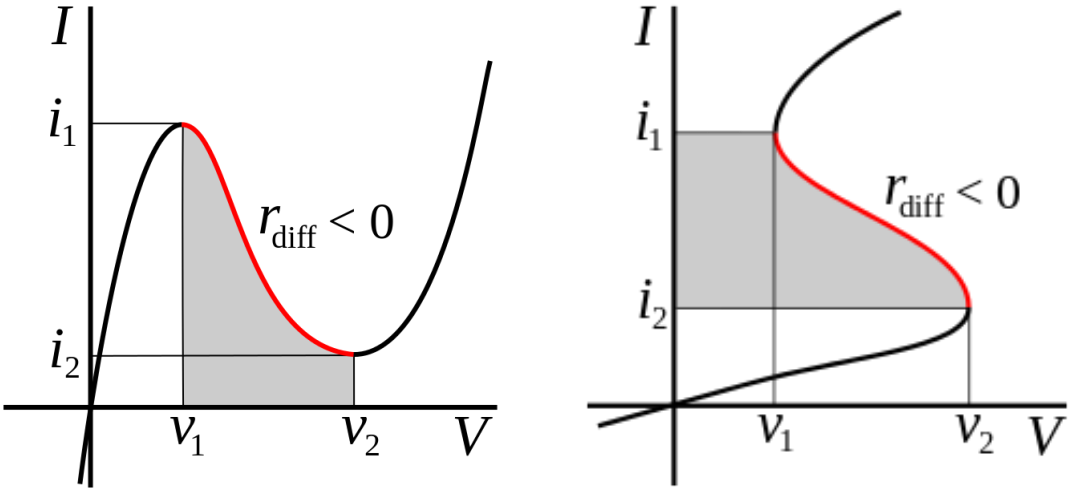

(a) (b)

Figure 1.5 Types of negative differential resistance a) voltage controlled negative resistance and b) current controlled negative resistance.

1.4.2 STRIATIONS REGIME – SELF INDUCED STANDING/MOVING WAVES

Striations are one of the most conspicuous features for electrical discharge in gases, especially observed in the low pressure system. It is a well-recognized phenomenon in the positive column observed as a periodic bright and dark space and attracted physicists throughout the 18th and 19th-century after being discovered by Abria in 1843. It captivated physicists for a long time because of its spectacular manifestation in the positive column and in a complicacy to form general theory, and as a result, both hydrodynamics and the kinetics-based model was studied to understand the phenomenon. However, from an engineering point of view, stratification of the positive column is undesirable as it reduces the efficiency of practical applications like gas laser or light sources. Interests in recent

times have renewed as it deteriorated the display quality of plasma display panel and was also observed in microplasma discharge system.

Figure 1.6 Experimental observation of Striations in a low pressure discharge system

Figure 1.6 is an experimental manifestation of Striations in diatomic gases where a clear bright and dark pattern can be observed in the positive column. The bright region is the location where maximum ionization takes place and has the maximum electron and ion number density. Away from this region all the values steadily diminish to lower values, and the darker region appears. The light coming from the bright area of the strata gives a many lined spectrum and thought to originate from molecules in excited states. The periodic change in light intensity in the strata region indicates that the energy acquired by electrons between each strata corresponds to an excitation voltage.

It is well established that pressure, current density, tube diameter, and impurity have an important role in the formation and wave pattern of strata. An increase in gas temperature can also affect the striations, particularly at the low pressure and high currents, when an increment of wave frequency and a decrement of amplitude was observed. In fact, it is a periodic wave in electron/ion density and is caused not by the redistribution of fixed electrons/ions but by the periodic production and recombination of electrons/ions. However, wave during the striations phenomenon cannot be described by any known

waves (such as acoustic), rather it is governed by the change in ionization rate and sometimes referred as ionization waves.

Stratification can be observed both as standing (molecular gases) and moving (monoatomic gases) referred as ionization waves of positive column. In addition, artificial striations can be generated by auxiliary electrodes or by the modification of discharge current. Moving striations can observe only in monoatomic gases (He, Ne, Ar. etc.) cannot be seen in eyes as has a very high velocity ranging from $10 \sim 10^3$ m/s. Whereas the standing striations can be observed in diatomic gas discharges, such as H_2, N_2, and O_2.

1.5. MOTIVATION

Over the past decade, there has been a research thrust directed towards the development of high pressure non-thermal plasma with a focus to overcome the limitations of their low pressure counterparts. Among the different high pressure non-thermal discharges system, microplasma continues to be a topic of immense interest. Even though micron sized inter-electrode separation has been successful in attaining non-thermal plasma conditions at atmospheric pressure, the small size causes the effect of other operating parameters to be crucial in stable operation. Hence, the microplasma discharge system is susceptible to instabilities. The two major instability that is commonly observed is the instability in the negative differential resistance (NDR) region and the striations. The instability in the NDR region has been studied mostly for low pressure discharge. However, the physics and reaction kinetics of NDR instability for high pressure system is not well understood. This study pursues to solve this problem that concerned both experimental characterization and development of theoretical models to understand the

physicochemical processes of direct current driven self pulsing non-thermal plasma discharge.

The second category of instability that is recently found in microplasma discharges is striations, which was previously observed in the low pressure discharges. Striations in the positive column is a major efficiency barrier for many potential applications in microplasma discharge system. Striations can be both stationary and moving. The moving Striations has been studied well studied. However, even though there are several investigations, a consistent theoretical framework for describing this phenomenon especially for diatomic gases is absent. For this purpose, we proposed a detailed mathematical model that considers elaborate vibrational kinetics that is associated with diatomic gases and has shown that for diatomic gases the energy cascades from electrons to vibrational excited states contributes to the striation formation.

One of the important application of plasma discharge is the application in plasma enhanced chemical vapor deposition and micro patterning where the smallest feature size is dictated by smallest discharge current at which stable discharge can be attained. Currently there is no existing technology that is aimed at suppressing the instability of atmospheric and high pressure. In this study, a mathematical model was developed to suppression of NDR instability through an external circuit. The mathematical model was validated experimentally and was found that the instability in the NDR region can be modulated and suppress using a suppressing circuit element.

Although microplasma offers significant technical benefits, the small size of the system make it extremely difficult to perform diagnostics and ion detection. In addition

traditional OES, Laser or other spectroscopic measurement is challenging due to the high collisionality of microplasma discharge at elevated pressure. In this study a theoretical model is proposed to predict the ion number density in the microplasma discharges based on the readily available relaxation frequency in the NDR region. The model was validated experimentally and was found to be in a good quantitative agreement with the multiphysics numerical model.

1.6. OBJECTIVES

The main objective of this study is to develop theoretical model and experimental system to characterize, stabilize and utilize the instability in microplasma discharges for applications.

The objectives of the completed research were:

- Develop multiscale and multiphysics model of discharge physics to study the NDR instability in microplasma discharge and to find its various modes.
- Develop the experimental setup and procedure to thoroughly investigate the NDR instability in microplasma.
- Develop the ion kinetics model to study the effect of trace impurity on the self-pulsing oscillation in the NDR region.
- Develop multiscale and multiphysics model of discharge physics to simulate the standing striations' in diatomic gas discharges.
- Develop the reaction kinetic model (ionization, excitation, and vibrational) for the simulation of striations in nitrogen discharges.

- Develop mathematical model and experimental technique to stabilize the microplasm discharge from the NDR instability.
- Develop mathematical model and experimental technique to utilize the relaxation frequency in the NDR region as an ion detection tool.

1.7. OUTLINE OF THE THESIS

The four primary chapters of this thesis are based on four basics problems as it has been described as a challenging problem by another researcher for a while.

Chapter 1 covers the motivation and introduction of the research. A literature review has been presented in Chapter 2. The building block of the problem solving, the mathematical modeling are covered in Chapter 3.

Chapter 4 will present a thorough analysis of NDR instability, which will cover 1D model with parametric study and kinetics, a 2D model with results, and experimental results on voltage-current characteristics curve.

Chapter 5 covers the proposal of suppression of NDR instability using external circuit is presented. It includes the mathematical model, numerical model, and experimental validation.

Chapter 6 proposes a novel ion detection model is presented with experimental help. It includes mathematical model and experimental validation.

Chapter 7 will attempt to explain the striations based on numerical modeling and simulation and a 1D model. The reaction kinetics developed for this model is also presented here.

In Chapter 8 we look back in retrospect and try to take stock of the learnings and limitations of the project.

In the Appendix, a three temperature modeling approach is proposed to predict the three different temperature modes in diatomic gas discharges. Moreover, an application of nonequilibrium and nonthermal plasma for industrial application is presented. The results found that corona plasma can increase the piezoelectricity of PVDF fiber during the electrospinning process. This chapter is included for finding plasma treatment for surface treatment and material science application.

CHAPTER 2

BACKGROUND

2.1 NON-THERMAL PLASMA INSTABILITY

The key reaction process responsible for forming and sustaining a plasma state is the ionization process. Ionization process can be divided into five major groups (M. A. Lieberman & Lichtenberg, 2005):

- Direct ionization by electron impact
- Stepwise ionization by electron impact
- Ionization through heavy particle collision
- Photoionization processes
- Surface ionization or thermal ionization

A schematic of the aforementioned ionization processes is presented in Figure 2.1. The first two of the ionization process requires shooting of energetic electrons into a neutral medium, which consequently produces positive charges. A less effective interaction brings the neutral into an electronically excited state without ionizing it. The third category of ionization process occurs when electronically excited neutrals like noble gas atoms, A* collide with a ground state molecule, M, and produces positive ions and electron. This

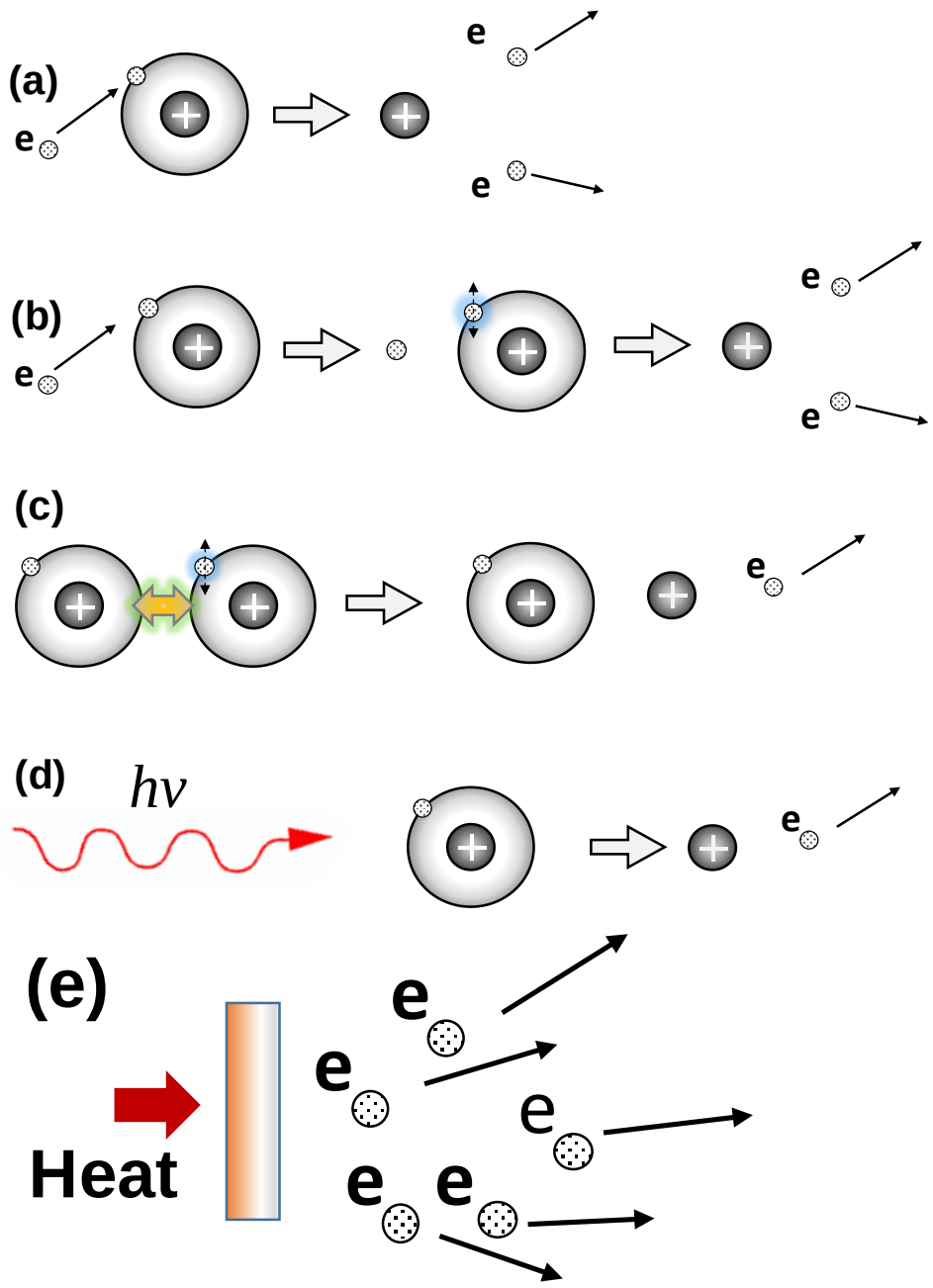

Figure 2.1 Elementary processes of ionization (a) Direct impact ionization (b) Stepwise ionization by electron impact (c) Ionization through heavy particle collision (d) Photoionization process (e) Surface ionization

process also referred as Penning ionization. The photoionization aspect of ionization process happen when an incident photon can release one or more electrons from atomic or molecular gas system. The surface ionization process, such as thermal ionization, takes place when application of heat emits electrons from the metal surface. The different ionization process is presented below by the following set of equations.

(a) $e + A \rightarrow \mathrm{e} + e + A^{+}$ (2.1)

(b) $e + A \rightarrow \mathrm{e} + A^{*}$ (2.2)

$e + A* \rightarrow \mathrm{e} + \mathrm{e} + A^{+}$ (2.3)

(c) $A + A* \rightarrow \mathrm{A} + A^{+}$ (2.4)

(d) $h\nu + A \rightarrow \mathrm{e} + A^{+}$ (2.5)

(e) $\dot{\mathrm{q}} + \mathrm{M} \rightarrow \mathrm{e}$ (2.6)

The ionization process when not controlled may lead to instabilities due to abrupt increase in the ionic species resulting in an exponential growth in electrons as well. This abrupt increase in the charged species concentration results in the following instabilities:

- Ionization Instability
- Stepwise Ionization Instability
- Electron Maxwellization Instability
- Instability in fast oscillating fields

A brief description of the aforementioned instabilities is provided in the following sections.

2.1.1 IONIZATION INSTABILITY

Ionization instability also called the thermal instability happens due to the strong exponential dependence of the ionization rate coefficient and thus the electron concentration in the reduced electric field (E/N). This is the most readily observed type of instability in high pressure system and, thus received a special attention in the literature. It is also one of the common forms of instability in MHD generator and hence was a topic of historical interests. The general criterion for the thermal instability was studied by Ecker et al.(Ecker, Kröll, & Zöller, 1964; Petit, J.-P.; Valensi, 1969; Petit, 1969), Solbes (Solbes, 1968),Velikhob et al. (Velikhov, Kovalev, & Rakhimov, 1987), Raizer (Raizer 1991), Hall et al.(Vitruk, Baker, & Hall, 1992), Wagner et al.(Wester, Seiwert, & Wagner, 1991), Chirokov et al.(A Chirokov et al., 2009), Kaganovich et al. (I. D. Kaganovich, M. A. Fedotov, 1994), Tanim (Islam, 2012), Rui and Kunz (R. Xu & Kunz, 2016) etc. A number of experiments was performed by Velikhob, Dykhne, and Shipuk; which supported the theory and mechanism (Velikhov, E. P.; Dykhne, A. M.; Shipuk, 1965; Velikhov, E. P.; Dykhne, 1963).

The ionization instability occurs very quick, such as in few microseconds. The following graph can be used to graphically demonstrate the thermal instability mechanism (Ecker et al., 1964):

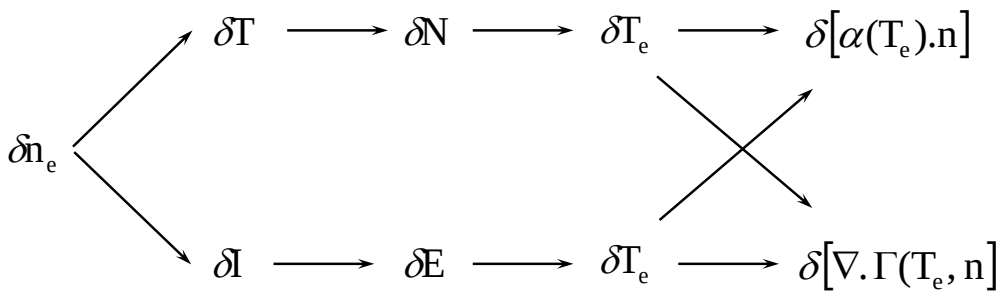

Where, n, N and T_e, T are the number density and temperature of the electrons and neutrals, respectively, I is the total current, E is the longitudinal electric field, α is the Townsend coefficient per unit volume and time, and Γ is the current density of the electrons. The solid line represents the typical influence which leads to the thermal instability of the discharge. To better explain this condition, thermal instability sometimes can be presented in terms of the following chain of reactions (Alexandre V. Chirokov, 2005)

$$\delta n_e \uparrow \rightarrow \delta(J_e E) \uparrow \rightarrow \delta T \uparrow \rightarrow \delta N \downarrow \rightarrow \delta(\frac{E}{N}) \uparrow \rightarrow \delta \Gamma_e \uparrow \rightarrow n_e \uparrow \qquad (2.7)$$

A small increment in the electron number density δn_e increases the electron current density δIe as electron drift makes up most of the discharge current. An increase in electron current density results in an increase in power dissipation, $\delta(J_e E)$, when electric field remains constant. In a consequence, an increase in power dissipation $\delta(J_e E)$ leads to an increase in gas temperature δT. As the pressure is constant, an increase in gas temperature, δT, decrease gas density, δn, and in turn increases the reduced electric field, $\delta(E/N)$. An increase in $\delta(E/N)$ causes an increase in electron temperature δT and hence increase the ionization processes that further increase δn. The aforementioned chain reaction is based on the assumption that the electric field remains unchanged during the fluctuation process.

In a more generic form, the thermal instability condition explains in such a way that the discharge is unstable is the rate of gas heating (υ_h) is higher than the rate of cooling (

υ_c), by convection and radiation. This is sometimes expressed in terms of logarithmic sensitivity as below (Ecker et al., 1964; Yuri P. Raizer, 1991).

$$\upsilon^* = \frac{d(\ln(\upsilon_i(E/N) - \upsilon_a(E/N)}{d(\ln(E/N))} \tag{2.8}$$

Where υ_i is the ionization frequency (s^{-1}) and υ_a is the attachment frequency (s^{-1}). The growth rate of thermal fluctuation, Ω

$$\Omega = \upsilon_h(\upsilon^* + 1) - \upsilon_c \tag{2.9}$$

If $\Omega < 0$ implies that discharge is thermally stable, and when $\Omega > 0$, implies discharge is not stable.

The study of electrothermal instability has diverted towards the suppression of this instability. Various researcher in the history comes out with different solutions to suppress the ionization or thermal instability condition. Among them the study by Hatori and Shioda (Hatori, S.; Shioda, 1974), Shapiro and Nelson (Shapiro, G. I.; Nelson, n.d.), Petit et al.(Petit, J.-P.; Billiotte, 1981) , Murakami et al. (Murakami, Okuno, & Yamasaki, 2005), and Chirokob (Alexandre V. Chirokov, 2005) is well known. Ecker also discussed the importance of external ballast resistor (Ecker, 1967), which is applied to all plasma circuit, and proposed the critical limit of external ballast resistor to suppress the ionization instability or thermal instability.

2.1.2 STEPWISE IONIZATION INSTABILITY

As the name suggests, this instability mechanism is governed by the stepwise nonlinear ionization of atoms by electron impact and often believed to be the underlying mechanism behind the Striations mechanism (Fridman & Kennedy, 2004b; Smirnov, 2001). This type of instability is related to the vibrational excitation of molecules. Therefore, this is not directly related to gas overheating or thermalization of the discharge. It refers to a condition when an increase of electron density leads to a growth in the concentration of excited species (electronically excited species), leading further ionization and results in a further increase of ion density. The increment of instability is directly related to the frequency of electronic excitation.

2.1.3 ELECTRON MAXWELLIZATION INSTABILITY

The electron energy distribution functions are restricted at high energies by different ionization channel. Maxwellization of electrons at higher electron densities provides larger amounts of high energy electrons and a related simulated ionization. Instability can be illustrated by the following sequence of events:

$$\delta n_e \uparrow \rightarrow \delta(\max wellizatio n) \uparrow \rightarrow \delta f(E) \uparrow \rightarrow \delta n_e \uparrow \qquad (2.10)$$

An increase of electron number density leads to Maxwellization, therefore, the growth of the electron energy distribution functions at high energies; intensification of dissociation; and finally, further growth of electron concentration. This instability

mechanism along with stepwise ionization may lead to striation or contraction at sufficiently high electron densities.

2.1.4 INSTABILITY IN FAST OSCILLATING FIELDS

Instability in the oscillating fields is similar to that related to the modulation instability in hot plasma. An example of this type of instability is the ionization instability of a microwave plasma in low pressure monoatomic gases. An increase of electron density in a layer (perpendicular to the electric field) provides growth of plasma frequency, which approaches the microwave field frequency and leads to an increase of electric field. The growth of the electric field results in an intensification of ionization and a further increase in electron density, which determines the instability. At higher pressure, temperature perturbation also plays a significant role in the development of the ionization instability.

2.2 THEORETICAL BACKGROUND ON PLASMA AND INSTABILITY STUDY

Any problem of plasma physics can be explained and solved based on either kinetic or fluidic based description. A brief description of the theoretical approach is included below to put the fundamentals of plasma and instability study.

The kinetic theory attempts to describe and predict the properties of gases and liquids in terms of the microscopic interactions and motions of its constituent molecules. The kinetic model is the fundamental way to describe plasma and producing a distribution function. For dilute gases, the Boltzmann kinetic equation has satisfactorily achieved the basic goals of kinetic theory. However, since it is based on the assumption of uncorrelated binary collisions, the Boltzmann equation gives a satisfactory description of the behavior

of sufficiently low density gases with short-range interactions only, and is inadequate to describe dense fluids and plasmas. In spite of numerous efforts, no one has yet succeeded in deriving a comparable equation for dense gases and liquids, so thus the strongly coupled Coulomb systems. In this case, particles interact via long-range screened Coulomb forces and their interaction energy dominates their average kinetic energy.

The Debye length characterizes the screening spatial scale of a charge in a plasma. The Debye length is the distance over which significant charge separation can occur(Fridman & Kennedy, 2004a)

$$\lambda_D = \sqrt{\frac{\varepsilon_0 \, \mathrm{k_B} / q_e^2}{n_\mathrm{e} \Big/ T_\mathrm{e} + \sum_j z_j^2 n_\mathrm{j} / T_\mathrm{i}}} \tag{2.11}$$

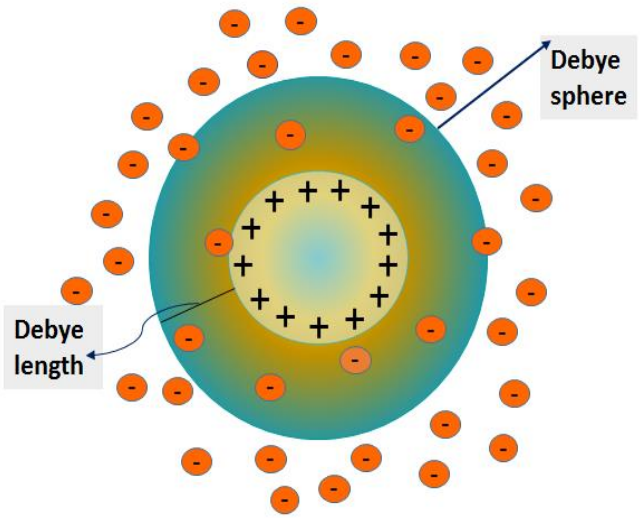

Figure 2.2 A graphical representation of Debye length and Debye sphere

where

λ_D is the Debye length,

ε_0 is the permittivity of free space,

k_B is the Boltzmann constant,

q_e is the charge of an electron,

T_e and T_i are the temperatures of the electrons and ions, respectively,

n_e is the density of electrons,

n_j is the density of atomic species j, with positive ionic charge $z_j q_e$

When the ion term is dropped

$$\lambda_D = \sqrt{\frac{\varepsilon_0 \, k_B T_e}{n_e q_e^2}} \tag{2.12}$$

As a simple illustration, a positive charge in a plasma (such as an ion) tends to be surrounded by an electron shell of typical radius λ_D, called the Debye sphere. The interaction of two particles on a scale smaller than the Debye length is called a collision. The mean-free-path, λ_{mf}, represents the typical distance over which, due to cumulative small angle collision, a particle is detected.

In collisional plasmas, short-range interactions dominate the evolution of the particle populations. They tend to establish locally a Maxwellian velocity distribution of particles, which can be written for k_{th} species as

$$f_k^{(0)}(v) = \left(\frac{m_k}{2\pi T_k} \right)^{3/2} \exp\left(-\frac{m_k v^2}{2T_k}\right) \tag{2.13}$$

where m_k is the mass of the particles and v is the velocity vector. The above equation represents the statistical velocity distribution of particles at equilibrium if its parameter, the temperature T_k, is the same for all the species of the system. When the mean

free path becomes larger than the density or temperature gradient scale-lengths of the system, it is more likely to deviate from the Maxwellian equilibrium.

A kinetic effect is an effect which tends to deviate the system from this equilibrium, when the temperature of the species is not equal or even when the velocity distributions differ from the Maxwellian. This is possible when the particle interaction is dominated by interactions of range much larger than the Debye length. These long-range collisions are called collective effects as their typical range involves many Debye spheres. In such systems, short-range collisions are rare, hence the mean free path is long and the collision frequency is short compared with the typical spatial and temporal scales of variation of the distribution functions. This characterizes the collisionless plasmas, where a plasma dominated by long-range interactions. The relaxation processes in a highly non-equilibrium collisionless plasma frequently involve kinetic instabilities. Such processes generate long-range plasma oscillations through growing electric or magnetic fluctuations. Hence, the system tends to return to equilibrium via the feedback of the self-generated fields on particles.

Collisionless plasmas are described by the Vlasov equation, which predicts the evolution of the distribution function:

$$\delta_t\ f_k + \frac{P}{m_k \gamma} \cdot \delta_r\ f_k + \mathrm{F}.\delta_p\ f_k = 0 \qquad (2.14)$$

where F is the Lorentz force. The electric and magnetic fields, E and B, are described by the Maxwell set of equations

$$\nabla . \mathrm{E} = \frac{\rho}{\varepsilon_0} \tag{2.15}$$

$$\nabla \times \mathrm{E} = -\partial_t B \tag{21.6}$$

$$\nabla . \mathrm{B} = 0 \tag{2.17}$$

$$\nabla \times \mathrm{B} = \mu_0 \mathrm{j} + \mathrm{c}^{-2} \partial_t E \tag{2.18}$$

Equation (2.5), (2.6), (2.7), and (2.8) respectively the Maxwell-Gauss, Maxwell-Thomson, Maxwell Faraday and Maxwell Ampere equations. Here c the light speed in vacuum, permittivity of vacuum and magnetic permittivity c, ε_0 and μ_0 respectively.

The solution of this set of equations can be unstable with respect to infinitesimal perturbations in the momentum distributions or the fields. In the most general case, non-equilibrium plasma states result in the growth of coupled electromagnetic and kinetic fluctuations. Various kinetic instabilities can be identified according to their spectral properties and the nature and number of the particle species at play. Among those few instabilities have been studied intensively. Figure 2.3 summarizes the major waves and instabilities in plasma.

2.3 LITERATURE REVIEW ON INSTABILITY STUDIES FOR MICROPLASMA DISCHARGES

This section will discuss two types of instability, such as NDR instability and Striations which is the topic of interest for the current research.

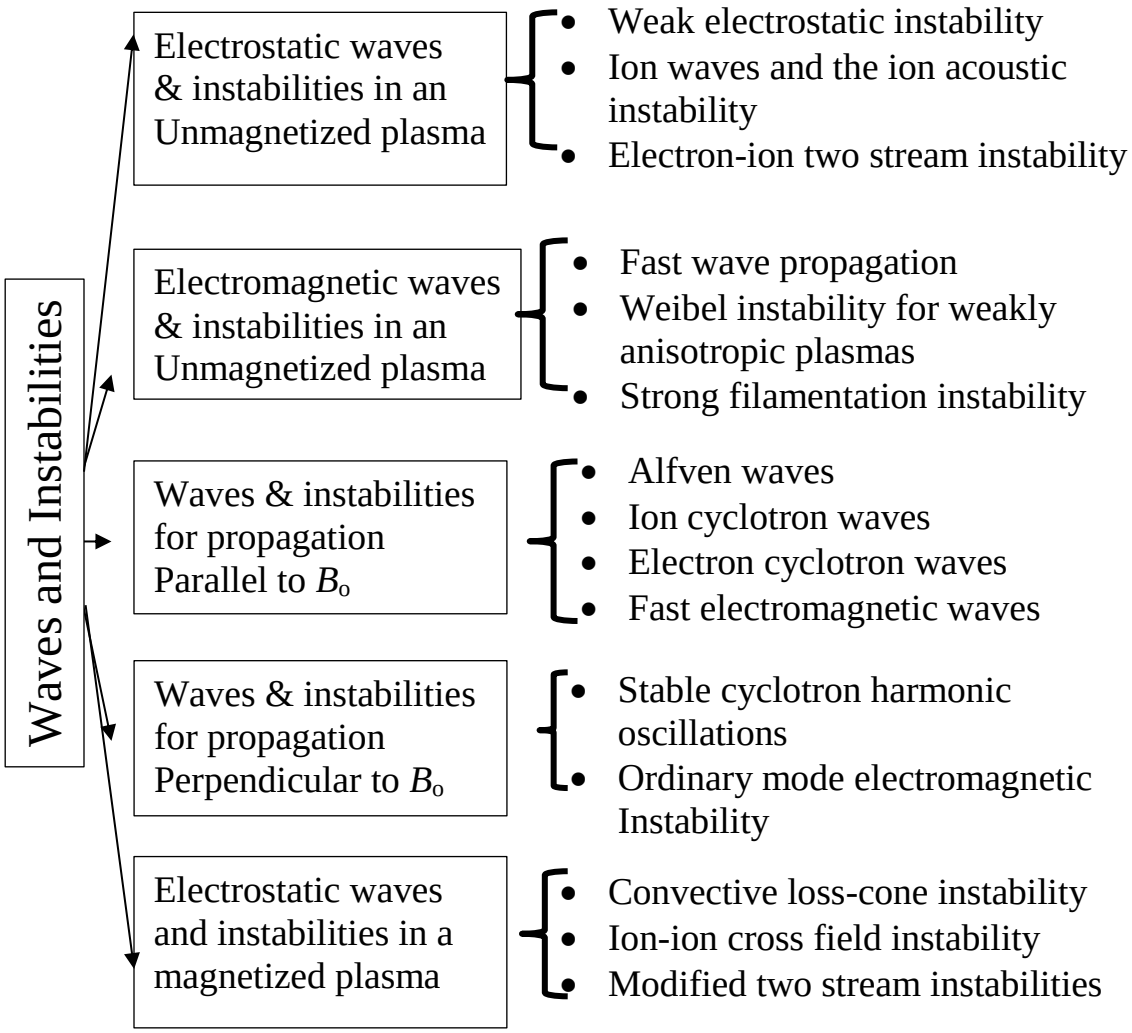

Figure 2.3 Kinetic waves and instabilities in uniform plasmas

2.3.1 NDR INSTABILITY

Negative differential resistance (NDR), i.e., a decrease in voltage with current increment, received considerable attention in the literature, primarily because it causes undesirable instabilities. The existence of NDR instability was hypothesized by Kaufmann, Gawhen, Chr. Van Geel, in 1900, 1934, and 1956; respectively. The first mathematical model was first described by Phelps, Petrovic and Jelenkovic in 1992 for a parallel plate geometry(Phelps et al., 1993a); and in similar time found by the work of Kolobov and Tsendin(Kolobov & Tsendin, 1992), Sijacic and Ebert(Šijačić & Ebert, 2002; Šijačić, Ebert, & Rafatov, 2005) , Kudryavstev and Tsendin(Kudryavtsev & Tsendin, 2002), Kolobov and Fiala(Kolobov & Fiala, 1994), Arslanbekob and Kolobov(Robert R Arslanbekov & Kolobov, 2003). Those studies were focused on low pressure system. Recent mathematical model can be found by the work of Chabert, Lazzaroni, Rousseau for microhollow cathode discharge(P. Chabert, Lazzaroni, & Rousseau, 2010a); Rousseau and Aubert for medium pressure system; Aubert et al. for microdischarges(Aubert et al., 2007a); Du, Mohr, Luggenhölscher and Czarnetzki for micro thin cathode discharges (Du, Mohr, Luggenhölscher, & Czarnetzki, 2011); Stefanovic et al for microdischaares(Petrovic, Stefanovic, Vrhovac, & Zivkovic, 1997; Stefanović et al., 2011a); Qin et al. for hollow cathode discharges(Y. Qin, He, Jiang, Xie, & Ouyang, 2014; Yu Qin, Xie, Zhang, & Ouyang, 2016); Wolllny et al. for micothin cathode discharges; and for microplasma discharges(R. Mahamud & Farouk, 2016; Rajib Mahamud & Farouk, 2013).

The experimental work of NDR instability is not comprehensive in the literature. It is until recently when Stefanovic et al, Aubert et al.(Rousseau & Aubert, 2006; Stefanović

et al., 2011a), and others author pursued experiment work on NDR instability (R. Mahamud & Farouk, 2015; Rajib Mahamud & Farouk, 2013). Recent work on NDR instability can be found in the following references (Fu, Verboncoeur, Christlieb, & Wang, 2017; Yu Qin et al., 2016).

2.3.2 STRIATIONS

Striations are the stratification of the positive column into a periodic glow and dark pattern for dc glow discharge and have studied significantly in the literature (compared to NDR instability). The first observation of striations was found from the notebook of Michael Faraday in 1830. It can be observed both as standing, for molecular gases, and moving for monoatomic gases. The standing striation was reported by Abria in 1834(M, 1843), whereas the moving striation was reported by Wullner in 1874 for hydrogen (Wullner A, 1874) and by Spottiswood in 1874 for other gases (H_2, N_2, and O_2) (Spottiswoode, 1874)(Spottiswoode, 1876).

The experimental and theoretical study of striations has also received some attention throughout the 19^{th} century by a number of notable physicists. Among them, Sir J. J. Thompson, in 1909, hypothesized that the periodical electric field associated with striated pattern permits the replenishments, with the least total expenditure of energy, of the electrons lost along the path of the discharge either by diffusion to the walls of the tube or by attachment to positive ions or neutral molecules (Thomson, 1909) (Thomson, 1929) (Zeleny, Physics Labqratqry, & Univfrsity, n.d.). However, it should be noted the moving striations has received a more attention compared to that of standing one. Kikuchi studied moving striations in Neon tube (T. Kikuchi, 1921); Chow and Fox studied in Argon tube (Chow, 1931); Fox G studied both in Argon and Neon (Fox, 1930)(Fox, 1931) ;Pekarek

published theory of moving striations based on waves theory (Pekárek, 1957); moving striations in a low pressure mercury vapor was studied by Foulds (FOULDS, 1956); Oleson and Cooper experimentally measured velocity of moving striations as 25~500 m/sec at very low pressure (Oleson & Cooper, 1968); Perina and coauthors performed a direct solution for low pressure helium discharge with experimental comparison (Peřina, Rohlena, & Růžička, 1975); Gentle performed theoretical and experimental study of moving striations in Argon based on fluidics approach (Gentle, 1966); David Swain worked on for low pressure Ar discharges (Swain, 1971).

The observation of striations is very common in DC plasma system and a number of contradictory theories is available in the literature. Some of the well-known theories are presented below:

- Vlasov, in 1962, developed a theory of striations based on the kinetic equation of a collisionless plasma (Vlasov, 1968). Therefore, it disregards collision with neutral atoms, the ionization, and the recombination happening in the discharge. However, striations only happen when tens of electron mean free path lengths are contained between adjacent striae heads. Therefore, the kinetic equation of collisionless plasma cannot be applied to describe the periodic structures of the strata.
- Gordeev, Gertsenshtein attempted to connect the striations as a Langmuir oscillation of the electrons and the ions (G. V. Gordeev, 1954)(Gertsenshtein, 1952). Gordeev obtained the condition for the excitation of ion-acoustic waves by a current flowing through the plasma. The existence of such an excitation in a positive column also found in the experiment. However, striations are observed for a condition when the ion sound cannot be excited as a result of a frequent collision between the ions and neutral atoms.

It was found that striations and ion sound have different natures due to the difference in the frequency spectra and wave dispersion.

- Pekarek and his coworkers attributed striations due to deviations from quasineutrality of the plasma (Rohlena, Růžička, & Pekárek, 1972). The need for regarding striations as quasineutral waves were also noted by Druyvesteyn (Druyvesteyn & Penning, 1940).
- Chapkin attempted to interpret striations as waves of electron temperature Te, assuming their concentration to be constant (I. M. Chapnik, 1957). The variation of Te was determined in this case not from the energy equation, but from the continuity and motion equation. However, such theoretical premises contradict the experimental data and exclude from consideration certain essential phenomena and they were unsuccessful.
- Some authors interpret striations as ionization-diffusion relaxation oscillation, such as Ph.D. dissertation of Nedospasov published in 1964 (A. V. Nedospasov, 1964). This explanation, however, is not valid near the stratification boundaries and does not indicate in which cases the column becomes stratified and in which case it remains homogeneous. Investigation near the existing boundaries and data on striations excitations show that the striations are a manifestation of the vibrational instability of the discharge plasma.

Review work on striations has been performed by Nedospasob (Artur V Nedospasov, 1968), Pekarek (Pekarek, 1968), and Oleson (Watanabe & Oleson, 1955); by Landa in 1980; by Kolobov in 2006. Recent work on striation can be found by Tochikubo et al (Tochikubo, Shirai, & Uchida, 2011), Fujiwara et al. (Fujiwara et al., 2016).

2.4 MATHEMATICAL MODELING APPROACHES FOR SIMULATING NON-THERMAL PLASMA DISCHARGES

The modeling of plasma discharges is not new and has studied in the literature, though most of the study was for a low pressure system. Three different modeling approach can be found to model the discharge physics, such as fluid based approach, Particle-in-cell approach, and Hybrid approach. The choice of modeling approach can be varied from statistical mechanics to continuum mechanics depending on the Knudsen number, which can be defined as $K_n = \lambda / L$, where λ is the mean free path, and L is the representative physical length scale, characterize whether the statistical mechanics or the continuum mechanics formulation of fluid dynamics model should be taken into account for the modeling of discharge. The regime in which $K_n << 1$ is known as the hydrodynamic regime while that in which $K_n >> 1$ is known as the Knudsen regime. In the former, the gas obeys the Navier-Stokes equations and of continuity equation of hydrodynamics while in the latter, rarefied gas dynamics apply.

2.4.1 KINETIC MODEL

Kinetic models generate the particle distribution functions as an output of the simulation. In addition, the electron energy distribution is used to calculate the electron transport (mobility and diffusivity) and electron impact reaction rate coefficients. Whereas, averaging over distribution functions results in number density, velocity, and the average energy of the species. Kinetic simulation is more accurate than fluid simulations, especially for low pressure. However, it is more computationally expensive when compared to fluid simulations. The kinetic model can off two kinds based on solution approach:

- Particle in cell with Monte Carlo Collisions (PIC-MCC)
- Direct simulation Monte Carlo (DSMC)

The Boltzmann equation essentially describes the plasma particle kinetics and can be expressed as

$$\frac{\partial f_k}{\partial t} + v \cdot \nabla f_k + a_k \cdot \nabla_v f_k = C_s(f) \tag{2.19}$$

The PIC-MCC simulations solve the Boltzmann equation. In the PIC/MCC method, a collection of particles is followed by space and time taking into account particle-particle and particle-wall interactions as well as the effect of the self-consistently determined space charge field. Whereas, the Direct Simulated Monte Carlo (DSMC) method is the Monte Carlo method for simulation of dilute gas flows on a molecular level, i.e., on the level of individual molecules. One of the basic criteria of DSMC method is that the motion of simulated molecules can be decoupled from their collisions over a time step. The size of the time step is selected to be a small fraction of the mean collision time, $\Delta t = \pi\gamma/(2\bar{u})$, where $\bar{u}$ is the most probable speed and γ is the mean free path.

2.4.2 FLUID MODEL

Most of the phenomenon of physics and visible matter can be studied under the fluid dynamics description. Fluid dynamics approach can explain the most complicated problem of physics and astrophysics. In plasma modeling, fluid dynamics approach has an important role as well. Fluid dynamics approach has several benefits as described by Richard Fitzpatrick:

- First, fluid equations involve fewer dimensions than the Vlasov equation. That is, three spatial dimensions instead of six phase-space dimensions. This advantage is especially important in numerical simulations.
- Second, the fluid description is intuitively appealing. It is easy to understand the significance of fluid quantities such as density and temperature, whereas the significance of distribution functions is far less obvious. Moreover, fluid variables are relatively easy to measure in experiments, whereas, in most cases, it is extremely difficult to measure a distribution function accurately. There seems a remarkably little point in centering our theoretical description of plasmas on something that we cannot generally measure.
- Finally, the kinetic approach to plasma physics is spectacularly inefficient. The species distribution functions f_k provide vastly more information than is needed to obtain the constitutive relations that close Maxwell's equations. After all, these relations only depend on the two lowest moments of the species distribution functions.

In plasma fluid theory, a plasma is characterized by a few local parameters--such as the particle density, the kinetic temperature, and the flow velocity--the time evolution of which are determined by means of fluid equations. These equations are analogous to, but generally more complicated than, the equations of gas dynamics. Fluid equations are conventionally obtained by taking velocity space moments of the kinetic equation

$$\frac{\partial f_k}{\partial t} + v \cdot \nabla f_k + a_k \cdot \nabla_v f_k = C_s(f) \tag{2.19}$$

$$a_s \cdot = \frac{e_s}{m_s}(E + v \times B) \tag{2.20}$$

In general, it is extremely difficult to solve the kinetic equation directly, because of the complexity of the collision operator. However, there are some situations in which collisions can be completely neglected. In such cases, the kinetic equation simplifies to give the so-called Vlasov equations as mentioned in the previous section in Equation (2.4)

It requires solving the equations of magneto-hydrodynamics (MHD) which comprises conservation laws of mass, momentum, energy, and magnetic flux.

$$\frac{\partial \rho}{\partial t} + \nabla.(\rho v) = 0 \tag{2.21}$$

$$\frac{\partial (\rho v)}{\partial t} + \nabla.[\rho v v - \mathrm{BB} + \mathrm{P}^*] = 0 \tag{2.22}$$

$$\frac{\partial E}{\partial t} + \nabla.[(E + \mathrm{P}^*)v - \mathrm{B(B.v)}] = 0 \tag{2.23}$$

$$E = \rho v^2/2 + e + B^2/2 \tag{2.24}$$

$$\mathrm{P}^* = \mathrm{P} + B^2/2 \tag{2.25}$$

Where ρ is mass density, v is velocity, B is magnetic field, E is total energy, and P* is total pressure.

2.4.3 HYBRID MODEL

Hybrid models have been developed to preserve the accuracy and information of kinetic models and at the same time increase the computational efficiency. For example,

Fluid-EEDF hybrid is a fluid description of the discharge, except that the electron transport properties and electron impact reaction rate coefficients are obtained from a calculation of the electron energy distribution function (EEDF). Which is found by solving the Boltzmann equation either directly or by the Monte Carlo scheme. The fluid module can include the species mass, momentum, and energy continuity equation, and Poisson equation for the electric field. Space and time variation of the electric field is used to solve the Boltzmann equation, which comes from the fluid simulation. The fluid model also provides the electron density to taken into account the electron-electron collision. In the hybrid model, the overall simulation alternates between the fluid model and the EEDF model until convergence.

2.5 PLASMA MODELING

2.5.1 ELECTRON ENERGY DISTRIBUTION FUNCTION

The electron energy distribution functions is very much a fingerprint of the discharge. For low pressure discharge, the rates of collisional and radiative process are mainly governed by the electron distribution function (EDF). Therefore, the electron distribution function is needed for the construction of reliable models for the radiation or ionization balance in nonequilibrium plasmas. Below is the description of the several electron energy distribution functions.

2.5.1.1 MAXWELLIAN DISTRIBUTION FUNCTION

The Maxwellian distribution function can be used when the system is in thermodynamic equilibrium. Therefore, the Maxwellian distribution can be used for a system with high ionization degree. It is derived for a system with thermal equilibrium condition

$$f(v) = n(\frac{m}{2\pi kT})^{3/2} \exp(-\frac{mv^2}{2kT}) \quad (2.19)$$

For a degree of ionization above 10^{-4}, the electron-electron collision drives the electron distribution function in a Maxwellian distribution shape. However, the inelastic collision of electrons with heavy particles lead to a drop of the EEDF at higher energies. In this case, Druyvesteyn distribution function gives more accurate results for a lower ionization degree.

2.5.1.2 DRUYVESTEYN DISTRIBUTION FUNCTION

The Druyvesteyn EEDF is based on a constant (electron energy independent) cross section, the Maxwellian EEDF is based on constant collision frequency. The distribution functions assume that elastic collisions dominate, thus the effect of inelastic collisions (e.g., excitation or ionization) on the distribution function is insignificant. In such a case, the distribution function becomes spherically symmetric.

$$f(v) = n(\frac{m}{2\pi kT})^{5/2} \exp(-\frac{mv^2}{2kT}) \quad (2.19)$$

In elastic collisions with neutral atoms, the electrons' direction of motion is changed, but not their energies (due to the large mass difference).

The profile of distribution (either Maxwellian or Druyvesteyn) depends on kinetic theory, and on details of the collision cross section and on the external forces applied to the plasma particles. A Maxwellian distribution of electron velocities occurs if the collision frequency is independent of velocity, v.

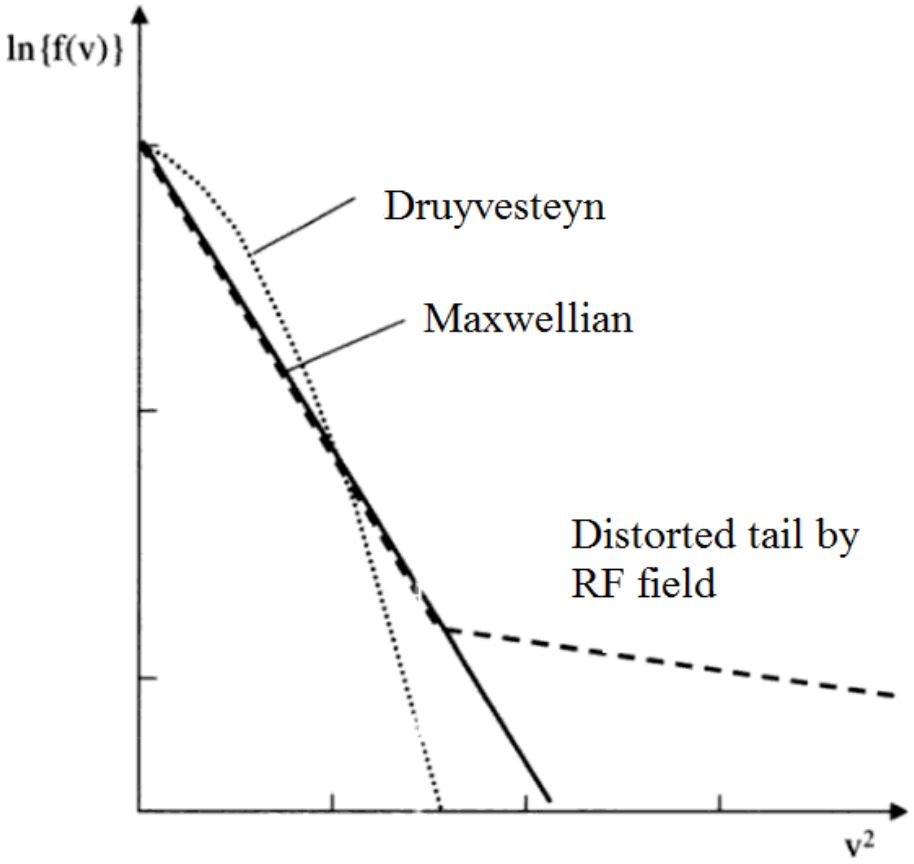

Figure 2.4 Maxwellian and Druyvesteyn velocity function

Electron-electron collisions, where the collision frequency scales as v-3, also tend to produce a Maxwellian distribution. For the Druyvesteyn distribution, the distribution function scales as exp(-cv4), therefore has a fewer high energy electron than a Maxwellian. A Druyvesteyn distribution occurs when the collision frequency is directly proportional to velocity and when the electrons are heated by a weak electric field. Druyvesteyn distribution is sometimes happens in gases whose cross section increases with velocity. In addition, for inelastic collision with a high energy cross sectional threshold can also deplete the number of high energy electrons and produce a Druyvesteyn like distribution.

The electron velocity distribution function often depends on the degree of ionization. High energy plasma sources typically have an ionization fraction above 10-3,

which is sufficient for electron-electron collisions to be the dominant mechanism for energy exchange and produce a Maxwellian distribution of velocities. Sometimes external forces acting on particles of particular energy can also distort the distribution function form a Maxwellian. Such an example of distorted electron distribution occurs when strong radio frequency (RF) electric fields act preferentially on a small number of superthermal electrons. In a consequence, the high energy electron tail in enhanced and an increased rate of ionization will be observed as compared to a Maxwellian distribution.

2.5.2 MULTISCALE MULTIPHYSICS MODELING

The multiphysics simulation of instability is more rigorous because it requires a special attention to the reaction kinetics, cross sectional data and nonequilibrium electron energy distribution function. The modeling of plasma involves species conservation equation for charged particles and neutrals, charge particles kinetics, Maxwell equation, surface and volume reactions. The multiscale model is considered which resolved different time and spatial scale simultaneously and self-consistently. All this aspect of multiphysics model into one combined does not work, therefore a different solver is generally used to cover the multi aspect of physics.

In addition, the modeling of plasma imposes several more difficulties. They are plasma module is stiff in space (space charge separation needs to be taken into account), it has a large degree of freedom, a strong coupling between electron energy and electric field and the plasma chemistry data. The complexity of plasma modeling lies in the fact that it combines elements of reaction engineering, statistical physics, fluid mechanics, physical kinetics, heat transfer, mass transfer, and electromagnetics. The net result is a true multiphysics problem involving complicated coupling between the different physics. The

physics interfaces include all the necessary tools to model plasma discharges, beginning with a Boltzmann Equation, Two-Term Approximation solver that computes the electron transport properties and source coefficients from a set of electron impact collision cross sections.

The various constitutes of a self-consistent plasma model comprise following sections:

- Electrostatics**:** To compute the electrostatic field in the plasma caused by separation of space charge between the electrons and ions. This is governed by the Maxwell equation. In absence of any magnetic field, it is governed by poison equation for the electric field. Poisson's equation is created from Coulomb's law and Gauss's theorem. It is a partial differential equation with broad utility in mechanical engineering, electrostatics and theoretical physics.
- Heavy Species Transport: A mass balance interface for all non-electron species. This includes charged, neutral, and electronically excited species.
- Boltzmann Equation, Two-Term Approximation: To compute the electron energy distribution function
- Electrical Circuits: To taken into account the external electrical circuit to the discharge
- Transport: Different transport's play a role in plasma modeling such as
    - Electric fields (Instantaneous)
    - Electron energy (<nsec)
    - Electron transport (nsec)
    - Ion transport (microS)

- Excited species transport (0.1msec)
- Neutral gas temperature/flow (msec)

The different range of characteristic times creates a computational difficulty and plasma modules are generally stiff in time.

2.5.3 LITERATURE OF MATHEMATICAL MODELING APPROACH

The modeling and simulation approach has recently become popular in proportional to the computational power for the study of discharge behavior and the investigation of different plasma reactors. Though diagnostics is an essential tool for characterization, it poses limitation for reaction kinetics study and temperature measurement for many applications and high pressure system. Paradoxically, the study of reaction kinetics would be more interesting because it determines the mechanism of discharge in versatile reactors. Instabilities observed in nonequilibrium plasma are such a topic which cannot be clearly understood from a theoretical point of view or experimental studies.

In the PIC/MCC method, a collection of particles is followed by space and time taking into account particle-particle and particle-wall interactions as well as the effect of the self-consistently determined space charge field. Fluid (or continuum) models, which are based on a hydrodynamic description of the plasma are less computationally demanding and more popular approach. The continuum based approximation has been primarily investigated in the literature in the following reference: (Almeida, Benilov, Cunha, & Gomes, 2017; Tanvir Farouk, Farouk, Staack, Gutsol, & Fridman, 2006; Hasan, Antao, & Farouk, 2014; Hong, Liu, Zhang, Niu, & Han, 2015; Hsu & Graves, 2003; F. Iza & Hopwood, 2005; Li, Ebert, & Hundsdorfer, 2010; Liu, Bruggeman, Iza, Rong, & Kong,

2010; Peng et al., 2017; U Ebert, F Brau, G Derks, W Hundsdorfer, C-Y Kao, C Li, A Luque, B Meulenbroek, S Nijdam, 2010; U Ebert1, 2, F Brau3, G Derks4, W Hundsdorfer1, C-Y Kao5, C Li2, A Luque6, B Meulenbroek7, S Nijdam2, 2008; Qiang Wang et al., 2006; Wormeester, Nijdam, & Ebert, 2011; X. "Peter" Xu & Kushner, 1998; C. Zhang, Shao, Ren, Yan, & Niu, 2016)etc.. Where Bogaerts et al.(Bogaerts & Gijbels, 1995), Lieberman et al.(Wu & Lieberman, 1998), extensively worked with hybrid Monte Carlo based simulation for DC glow discharge system.

The comparison between fluid and PIC/MM-based was elaborately presented in the literature by Surendra et al.(Surendra, Graves, & Jellum, 1990), Derzsi et a l.(Derzsi et al., 2009), Lymberopoulos et al.(Lymberopoulos & Schieber, 1994), Rafatov et. al.(Rafatov, Bogdanov, & Kudryavtsev, 2012), Diomede et al., and Becker et al. , etc. In the literature, the hybrid model is sometimes referred as better than the continuum based model in predicting electric and spatial characteristics of the discharge. The electron densities obtained from the continuum have scattered over several orders of magnitude than the experimental data. The mathematical modeling performed in this study primarily focused on microplasma system which operates at atmospheric and higher pressure with the characteristic length of micrometer ranges. Therefore, the Knudsen number reach in such a condition that $K_n << 1$ and continuum based approximation can be applied.

2.6 EXPERIMENT ON MICROPLASMA DISCHARGES

The microplasma concept is a high pressure scaled version of the common low pressure plasma system that was proposed recently (Karl H Schoenbach, El-Habachi, Shi, & Ciocca, 1997; Tachibana, 2006). The original idea was to generate plasma of required

size and property at the required location for each specific application. Atmospheric pressure microplasma system can replace many of the current low pressure applications with low power and space consumption. Research activies on the microplasma system recently gained attention for different applications with respect to their (i) generation methods (Karl H. Schoenbach, El-Habachi, Moselhy, Shi, & Stark, 2000) (ii) diagnostics and simulation (Tanvir Farouk, Farouk, Staack, Gutsol, & Fridman, 2007; Gregório, Hoskinson, & Hopwood, 2015; David Staack et al., 2005a; Qi Wang, Sun, Zhang, Liu, & Wang, 2013; Z. Zhang, Petersen, & Shneider, 2010), and (iii) new application and technologies (David B Go et al., 2009; Felipe Iza et al., 2008a; R Mohan Sankaran & Giapis, 2003).

However, instability in the discharges is one of the major barriers to reaching the goals of atmospheric pressure plasma generation and applications.

One of the major instabilities observed in the atmospheric pressure system is the thermal ioniozation instability that was studied by Staack et al (D. Staack, Farouk, Gutsol, & Fridman, 2009a). Microplasma is an established method in this regard to obtain nonthermal plasma discharges at atmospheric or higher pressure. In recent times, NDR instability is being considered as a major barrier to obtain a stable dischrage for a wide range of current for a microplasma discharge system (Aubert et al., 2007a; P. Chabert, Lazzaroni, & Rousseau, 2010b; Du, Mohr, et al., 2011; He, Ouyang, He, & Jia, 2012; Rajib Mahamud & Farouk, 2016; Y. Qin et al., 2014). Research activies on the instability in the NDR region have been pursued mostly through mathematical and numerical analysis (R.R. Arslanbekov & Kolobov, 2005; Hasan et al., 2014; Lazzaroni & Chabert, 2011; Rousseau & Aubert, 2006). However, the experimental study is not sufficient and the purpose of the

experimental section of this study is to characterize the NDR region to enhance the microplasma device operation.

To characterize the instability phenomenon in plasma discharges, the present study has two primary experimental objectives. Firstly, we proposed to realize the suppression of NDR instability concept through external circuit modification. Secondly, we introduced the concept of ion detection in order to leverage the NDR instability in micro plasma discharge that is otherwise challenging at atmospheric or high pressure conditions. In addition, an application of atmospherics pressure microplasma is presented in this study. An atmospheric pressure corona plasma is applied to the electrospinning process to increase the piezoelectricity of PVDF fiber. The details of the experimental setup will be discussed here with the results and discussion will be included in the Appendix.

2.7 NONEUILIBRIUM-NONTHERMAL PLASMA APPLICATIONS

Nonequilibrium and nonthermal plasmas are the most energy efficient as it is not necessary to put energy equally to all degrees of freedom, i.e., translational, rotational, and vibrational molecules, but only to that degree of freedom that can efficiently create the desired final reaction products (Nijdam S, Bruggeman P, 2012). Due to these characteristics, the nonequilibrium plasmas are increasingly used for chemical processing of gases, plasma enhanced combustion, surface treatment, biomedical applications, synthesis of gases and conversion, lighting, sterilization, water treatment, etching, functionalization of surfaces, nanomaterial synthesis, and synthesis of oxide nanowires etc.(Mozetič et al., 2015) (Aleynik et al., 2012)(Suhr, 1989)(Han, 2013)(Kruger, Owano, Laux, & Zare, 1997). The applications of nonequilibrium plasma can be more, however, in this chapter, some of the recent and growing applications are mentioned briefly.

Spark system for combustion is a thermal equilibrium plasma configuration which has been widely used for years. Recently, the nonequilibrium plasma for ignition and combustion control has gained increasing interest due to the possibility of plasma-assisted approaches for ignition and flame stabilization (Starikovskaia & Starikovskii, 2010)(Ju et al., 2016) (L. Xu, Garner, Tao, & Keener, 2017). It was also found that a nonequilibrium plasma formed by the discharge is an effective way to reduce the specific fuel consumption as well as the concentration of nitrogen oxides in the engine exhaust gases (Tropina, Kuzmenko, Marasov, & Vilchinsky, 2014). The kinetic study showed that radicals produced by dissociation of the reactants in plasma plays an important role in initiating the reaction, where the oxidation reaction was reduced to a lower temperature with plasma discharges compared to the case without plasma (Togai, 2015)(Choi, Yin, Adamovich, & Lempert, 2011)(Takashima, Yin, & Adamovich, 2012)(Togai, Tsolas, & Yetter, 2016). Nanosecond discharges have been considered as an energy efficient option for uniform and reduced emission combustion (Pancheshnyi, Lacoste, Bourdon, & Laux, 2006; Pineda et al., 2015; Tropina et al., 2014). Nanosecond pulse discharges have been demonstrated recently for flame stabilization at low and high frequencies (Kim, Godfrey Mungal, & Cappelli, 2010; Mintoussov, Pancheshnyi, & Starikovskii, 2004; Pancheshnyi et al., 2006; Pilla et al., 2006). Microwave-enhanced ignition technology could provide an effective means of enabling increasingly lean combustion in spark-ignited engines, allowing reduced throttling losses and improved efficiency (DeFilippo et al., 2011; Kettner, Nauwerck, Spicher, Seidel, & Linkenheil, 2006). However, ignition systems based on the nanosecond pulsed discharge suffer from noise problems. Generation or enhancement of plasma in a combustion environment through the use of microwaves, radio frequency waves (RF), and

dielectric barrier discharge (DBD) has been shown to improve ignition characteristics and flame speeds under a variety of conditions and is thus an active area of research (Mariani & Foucher, 2014; Wolk et al., 2013). However, one of the main disadvantages of this systems is a need to create a preionization zone with the following addition of the microwave or RF discharge energy, which also complicates the overall design of the ignition system.

Detonation has a great potential to energy conversion due to the fact that rapid combustion does not allow fuel/air mixture to expand and leads to a constant volume process. The constant volume system (pulse detonation engine) provides a better fuel efficiency than the conventional constant pressure system, i.e., gas turbine. However, the major challenges are starting the detonation which requires a high energy initiators. In a different approach, Starikovskiy proposed nonequilibrium plasma discharge for the initiation of DDT by means of preliminary gas excitation and by the reduction of the chemical induction time in the mixture (Starikovskiy, Aleksandrov, & Rakitin, n.d.). It was shown that the synchronization of the ignition of different parts of the gas using gas discharge excitation could lead to a sufficient reduction in the DDT length and time. A separate study of Want et al. suggested that plasma discharge can reduce the residence time of the low speed combustion stage (F. Wang et al., 2004). The experimental investigation high voltage nanosecond pulse discharge for detonation initiation was also performed by Kukaev et al., where three modes of flamefront propagation, deflagration, transient detonation and Chapman-Jouguet (CJ) detonation were observed (Kukaev, Tsyganov, Zhukov, Starikovskaia, & Yu Starikovskii, n.d.). Similarly, experiments were carried out by the group of Lieberman to determine the effectiveness of corona discharge to initiate

detonation in a short tube (D. Lieberman, Shepherd, Wang, & Gundersen, 2005). Here, 90kv voltage pulse was applied for 50 ns which produces corona discharge with many radial streamers. Their results indicate that their plasma initiator can initiate a detonation up to 45% N2 dilute compared to a spark which is limited to 40% N2 dilution. By using obstacles to enhance DDT, they increased this dilution upto 60%. However, one of the limitation is that the corona discharge is an excellent method to achieve very rapid combustion of the region near the electrodes. An additional means appeared to be needed to accelerate the resulting flame to a detonation for mixtures with greater than 40% nitrogen dilution.

In a recent collaborative effort, experiments have been conducted in the University of Southern California with the researchers at the Naval Postgraduate School, Wright Patterson Air Force Research Laboratory, Stanford University, Ohio State University, and the University of Cincinnati for testing and evaluating the transient plasma for pulse detonation ignition (Cathey et al., 2007). Where the transient plasma was produced by a DBD actuator with a pulse duration of less than 100 ns. The results suggest that the short timescale of the pulse prevents formation of an arc and a voluminous uniform array of streamer for the ignition. In this study, a reduction in delay times in both static and flowing system was observed under transient plasma ignition. They proposed that the energetic electrons in the highly nonequilibrium electron energy distribution of the streamers cause dissociation of hydrocarbon chain molecules, producing active radicals throughout the ignition volume (Ganguly & Parish, 2004). Therefore, as it reduces the ignition delay time, it can reduce the Deflagration to Detonation (DDT) transition time and can ignite under leaner condition. They believed that it allows the use for high repetition rates, high altitude

operation, and for reduced NOx emission. In a test conducted by Lefkowitz et al. predicts a finer details where that both richer and leaner ignition was achieved for aviation gasoline air mixture by nanosecond pulse DBD (Mani et al., 2015). In addition, their study obtained a larger reduction of ignition delay for aviation gas mixture than that of automotive multiple capacitive discharge system. Microwave plasmas have significant technical benefits due to the fact that it generates a very high frequency oscillations of the electric field, and hence, electrons, consequently producing high concentration of radicals at lower electron temperature. A series of experimental study by Ikeda et al. and researchers at West Virginia University have shown that microwave plasma have shown the potential to enhance the fuel economy and ignition characteristics (Ikeda, Nishiyama, Katano, Kaneko, & Jeong, 2009; Ikeda, Nishiyama, Wachi, & Kaneko, 2009; Mcintyre, Thompson, & Smith, 2001; Pertl, Clarke, & Smith, 2011; Stevens, Pertl, Hoke, Schauer, & Smith, n.d.). Though DDT time and length was not significantly improved, microwave coupling can increase the flame speed, reduces the lean combustion limit and ignition delay time with a significantly lower microwave energy (Fuh, Wu, & Wang, 2016; Stevens et al., n.d.). It enables noble applications of detonation for efficient power conversion and small scale power devices.

DBD plasma actuators are very powerful devices that make novel aerodynamic applications possible. Some of the applications are: pitch and roll control of aircraft can be made without a movable control surface on the wing; streamwise vortices can be generated without mechanical vortex generators; wall-normal jets can be generated without a pneumatic source, which can be vectored in any direction on demand; and lift can be augmented as and when required without slats or flaps attached to the wing.

CHAPTER 3
MATHEMATICAL MODELING AND NUMERICAL SCHEME

3.1 BACKGROUND

This chapter presents the mathematical and numerical modeling approach to model the plasma discharges. It has different subsections, such as plasma dynamics, transport, gas phase reaction kinetics, surface reaction kinetics, and an external circuit solver section.

3.2 MATHEMATICAL MODEL

3.2.1 PLASMA DYNAMICS

The objective of the plasma dynamics system is to solve the species transport (electrons, ions and neutral), electric field, and electron energy equations. The conservation equation for the electrons and the ions and the neutrals are defined by the continuity equation. The drift diffusion approximation was used for flux definition. The equations are described as below.

$$\frac{\partial n_e}{\partial t} = -\nabla \cdot \left(-D_e \nabla n_e + n_e \mu_e \vec{E}\right) + \dot{n}_e \tag{3.1}$$

$$\frac{\partial n_i}{\partial t} = -\nabla \cdot (-D_i \nabla n_i + n_i \mu_i \vec{E}) + \dot{n}_i \tag{3.2}$$

Where n is the species number density, μ is the mobility, D is the diffusion coefficient, $\vec{E}$ is the electric field, and $\dot{n}$ is the source of the species produced or consumed due to ionization and recombination. The subscript e and i represent electrons and ions respectively.

The electron temperature can be obtained from the electron energy conservation equation. The electron energy equation consists energy gained by joule heating, and the energy lost in elastic and inelastic collision.

$$\frac{\partial}{\partial t}(n_e \varepsilon) + \nabla.\left[n_e \varepsilon \mu_\varepsilon \vec{E} - D_\varepsilon \nabla(n_e \varepsilon) \right] = \vec{j}_e.\vec{E} - \sum_j \Delta E_j K_i - 3\frac{m_e}{m_{neutral}} K_{el} k_B (T_e - T_g) \tag{3.3}$$

where, ε is the mean electron energy, μ_ε is the electron energy mobility, D_ε is the electron energy diffusion coefficient, ΔE_j and K_j are the energy loss due to inelastic collision j ε and corresponding reaction rate. m_e and $m_{neutral}$ are the mass of the electrons and neutral species respectively, K_{el} is the momentum transfer rate between the electrons and neutrals. k_B and T_g is the Boltzmann constant and gas temperature respectively. T_e is the electron temperature and is obtained from the electron mean energy, $T_e = 2\varepsilon / 3k_B$. The first term in the right hand side represents the energy gain due to electron joule heating and the second and third term represents the energy loss due to inelastic and elastic collisions respectively.

The electrostatic potential is obtained by solving the Poisson's equation which is given as:

$$\nabla^2\phi = -\nabla.\vec{E} = -\frac{e}{\varepsilon_m}(\sum_i q_i n_i - n_e) \tag{3.4}$$

Where ϕ the electrostatic potential, e is is the elementary charge, ε_m is the electrical permittivity of the medium, q_i is the charge number, n_i is the ion density and n_e is the electron density.

3.2.2 NEUTRAL TRANSPORT

The conservation equation for the neutrals is defined by the continuity equation with the drift diffusion approximation for fluxes.

$$\frac{\partial n_k}{\partial t} = -\nabla \cdot (-D_k \nabla n_k) + \dot{n}_k \tag{3.5}$$

Where n_k is the species number density, D_k is the diffusion coefficient, and $\dot{n}_k$ is the source of the species produced or consumed due to ionization and recombination.

The neutral gas temperature T_g obtained from the following form of the energy equation. It accounts the heating from elastic and inelastic collisions with electron, enthalpy of heavy particle reactions,

$$\frac{\partial(\rho c_p T_g)}{\partial t} = \nabla \cdot (\kappa_g \nabla T_g) + \dot{Q}_k + \sum_i \vec{j}_i \cdot \vec{E} + 3\frac{m_e}{m_{neutral}} K_{el} k_B (T_e - T_g) \quad (3.6)$$

Where ρ is the gas density, c_p is the specific heat, κ_g is the thermal conductivity of the gas, $\dot{Q}_k$ is the rate of change of gas temperature due to the chemical reactions associated with the heavy particles and elastic collisions and $\vec{\Gamma}_k$ is the flux of species k. The last two terms in equation (3.6) account for Joule heating due to the acceleration of ions in the electrostatic field having current density j_i and energy gain due to elastic collisions.

The background gas number density, N is obtained from the ideal gas law with the assumption of constant pressure.

$$N = \frac{P}{RT_g} N_A \quad (3.7)$$

where N_A is the Avogadro number and P is the ambient pressure.

3.2.3 GAS PHASE REACTION KINETICS

A gas phase kinetics solved the electron transport coefficients (electron mobility and diffusivity), electron induced reaction rates and also the source and sink terms required for the different species conservation equation. The transport coefficient (mobility and diffusivity) and rates of the electron induced reactions are calculated using the electron energy distribution function (EEDF) obtained as a solution of the Boltzmann equation and

using the two-term spherical harmonic expansion. The approach results in a four dimensional (3D in space and 1D in energy) EEDF.

$$\frac{\partial f_0}{\partial t} + \nabla . D_r \nabla f_o + \frac{1}{\upsilon}\frac{\partial}{\partial \varepsilon}\left(v\left[D_\varepsilon \frac{\partial f_0}{\partial \varepsilon} + V_\varepsilon f_o \right]\right) = S_f \tag{3.8}$$

Where ε is the total electron energy, φ is the electrostatic potential, Dr is the electron diffusion coefficient in physical; space, v is the electron transport collision frequency, De and Ve are electron diffusion and convection coefficient along the energy axis caused by the quasi elastic collisions and Sf is the source terms describing inelastic collisions. The EEDF for normalized to the electron density as, ne

$$n_e = \int_0^\infty f_0(\varepsilon)\sqrt{\varepsilon} d\varepsilon \tag{3.9}$$

In order to simplify the numerical efforts, we used the 'local field approximation'. According to the 'local field approximation,' all electron parameters can be considered to be functions of local electric fields. Based on this approximation, we calculate EEDF's as functions of the reduced electric field E/N (ratio of electric field to neutral density).

In this study, energy transport coefficient (mobility, diffusivity D_ε) were also obtained from the EEDF instead of using the $\mu_\varepsilon = \frac{5}{3}\mu_e$ and $D_\varepsilon = \frac{5}{3}D_e$ relationship. This relationship for the energy transport coefficients is typically obtained by assuming a Maxwellian EEDF, a constant momentum transfer frequency, and constant kinetic

pressure. It has been shown by Hagelaar and Pitchford that energy transport coefficients obtained from electron transport coefficient relationships differed by a factor of two from those obtained from EEDF solutions specially for monatomic gases. One dimensional lookuptable are generated for the reaction rates, electron transport and electron energy transport coefficients as a function mean electron energy. In this study, BOLSIG+ is used to estimate EEDF for different values of the reduced electric field.

The reaction rate, electron mobility, and electron diffusion coefficient are obtained by integrating the EEDF and are expressed as:

$$n_i = \int_0^\infty \sigma(\varepsilon)\sqrt{\varepsilon}\, f_o(\varepsilon) d\varepsilon \tag{3.10}$$

$$\mu_e = \frac{1}{n_e} \int_0^\infty D_r \sqrt{\varepsilon}\, f_o(\varepsilon) d\varepsilon \tag{3.11}$$

$$D_e = \frac{1}{n_e} \int_0^\infty D_r \sqrt{\varepsilon}\, f_o(\varepsilon) d\varepsilon \tag{3.12}$$

Where σ is the cross section, ε is the electron energy and f_0 is the electron energy distribution function. The cross section data as a function of electron energy for different electron induced reactions were obtained from LXcat website. The electron temperature can be determined by two different methods, such as the local field approximation (LFA) and solving the electron energy equation (EEE) as described in equation (3.3). In the local field approximation method (which is more popular in high pressure discharge modeling) the local reduced electric field (E/N) is used to obtain the electron temperature using a

tabulated data from the Boltzmann equation solver. However, solving the energy equation is a hydrodynamic approach which allows the use of the electron energy fluxes in the calculation of electron temperature and captures the strong gradients in electric filed and electron density.

Sakiyama and Graves studied the comparison between the local field approximation (LFA) and the electron energy equation (EEE) and discuss the importance of an electron energy equation than the simpler LFA to achieve converge solutions in the high power mode in RF discharges. However, LFA can correctly predict the existence of α-γ mode transition. (Sakiyama & Graves, 2007a)

3.2.4 SURFACE REACTION

The surface reaction in the mathematical model provides the boundary conditions for the different ions, radicals, and neutral species. It also determines the probabilities of returning fluxes of reactant from the surface which was incident on the surface (Dorai & Kushner, 2003; T. Farouk, Farouk, & Fridman, 2010). A general form of surface reaction is expressed either as below:

$$A_g + B_s \rightarrow C_g + D_s \qquad (3.13)$$

$$A_g + E_s \rightarrow F_d \qquad (3.14)$$

Where, the subscript g,s and d denotes gas species, surface species and deposited species respectively. The reaction rate for the reaction (3.13) in between species A_g and B_s on material m can be expressed as

$$R_m = K_i \Phi_{Am} \Theta_{Bm} \quad (3.15)$$

Where, K_i is the reaction probability or reaction rate coefficient for the ith species, Φ_{Am} is the incident flux of plasma species A on material m, Θ_{Bm} is the fractional occupancy of the surface species B_s. The surface reactions can be specified in terms of rate or sticking coefficients. The surface rate constant and sticking coefficient can be obtained from following equations

$$k_i = \left(\frac{\gamma_i}{1 - \gamma_i / 2} \right) \frac{1}{(\Gamma_{tot})^{n-1}} \sqrt{\frac{RT}{2\pi M}} \quad (3.16)$$

$$\gamma_i = a_i T^{bi} \exp(-\frac{e_i}{RT}) \quad (3.17)$$

Where n is the reaction order, T is the surface temperature, R is the gas constant, M is the mean molecular weight of the gas mixture, γ_i is the dimensionless sticking coefficient, Γ is the surface site concentration.

3.2.5 CIRCUIT EQUATION

A circuit model is employed to obtain the discharge voltage V_d (used as boundary condition for the Poisson's equation) as well as the determine the influence of the external circuit parameters on the discharge characteristics. The circuit model consisting of a ballast resistor, parasitic capacitance, and a power supply voltage has the following expression:

$$\frac{dV_d}{dt} + \frac{1}{C}(I_d - \frac{V_s - V_d}{R}) = 0 \quad (3.18)$$

Where R is external ballast resistance, C is the capacitance, V_S is the power supply voltage, V_d is the discharge voltage, and I_d is he discharge current.

The plasma model is coupled to the external circuit model by the discharge current. The total current is calculated using the electron conduction, ion conduction, and the displacement current. Since the self-pulsing discharges pass through a time varying electric field, therefore, it is critical to include the displacement current as well.

$$I_d = \int_{cathode} (J_e - J_{ion})\, dA + \varepsilon_m \int_{cathode} \left(\frac{dE}{dt} \right) dA \qquad (3.19)$$

Where J is the current density, ε_m is the permittivity of the medium and E is the electric field. The discharge current has a contribution from electron, ion and displacement current.

3.2.6 BOUNDARY CONDITIONS

Flux boundary conditions are provided for the electrons at the electrodes. The electron flux to the electrode is given by the sum of thermal flux and flux of secondary electron due to ion bombardment. The expression is as follows:

$$\vec{\Gamma}_e = \frac{1}{2} n_e u_{th} - \left(\sum_i \gamma_i (\vec{\Gamma}_i) + x D_e \nabla n_i \right) \qquad (3.20)$$

Where n_e is the electron number density, γ is the secondary electron emission coefficient, and u_{th} is the electron thermal velocity.

[For He, $x = 1$ at cathode, and $x = 0$ at anode]

The boundary conditions for the ions considering both the drift and thermal flux

$$\vec{\Gamma}_i = \frac{1}{2} v_{th,i} n_i + n_i(\mu_i \vec{E}) - x\, D_e \nabla n_i - x \sum_i \gamma_i \vec{\Gamma}_i \quad (3.21)$$

[For He, $x = 1$ at cathode, and $x = 0$ at anode]

The secondary electron emission coefficient was varied in the simulations. Best agreement with experimentally measured voltage-current characteristics was obtained for a $\gamma_i = 0.11$. Simulation results presented here are for $\gamma_i = 0.11$ unless mentioned otherwise.

The boundary condition for the electron energy is expressed as:

$$\vec{\Gamma}_\varepsilon = \frac{5}{6} n_\varepsilon u_{th} - \left(\sum_i \gamma_i \varepsilon_i (\vec{\Gamma}_i) + \varepsilon (D_e \nabla n_i) \right) \quad (3.22)$$

Where n_e is the electron energy density, ε_i is the mean energy of ion, and D_e is the electron diffusion coefficient.

The outer boundary b-c-d is assumed to be a dielectric surface and the following boundary conditions are applied

$$n \cdot (D_1 - D_2) = \rho_s \qquad (3.23)$$

Where, ρ_s is the surface charge density. It is estimated by solving the following ODE on the surfaces

$$\frac{d\rho_s}{dt} = n \cdot j_i + n \cdot j_e \qquad (3.24)$$

Where, $n \cdot j_i$ and $n \cdot j_e$ are the normal component of the total ion current density and total electron current density respectively.

For the boundary conditions of different ions and excited states a surface chemistry model is also implemented having a sticking coefficient of 1.0. The electrode surfaces are set to be isothermal walls with room temperature 300 K for solving the gas mixture temperature.

3.3 NUMERICAL MODEL

The numerical model allows solving the governing equation using the numerical algorithm. Time scales in plasma discharges modeling varies over a large range, varying from picosecond (for electron transport) to seconds (for gas temperature transport). As a result, a vary small time step generally being considered to capture all the physics which also makes the model computationally expensive. As a result, the numerical simulations have been performed by employing a dynamic time stepping algorithm. The partial differential equations for plasma discharges are very still, therefore, a second order backward differential formula is used to overcome this issue.

3.3.1 1D MODEL

The schematic of the discharge system modeled is presented in Figure 3.1. The external power circuit consisted of a voltage source, a ballast resistance, R, a capacitor C. The capacitance C is present intrinsically due to the external cables and is known to be the parasitic capacitance.

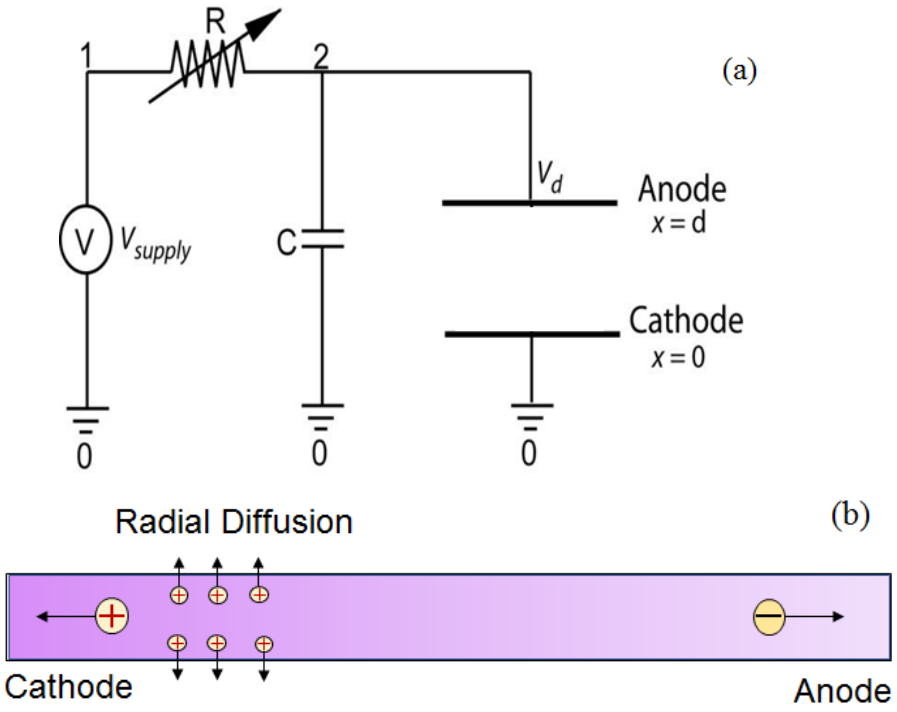

Figure 3.1: (a) The schematic of the plasma glow discharge. The numbers represent the node in the circuit, '0', indicates ground nodes. (b) A radial diffusion loss is included in the model.

For the one dimensional model, it was necessary to specify the electrode surface area to couple the discharge current between the external power circuit and plasma model. In these simulations, the inter-electrode separation was fixed at d = 400 μm.

3.3.2 2D MODEL

The discharge physics model is based on the 2D axisymmetric model phenomena. Schematic of the microplasma discharge system studied is shown in Figure 2 and 3. The external circuit consisting of a voltage source Vs, a ballast resistor R, and a capacitor C coupled with the plasma domain. The capacitor C, also known as parasitic capacitance, is present intrinsically in the wire. In these simulations, the inter-electrode separation was fixed at d = 200 μm. The simulation was carried out for a two dimensional axisymmetric domain. The schematic of the computational domain is depicted in Figure 3 where a-b represents the anode, d-e represents the cathode surface and b-c-d is the dielectric wall. The interelectrode distance a-e is set to be 200 μm. The mesh of the discharge domain consists of '22500' mapped triangular elements and has '342168' degrees of freedom.

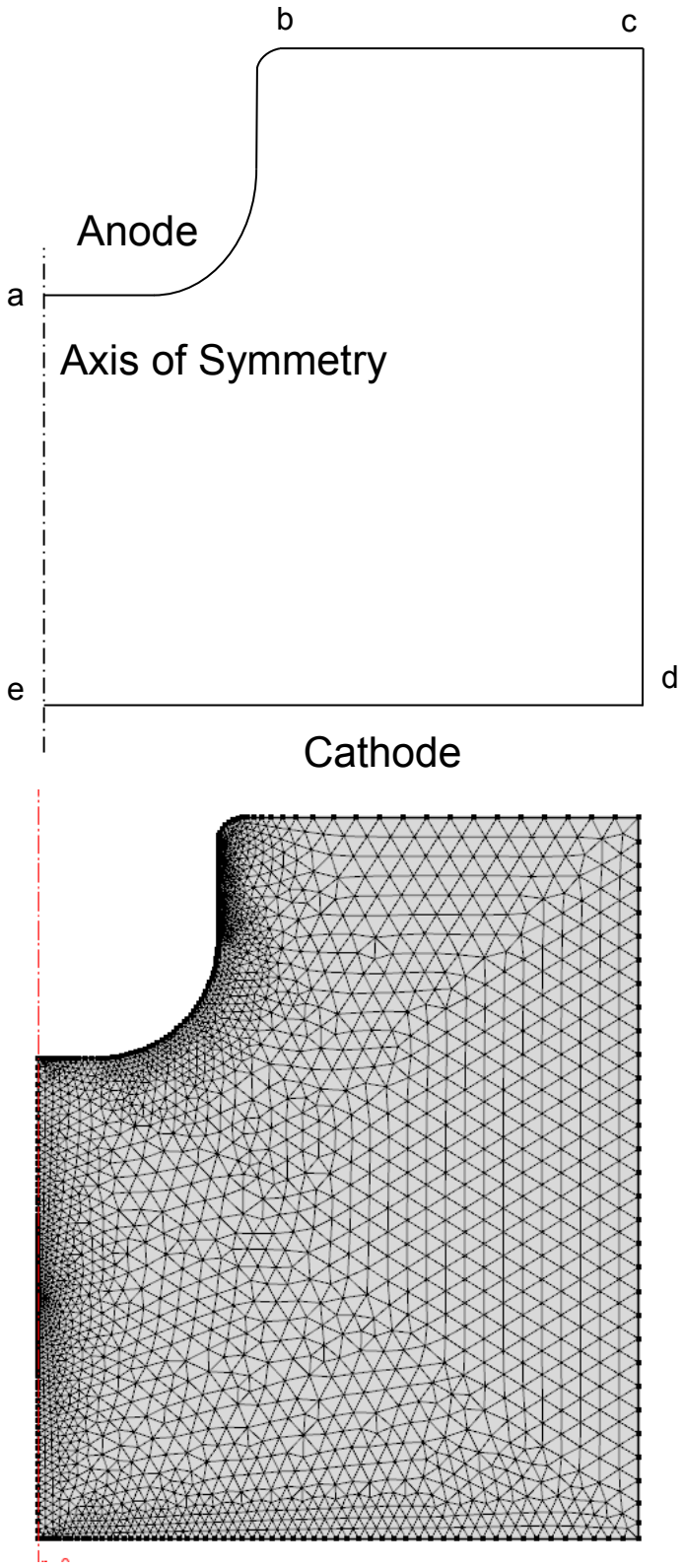

Figure 3.2 Schematic of the 2D computational domain. The dotted line represents the boundary

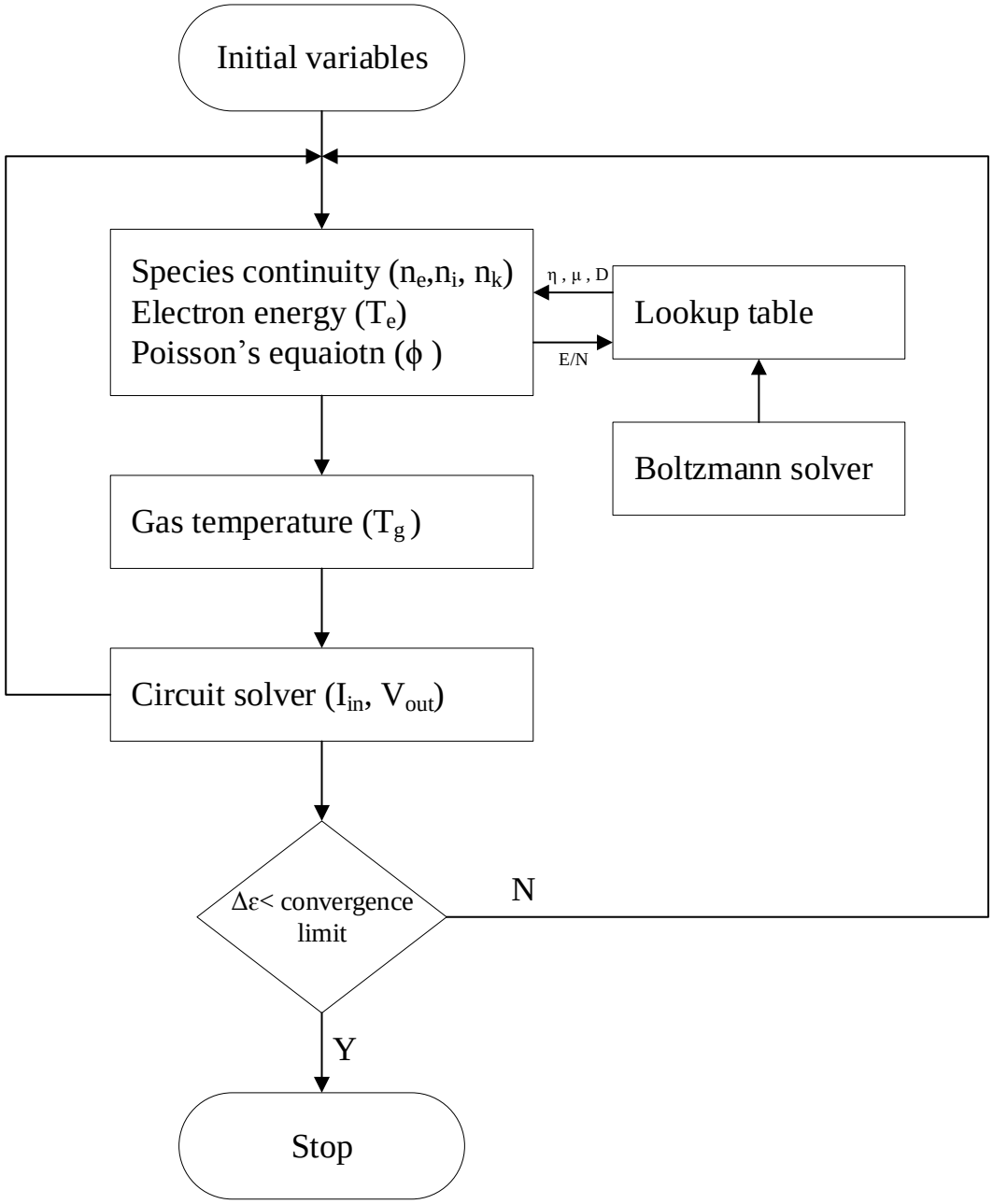

Figure 3.3 Numerical algorithm for the plasma discharge system. Symbols represent which variables are updated.

CHAPTER 4

CHARACTERIZATION OF NDR INSTABILITY

4.1 INTRODUCTION

The negative differential resistance region of a voltage-current characteristic curve, between the transitions to Townsend to normal glow region, exhibit an instability in the discharge. Instability in the NDR region, resulting in oscillation of discharge voltage and current, with a consequence of current filamentation, tends to hampers the device operation. As a result interest instability in the NDR region has been stirred in recent years by experiments and numerical simulation, in order improve the preformation of the plasma system and low current operation. Both low and high pressure system predicts similar kind of behavior. Most of the study on NDR oscillation has been conducted for the low pressure plasma discharge system, where high pressure system is not available in the literature. This chapter will present the numerical results on the NDR instability for high pressure plasma system. Also, brief results on the experimental voltage current characteristics curve will be presented. This chapter includes experimental study, 1D modeling and 2D modeling

4.2 BACKGROUND OF THE STUDY

High pressure non-thermal plasma discharge has been studied for a variety of applications, such as surface modification/treatment (Babayan et al., 1998; Schutze et al.,

1998), thin film deposition (Benedikt, Raballand, Yanguas-Gil, Focke, & von Keudell, 2007; Ricci Castro, Kodaira, Prysiazhnyi, Mota, & Kostov, 2017; D. Staack, Farouk, Gutsol, & Fridman, 2007) , microreactors (Jensen, 2005; Kogelschatz, 2007; Lindner & Besser, 2012; Mehran Keshe Tavakoli, 2005), biomedical applications (Stoffels, Flikweert, Stoffels, & Kroesen, 2002), microelectromechanical systems and sensors (Becker, Schoenbach, & Eden, 2006b; F. Iza & Hopwood, 2003). The high charge density and added ease of operation due to the absence of vacuum systems make these discharges a topic of growing interest. One of the main challenges in maintaining the non-thermal mode of plasma at atmospheric and higher pressure is preventing the ionization overheating instability (Fridman & Kennedy, 2004a; Nighan, 1977; Yuri P. Raizer, 1991) and hence the thermalization of the discharge itself. The ionization overheating instability results in an abrupt increase in the gas temperature if not suppressed. At high pressure discharges (i.e., atmospheric and higher), these ionization instabilities are more likely to happen due to the increased rate of collisionality from a lower mean free path distance. Among the various ways of attaining non-thermal plasma discharges at elevated pressures, microplasma has been accepted to be a traditional method. Microplasmas are essentially density scaled versions of typical low pressure glow discharges (Kushner, 2005) and are characterized by their small size with characteristic dimensions of tens to hundreds of microns. A wide variety of power supplies including radio frequency (RF), microwave and dc as well as different electrode geometries – micro hollow cathode (MHC), planar, pin-to-plate have been utilized to create stable micro plasma discharges.

Even though micro discharge suppresses the ionization overheating instability at higher pressure, their small dimensions make them susceptible to instabilities resulting

from external parameters. Such instability for a micro hollow cathode configuration was experimentally observed by Hsu and Graves (Hsu & Graves, 2003) and by Aubert et al.(Aubert et al., 2007a). The instability observed by Hsu and Graves was found to be self-pulsing and was termed as a *"relaxation"* oscillation. Their proposed equivalent circuit model and simulations identified that the self-pulsing mode was due to an instability resulting from the interaction between a negative differential resistivity in the current-voltage characteristics of the MHC discharge and the load line of the external circuit. Aubert et al. (Aubert et al., 2007a) also studied a self-pulsing MHC discharge resulting from plasma instability where the discharge fluctuates between a hole-confined abnormal glow and a normal glow that is expanded to the outer cathode surface. They proposed a simple equivalent circuit model, using a bistable voltage-controlled variable resistor that provided reasonable predictions of the temporal evolution of the electrical parameters. In a more recent study, Deconinick and Raja (Deconinck & Raja, 2009) developed a multi-dimensional fluid model for the MHC configuration studied by Aubert et al. The presence of an external circuit was not considered. Their model was able to predict the pulsing patterns observed by Aubert et al. Their study however identified that field dependent secondary electron emission coefficient is critical for predicting the self-pulsing regime. Chabert and coworkers developed a circuit model to simulate MHC discharge operating in moderate pressure. A nonlinear plasma resistance was prescribed to analyze the dynamics associated with a confined and over expanded pulsing MHC discharge. Even though the MHC configurations studied involved micro discharges the maximum operating pressure did not go beyond a few hundred Torrs; operating pressure of one atmosphere or higher was not explored that are even more critical for the stable and pulsing regime of operation.

It is not until recently that the pulsing characteristics of an atmospheric pressure MHC discharge have been investigated by et al. (Du, Mohr, et al., 2011). Du et al. characterized the pulsing behavior of MHC discharge operating in argon over a range of pressure conditions.

Instabilities typified by self-pulsing behavior for a dc driven atmospheric pressure micro glow discharge was examined by Staack et al. (D. Staack, Farouk, Gutsol, & Fridman, 2009b)for a pin to plate electrode configuration. Their experimental study identified that the parasitic capacitance of the external circuit played a significant role in the stability of the discharge by acting to control the rate at which the applied voltage to the plasma and hence the electric field changed across the discharge gap. Farouk et al. (Tanvir Farouk, Antao, & Farouk, 2014b)conducted multi-dimensional, multi-physics simulations of an atmospheric pressure hydrogen enriched micro plasma discharge – which has increased susceptibility to instability due to the presence of high concentration of hydrogen. Their simulations showed that the self-pulsation resulting from the parasitic capacitance operated in the *subnormal* regime. However, their study did not elaborate on the influence of increasing pressure neither on the possible influence of different ion kinetics on the self-pulsing behavior. Oscillation in the *subnormal* regime for plasma discharges operating in low pressure has been extensively studied (Robert R Arslanbekov & Kolobov, 2003; Donkó, 1999; Petrovic et al., 1997; Stefanović et al., 2011b; Stefanović & Petrović, 1997). Petrovic et al. (Petrović & Phelps, 1993b) reported self-sustained oscillations between a parallel plate electrode configuration operating at low pressure. They found that the self-pulsing mode occurs in the negative resistivity region of the glow discharge. Arslanbekov and Kolobov (Robert R Arslanbekov & Kolobov, 2003) conducted

self consistent simulations for the identical geometrical configuration similar to Petrovic's study but for argon feed gas instead of hydrogen. Their numerical analyses denoted these oscillations to be a consequence of comparable circuit response and ion transit time. Stefanovic et al. (Stefanović et al., 2011b) conducted an experimental study of oscillation in a low pressure plasma discharge having a parallel plate electrode configuration and reported the presence of low and high frequency oscillations in the negative resistivity region. Oscillation patterns for a low pressure hollow cathode discharge configuration were simulated by Donko (Donkó, 1999) employing a hybrid model together with an external electrical circuit. Even though significant amount of literature exists on self-pulsing low pressure discharge, to the best of the authors knowledge, an extensive study on self-pulsing high pressure micro plasma discharges that focuses on the different oscillation patterns and the influence of the high operating pressure and other external operating parameters on the oscillation characteristics is not readily present in the literature (Sakiyama & Graves, 2007b).

4.3 EXPERIMENTAL SETUP

An atmospheric pressure microplasma setup with parallel plate geometry configuration operating at helium was investigated. Three inter-electrode separation distances were investigated 100 μm, 200 μm and 400 μm corresponding to pd values of 7.6, 15.2, and 30.4 Torr-cm. The electrode arrangement consisted of a spherical anode and a flat cathode disk having diameters of 12.7 and 10 mm respectively. A stainless steel spherical anode was used to maintain the discharge in the central region (i.e. the smallest gap) to ease the visualization process.

The anode electrode was attached to a micropositioner for varying the inter-electrode separation distance. The electrodes are contained inside a stainless pressure chamber with quartz window viewports for discharge visualization. The chamber is sealable and there are gas inlets and outlets for testing in a variety of pressures and discharge gases. The experiments were conducted using a Spellman SL20P2000 DC power supply setup connected in series to a 100 kΩ ballast resistor, an inductor (oscillation suppression experiments) and the discharge.

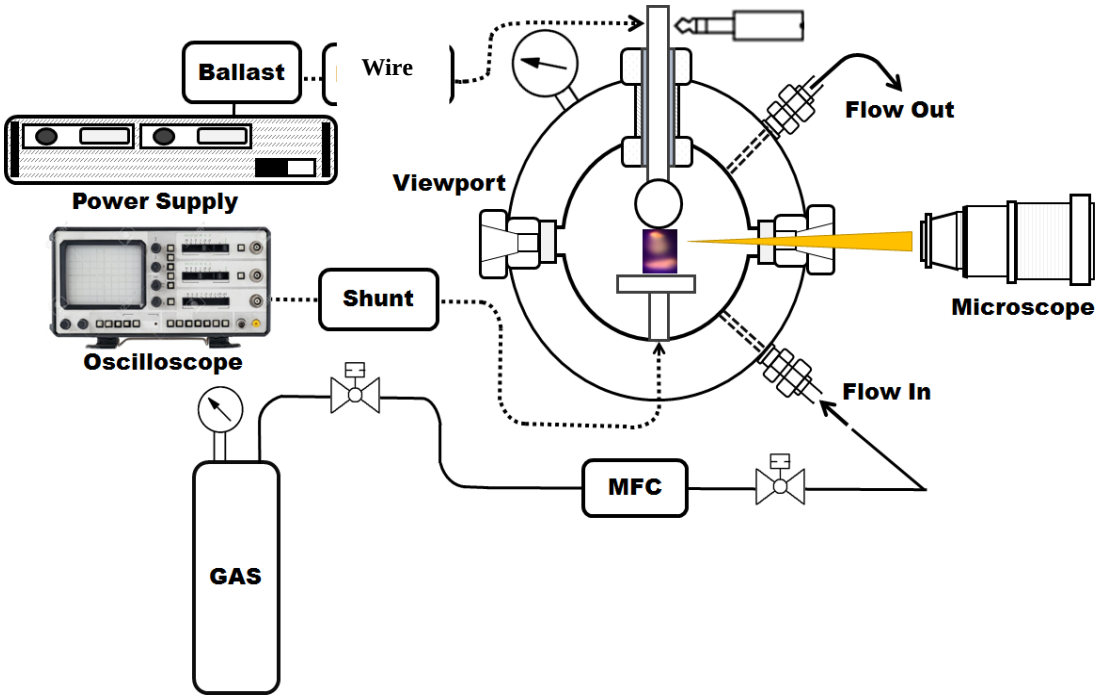

Figure 4.1 Schematic of the experimental setup parallel plate used for the microplasma instability study.

4.4 REACTION KINETICS STUDY

4.5 GAS PHASE REACTION KINETICS

The mechanism contains reactions for both helium and nitrogen trace impurities. 12 species were considered in the simulations; electrons (e), ions (He^+, He_2^+, N_2^+, N_4^+), meta-stables (He(21S), He(23S), electronically excited species (He*, He2*) and neutrals (He, N_2, N). The chemical kinetics included in this study is summarized in Table 4.1 at the end of the chapter. The reaction mechanism consists of elastic scattering, ionization, excitation and de-excitation, three body recombination, dissociative recombination, charge transfer, molecular ion conversion reactions, etc. The electron transport coefficients (mobility μ_e, diffusivity D_e) and electron induced reaction rates (η) are calculated using the electron energy distribution function (EEDF) obtained as a solution of the Boltzmann equation employing the two terms spherical harmonic expansion (SHE). Energy transport coefficient (mobility, diffusivity D_ε) were also obtained from the EEDF instead of using the $\mu_\varepsilon = \frac{5}{3}\mu_e$ and $D_\varepsilon = \frac{5}{3}D_e$ relationship. The aforementioned expressions for the energy transport coefficients are typically obtained by assuming a Maxwellian EEDF, a constant momentum transfer frequency, and constant kinetic pressure. It has been shown by Hagelaar and Pitchford (Hagelaar & Pitchford, 2005) that energy transport coefficients obtained from electron transport coefficient relationships differed by a factor of two from those obtained from EEDF solutions especially for monatomic gases. Since our study involves helium gas, we refrained from substituting the energy mobility and diffusivity with the 5/3 relationships and instead utilized electron energy coefficients obtained directly from the EEDF solutions. BOLSIG+ (Hagelaar & Pitchford, 2005) is employed to calculate the EEDF for different values of the reduced electric field (E/N) and generate lookup tables

for the reaction rates, electron transport, and electron energy transport coefficients. The lookup tables are generated as a function of the mean electron energy to take into account the non-local effects.

4.5.1 SURFACE REACTION KINETICS

The reactions happening at the electrodes and the wall of the plasma chamber is the matter of attention to surface reaction kinetics. By thermodynamic principle, the surface is the energy sink, and hence the excited species and ions will become neutral in contact with the surfaces. Table 4.2 shows the major surface reaction taken into account for the study.

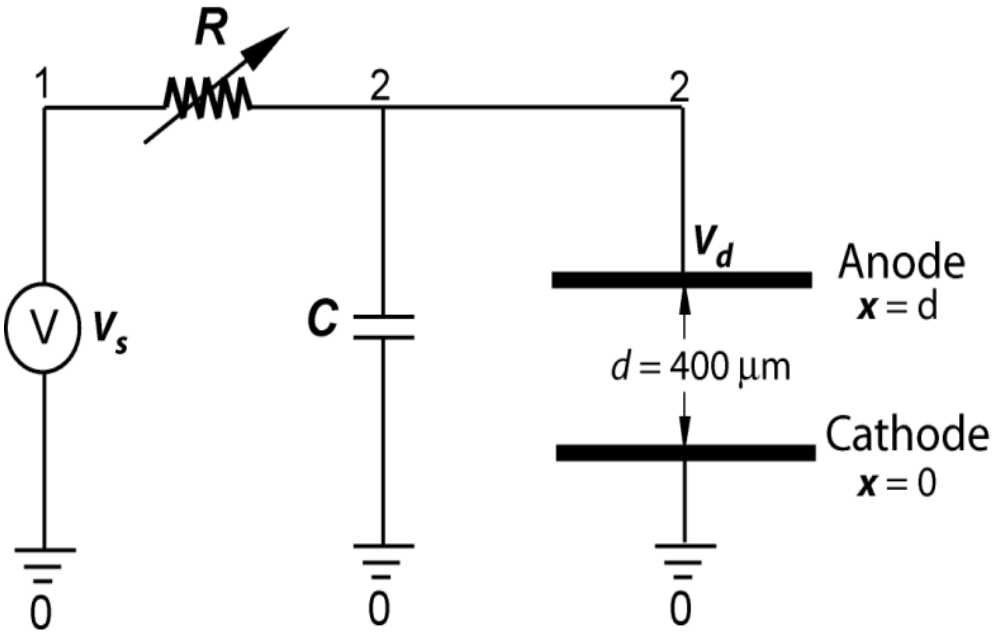

Figure 4.2 Schematic of the parallel plate plasma glow discharge circuit. The numbers represent the node in the circuit, '0' indicates ground nodes.

4.6 MODELING APPROACH

4.6.1 SCHEMATIC OF THE DISCHARGE SYSTEM

The schematic of the discharge system modeled is presented in Figure 4.2. The external power circuit consisted of a voltage source, a ballast resistance, R, a capacitor C. The capacitance C is present intrinsically due to the external cables and is known to be the parasitic capacitance.

Due to the one dimensional model, it was necessary to specify the electrode surface area to couple the discharge current between the external power circuit and plasma model. The total current is calculated using the electron conduction, ion conduction and the displacement current. Since the self-pulsing discharges pass through a time varying electric field, therefore, it is critical to include the displacement current as well. In these simulations, the inter-electrode separation was fixed at d = 400 μm. The electrode surface area was prescribed to be 0.006 cm^2 resulting in an electrode radius of ~ 437 μm. For higher pressure (> 1 atm), a pressure/$radius^2$ scaling method is applied to get the reduced surface area of the simulation. The electrode area was so chosen to be consistent with that of Wang et al. (Qiang Wang et al., 2006) since the model was validated against their experimentally measured voltage-current characteristics.

4.6.2 1D MODELING APPROACH

The system of equation is discretized on the basis of finite element method and is solved using a time-dependent solver in COMSOL ("COMSOL Multiphysics," 2013). A non-uniform mesh was employed with denser grids present closer to the electrodes. A total

of ‘600’ grids are used with a maximum and minimum grid size of ‘2.2’ μm and ‘0.732’ μm respectively and the total number of degrees of freedom were around ‘6914’. The time integration was performed using a fully implicit backward difference formula (BDF) and a variable time stepping. The numerical solution was obtained utilizing the Parallel-Sparse Direct Solver (PARADISO) (Schenk & Gartner, 2004).

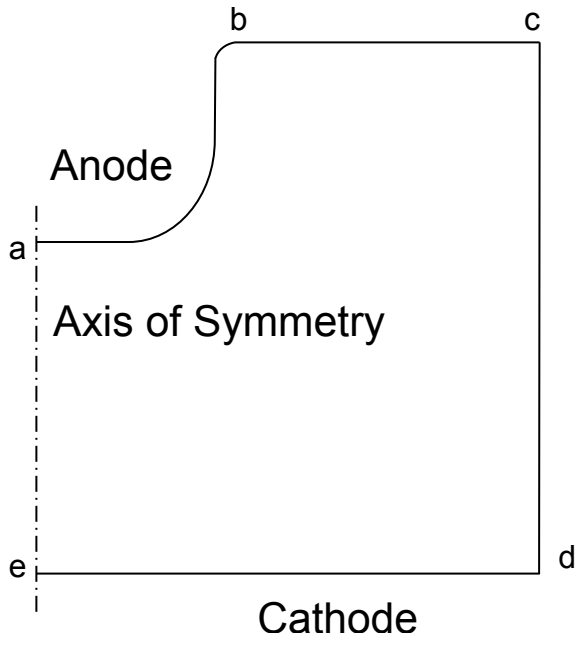

Figure 4.3. Schematic of the computational domain. The dotted line represents the boundary.

4.6.3 2D MODELING APPROACH

The system of equation is discretized by finite element method and is solved using a time-dependent solver in COMSOL (“COMSOL Multiphysics,” 2013). A non-uniform mesh was employed with denser grids present closer to the electrodes. A total of ‘600’ grids are used with a maximum, and a minimum grid size of ‘2.2’ μm and ‘0.732’ μm respectively and the total number of degrees of freedom was around ‘6914’. The time integration was performed using a fully implicit backward difference formula (BDF) and

a variable time stepping. The numerical solution was obtained utilizing the Parallel-Sparse Direct Solver (PARADISO) (Schenk & Gartner, 2004).

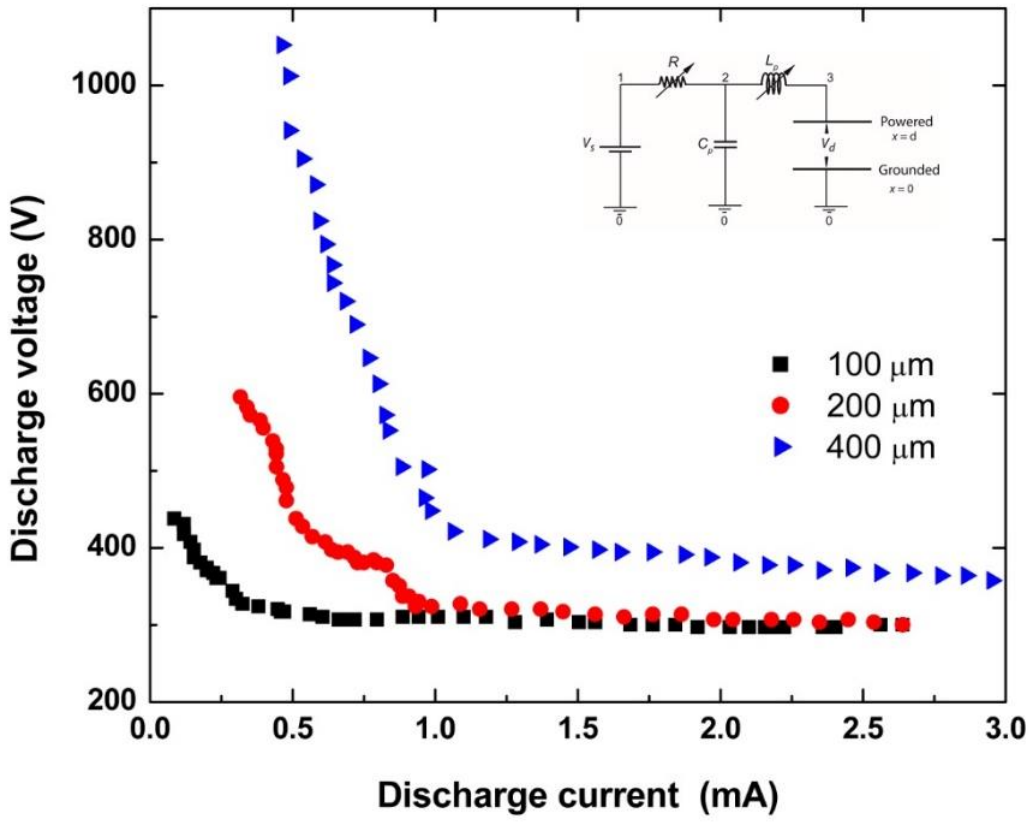

Figure 4.4. Experimental voltage current characteristics curve for different 'pd' values.

4.7 RESULTS AND DISCUSSIONS

4.7.1 EXPERIMENTAL RESULTS

The experimental voltage current characteristic curve is presented in Figure 4.4 for a very low current (0.1 mA) subnormal oscillatory mode to a high current normal glow mode (3mA). The discharge voltage and current in the NDR region are measured regarding their RMS value due to the oscillatory nature of the self-pulsing nature. The cathode surface area (A_c = 0.7854 cm^2) is being sufficiently low enough to see any onset of abnormal discharge modes. The V-I curve is presented for three different 'Pd' values, 15.2 Torr cm,

30.4 Torr cm and 60.8 Torr cm. The corresponding 'Pd' values are measured by varying the pressure and keeping the interelectrode spacing constant. The transitional point of subnormal to normal glow region was found to be at 0.56 mA, 0.78 mA and 0.9 mA for a 'Pd' values of 30.4 Torr cm, 45 Torr cm, and 60.8 Torr cm respectively. This transition happens for a higher current for a higher value of '*Pd*' but does not scale linearly with '*P*d'. Once the normal glow mode achieved, the discharge voltage remains constant regardless of any current increment predicting the classical pattern. It is known that higher the chamber pressure is higher power supply is needed for any discharge to happens.

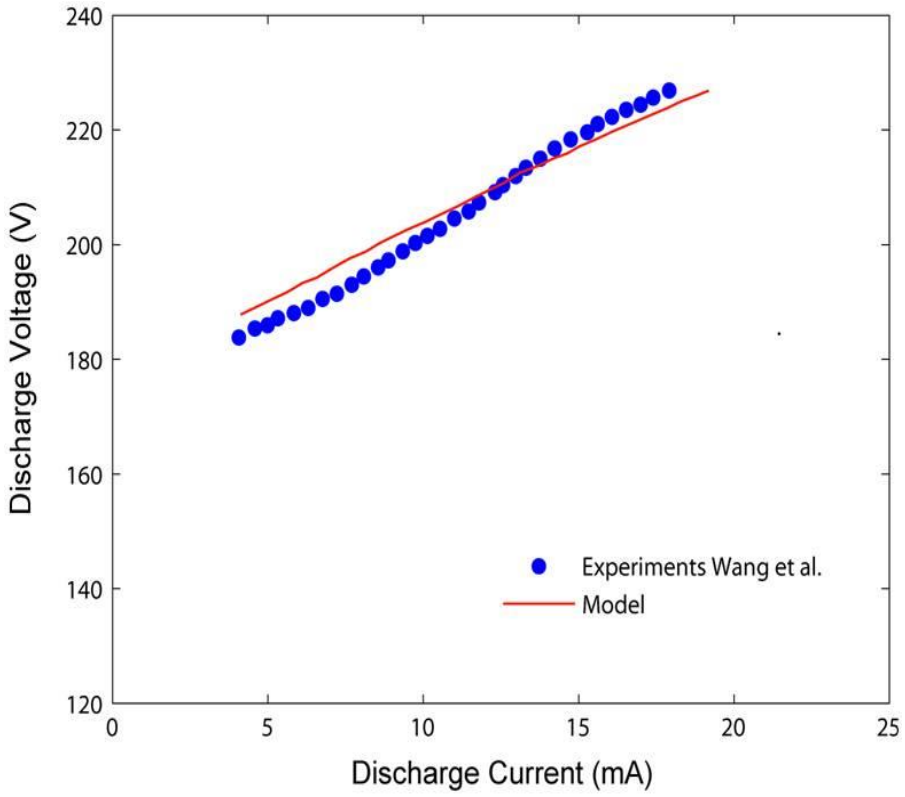

Figure 4.5. Simulated voltage-current (VI) characteristics for a parallel plate helium DC microplasma discharge. The experimental data are that of Wang et al. (Qiang Wang et al., 2006). Operating pressure one atmosphere, inter-electrode separation 200 m. The simulated voltage-current characteristics are obtained for a secondary electron emission coefficient γ = 0.11.

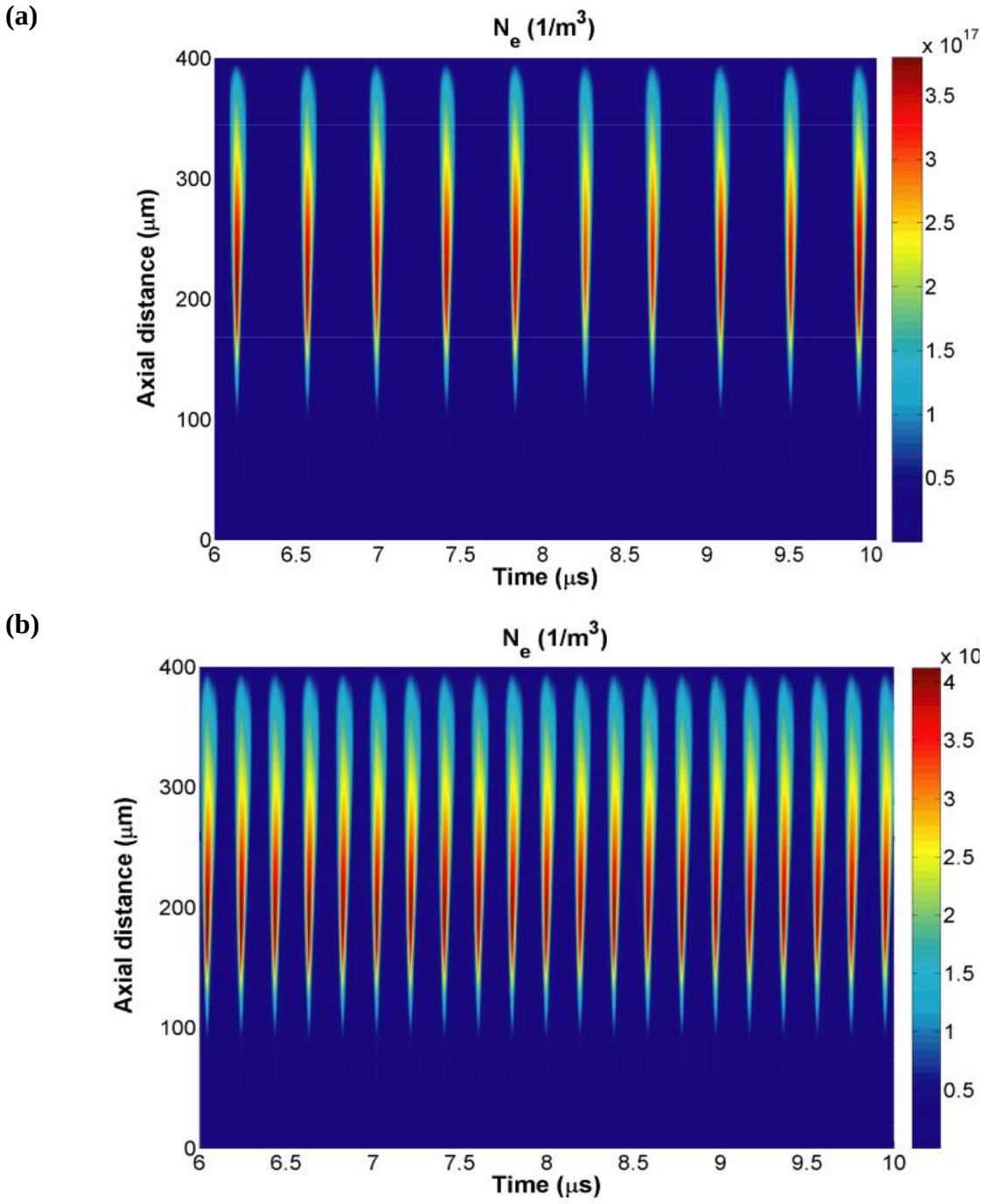

Figure 4.6. Spatio-temporal contour plots of electron number density for a pulsing discharge in pure helium operating at atmospheric pressure, (a) low frequency oscillation j_{rms} = 27.4 mA/cm^2, V_{rms} = 336.8 V; external circuit parameters V_s = 5000 V, R=50 MΩ, C = 0.1 pF and (b) high frequency oscillation j_{rms} = 50.0 mA/cm^2, V_{rms} = 306.9 V; external circuit parameters V_s = 5000 V, R= 20 MΩ, C = 0.1 pF.

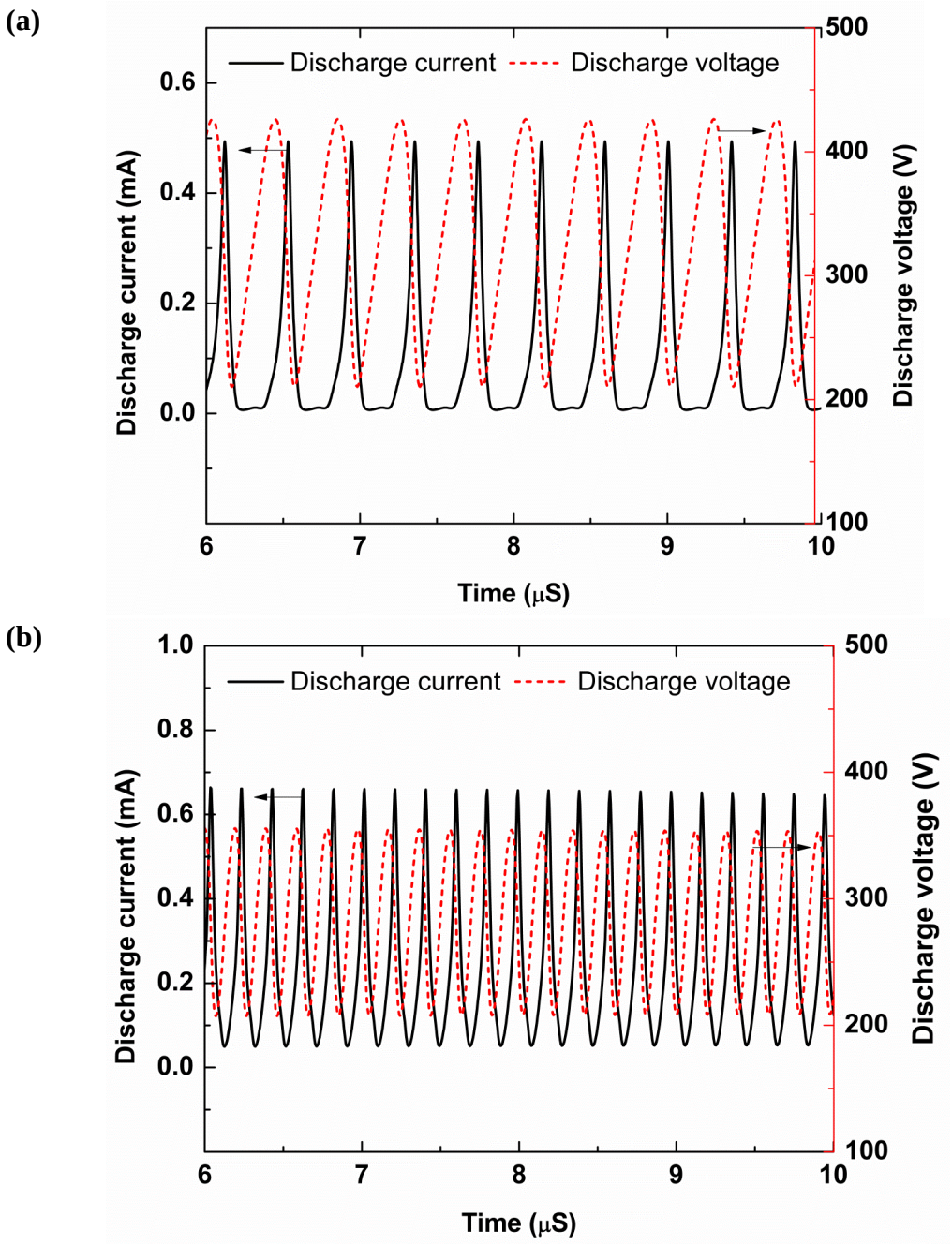

Figure 4.7. Simulated temporal evolution of discharge current and voltage for a) low frequency oscillation (j_{rms} = 27.40 mA/cm^2, V_{rms} = 336.8 V; external circuit parameters V_s = 5000, R= 50 MΩ, C = 0.1 pF) and b) high frequency oscillation (j_{rms} = 50.0 mA/cm^2, V_{rms} = 306.9 V; external circuit parameters V_s = 5000 V, R= 20 MΩ, C = 0.1 pF) for a plasma discharge operating in pure helium at atmospheric pressure.

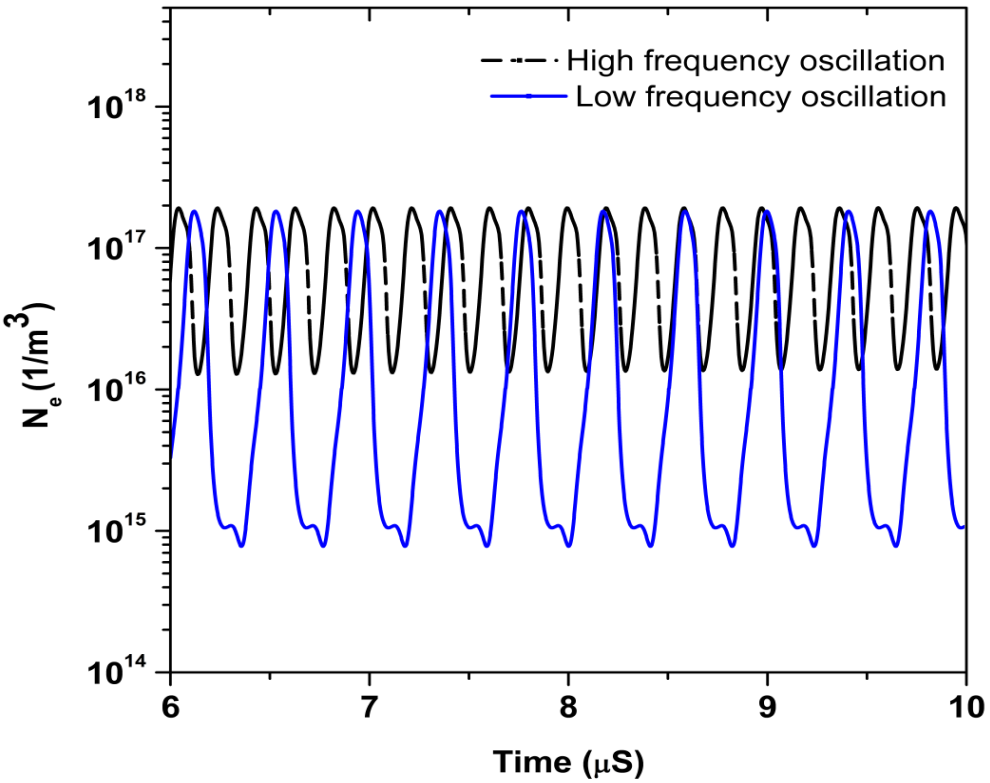

Figure 4.8. Temporal evolution of electron number density at an axial distance of 350 μm for the low and high frequency oscillation operating at atmospheric pressure pure helium feed gas. Low frequency oscillation has j_{rms} = 27.40 mA/cm^2, V_{rms} = 336.8 V and for the high frequency oscillation j_{rms} = 50.0 mA/cm^2, V_{rms} = 306.9 V.

4.7.2 NUMERICAL RESULTS AND DISCUSSION

4.7.3 CHARACTERIZATION USING 1D MODEL

As a validation of the present model, the experiments of Wang et al. (Qiang Wang et al., 2006)were simulated. The simulations were conducted for a pure helium microplasma discharge configuration having an inter-electrode separation of 200 μm driven by a DC power source at atmospheric pressure conditions. The model was validated against the measured voltage-current (VI) characteristics. Figure 4.5 summarized the comparison between the experimental and predicted VI characteristics which are global plasma targets. The one dimensional model was able to successfully capture the experimentally observed positive slope of the VI curve - indicative of an abnormal glow

operation regime. The predicted VI curve was sensitive to the choice of the secondary electron emission coefficient. We found that the best agreement could be obtained for $\gamma_i = 0.11$. As such all the additional simulations and parametric studies are conducted with a secondary electron emission coefficient of 0.11. The benchmark model was employed to investigate the self pulsing regimes of a pure helium microplasma discharges. The inter-electrode separation was set at 400 μm with the stainless steel considered as electrode materials. For a fixed parasitic capacitance (C = 0.01 pF) the ballast resistance was varied to obtain different currents in the NDR region hence different pulsing behavior. The pulsing characteristics in pure helium are summarized in Figures 4.6, 4.7, and 4.8,. Figure 4.6 shows spatio-temporal contour plots of electron number density. It is apparent that under these conditions the discharge is self pulsing with a DC power source.

Low and high frequency oscillations are observed as current is increased (i.e., ballast resistance decreased). At j_{rms} = 27.4 mA/cm^2 discharge oscillates at ~1.5 MHz and increases to ~ 4.7 MHz at jrms = 50.00 mA/cm^2. It can be seen that at a low pulsing frequency in pure helium the discharge undergoes a complete relaxation cycle – i.e., discharge initiation, formation followed with complete extinguishment. This complete relaxation characteristic are distinct of the discharge current (Figure 4.7) and electron number density (Figure 4.8) temporal evolution. During this relaxation cycle, the voltage increases almost in a linear fashion which is followed by a sharp decrease. In the complete relaxation cycle, the electron number density varies by three orders of magnitude and the spike in discharge current is followed by the extremely low current which sustains itself for a significant duration of a pulsing period. The low current region coincides with the rise in the voltage as sufficient electrical field is required for discharge initiation

/breakdown. As the pulsing frequency increases with increasing discharge current, the pulsing behavior of the discharge transitions to an incomplete relaxation oscillation which is distinct in the discharge current and electron number density temporal evolution. The amplitude of the electron density fluctuation reduces. The electron density oscillates between ~2 x 10^{17} $1/m^3$ – 1 x 10^{16} $1/m^3$, unlike the complete relaxation oscillation where it varies over three orders of magnitude. A saw tooth like wave form is established in pure He which is similar to a classical subnormal oscillation pattern. The electron number density at high pressure system is also presented in Figure 4.9 where the discharge was found to went through a similar complete and partial relaxation oscillation at 2 and 4 atm pressure.

The influence of ion kinetics on the pulsing behavior was investigated by introducing trace amount of nitrogen impurity in the feed gas. The trace nitrogen in the feed gas can readily alter the overall ion dynamics and concentrations via the additional kinetic pathways related to the electron as well as heavy particle reactions. The nitrogen concentration was prescribed to be 0.02% for a baseline simulation. It is well known that trace impurities change the discharge characteristics of helium plasma especially the breakdown and discharge voltage but its influence on NDR regime self pulsing discharge is not well documented. Figures 4.10 and 4.10 summarize the predicted oscillation pattern for the electron density, discharge voltage and discharge current for Vs. = 900 V, R = 50 MΩ, C = 0.01 pF and atmospheric pressure condition. It can be seen that the discharge attains quasi-steady pulsing state in tens of microseconds. Under these operating conditions, the oscillation frequency of the discharge is ~ 280 kHz.

(a)

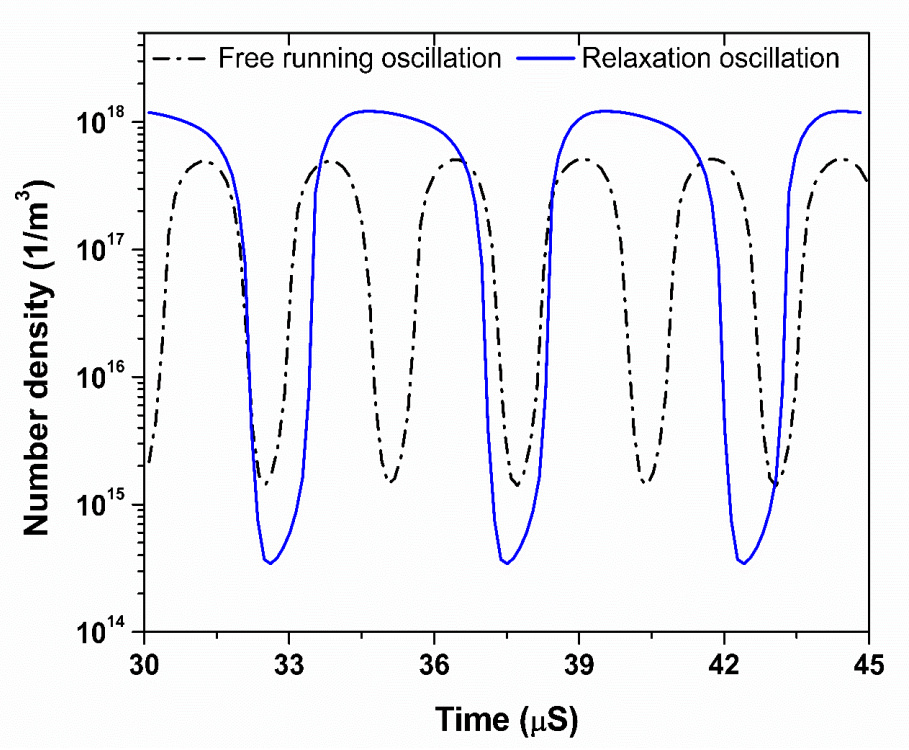

(b)

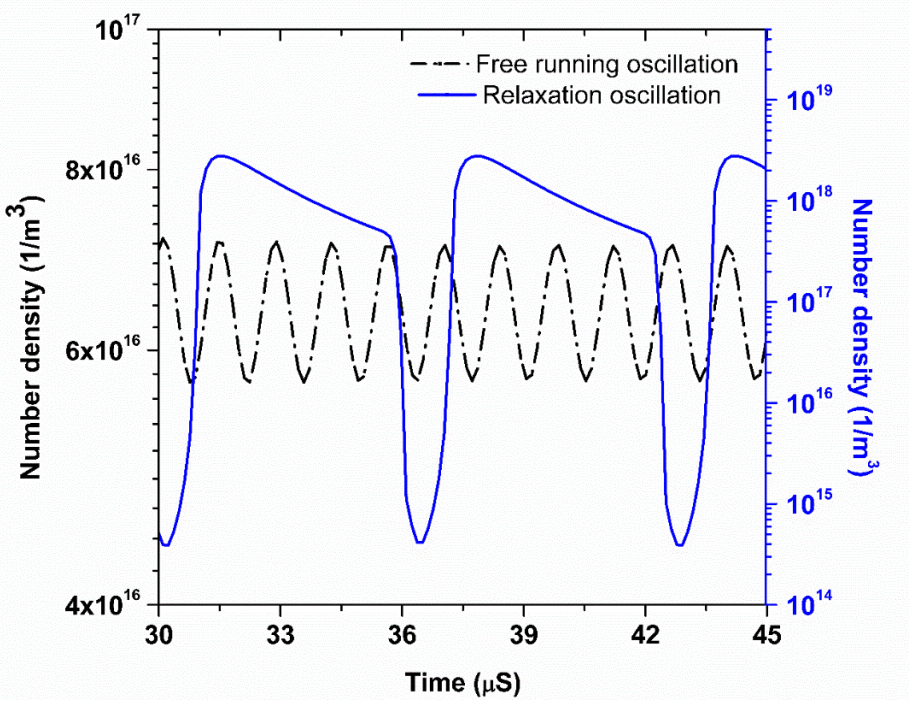

Figure 4.9. Temporal evolution of maximum electron number density for the low and high frequency oscillation at (a) 2 atm pressure and (b) 4 atm pressure

The temporal evolution of the electron number density is recorded at an axial distance of 350 μm . The electron number density is found to vary by three orders of magnitude; having values of ~ $1x10^{18}$ m^{-3} and ~$1x10^{15}$ m^{-3} in one oscillation cycle. The corresponding transient variation of the discharge voltage and current is presented in Figure 10. Trace amount nitrogen can (in the feed gas is found to, same as abstract) significantly influence the pulsing behavior. The discharge voltage and current waveforms are drastically different from those seen for pure helium as well as those of conventional "subnormal" oscillations predictions where saw-tooth like profiles are typically observed for both molecular and polyatomic gases. Here the discharge is found to sharply jump from a low current (high voltage) to a high current (low voltage) mode after which the current starts to sharply decrease until it reaches a "moderate" current value. The discharge maintains itself in this "moderate" current regime for the longest duration which is then followed by a sharp decrease in the lowest current. It is interesting to note that the transition from the high current to the low current in a pulse cycle takes place in three stages; sharp decrease in "moderate" current, a steady slow decrease in "moderate" current range and a sharp decrease in low current. This is counter to that observed in low pressure and atmospheric pressure "subnormal" discharge operating in the NDR region, where a gradual decrease from the high in low current takes place. Additionally, it can be seen that in this pulsing regime the discharge voltage and current are phases shifted by ~ 45◦. The heavy particle kinetics is one of the key contributors to the observed differences in the pulsing characteristics between the pure helium and trace impurity nitrogen case. The spatio-temporal contour plots of the electron, ion density, electric field and electron temperature for the base trace nitrogen impurity case is shown in Figure 4.11.

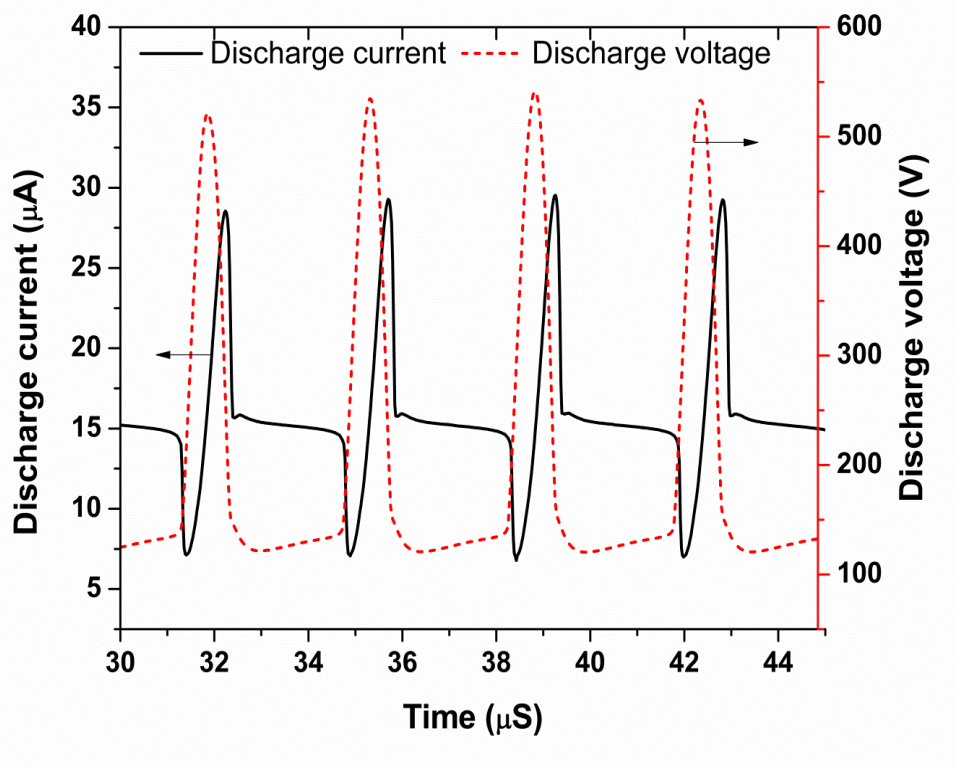

Figure 4.10. Simulated temporal evolution of discharge current and voltage (V_s = 900 V, R = 50 MΩ, C = 0.01 pF, inter-electrode separation of 400 μm, feed gas composition 99.98% He + 0.02% N_2).

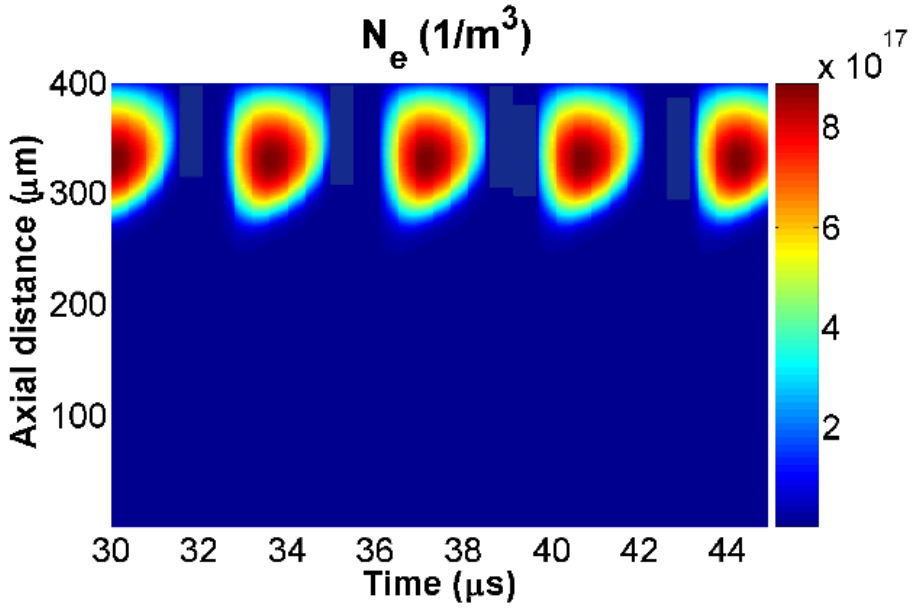

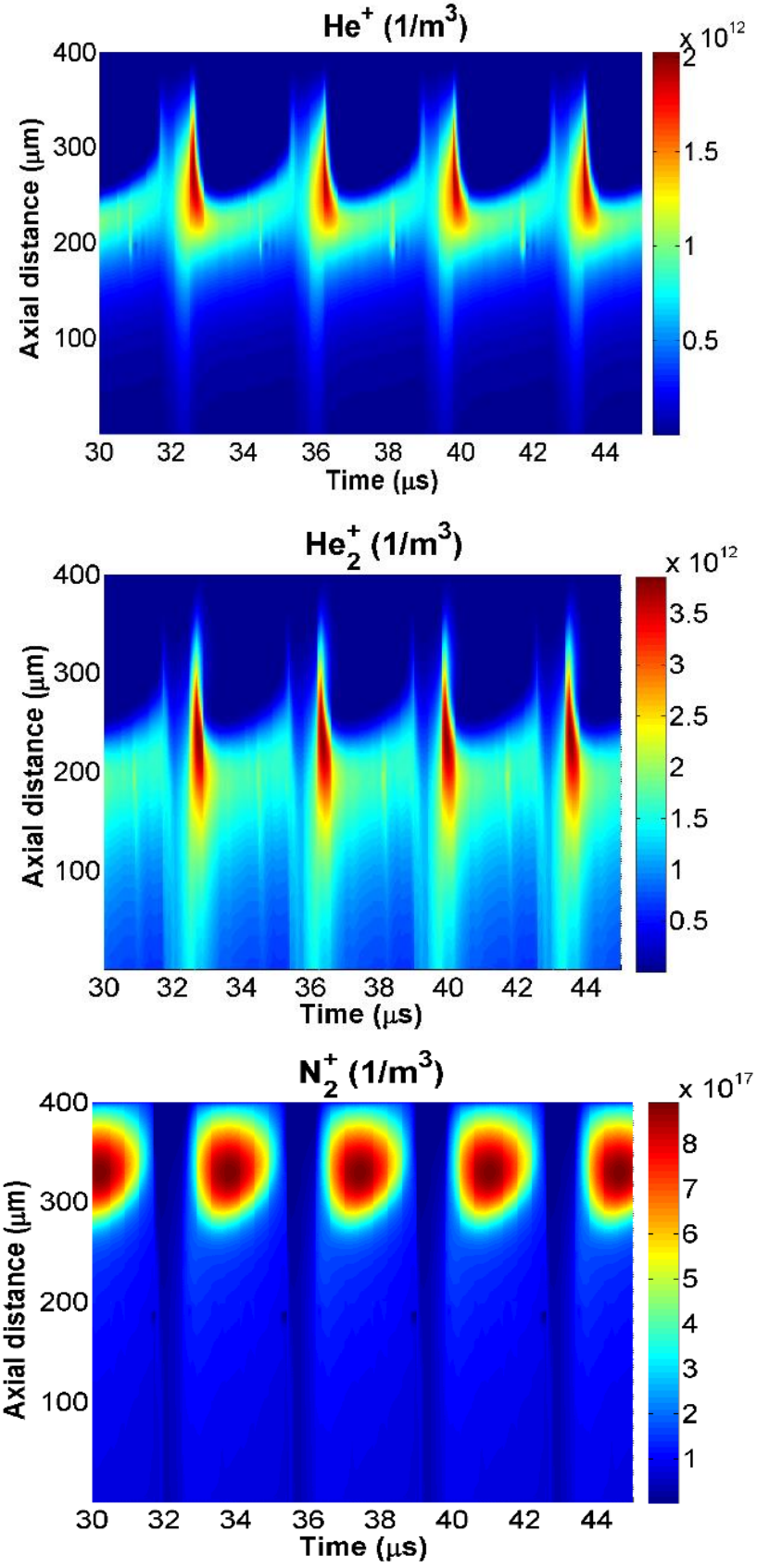
He+ (1/m3)
x 10^12
2
1.5
1
0.5
400
300
200
100
Axial distance (μm)
30
32
34
36
38
40
42
44
Time (μs)
He2+ (1/m3)
x 10^12
3.5
3
2.5
2
1.5
1
0.5
400
300
200
100
Axial distance (μm)
30
32
34
36
38
40
42
44
Time (μs)
N2+ (1/m3)
x 10^17
8
7
6
5
4
3
2
1
400
300
200
100
Axial distance (μm)
30
32
34
36
38
40
42
44
Time (μs)

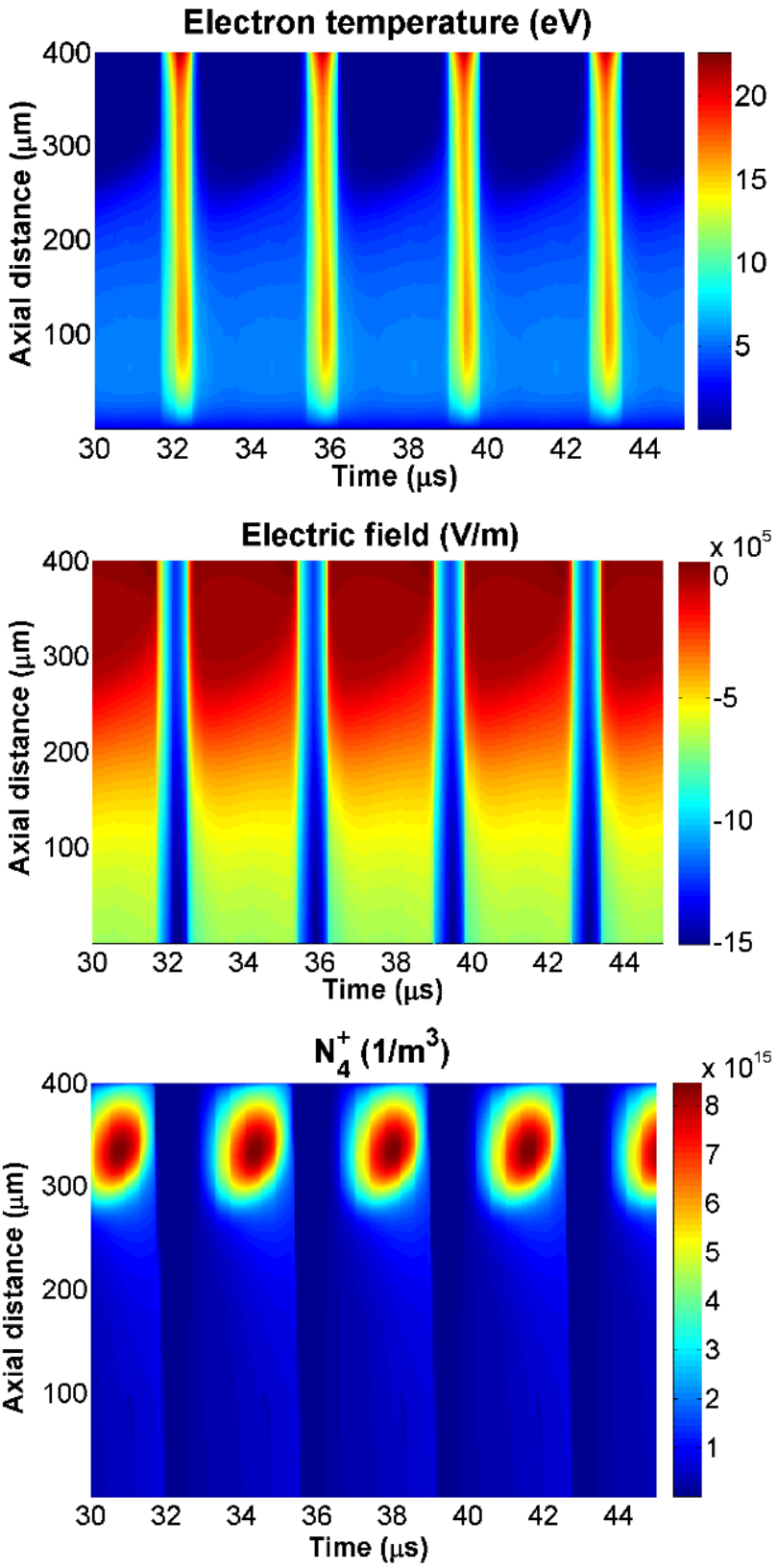
Electron temperature (eV)
Axial distance (μm)
400
300
200
100
30
32
34
36
38
40
42
44
Time (μs)
20
15
10
5
Electric field (V/m)
x 10^5
0
-5
-10
-15
N4+ (1/m3)
x 10^15
8
7
6
5
4
3
2
1

Figure 4.11. Simulated spatio-temporal contour plots of a) electron number density b) He^+ number density c) He_2^+ number density d) N_2^+ number density e) N_4^+ number density f) electric field and g) electron temperature. The contour plots represent a quasi-steady pulsing phenomena. (V_s = 900 V, R = 50 MΩ, C = 0.01 pF, inter-electrode separation of 400 μm, feed gas composition 99.98% He + 0.02% N_2).

The profiles are for a time when quasi-steady periodicity is attained. In the pulsing regime, the electron number density is observed to peak near the anode. In between pulses, the electron number density diminishes significantly indicative of near extinguishment. Among the different ions, N_2^+ is the most prominent followed by N_4^+, He_2^+ and He^+. Despite being a trace impurity the ion concentrations resulting from N_2 (i.e., N_2^+, N_4^+) is the maximum. This is not just due to the lower ionization potential of ~ 15.6 eV for the formation of dimer ions but also because of additional ionization channels via heavy particle reactions i.e. Penning ionization (G27, G28), charge transfer (G23, G24, G25, G26), ion conversion (G30, G31) that contribute to both dimer (N_2^+) and tetramer (N_4^+) ion formation. Among the different ions, He+ has the lowest density due to its very high ionization potential ~ 24.6 eV. Even though He+ are formed by the stepwise process associated with He(21S) and He(23S) metastable states also requires higher energy. The monomer ions convert to He_2^+ which also contributes to the low He+ ion density. The peak ion number densities are found to coincide with the location of the peak electron number density. It can be seen from the electric field and electron temperature spatio-temporal evolution that at the near extinguished state the electric field and consequently the electron temperature ramps up to high values. The electron temperature reaches a value of ~ 24 eV; close to the ionization

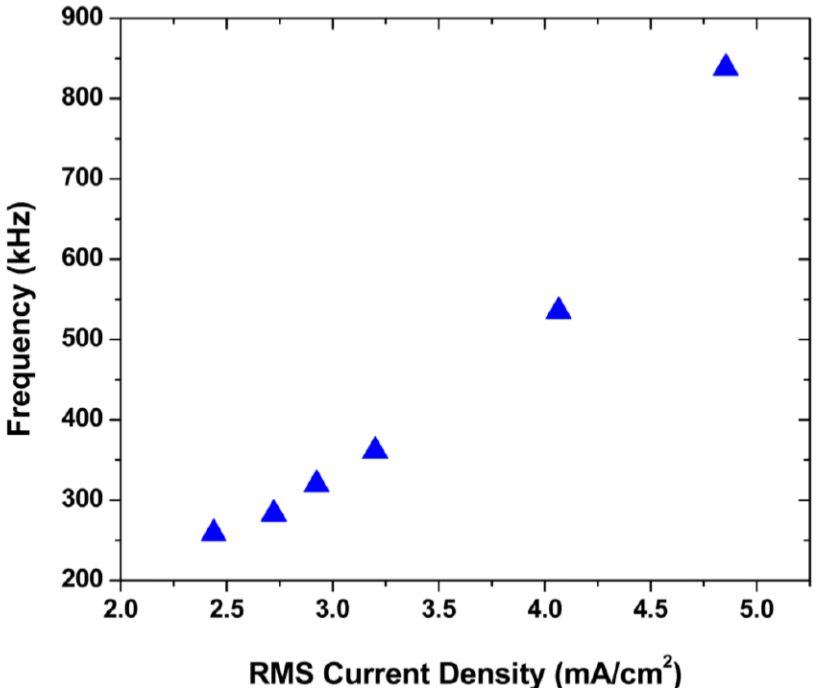

Figure 4.12. Oscillation frequency as a function of rms discharges current density for plasma discharge operating at atmospheric pressure. Feed gas composition 99.98% He + 0.02% N_2.

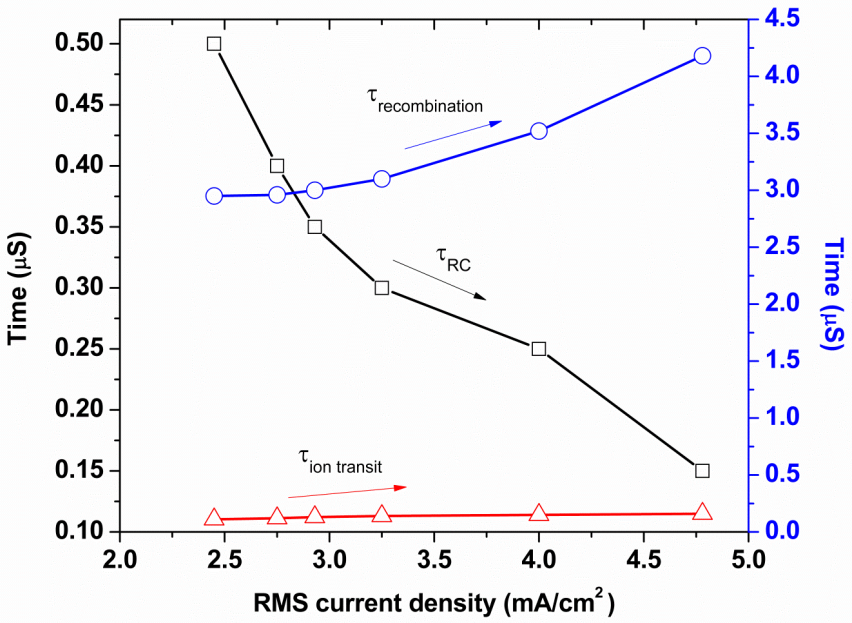

Figure 4.13 Ion transit, circuit response and ion recombination time as a function of rms discharge current density for plasma discharge operating at atmospheric pressure.

Feed gas composition 99.98% He + 0.02% N_2.All the simulations are conducted for V_s = 900 V, C = 0.01 pF and varying R.

Potential of helium. During this stage, the necessary electron energy for breakdown is attained which results in the production of higher electron number density in the subsequent stage. The high and low electron energy in the temporal space overlaps with the low and high electron number density. This is a direct result of most of the electron energy being consumed for ionization. It is interesting to note that unlike N_2^+, N_4^+ the spatio-temporal location of the high He^+ and He_2^+ concentration overlaps with the high electron temperature and an electric field region. The He^+ ions are formed by direct electron impact ionization and once formed contributes to the He_2^+ formation and therefore is associated with the high electron temperature region. Despite the presence of electron direct impact ionization pathway to the N_2^+ bulk of it is still generated via Penning ionization and charge transfer reactions. As such the peak N_2^+ number densities do not overlap with peak electron temperature rather it is offset. The N_2^+ formation continues beyond the electron temperature ramp up and persists during the decay period – a direct consequence of the ion kinetics associated with the heavy particle interactions. Our path flux analysis of the different ion production routes identified charge transfer and Penning ionization process as the most dominant channels. It also highlighted the fact that these ionization processes continue to take place for longer durations in a self-pulsing cycle. Both these reactions are the prominent N_2^+ production channels. The heavier tetramer N_4^+ is formed by three body ion conversion reactions of N_2^+ reacting with N_2 and He (G30, 31). For a peak, N_2^+ density of ~ 9 x 10^{17} 1/m^3 the two three body reactions (G30, G31) are found to have a maximum production rate of ~ 6.5 x 10^{24} 1/m^3 s (G30) and 1.3 x 10^{21} 1/m3 s respectively. On the

basis of $\tau_{ion\ conversion} = \frac{1}{k_{ion\ conversion} n_{N_2} n_{i=N_2/He}}$ the shortest time related to these two reactions are found to be ~ 0.14 μs and 0.69 ms. Therefore for a period of ~ 3.57 μs (i.e., pulsing frequency of 280 kHz) the three body ion conversion associated with He have the necessary time to generate N_4^+ ions of sufficient quantities (Figure 4.12). As for electron impact ionization of He and N_2 they were found to coincide with the lowest current and highest electron temperature spatio-temporal location. Both these channels have very low reaction rates. The electron impact ionization is followed by the Penning ionization process which has the highest reaction rate under these conditions. The electron impact ionization and the highest rate of the Penning ionization coincide with the highest discharge current (Figure 4.11). The formation of N_2^+ via the charge transfer reaction has equally long duration as that of the Penning process. The decreasing Penning ionization and the steady charge transfer rate contribute to the "moderate" current regime of the pulsing cycle.

The self-pulsing behavior of the plasma discharge was found to be strongly dictated by the discharge current. In the simulations for the same level of N_2 impurity, the discharge current was varied by changing the ballast resistance value. Figure 4.12 presents the pulsing frequency for different discharge current for plasma discharge operating at atmospheric pressure. In the self-pulsing regime, the plasma pulsing frequency does not vary with the discharge current in a linear fashion. The plasma initially operates in the complete relaxation mode and then with increasing discharge current pulsing with incomplete relaxation becomes prevalent. In the range of discharge current studied the pulsing frequency varied from ~ 260 kHz to ~ 850 kHz. Kinetics processes having micro- second and shorter time scales will therefore have sufficient contributions within a single pulse.

Apart from the increasing frequency there exist distinct differences in the peak electron number density as well as the electric field. In comparison, the peak electron

Number density and electric field at lower discharge current are higher than that of the higher discharge current. The peak electron density and electric field were ~ 1.2 x 10^{18} $1/m^3$ and ~ 20 x 10^5 V/m for jrms = 2.48 mA/cm^2 which was higher by an order and a factor of two respectively than the jrms = 3.25 mA/cm^2 case. An interesting aspect of these two pulsing cases is that at low currents and low pulsing frequency the discharge has sufficient time to go through a complete cycle,initiation and near extinguishment; oscillations with larger amplitude. Whereas at higher discharge current and frequency an incomplete relaxation takes place and the oscillation amplitudes are smaller.

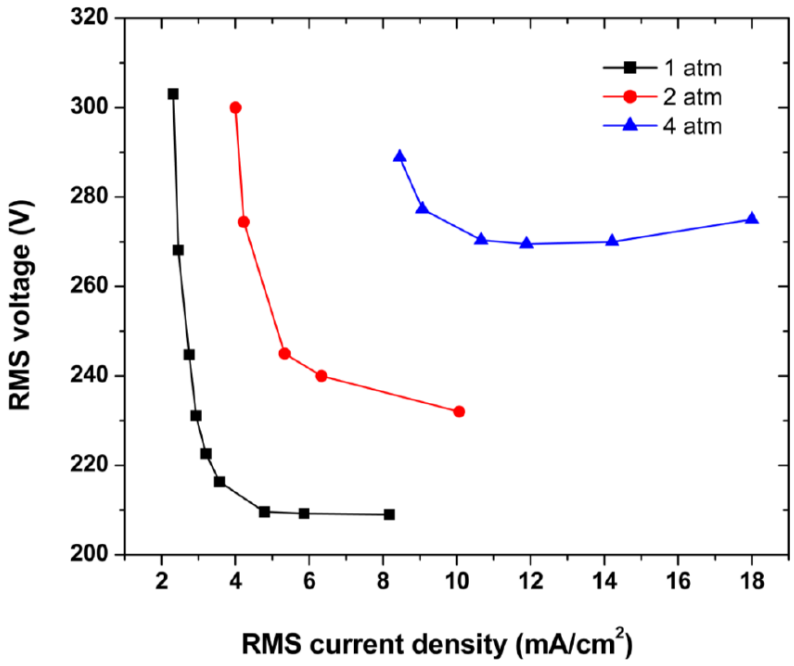

Figure 4.14. Voltage current characteristics of self-pulsing discharge at different operating pressures. Feed gas composition 99.98% He + 0.02% N_2.

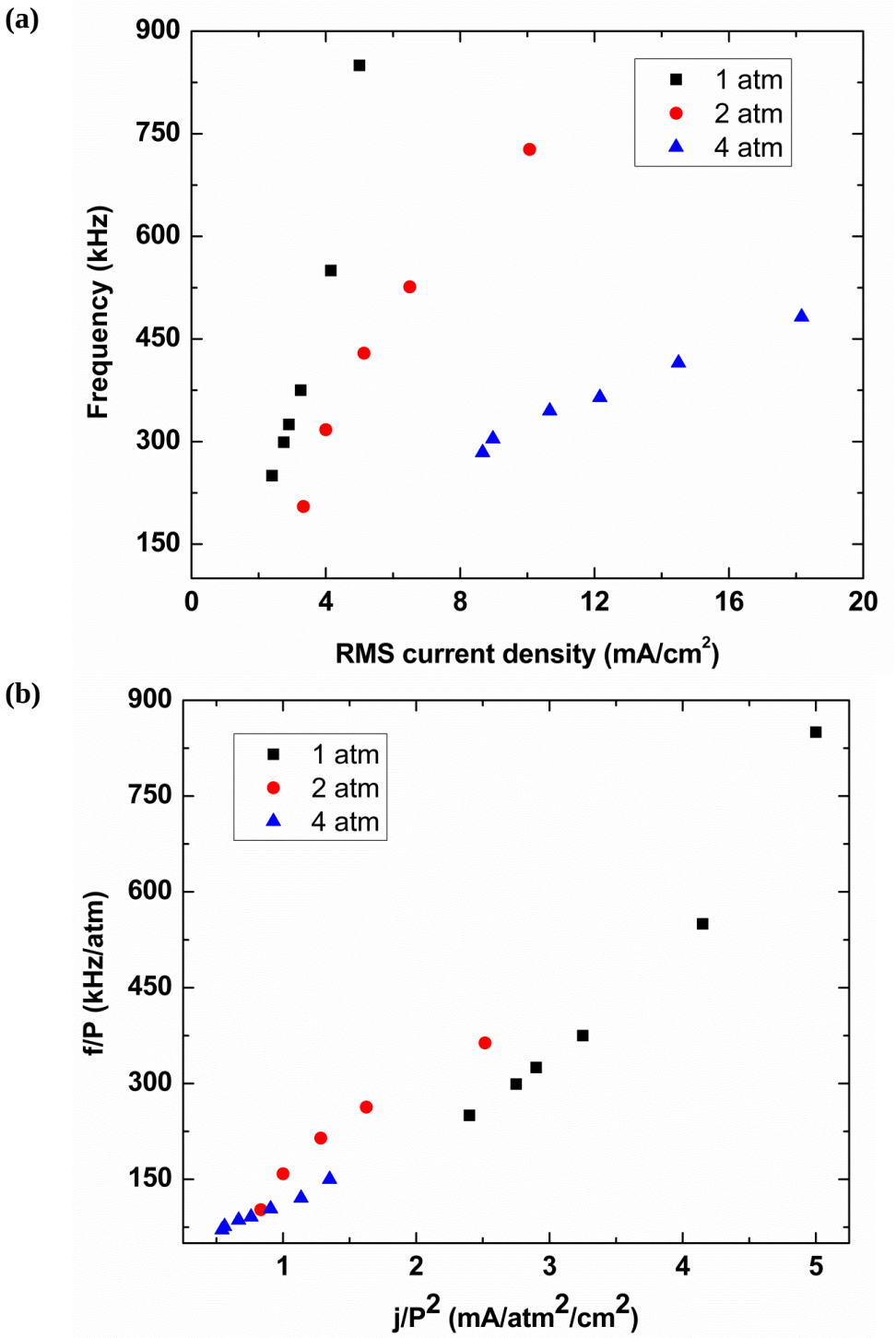

Figure 4.15. a) Oscillation frequency as a function of rms current density for different operating pressures, b) normalized frequency versus normalized current density. Feed gas composition 99.98% He + 0.02% N_2.

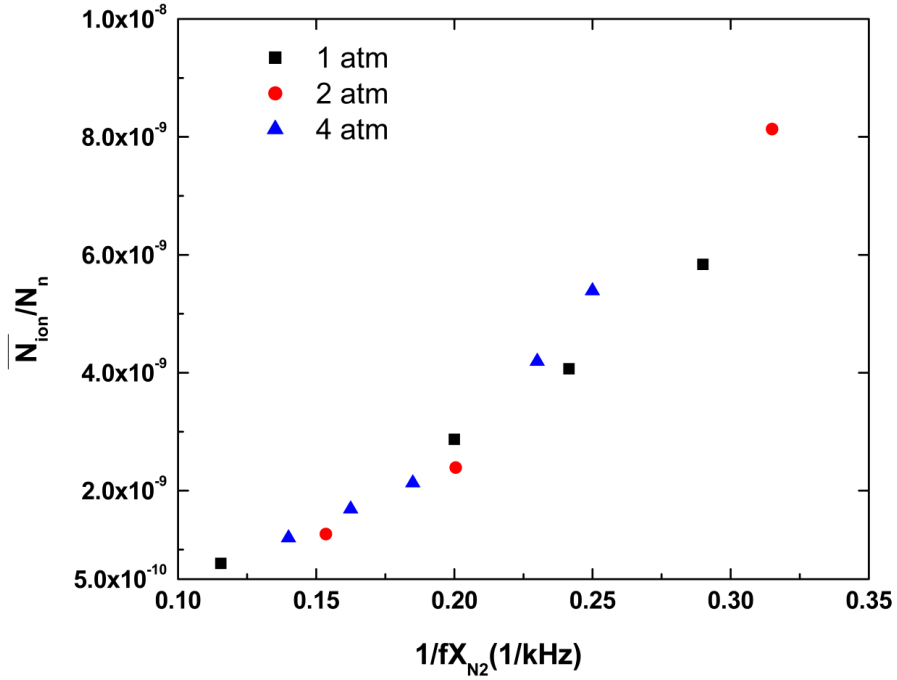

Figure 4.16. Average ion fraction as a function of pulsing frequency and trace nitrogen concentration for different operating pressures in a He-N_2 micro plasma discharge.

The variation in the pulsing frequency and the distinct regimes of operation can be explained in terms of the different and competing characteristics time – circuit response time, ion transit time and recombination time summarized in Figure 4.13. For all the entire discharge current range the ion transit time is smaller than the circuit response time which is the driving mechanism of the observed "self pulsation". As the discharge current is increased the circuit response time decreases, which is due to the fact that in the simulations the discharge current was increased by lower the ballast resistance. The ion transit time is calculated from $\tau_{ion} = \frac{d_{electrode}}{v_{ion}}$, where electrode is the inter-electrode separation, and vion is the ion velocity obtained from the ion mobility and electric field ($v_{ion} = \mu_{ion} E$). The bulk electric field was used to calculate the ion transit time. The procedure for ion transit time determination is similar to the one employed by other researchers (Tanvir Farouk et al.,

2014a; Qiang Wang et al., 2006). The ion transit time is determined for the slowest ions (He_2^+). It does not undergo large variations and remains fairly constant. Arslanbekov and Kolobov (R.R. Arslanbekov & Kolobov, 2005) showed that for a low pressure system, instability in the presence of an external circuit can arise if the characteristic time for instability development (τinst, which is equivalent to the ion transit time) is less than the external circuit time constant ($\tau_{RC} = R \times C$). Farouk and co-workers (Tanvir Farouk et al., 2014a)had observed similar instability in discharges operating at atmospheric pressure. However, none of the previous works identifies the role of kinetics associated with trace species on the pulsing behavior that can result from this type of instability. Despite the constant capacitance value that was prescribed, the pulsing frequency of the discharge increased (Figure 4.12) as the difference between τ_{RC} and τ_{ion} decreased. The discharge becomes stable when $\tau_{ion} > \tau_{RC}$. At the lowest discharge current the ratio between τ_{RC} and τ_{ion} is ~ 5 μs denoting that the circuit required a factor of five longer to respond to the plasma transients. Due to the long reaction time, the oscillation frequency is lower, and the amplitude of the modulation is larger. At the highest discharge current the ratio reduces to ~ 1.3 and so does the amplitude. As the circuit response time starts to become comparable the frequency increases and the modulation becomes shallower. The ion recombination time, $\tau_{recombination}$ presented in Figure 4.10 is for N_2^+ which is the most abundant of ions. The ion recombination time is significantly larger than both τRC and τion. However, the interesting feature is that during the low frequency oscillation the ions have sufficient time to undergo near complete recombination. The different pulsing characteristics is a consequence of the competing ion recombination time. The period, Tpulse for the low frequency discharges, i.e., 260, 280 and 325 kHz are 3.85, 3.57 and 3.08 μs respectively.

The corresponding ion recombination time is ~ 3.0 μs. Therefore, in a pulsing period, ion recombination takes place that drives the discharge to near extinguishment resulting in a complete relaxation oscillation. As the pulsing frequency increases the period decreases and ions cannot undergo complete recombination, and incomplete relaxation oscillation starts to take place. For a pulsing frequency of ~ 325 kHz (i.e., a period of ~ 3.08 μs), the recombination time starts to become comparable to the pulsing period $\tau_{recombination} \approx T_{pulse}$. It is perceived that under these conditions the discharge starts to undergo incomplete relaxation oscillation.

To assess the role of pressure dependent ion kinetics on the pulsing behavior we conducted simulations for higher pressures for the same inter-electrode separation of 400 μm. Simulations were conducted for three different pressures 1, 2 and 4 atm for generating the VI characteristics curves. The power supply voltage, Vs. and the parasitic capacitance, C was constant at 900 V and 0.01 pF for all the cases. By varying the ballast resistance, R from 1 MΩ to 100 MΩ, the discharge current density is changed. The resulting VI characteristics curves are shown in Figure 4.14. Due to the .oscillatory nature of the discharge, the VI curve is presented in rms discharge current density and voltage. One can see the VI curves manifest the usual shape that corresponds to the NDR regime. With an increase in pressure the VI curves shift towards right and shows higher rms voltage for similar discharge current density reflecting the classical pressure dependency of the VI characteristics. It is important to follow the evolution of the self pulsing frequency with the discharge current for different operating pressure. The results are presented in Figure 4.15. For the three pressures reported here, the frequency increases strongly with the discharge current and the frequency is higher at lower pressure. At the same time, it can be seen that

frequency increases faster with current at lower pressure. Similar pressure dependence was reported by Lazzaroni and Chabert (P. Chabert et al., 2010) for a hollow cathode discharge operating at sub atmospheric pressure. Simulations indicate that pulsing frequency of the discharge does not vary linearly with pressure. This observed non-linearity is due to the fact that even though ion mobility decreases linearly with pressure due to the increased gas density, the electric field does not increase linearly which is evident in the pressure dependent VI characteristics (Figure 4.14); resulting in a nonlinear variation in the ion transit time and the consequential pulsing frequency. Following the classical scaling (Fridman & Kennedy, 2004c; Yuri P. Raizer, 1991) and normalizing the current density with pressure squared and the pulsing frequency with pressure one can readily see that the pressure and current density dependence of the pulsing frequency collapse into a single trend line (Figure 4.15). The lower j_{rms}/p^2 and f/p correspond to the high pressure data and vice versa for the higher j_{rms}/p^2 and f/p values.

The base case simulations showed that trace N_2 could significantly affect the pulsing characteristics, especially through the heavy particle kinetics. The distinct multi-step discharge current temporal profile was found to take place due to the trace N_2. To identify the effect of trace N_2 concentration on the oscillation behavior hence the pulsing frequency a series of simulations were conducted by systematically varying the feed gas N_2 concentration. The N_2 concentration was varied in between 0.01 – 0.08 % keeping all other external parameters constant. Within this N_2 concentration range at atmospheric pressure pulsing frequency of the discharge was found to vary from ~ 200 kHz to ~ 1200 kHz having peak N_2^+ density of ~ 2.5 x 10^{18} $1/m^3$ and 3.0 x 10^{17} $1/m^3$. The second most prominent ions N_4^+ varied from ~ 2.3 x 10^{16} $1/m^3$ and 2.5 x 10^{15} $1/m^3$. At higher frequency,

the pulse period decreases to 0.80 μs thereby significantly reducing the time duration for the possible kinetic processes. At the same time with the higher pulsing frequency the discharge starts to undergo incomplete relaxation cycles. The simulations indicated that the peak ion density of the discharge decreased with increasing N_2 concentration as a consequence of increasing pulsing frequency. Due to the inverse relationship, the average ion number density could be correlated to frequency and N_2 concentration as $\frac{1}{f\ X_{N_2}}$. The average ion density is obtained by performing a spatio-temperal average of the ion number density over ten periods once quasi-steady pulsing behavior is attained. Figure 4.16 shows the variation in the average ion number density employing the $\frac{1}{f\ X_{N_2}}$ dependence. To represent the ion density at different operating pressures in the same viewgraph with the possibility of forming a single trend line the obvious intuitive step was to normalize the average ion number density with the neutral number density. Each of the symbols in Figure 4.16 represents an individual simulation. It can be seen that the normalization and $\frac{1}{f\ X_{N_2}}$ functional dependence collapses all the simulation data into a single trend line where the average ion density varies non-linearly with $\frac{1}{f\ X_{N_2}}$. For all the cases studied a higher value of $f\ X_{N_2}$ resulted in a lower average ion concentration and vice versa. Despite being a pure numerical result, it is envisioned that one can utilize the dependence/variation in the plasma pulsing frequency to ion density as means of experimentally detecting trace impurities in feed gas as well as a method of indirect measurement of ion density by injecting a known concentration of trace gas.

4.7.4 RESULTS FROM 2D MODEL

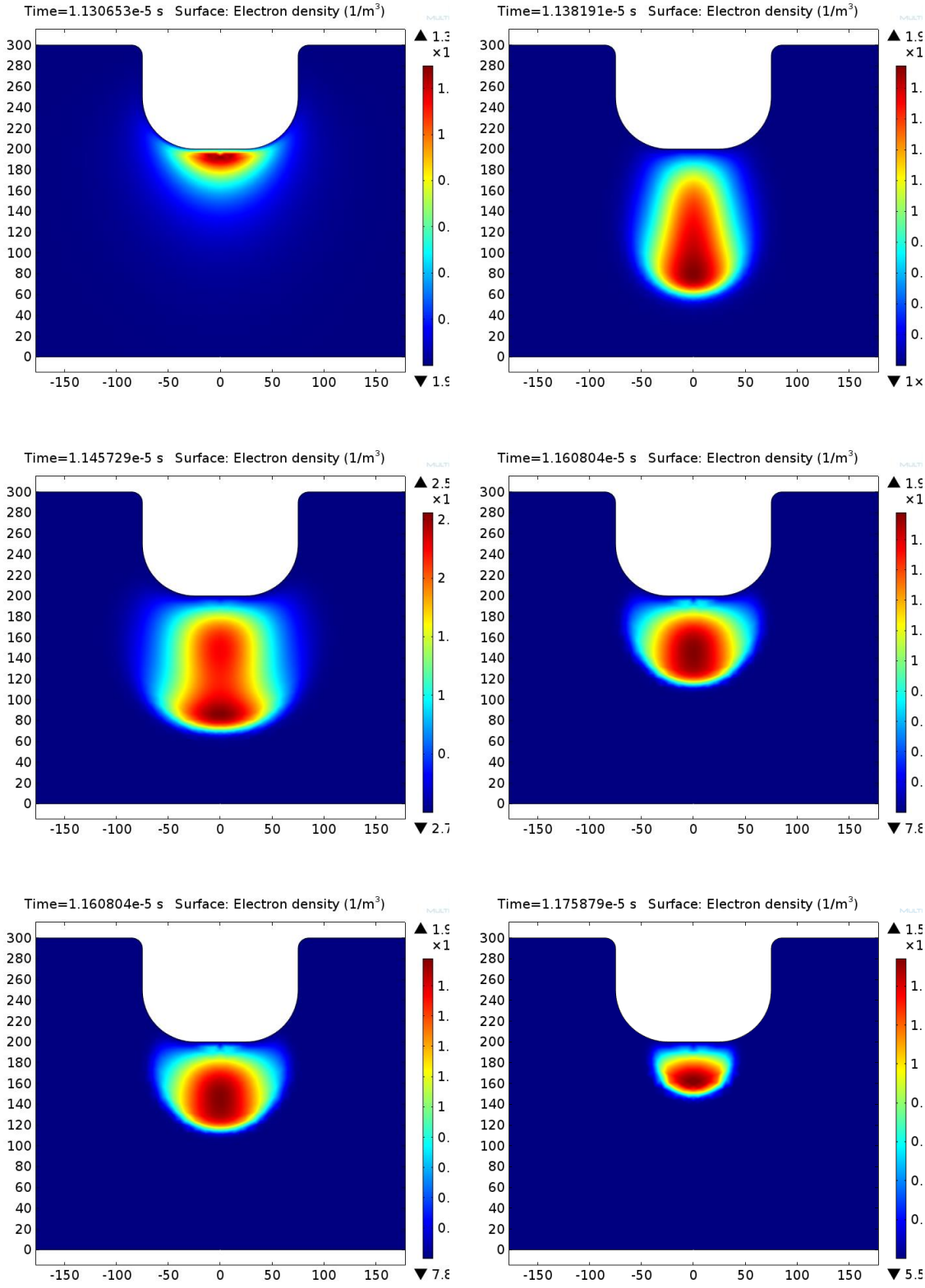

Figure 4.17: The spatial distribution of electron number density over a cycle from the 2D simulation

The 2D axis symmetric model envisages the distribution of ions, electrons, excited species and neutral in the radial direction which is proposed to overcome the limitation of a 1D model (Rajib Mahamud & Farouk, 2013). During a quasi-steady cycle of a self-pulsing mode, the spatio-temporal distribution of species tells the possible state changes that may happen over a cycle. Moreover, numerical diagnostics of ion and species variation and temperature with discharge current is also presented there.

The temporal profile of discharge voltage and current from the numerical results is presented in Figure 4.17. The numerical results from the 2D simulation have a different pattern than one obtained by our 1D model. It is interesting to note that the discharge current profile matches with the experimental profile for a 2D simulation, whereas, the discharge voltage profile can be predicted well by the 1D simulation. This can attribute to the fact that 2D model considers the spatial inhomogeneity of the discharge current in the radial direction. As a result, during the extinction state, the discharge current has supposed to stay at a very low current stage which would be hard to capture with a 1D model. It is recently discussed that the temporal profile of the discharge current can also be obtained with the solution of circuit equation and a proper choice of the discharge resistance. The proper choice of the discharge current results in a correct approximation of power dissipation in the NDR region. The discharge voltage predicts a sawtooth shape for this 2D simulation. The sawtooth profile for discharge current also obtained for 2D simulation at low pressure discharge and for a discharge resistance based circuit equation solver . The experimental results show that the discharge voltage might follow a longer time to rise during the initiation stage like that was obtained in the simulation. The time lagging

between the voltage and current is obtained as 20^{o} from this case. The frequency of oscillation is in in the MHZ ranges for the numerical simulation. It should be noted that the frequency of oscillation is mostly governed by the parasitic capacitance value of the external circuit. The parasitic capacitance value was considers as 1pF whereas the experimental parasitic capacitance was in the nF ranges. As a result, the high frequency oscillation for the 2D simulation is comprehensible.

4.8 CONCLUSIONS

Self-pulsing micro-discharge operating at atmospheric and higher pressure in pure He and He-N_2 feed gas is studied numerically using a validated mathematical model. The self-oscillatory modes are characterized by a repetitive form of discharge voltage and current pulsation when the ion transit time becomes comparable or larger than the external circuit time constant. The presence of trace N_2 in the feed gas was found to significantly alter the pulsing behavior due to the heavy particle kinetic interaction especially Penning ionization, charge transfer and three body ion conversions. The classical "saw tooth" like subnormal oscillation was observed for pure helium gas. For trace N_2 the discharge is found to sharply jump from a low current (high voltage) to a high current (low voltage) mode after which the current starts to sharply decrease until it reaches a "moderate" current value. The discharge maintains itself in this "moderate" current regime for the longest duration which is then followed by a sharp decrease in the lowest current. The transition from the high current to the low current in a pulse cycle takes place in three stages; sharp decrease in "moderate" current, a steady slow decrease in "moderate" current range and a sharp decrease in low current.The discharges were found to be pulse over a broad range of frequency; kilohertz – megahertz depending on the discharge current, pressure and trace

N_2 concentration. At low frequency, the discharges were observed to undergo complete relaxation with larger amplitude modulation. In high frequency pulsing due to the shorter period, the slower kinetic processes do not have the sufficient time for participation resulting in an incomplete relaxation of discharge. The pulsing, therefore, was found to be dictated by the recombination time of the most prevalent ions. If the recombination time is comparable to the pulsing period of the discharge, the discharge undergoes initiation and near extinguishment to undergo a complete relaxation type of oscillation. Whereas, an incomplete relaxation oscillation took place when the ion recombination time was significantly larger than the pulsing period, and near extinguishment did not take place. It was found that at low frequency the electron number density modulated over three to four orders of magnitude reducing to factors at high frequency. The modulation amplitude was governed by the ratio of τ_{RC} / τ_{ion}. Deeper modulations are obtained when the circuit response time is longer and slow. The predicted voltage-current characteristics of the self pulsing state showed the discharge to be operating in the NDR region. The model predictions further indicated that at higher pressure the discharge pulsated at higher currents and the rate of change of frequency as a function of discharge current decreased as pressure increased. On the basis of simulation results in a functional dependency of ion number density to pulsing frequency and trace N_2 concentration is proposed. The results indicated that frequency of a self pulsing DC discharge could be utilized to quantify impurities present in a feed gas as well as an indirect measurement of ion number density in such small systems.

Table

Table 4.1: Gas phase kinetic processes taken into account in the NDR region modeling[+]

	Reactions	***Reaction Rate***
G1	$e + \mathrm{He} \rightarrow \mathrm{He} + \mathrm{e}$	$f(\varepsilon)$
G2	$e + \mathrm{He} \rightarrow \mathrm{He}(2^1\mathrm{S}) + \mathrm{e}$	$f(\varepsilon)$
G3	$e + \mathrm{He}(2^1\mathrm{S}) \rightarrow \mathrm{He} + \mathrm{e}$	$f(\varepsilon)$
G4	$e + \mathrm{He} \rightarrow \mathrm{He}(2^3\mathrm{S}) + \mathrm{e}$	$f(\varepsilon)$
G5	$e + \mathrm{He}(2^3\mathrm{S}) \rightarrow \mathrm{He} + \mathrm{e}$	$f(\varepsilon)$
G6	$e + \mathrm{He} \rightarrow \mathrm{He}^{+} + 2\,\mathrm{e}$	$f(\varepsilon)$
G7	$e + \mathrm{He}(2^1\mathrm{S}) \rightarrow \mathrm{He}^{+} + 2\mathrm{e}$	$f(\varepsilon)$
G8	$e + \mathrm{He}(2^3\mathrm{S}) \rightarrow \mathrm{He}^{+} + 2\mathrm{e}$	$f(\varepsilon)$
G9	$2e + \mathrm{He}^{+} \rightarrow \mathrm{He} + \mathrm{e}$	A
G10	$2e + \mathrm{He}^{+} \rightarrow \mathrm{He}^{*} + \mathrm{e}$	A
G11	$2e + \mathrm{He}_2^{+} \rightarrow \mathrm{He} + \mathrm{He}^{*}$	A
G12	$2e + \mathrm{He}^{*} \rightarrow \mathrm{He}^{+} + \mathrm{e}$	A
G13	$2e + \mathrm{He}_2^{*} \rightarrow \mathrm{He}_2^{+} + e$	A

G14	$e + N_2 \rightarrow N_2 + e$	$f(\varepsilon)$
G15	$e + N_2 \rightarrow N_2^+ + 2e$	$f(\varepsilon)$
G16	$2e + N_2^+ \rightarrow N_2 + e$	A
G17	$e + N_4^+ \rightarrow 2N_2$	A
G18	$e + N_4^+ \rightarrow N + N + N_2$	A
G19	$He^+ + 2He \rightarrow He_2^+ + He$	A
G20	$He(2^1S) + He \rightarrow 2He$	A
G21	$He(2^3S) + He \rightarrow He_2^* + He$	A
G22	$2He(2^3S) \rightarrow e + He + He^+$	A
G23	$He^+ + N_2 \rightarrow N_2^+ + He$	A
G24	$He_2^+ + N_2 \rightarrow N_2^+ + 2He$	A
G25	$He_2^+ + N_2 + He \rightarrow N_2^+ + 2He$	A
G26	$He_2^+ + N_2 + He \rightarrow N_2^+ + 3He$	A
G27	$He(2^3S) + N_2 \rightarrow e + He + N_2^+$	A
G28	$He(2^1S) + N_2 \rightarrow e + He + N_2^+$	A

G29	$He(2^3S) + N_2 + He \rightarrow e + 2He + N_2^+$	A
G30	$N_2^+ + N_2 + He \rightarrow N_4^+ + He$	A
G31	$N_2^+ + 2N_2 \rightarrow N_4^+ + N2$	A

[+] A: reaction rate in Arrhenius form, $f(\varepsilon)$: reaction rate obtained from EEDF (electron energy distribution function).

Table 4.2. Surface reactions considered in the NDR region modeling

	Reactions
S1	$He(2^1S) \rightarrow He$
S2	$He(2^3S) \rightarrow He$
S3	$He^* \rightarrow He$
S4	$He_2^* \rightarrow 2He$
S5	$He^+ \rightarrow He$
S6	$He_2^+ \rightarrow 2He$
S7	$N_2^+ \rightarrow N_2$
S8	$N_4^+ \rightarrow 2N_2$

CHAPTER 5

SUPPRESSION OF NDR INSTABILITY IN A DC DRIVEN MICROPLASMA SYSTEM

5.1 INTRODUCTION

The microplasma ranges from tens to thousands of micrometer and are attractive for the commercial application, e.g., plasma jet, plasma needle, biomedical applications, micropropulsion, microplasma actuation, MEMS technology due to their operational viability and low energy consumption (Aubert et al., 2007b; Becker et al., 2006b; Begum, Begum, Laroussi, & Pervez, n.d.; Dubrovin et al., 2010; D B Go & Venkattraman, 2014; O'Neill, Lee, Cofer, & Alexeenko, 2015; D. Staack et al., 2007; Tholeti, Shivkumar, & Alexeenko, 2016; Wirz, Mueller, Gale, & Marrese, 2004; Zhu & Lopez, 2012). They are widely used for attaining non-thermal and non-equilibrium discharge at atmospheric and higher pressures due to the fact that their small sizes inhibit the ionization overheating instability through rapid cooling (Becker, Kersten, Hopwood, & Lopez, 2010; Felipe Iza et al., 2008b). However, due to its small size, microplasmas are very susceptible to instability resulting from external disturbances. The source of these disturbances are external parameters, e.g., external circuitry constant which triggers self-pulsing oscillations (Rajib Mahamud & Farouk, 2014a, 2013, 2014b).

The oscillation in the NDR region varies from few hundreds to thousands of kHz (Aubert et al., 2007b; Kolobov & Fiala, 1994; Rajib Mahamud & Farouk, 2016; Petrović & Phelps, 1993; Stefanović et al., 2011). Due to negative differential resistance property, physics governing this device can be used actively as an oscillator. As this oscillation is above in microwave range, it has applications in radar speed guns and local oscillators for satellite receiver. Tunnel diodes are the first negative differential resistance (NDR) active devices in the microwave band which date back to Esaki's classical work in 1958 (Leo Esaki, 1960). NDR governed devices are a widely used source of microwave energy, and the only solid-state source of millimeter wave and terahertz energy (Haddad, East, & Eisele, 2003). Negative resistance microwave vacuum tubes such as magnetrons produce higher power outputs for applications like radar transmitters and microwave ovens (Räisänen & Lehto, 2003). Lower frequency relaxation oscillators can be made with UJTs and gas-discharge lamps such as neon lamps. The negative resistance oscillator can also be applied to feedback oscillator circuits with two port devices such as transistors and tubes. In addition, transistors are increasingly used as one-port negative resistance devices like diodes. The understanding of physics of NDR oscillation and the characterization of the NDR region for microplasma discharges has recently gained considerable attention (Aubert et al., 2007a; P. Chabert, Lazzaroni, & Rousseau, 2010c; Kudryavtsev & Tsendin, 2002; Rajib Mahamud & Farouk, 2013). The understanding of the NDR oscillation for MHCD and parallel plate geometry has been studied in experimental and numerical modeling (P. Chabert, Lazzaroni, & Rousseau, 2010d; Lazzaroni & Chabert, 2011; Rajib Mahamud, Mobli, & Farouk, 2014; Stefanović et al., 2011b). The effectiveness and reliable operation of DC microplasma devices depends on

stable discharge condition and is hindered by the self-driven and sustaining instability resulting from external parameters. Though parallel plates, pin-plates and micro hollow cathode discharge (MHCD) geometry are the most widely used configurations to obtain a stable discharge for a wide range of current and pressures, the instability in the NDR region is a norm and is unavoidable. However, the NDR region in discharge current space is not absolute.

In this chapter a method for the suppression of NDR instability is presented based on theoretical modeling on external circuit and a subsequent experimental study. As the studies suggested that the inset and sustaining of NDR instability is driven by the response of the external circuit, a method to damp the response time is presented by the addition of an external circuit element element. As the parasitic capacitance increases the external circuit response time, we propose to add an inductor element which, by definition, reduce the external circuit response time. The experimental modeling and numerical simulation was carried out to validate the concept (Rajib Mahamud & Farouk, 2016). For the numerical modeling circuit equation was numerically solved using the experimentally measured discharge resistance. The result shows that by using the suppressing circuit element it is possible to manipulate the instability in the NDR region, and an overall imporvment of the discharge system.

5.2 THEORY AND MODELING

In this study a theoretical concept of stability in the NDR region is proposed. A very few studies has discussed about obtaining the stability in plasma discharge from analytical and numerical studies (Asadullin, Galeyev, & Timerkayev, 2016; Felix et al., 2016; Miura & Hopwood, 2012; Phelps,Shneider, Mokrov, & Milikh, 2012). The low

pressure experiments of Phelps et. al. tells that a suppression in the self-pulsing region can be attained when the monitoring resistance is significantly higher than the discharge resistance (Petrović & Phelps, 1993a). Here the monitoring resistance Rm is connected in series and downstream of the discharge. An extremely value of Rm is required for establishing a stable discharge and this condition is not considered practical. Moreover, Kaganovich et. al. from mathematical modeling predicted that stability can be obtained in the NDR region when the ballast resistance becomes larger than the discharge resistance i.e. Rballast > Rdischarge for low pressure DC discharges operating at low currents (I. D. Kaganovich, M. A. Fedotov, 1994). A stability criterion for microplasma discharges has been proposed by Staack et. al by reducing the parasitic capacitance of the circuit (D. Staack et al., 2009b). However, this method has a minimum current bound due to the practical limits of reducing the parasitic capacitance of the external circuit. Those studies, however, has mostly focused on the perspective of suppression of ionization instability.

The parasitic capacitance presents intrinsically in the system in parallel to the discharge due to external wires and connections. The capacitance of the system place a circuit response time to the discharge which is responsible to trigger instability in the discharge (Robert R Arslanbekov & Kolobov, 2003). Therefore, the addition of an additional capacitor can be derogatory to the discharge as it will further increase the circuit response time. On the criticality of the external circuit condition, a static instability in the NDR region appears when the circuit response becomes higher than the ion transit time i.e.

$$\tau_{RC} > \tau_{ion} \tag{5.1}$$

The suppression circuit of the current disclosure comprises an inductor connected in series with the ballast resistance and the discharge, which increases the combined response time of the plasma and the inductor, such that

$$\tau_{L/R_{plasma}} > \tau_{RC} > \tau_{ion} \tag{5.2}$$

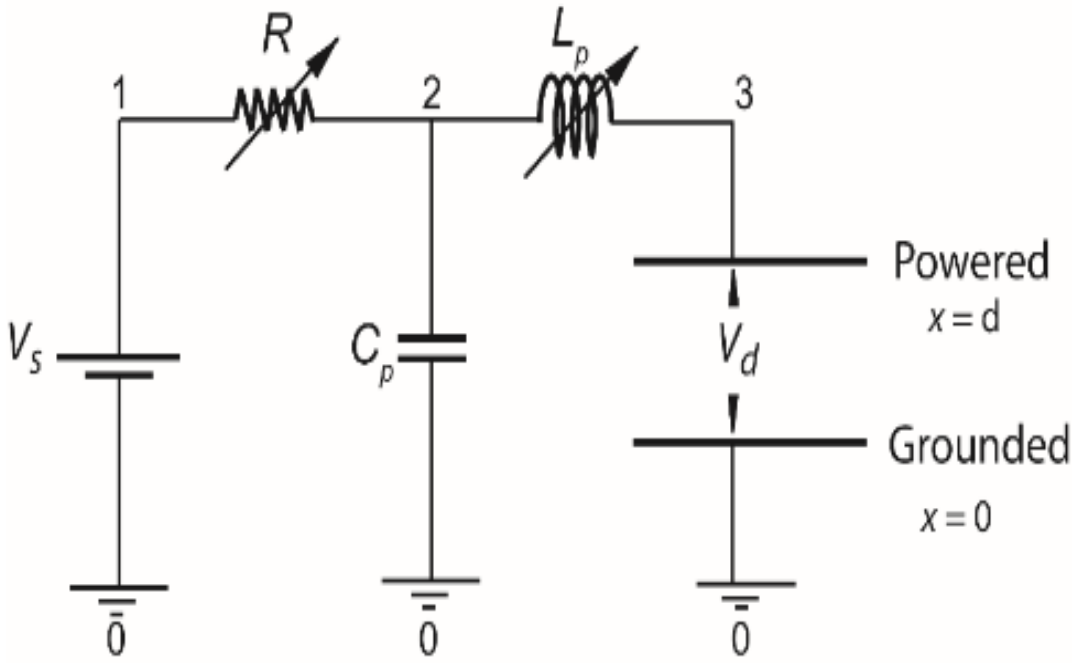

Figure 5.1: Schematic of the circuit diagram. R, L represents ballast resistance and external inductor, respectively.

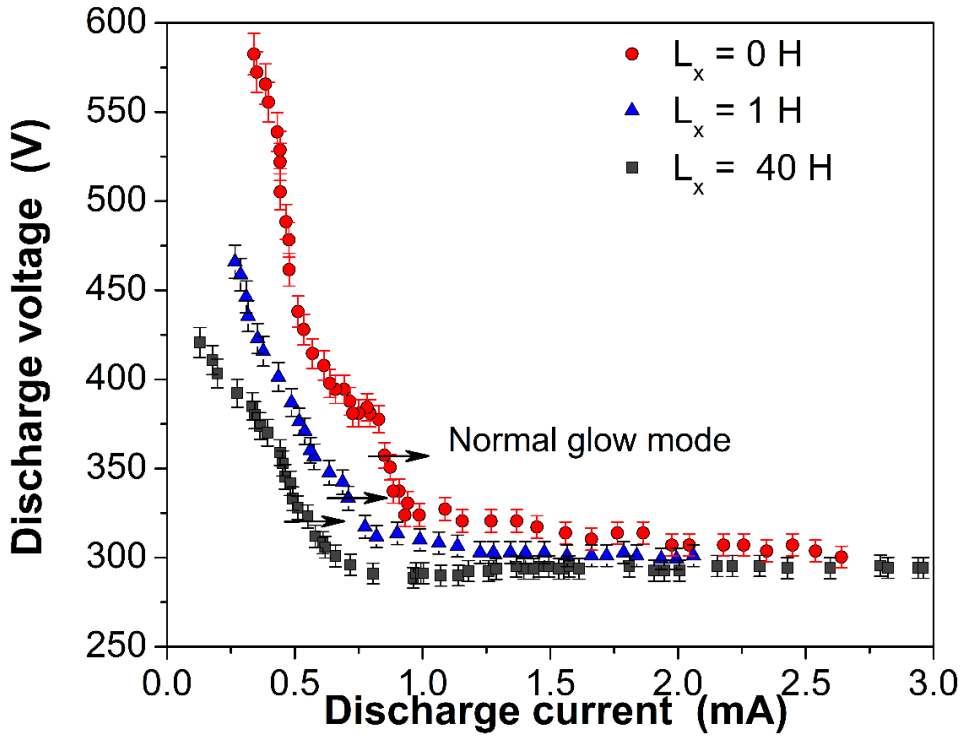

Figure 5.2: Voltage current characteristic of a dc driven micro plasma discharge operating in helium at atmospheric pressure ($d_{inter\text{-}electrode}$ = 200 µm, $R_{ballast}$ = 100 kΩ , *pd* = 15.2 Torr-cm) in presence of external inductor. Two different inductance value was considered for the study, L_x = 1H and L_x = 40 H.

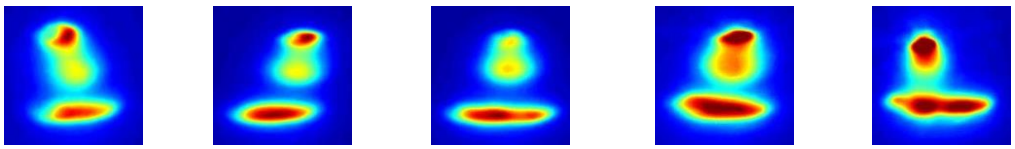

Figure 5.3: Pseudo color grayscale image of electron number density with the addition of an inductor, L_x=40 H aa shown in Figure 7.3, is shown for five different discharge current condition. The pseudo color image confirms that discharge is stabLe for a lower current (0.35 mA) in the presence of suppressing element which was unstable otherwise.

The schematic of the discharge element with the external circuit is shown in Figure 5.1. Here R is the ballast resistor, L is the inductor os supressign circuit element, and Cp is the parasitic capacitance presents intrinsically to the system. Based on the experimental results, a circuit model is solved to investigate the stability condition in details. The circuit model employed is similar to those reported in some recent works

$$V = L_x \frac{dI}{dt} + R_{discharge} I \tag{5.3}$$

$$V = V_s - IR_{discharge} - R_{ballast} C_p \frac{dV}{dt} \tag{5.4}$$

(Hsu & Graves, 2003; Taylan & Berberoglu, 2014). The discharge characteristics in the presence of the suppression element (i.e. inductor) can be obtained from the solution of Eq. (5.3) and (5.4).

The solution of the circuit model is based on the choice of the discharge resistance. It is a common norm to model the nonlinear NDR discharge resistance as a function of discharge current (Hsu & Graves, 2003; Lazzaroni & Chabert, 2011). For the current model the discharge resistance is expressed as:

$$R_{discharge} = C_1 \tanh(\frac{I - I_{\lim}}{p}) + C_2 \tag{5.5}$$

Where, the constants, C_1= -1920 Ω, C_2= 2000 Ω, I_{lim}= 0.317 mA, and p = 0.45 mA, were obtained from experimental fits. The system of equations for the circuit model is solved with an implicit Runge-Kutta solver in MATLAB with the accuracy level of 10^{-3} ~ 10^{-6}.

5.3 EXPERIMENTAL SETUP

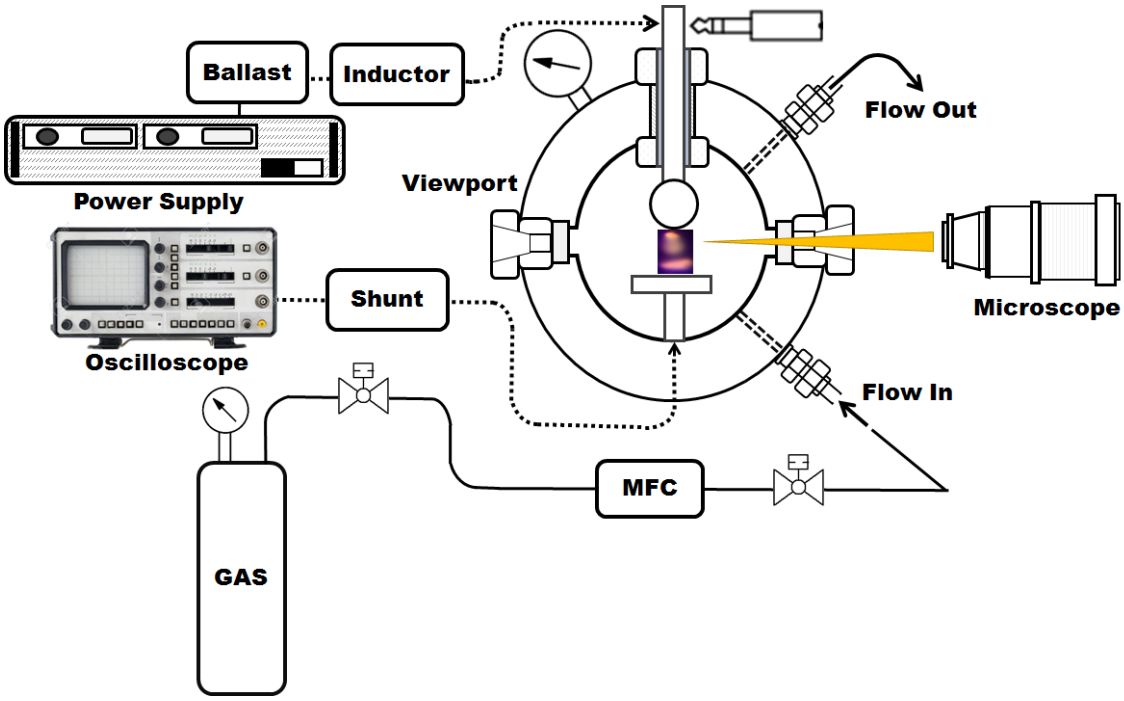

Figure 5.4 Schematic of the experimental setup of NDR suppression with ballast resistance, external inductor and shunt resistance

This experiment is the first experimental demonstration on the suppression of the self-pulsing regime of a DC driven microplasma discharge in a parallel plate configuration. The NDR instability is controlled here by including an additional elements in the external circuit configuration. The external circuit parameters has been widely used to characterize and study the self-pulsing regime of the NDR region. From the external circuit conditions, the self-pulsing in the NDR region is obtained when the external circuit response time

becomes higher than the ion transit time, i.e. $\tau_{RC} > \tau_{plasma}$. The proposed suppression circuit element consists of an inductor connected in series with the ballast resistance and the discharge itself which increases the combined response time of the plasma and the inductor, such that $\tau_{L/R_{discharge}} > \tau_{RC}$.

As a test case, an atmospheric pressure microplasma setup with parallel plate geometry configuration operating at helium was investigated. Three inter-electrode separation distances were investigated 100 μm, 200 μm and 400 μm corresponding to pd values of 7.6, 15.2, and 30.4 Torr-cm. The electrode arrangement consisted of a spherical anode and a flat cathode disk having diameters of 12.7 and 10 mm respectively. A stainless steel spherical anode was used to maintain the discharge in the central region (i.e. the smallest gap) to ease the visualization process. The anode electrode was attached to a micropositioner for varying the inter-electrode separation distance. The electrodes are contained inside a stainless pressure chamber with quartz window viewports for discharge visualization. The chamber is sealable and there are gas inlets and outlets for testing in a variety of pressures and discharge gases. The experiments were conducted using a Spellman SL20P2000 DC power supply setup connected in series to a 100 kΩ ballast resistor, an inductor (oscillation suppression experiments) and the discharge. For time dependent current measurements a current shunt (10 kΩ) was placed between one electrode of the discharge and the ground. A North Star PVM-4 high impedence 1000:1 voltage probe was placed directly adjacent to the anode the measure the discharge voltage. Both the voltage probe and the current shunt are connected to an oscilloscope (Agilent Technologies InfiniiVision MSO7054B) for DC or time dependent measurements.

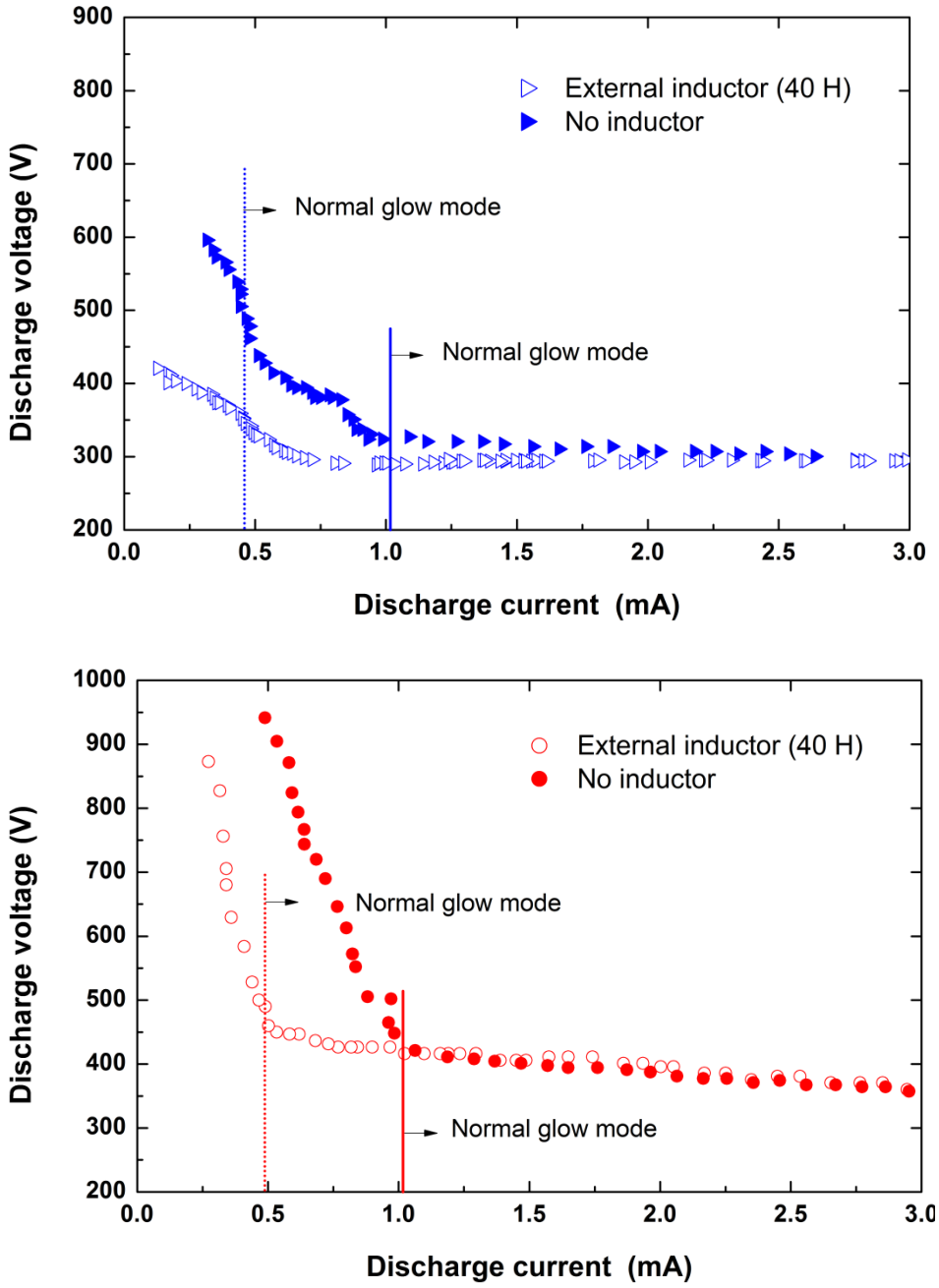

Figure 5.5: Voltage current characteristic of a DC driven micro plasma discharge operating in helium at atmospheric pressure with and without the suppression circuit for different inter-electrode separation distance a) $d_{inter\text{-}electrode}$ = 400 µm, $R_{ballast}$ = 100 kΩ, pd = 30.4 Torr-cm, b) $d_{inter\text{-}electrode}$ = 100 µm, $R_{ballast}$ = 100 kΩ, pd = 7.6 Torr-cm.

The parasitic capacitance of the external circuit was measured as 40 pF. Experiments are conducted with high purity helium feed gas (AirGas, 99.997% purity level). For

visualizing the discharge a Nikon D7000 camera was mounted on a microscope focused on the discharge. The microscope-camera setup provided a variable magnification. A schematic of the experimental setup is depicted in Figure 5.2.

5.4 RESULTS AND DISCUSSION

The voltage-current (VI) characteristics with and without the presence of the inductor element is shown in Figure 5.3. The VI characteristics curve in the NDR region, showing a complete relaxation oscillation, is obtained from the RMS voltage and current. The VI curves from the experiment maintain the usual shape i.e. *subnormal* mode at lower currents and then attains the "flat" *normal* glow as the discharge current increases. Though self-pulsing is a NDR phenomenon, region near the transition point attains a steady "non-pulsing" discharge condition. The presence of an inductor was found to extend the *normal* glow region operation to lower currents – shifting the NDR region. The measurement with different inductance value shows that, the '*normal*' glow region of the discharge can be extended to lower currents with increasing inductance value.

The transition from '*subnormal*' to '*normal*' glow occurs at 0.8 mA in absence of any external inductor element. The transition point shifted to 0.65 mA and 0.40 mA for a 1H and 40H respectively The NDR region is still retained with the different inductors however the slope changes significantly. The slope of the NDR region varies from 440 kΩ, 305 kΩ, and 225 kΩ for an inductance value of 0H, 1H, and 40H, respectively. The decrement of the slope of the NDR region is also an indication of the fact that the inductor element extenuating the NDR response of the system. The suppressing circuit element adds

a positive impedance to the system and the plasma become less sensitive to the change in voltage with respect to the change in current.

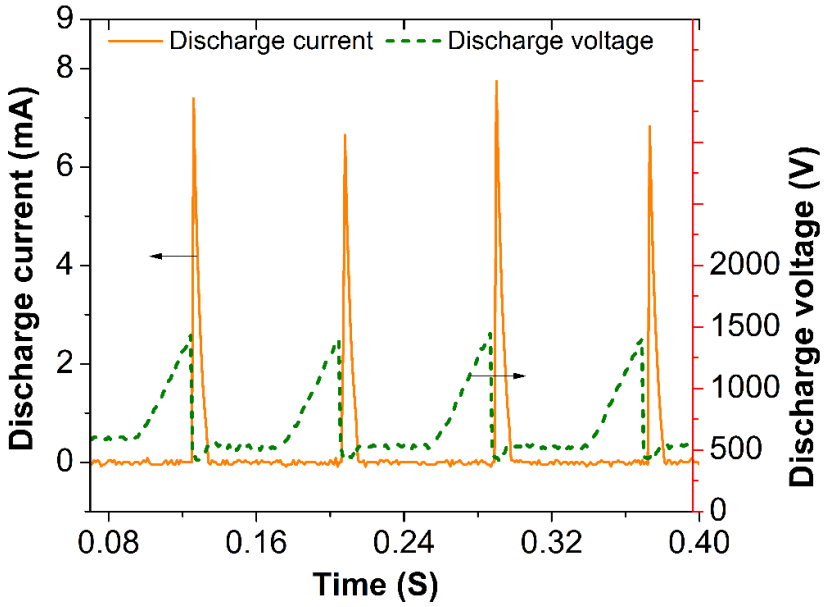

Figure 5.6: Transient discharge voltage and current profile in the NDR region without the presence of any suppressing circuit element ($d_{inter\text{-}electrode}$ = 200 µm, $R_{ballast}$ = 100 kΩ , pd = 15.2 Torr-cm)

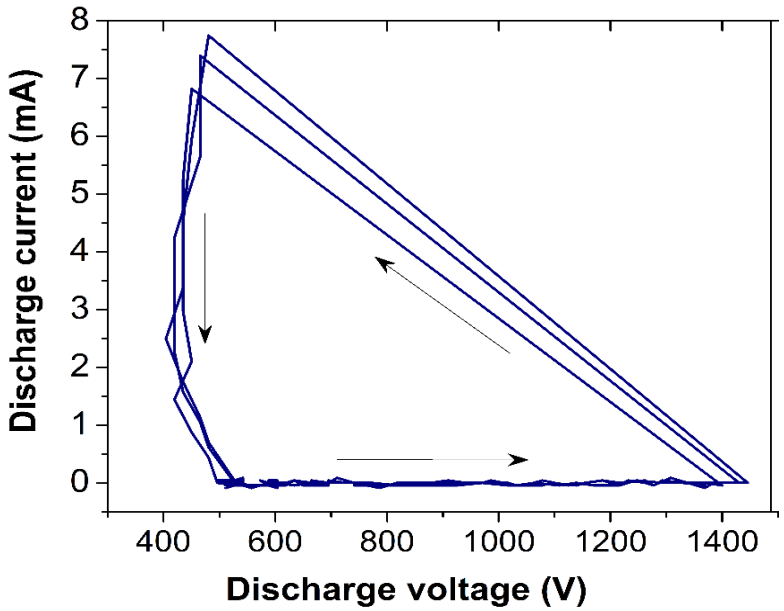

Figure 5.7: Lissajous plot, the discharge voltage vs discharge current which corresponds to the condition.

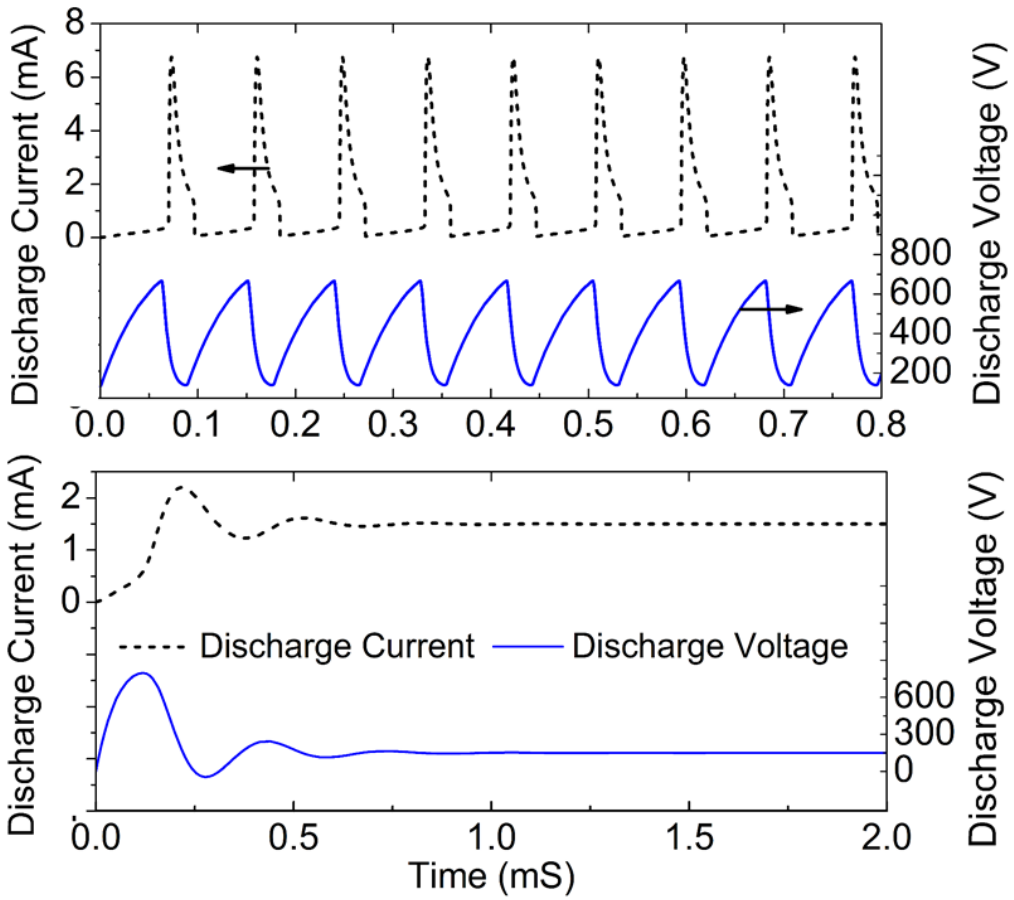

Figure 5.8: Discharge current profile with the presence of inductor a) self pulsation (L_x = 0.01H) b) damped oscillation (L_x = 20H) ($R_{ballast}$ = 100 kΩ , C_p = 100 pF).

It is interesting to note that as the inductor decreases the NDR slope it is also decreasing the positive static resistance of the system. This behavior is related to the oscillatory behavior of the discharge i.e. pulsing frequency. In the NDR region for the same discharge current it was observed that increasing the inductance decreased the pulsing frequency. For a discharge current of 0.25 mA the pulsing frequency was measured to be 21 Hz, 18 Hz and 16 Hz for inductance values of 0H, 1H and 40H respectively. In addition to the pulsing frequency the phase lag between the voltage and current is substantially decreased which was measured as ~ 13, 10 and 7 degrees for 0H, 1H and 40H respectively

for the same discharge current of 0.25 mA. The decrease in the positive static resistance is due to the increase in the pulse width hence decrease in the pulsing frequency of the discharge as well as some additional voltage drop across the inductor itself. Due to the RMS nature of the voltage current plots the frequency has a more direct influence. The role of the inductance on the static positive resistance can

The transition from '*subnormal*' to '*normal*' glow occurs at 0.8 mA in absence of any external inductor element. The transition point shifted to 0.65 mA and 0.40 mA for a 1H and 40H respectively The NDR region is still retained with the different inductors however the slope changes significantly. The slope of the NDR region varies from 440 kΩ, 305 kΩ, and 225 kΩ for an inductance value of 0H, 1H, and 40H, respectively. The decrement of the slope of the NDR region is also an indication of the fact that the inductor element extenuating the NDR response of the system. The suppressing circuit element adds a positive impedance to the system and the plasma become less sensitive to the change in voltage with respect to the change in current.

It is interesting to note that as the inductor decreases the NDR slope it is also decreasing the positive static resistance of the system. This behavior is related to the oscillatory behavior of the discharge i.e. pulsing frequency. In the NDR region for the same discharge current it was observed that increasing the inductance decreased the pulsing frequency. For a discharge current of 0.25 mA the pulsing frequency was measured to be 21 Hz, 18 Hz and 16 Hz for inductance values of 0H, 1H and 40H respectively. In addition to the pulsing frequency the phase lag between the voltage and current is substantially decreased which was measured as ~ 13, 10 and 7 degrees for 0H, 1H and 40H respectively for the same discharge current of 0.25 mA. The decrease in the positive static resistance is

due to the increase in the pulse width hence decrease in the pulsing frequency of the discharge as well as some additional voltage drop across the inductor itself. Due to the RMS nature of the voltage current plots the frequency has a more direct influence. The role of the inductance on the static positive resistance can summarized as $L_x \uparrow V_L \uparrow f \downarrow V_{discharge\ RMS} \downarrow R_{discharge\ RMS} \downarrow$. Similar behavior is also observed for a 100 and 400 μm inter-electrode separations (Figure 5.5).

Images of the discharges for different discharge currents in both the steady and pulsing regime for the same pd value is provided in Figure 5.5. Figure 5.5 corresponds to the experimental data of Figure 5.4 and for a condition when L_x=40 H. False coloring, or the pseudo color grayscale image, scaled as a function of emission intensity is employed to obtain a better insight of the discharge structure. The time averaged image of a pulsing discharge shows that the discharge has a uniform intensity (both the positive column and negative glow being equally bright) without the presence of a Faraday dark space. The discharge images in presence of the inductor clearly shows that the classical and distinctive DC glow structure is attained – anode glow, Faraday dark space and negative glow. The 'normal' glow is also retained which is confirmed by the increasing cathode spot and the constant current density of 1.8 A/cm2. For identical discharge current of 0.65 mA, the inductor suppresses the oscillation of the discharge and establishes a steady discharge that has the distinctive steady DC glow characteristics.

However a small increment of voltage was observed with the reducetion of current was observed from 0.75 mA to 0.4 mA in the normal glow region. Though the discharge was stable in this region, we attributed this small NDR slope due to temperature rise , which subsequecntly increases the discharge voltage slightly. As pseudo color image presented

to this low discharge current, such as 0.45 mA and 0.65 mA, we can clearly see a cathode fall region, faraday dark space and a positive column region in the discharge.

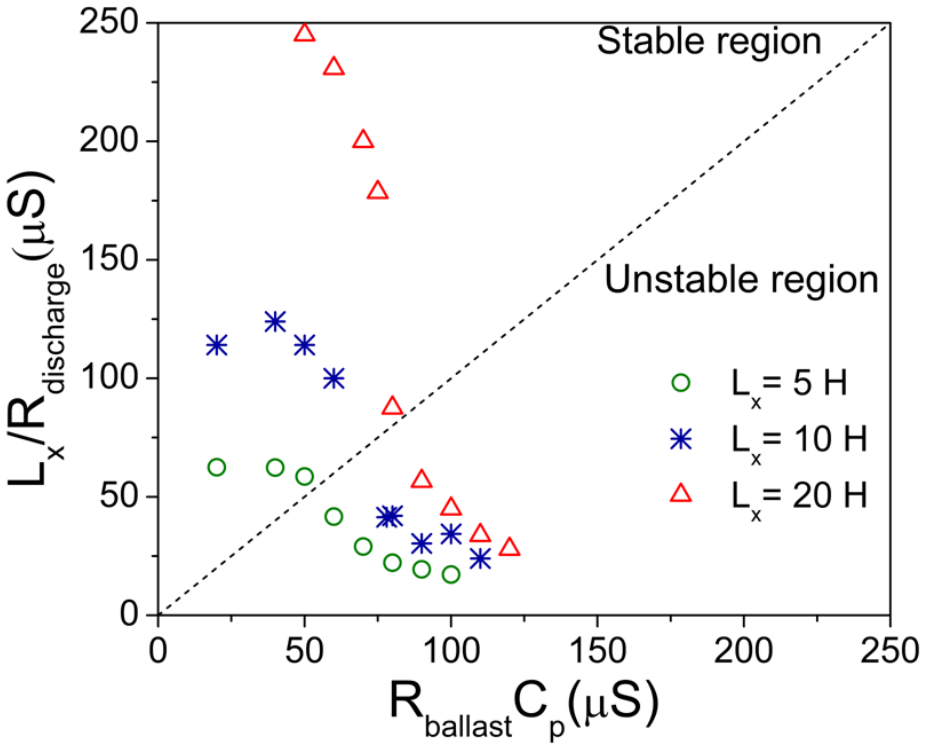

Figure 5.9: A stability map based on the suppression of oscillatory discharge with the inclusion of external inductance (Rballast = 100 kΩ , Cp = 100 pF). Each symbol represents an individual numerical experiment.

The suppression circuit element can generates a stable discharge at lower current condition. Hence provide an additional advantage to plasma aided micropatterning application where a smallest feature size is necessary. The VI characteristics for two other inter-electrode spacing, 100 µm and 400 µm corresponding to pd values of 7.6 and 30.4 Torr-com show similar instability suppression and extension of the normal glow regime in presence of external inductor element (Figure 5.5). The inclusion of 40H inductor altered the normal glow inception from 0.46 mA to 0.3 mA and from 0.90 mA to 0.50 mA for electrode spacing of 100 µm and 400 µm respectively.

The temporal evolution of the voltage and current for a standard self-pulsing discharge (without any suppressing circuit element) is presented in Figure 5.6. In the pulsing mode the voltage and current exhibit a phase difference of 15o. The temporal profiles have similarity to those obtained for a moderate pressure self-pulsing MHCD10. In a single pulse the discharge voltage exhibits three different stages. During the current spike, the discharge voltage shows a sudden dip which is followed by a gradual increase to a moderate voltage that is maintained for a significant duration. A linear ramping to the highest voltage is observed soon after. It was observed that this moderate voltage time duration decreases if current increases and discharges voltage can become saw tooth in shape. The phase space diagram for the voltage-current is presented in Figure 5.7 which is found to attain a triangular shape. The phase space diagram has three different regions. During the extremely low current stage the voltage sharply increases from 500V to 1250V (stage 1). One can then see a decrease in discharge voltage with an increase in the discharge current (stage 2). Following this stage the current decreases sharply followed with a slight increase in the voltage (stage 3).

The predicted transient discharge voltage and current profile from the circuit equation solver is shown in Figure 5.8. The numerical results are found to predict the experimental trends. For an inductance value of L_x = 0.01 H, pulsing of voltage and current (i.e. an oscillatory discharge) is observed (presented in Figure 5.8(a)). This lower value of inductance corresponds to a value, where $\tau_{L_x/R_{discharge}} < \tau_{R_{ballast}C_p}$, as a result the discharge shows oscillation without any amplitude attenuation. The discharge voltage has a sawtooth like pattern in close resemblance to those of the experiments. Simulation is also conducted in

the presence of an inductor of higher magnitude, such that $\tau_{L_x/R_{discharge}} > \tau_{R_{ballast}C_p}$; the oscillation for both the current and voltage is damped resulting in a steady discharge voltage/current at the end (Figure 5.8(b)). The model predictions are in qualitative agreement with the experimental results. The presence of an inductor acts as a damping element in the coupled plasma-external circuit. Based on the interaction of the different circuit element, especially the representative characteristics response time, a stability map denoting regimes of pulsing and stable operation can be proposed. Figure 5.9 shows such a stability regime map where each of the symbols represents an individual simulated case. The 45◦ degree line in the stability plot represents condition, where $\tau_{L_x/R_{discharge}} = \tau_{R_{ballast}C_p}$, and demarcates stable and unstable operation regime. For conditions, where $\tau_{L_x/R_{discharge}} < \tau_{R_{ballast}C_p}$, a self-pulsing DC discharge that undergoes relaxation type oscillation5 is observed. Varying/incrementing the inductance value the combined time response of plasma with inductor can be increased to a value, where $\tau_{L_x/R_{discharge}} > \tau_{R_{ballast}C_p}$, making the driving circuit response time comparably shorter and establishing a stable DC operation can be obtained.

5.5 CONCLUSION

The context of this chapter is to develop an instability suppressor circuit for self-pulsing DC driven micro-plasma discharge with a view to extending the stable region of operation. In this regard, we performed modeling and experiments for the development of a external suppressing circuit element for a dc driven microplasma system. The mathematical model predicts the possibility of suppression of NDR instability by the addition of external circuit element. Based on the modeling, an instability suppressor

circuit element was tested over a range of pd values for a helium feed gas. The negative differential resistance (NDR) region was observed to shift further left in the voltage-current parametric space (i.e. lower current) and the slope of the NDR region was decreased substantially. In addition, the suppressor circuit element was able to extend the 'normal' glow regime of operation to lower currents. Modeling of the discharge configuration indicated that the inductor element of the suppressor circuit increases the time lag of the plasma response which increases the stable region of operation.

The modeling and experiments suggests that the suppressing circuit element is able to successfully suppress the self-pulsing of the discharge over a range of pressure and electrode separation distance, extending the normal glow regime to lower currents. As it eliminates the instability of atmospheric pressure and high pressure discharges so that its application can be extended over a broader range of operating conditions. In the field of plasma enhanced chemical vapor deposition (PECVD), plasma aided micro-patterning the smallest feature size is dictated by smallest discharge current at which a stable discharge can be attained. The proposed method increases the stable operation mode of DC driven micro-plasma from extremely low to high current. Thus enhancing the regime of operation of plasma discharge system.

CHAPTER 6

ION NUMBER DENSITY QUANTIFICATION IN MICROPLASMA DISCHARGES

6.1 INTRODUCTION

There is significant interest in the understanding and application of micro plasma discharge due to its unique features microplasma discharges which includes stable operation at higher pressure (Annemie Bogaerts, Erik Neyts, Renaat Gijbels, 2002; Bruggeman & Brandenburg, 2013) , non-equilibrium characteristics (Becker, Schoenbach, & Eden, 2006c), high electron and excimer density (Park & Eden, 2002) , large surface to volume ratio and low energy consumption (Lin & Wang, 2015); all of them contributing towards novel applications of such systems. The characterization of DC driven microplasma discharges both experimentally and numerically (Du, Aramaki, et al., 2011; David Staack, Farouk, Gutsol, & Fridman, 2005b) has been of prime interest in the recent years. Both the experimental and numerical characterization has been complementary to each other. One of the major challenges in conducting diagnostics especially charged species density quantification of microplasma discharge is the inherently small size of this system. As a result, non-intrusive diagnostics involving optical emission spectroscopy (OES), laser absorption spectroscopy is prevalent for microplasma discharges.

Staack et al. performed OES to determine the rotational and vibrational temperature for atmospheric pressure normal glow discharges (David Staack et al., 2005b). Furthermore, they also attempted in estimating the dominant ion number density in air by utilizing emission intensity ratios and found the N_2^+ number density to be ~ 5.5 x 10^{16} m^{-3}. Spatially resolved OES of a micro hollow cathode discharge in helium feed gas was conducted by Wang et al. (Qiang Wang et al., 2006). In addition to their gas temperature measurements, electron number density in the bulk plasma was determined from spectral line broadening of H_β emission. The spatially averaged electron number density was found to be in the range of (4 – 7) x $10^{19}m^{-3}$.

Instability in microplasma discharges resulting from external parameters e.g. external circuit has also been studied in past. These studies involved characterizing the instability hence the pulsing behavior both experimentally and numerically. Methods on how to suppress these instabilities have also been proposed. In our prior work where we conducted a numerical simulation of the self-pulsing regime of a He-N_2 micro plasma discharge, it was observed that ion number density had a strong dependence on the pulsing frequency as well as the level of impurity (i.e. N_2) present in the system. In this letter, we propose a methodology of quantifying ion number density from the pulsing frequency of a discharge and utilize it directly in experiments. The estimated ion number density from the experimental results are also compared against predictions from detailed multi-physics simulations.

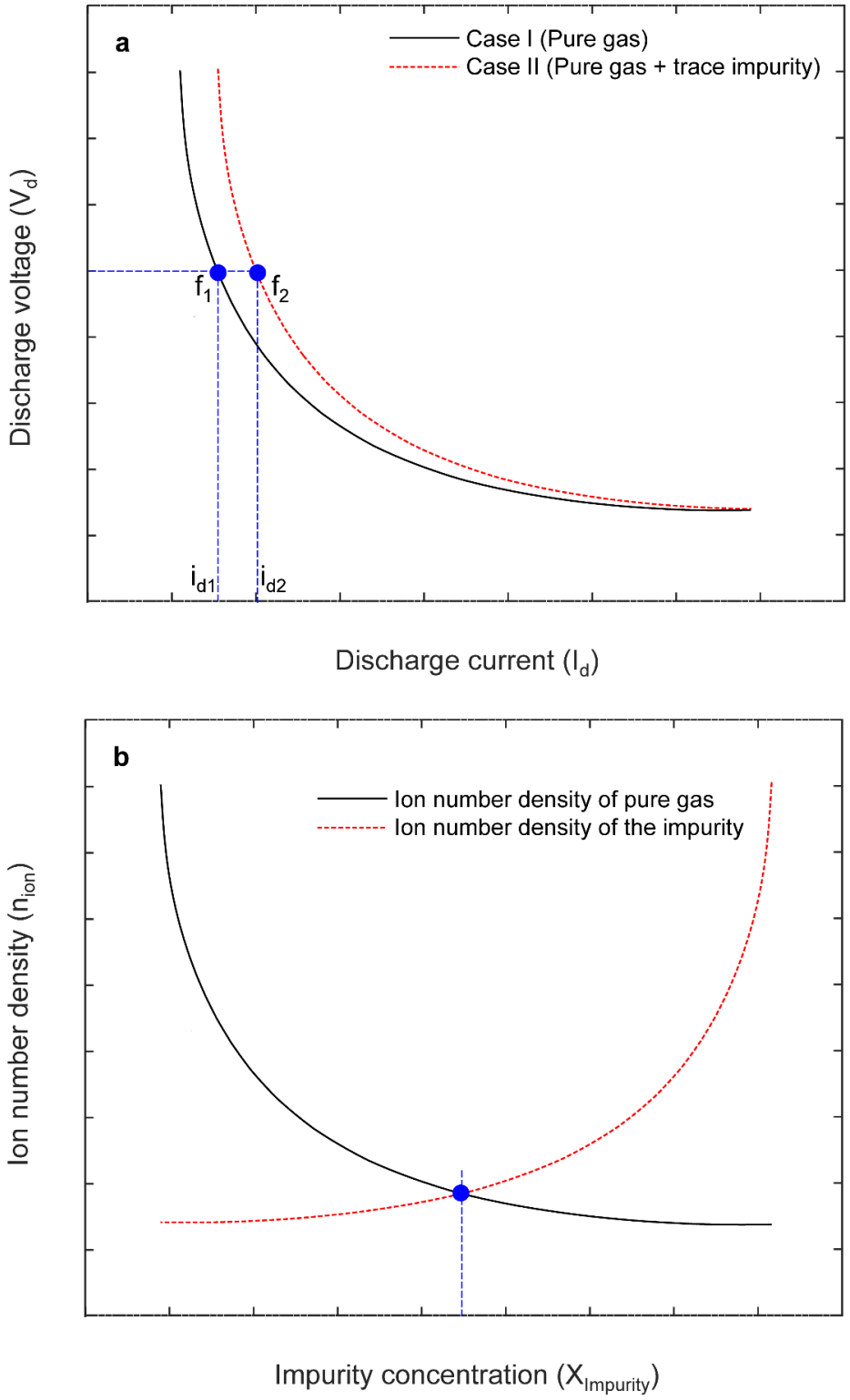

Figure 6.1. Schematic representation of a) voltage-current current characteristics of a DC driven microplasma discharge operating in the NDR regime in a pure feed gas and in presence of impurities, b) individual ion number density of the pure feed gas and the impurity as a function of the impurity concentration level.

6.2 THEORY AND MODELING

Similar to other prior experiments the methodology for ion number density quantification is based on introducing a trace impurity in the discharge; an impurity that has a lower ionization potential than the working feed gas. The ion quantification methodology is premised on the fact that the addition of trace impurity of lower ionization potential than bath/feed gas will result in an increment in the discharge while maintaining the same discharge voltage (Figure 6.1 (a)). Prior studies have reported that the ionization for the low ionization potential trace species is predominantly driven by the Penning ionization process which contributes to the incremental increase in the discharge current for a comparatively similar discharge voltage. Figure 6.1(a) represents a schematic representation of the voltage-current characteristics operating in the NDR regime for a pure feed gas (e.g. helium) and in the same feed gas with trace impurity present (e.g. nitrogen). The presence of the trace impurity results in a shift in the voltage-current characteristics for the same 'Pd' value. For the pure feed gas, the ion current density can be expressed as:

$$J_{i,p} = qN_{i,p}\, v_{d,p} = qN_{i,p}\, \mu_{i,p} \left(\frac{V_{d,p}}{d_{eff}} \right) \tag{6.1}$$

where $v_{d,p}$ is the drift velocity of the ions, $\mu_{i,p}$ is the ion mobility, E_p is the electric field, $V_{d,p}$ is the discharge voltage, and d is the effective spacing. The subscript p denotes pure feed gas. Since the NDR regime is being considered as the discharge operation region, the discharge voltage and current density represent RMS values.

In presence of trace amount of impurity in the feed gas, both species contributes to the ion current. The resulting ion current density can be expressed as the following:

$$J_{i,p+mp} = qN_{i,p}v_{i,p} + qN_{i,imp}v_{i,imp} = qN_{i,p}\mu_{i,p}E_{\mathrm{p}} + qN_{i,imp}\mu_{i,imp}\,E_{\mathrm{p}}$$
$$= qN_{i,imp}\mu_{i,imp}\left(\frac{V_{d,p}}{d_{eff}}\right) + qN_{i,imp}\mu_{i,imp}\left(\frac{V_{d,p}}{d_{eff}}\right) \qquad (6.2)$$

Where, the subscript imp denotes impurity. It should be noted that the trace impurity concentration is assumed to be such that the discharge voltage is not being affected due to its presence.

It is well known that the level of trace species in the feed gas has a strong influence on the overall discharge characteristics. At a higher concentration for an impurity having a lower ionization potential will dominate the ionization process and the discharge character will significantly differ from that of the pure feed gas case. As a result, there exists a critical value of the impurity level at which the ion number density of the impurity is at the same level as that of the feed gas itself (see Figure 6.1(b). A multi-dimensional simulation for a micro plasma discharge operating in helium with nitrogen as the trace impurity has been conducted using a kinetic model developed in our prior studies. It is found that for a nitrogen mole fraction (XN2) of 45 ppm the discharge starts to be dominated by N2+ ions and for XN2 = 250 ppm N4+ is the dominant ionic species. Similar results were obtained by Lazarou et al. in their simulations of He-N2 dielectric barrier discharge. Therefore, as the impurity level is increased beyond the critical concentration the ion current density expressed in the equation (6.2) can be rewritten as the following:

$$J_{i,\,p+mp} \approx qN_{i,imp}\ \mu_{i,imp}\left(\frac{V_{d,p}}{d_{eff}}\right) \tag{6.3}$$

The change in the current density due to the presence of trace impurity can be expressed as the following:

$$\begin{aligned} J_{i,\,p+mp} - J_{i,\,p} &= qN_{i,imp}\ \mu_{i,imp}\left(\frac{V_{d,p}}{d_{eff}}\right) - qN_{i,\,p}\ \mu_{i,\,p}\left(\frac{V_{d,p}}{d_{eff}}\right) \\ \Delta J_i &= qN_{i,\,p}\ \mu_{i,\,p}\left(\frac{V_{d,p}}{d_{eff}}\right)\left(\frac{N_{i,imp}\ \mu_{i,imp}}{N_{i,\,p}\ \mu_{i,\,p}} - 1\right) \end{aligned} \tag{6.4}$$

For a discharge operating in the NDR regime, the self-pulsing frequency is one of the readily available measurable parameter apart from the discharge voltage and current. The frequency in the self-pulsing regime of operation will be utilized in quantifying the ion number density of the discharge. Previous studies have shown that over a wide range of operating pressure and discharge current the NDR pulsing frequency of the discharge varies non-linearly. In this formulation, we approximate the pulsing frequency to vary quadratically with the discharge current. The pulsing frequency for the pure and the one with trace impurity can be expressed as the following:

$$f_p = CJ_{i,\,p}^{n},\ f_{p+mp} = CJ_{i,\,p+mp}^{n} \tag{6.5}$$

where C is a constant and n is the curve fitted value based on frequency current experimental relationship. Based on the experimental study this number was found to be varied between 1.5~2. In this study the value of n was considered to be 2 and will not change significantly for this range. It should be noted that the value of n will depends on gas composition, and hence, experimental frequency current data is required for a gas

composition which is different than the current study.. The ion number density ratios can, therefore, be expressed in terms of the pulsing frequency:

$$\frac{N_{i,p+imp}}{N_{i,p}} = \frac{J_{i,p+imp}\,\mu_{\mathrm{i,p}}}{J_{i,p}\,\mu_{\mathrm{i,imp}}} = \left(\frac{f_{p+mp}}{f_p}\right)^{1/n} \frac{\mu_{\mathrm{i,p}}}{\mu_{\mathrm{i,imp}}} \tag{6.6}$$

Combining equation (6.4) and (6.6), the ion number density in the pure feed gas can be expressed in terms of the change in the current density, the pulsing frequency for the pure feed gas and in presence of trace impurity, the discharge voltage, the inter-electrode separation distance and the ion mobility.

$$N_{i,p} = \frac{d_{eff}\, f \Delta J_i}{q\mu_{\mathrm{i,p}} V_d \left[\left(\frac{f_{p+mp}}{f_p}\right)^{1/n} - 1\right]} \tag{6.7}$$

Equation (6.7) can be normalized by the 'actual' ion number density $N_{i,actual} = J_i d / q\mu_{i,p} V_d$ and expressed as the following:

$$\frac{N_{i,p}}{N_{i,actual}} = \frac{d_{eff}\,\Delta J_i}{J_i \left[\left(\frac{f_{p+imp}}{f_p}\right)^{1/n} - 1\right]}$$
$$f_{p+imp} = f_p \left(\frac{\Delta J_i}{J_i} + 1\right)^n \quad \left[\text{for, } N_{i,p} \approx N_{i,actual}\right] \tag{6.8}$$

The frequency expression of equation (6.8) can be utilized in validating the methodology by comparing it with the measured frequency value in presence of trace impurity. Deviation between measured pulsing frequency and the one obtained from

expression in equation (6.8) would indicate that the impurity level is not at the critical limit for the ionic species to be in partial equilibrium with each other.

6.3 EXPERIMENTAL SETUP

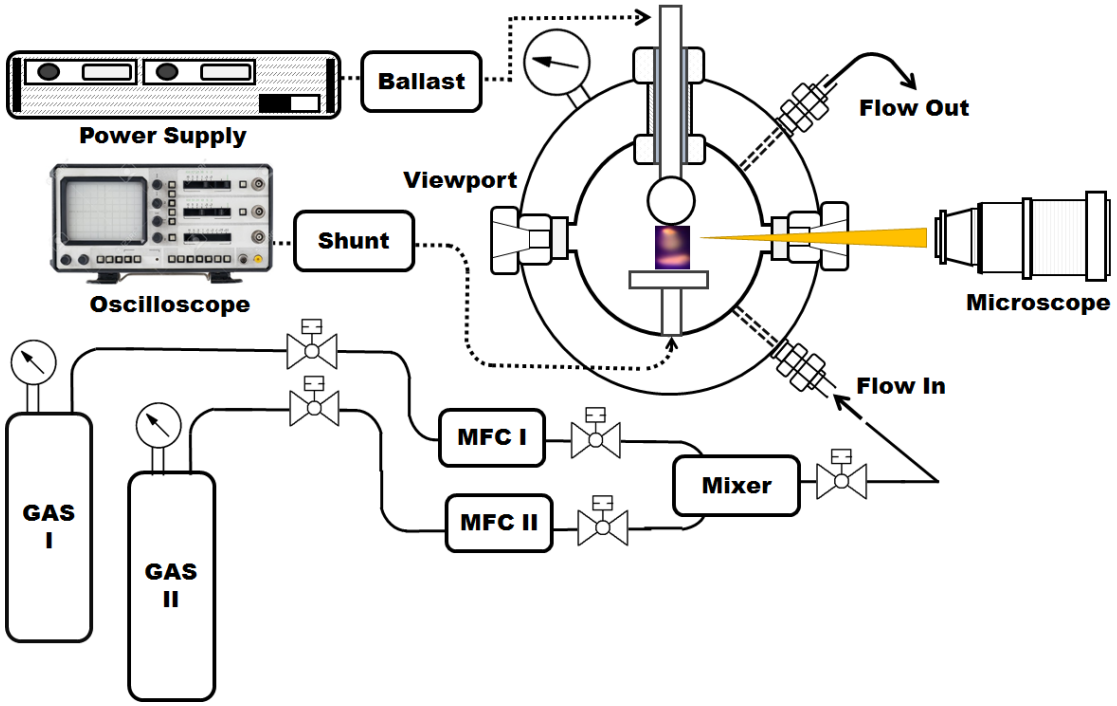

Figure 6.2 Schematic of the experimental setup of Ion detection with ballast resistance and shunt resistance

The proposed ion quantification methodology was employed in experiments for verification. Experiments were conducted with ultra-high purity helium feed gas (Praxair, 99.999% purity level) with a controlled amount of ultra-high purity nitrogen (Praxair, 99.999% purity level introduced as the impurity. A schematic of the experimental setup is presented in Figure 6.2. Two different mass flow controllers were utilized to monitor the helium and nitrogen flow rates. An MKS mass flow controller (Model 1179A) having a maximum flow rate of 7000 sccm and a Cole-Parmer mass flow controller (Model EW-

32935-40) that provided a maximum flow rate of 0.5 sccm was employed to control the flow rate of helium and nitrogen to generate a feed gas with a necessary trace impurity level. The lowest impurity concentration achievable was ~ 50 ppm. The two gas streams were passed through a zeolite desiccator unit to remove any possible water vapor from the gas streams and also to ensure mixing of the two gases. The experiments are conducted at 1100 Torr pressure and for an inter-electrode separation distance of 800 μm, which corresponds to a 'pd' value of 88 Torr-cm. The electrode arrangement consisted of a spherical anode and a flat cathode disk having diameters of 12.7 and 10 mm respectively. The spherical anode was used to maintain the discharge in the central region (i.e. the smallest gap) to ease the visualization process. It should be noted that despite the sphere-plate type electrode design the radial size of the discharge is sufficiently small such that the electrode configuration can be considered to be a parallel-plate arrangement. The electrodes are contained inside a stainless pressure chamber with quartz window viewports for discharge visualization. The chamber is sealable and there are gas inlets and outlets for testing in a variety of pressures and discharge gases. The experiments were conducted using a Spellman SL20P2000 DC power supply setup connected in series to a 100 kΩ ballast resistor. For time-dependent current measurements, a 10 kΩ shunt was placed between one electrode of the discharge and the ground. A North Star PVM-4 high impedance 1000:1 voltage probe was placed directly adjacent to the anode to measure the discharge voltage. Both the voltage probe and the current shunt are connected to an oscilloscope (Agilent Technologies InfiniiVision MSO7054B) for time-dependent measurements. The parasitic capacitance of the external circuit was measured to be ~ 250 pF. This included the capacitance added by the lead wires and the high impedance probe.

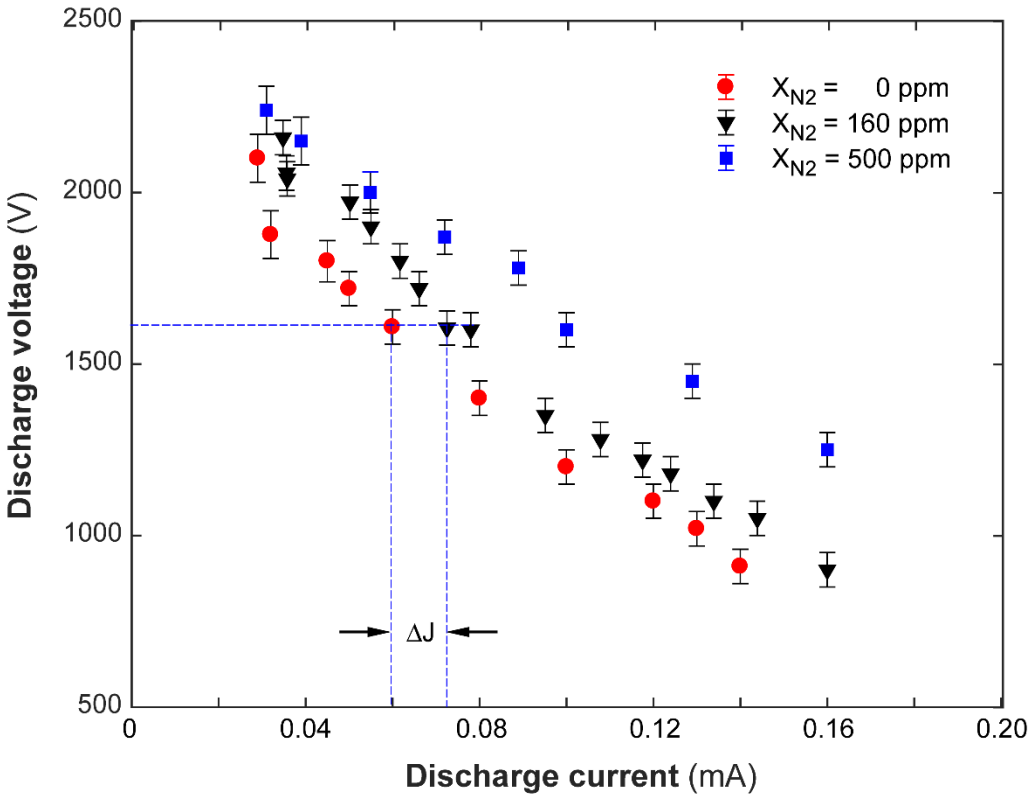

Figure 6.3. Voltage current characteristic of a DC driven microplasma discharge operating in helium with prescribed amount of nitrogen impurity. $d_{inter\text{-}electrode}$ = 800 µm, P = 1100 Torr. The vertical dotted lines denote the increase in the discharge current due to the presence of impurity in the feed gas.

6.4 RESULTS & DISCUSSION

Figure 6.3 presents the voltage current (VI) characteristic plot with and without the presence of nitrogen impurity in helium. Due to the oscillatory nature of the discharge in the NDR regime, the VI characteristics in the NDR region is obtained from the RMS voltage and current. The influence of impurity at two different concentrations - 160 and 500 ppm is also presented. We also conducted experiments with 50 ppm of nitrogen trace. However, the variation in the discharge current and voltage due to the presence of the trace species was not discernible. As such, the impurity level was selected to be above the critical limit (Figure 6.1(b)). It can be clearly seen that the VI curves representative of pure helium

and trace nitrogen cases manifest the usual profile that corresponds to the NDR regime – a decreasing voltage with increasing current. The VI characteristics was found to shift to higher currents with an increase in the impurity level. For an identical discharge voltage of ~ 1600 V, the discharge current increased by ~ 12.5 μA and 40.0 μA for a nitrogen level of 160 ppm and 500 ppm respectively. Furthermore, the slope of the VI curve with 160 ppm of nitrogen was almost identical to that of the pure helium case. However, as the nitrogen level is increased to 500 ppm the slope of the NDR regime decreases distinctly as result of nitrogen kinetics that contributes to increasing the discharge current for the same discharge voltage hence electric field level.

As a cross validation step, the measured self-pulsing frequency of the discharge was compared to those obtained from equation (6.8). Figure (6.4) compares the pulsing frequency for the two different impurity levels, 160 ppm and 500 ppm of nitrogen. The pulsing frequency for both the cases is found to increase with increasing discharge current. The frequency increased from ~ 5 kHz at ~ 0.03 mA to ~ 40 kHz at ~0.15 mA, increasing by a factor of ~ 8. The measured pulsing frequency of the discharge having 160 ppm of nitrogen impurity compares favorably with the values obtained from equation (8.8) by utilizing the measured increment in the discharge current resulting from the impurity, the discharge current, and pulsing frequency for the pure feed gas. Once the impurity level is increased the favor comparison of the pulsing frequency starts to fail. The deviation between the measurements and equation (6.8) starts to increase at higher currents where the increment in the discharge current is larger (Figure 6.3).

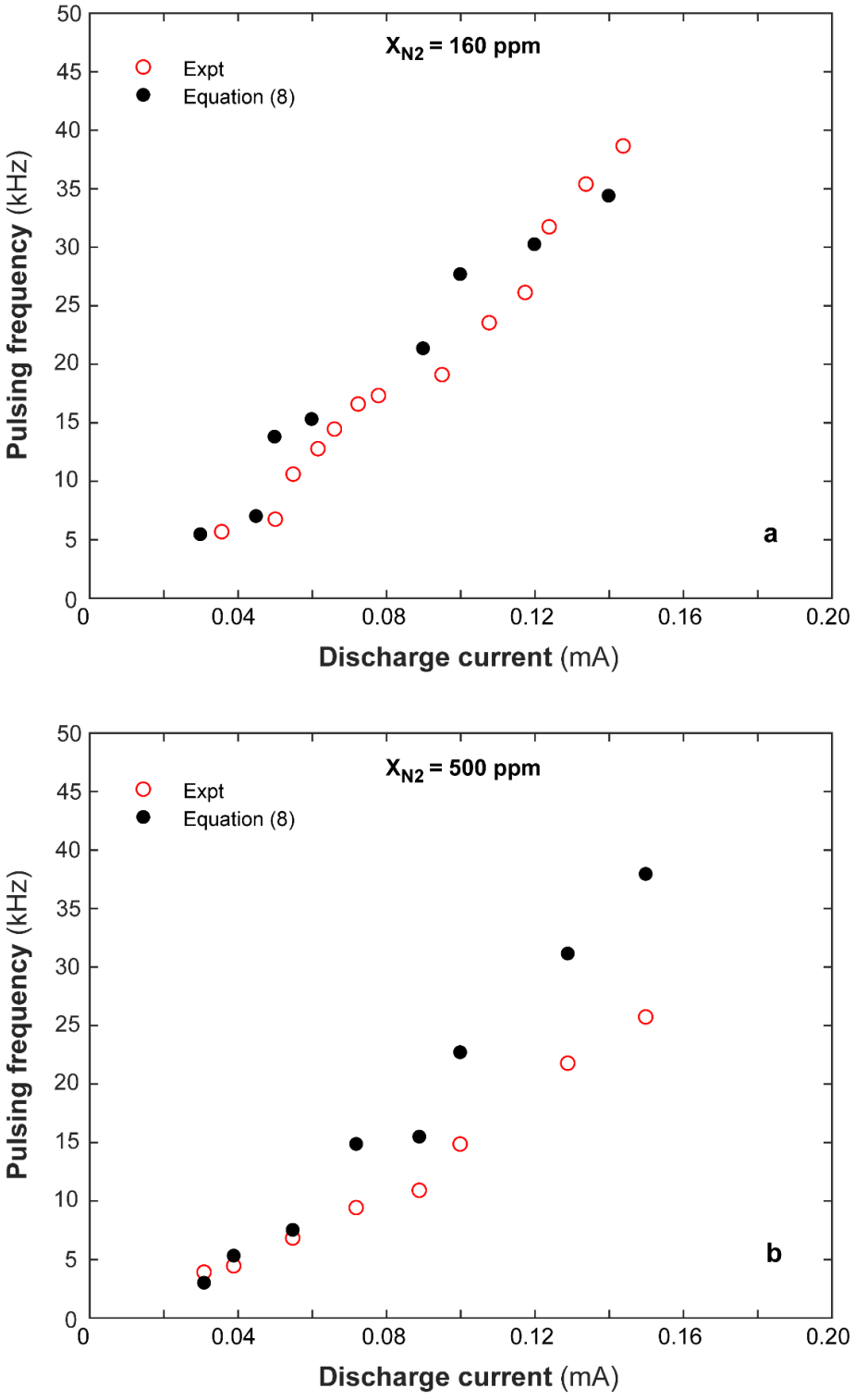

Figure 6.4. Comparison of measured and calculated frequency employing equation (8.8) for different discharge current for a) X_{N2} = 160 ppm and b) X_{N2} = 500 ppm. ($d_{inter\text{-}electrode}$ = 800 □m, P = 1100 Torr)

However, at the lower currents (0.03 mA – 0.06 mA) even for the 500 ppm nitrogen level case there exists good agreement between the pulsing frequencies. This further highlights the fact that maintaining the critical impurity level (Figure 6.1) is important for attaining the partial equilibrium of the different ionic species related to the feed gas and the trace gas. This discrepancy can be due to limitations in the kinetic mechanism.

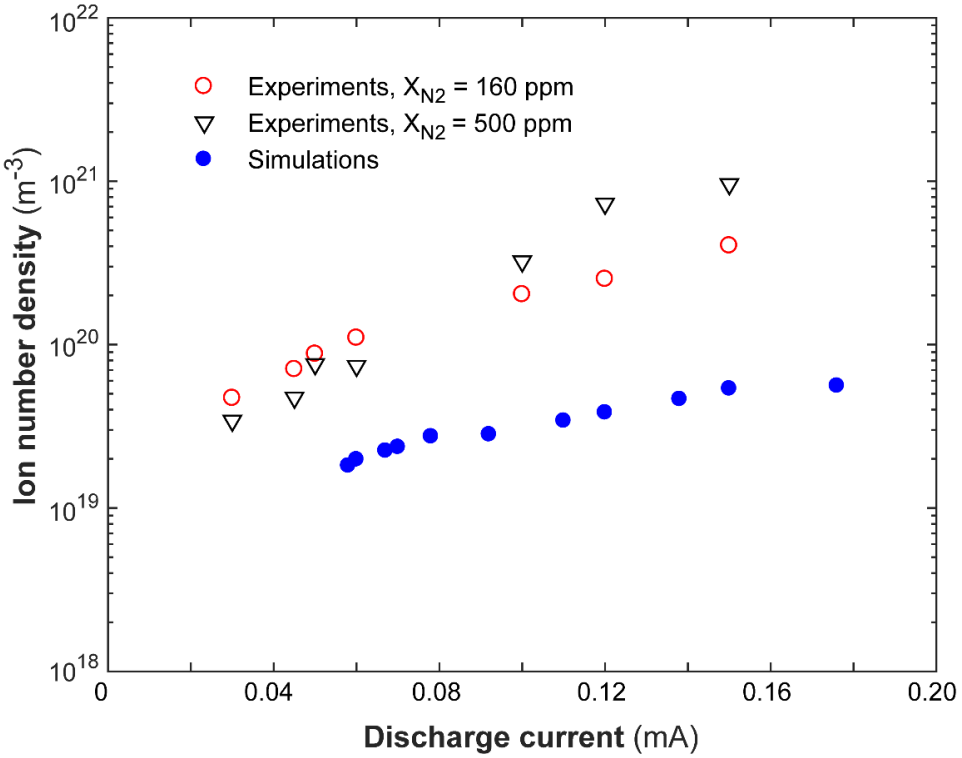

Figure 6.5. Comparison of simulated and measured ion number density employing equation (8.7) for two different impurity levels for a range of discharge current. The simulated ion number density is for a pure helium feed gas but identical pressure and electrode separation as that of the experiments.

In summary, an ion number density estimation methodology is proposed that utilizes the pulsing frequency and variation in discharge current due to trace impurities

for a discharge operating in the NDR regime. There exists a critical impurity level at which ion number density of the pure feed gas are in partial equilibrium with the trace species. It has been shown that at low impurity levels the estimated ion number density is in favorable agreement with multi-dimensional simulation predictions.

6.5 CONCLUSION

Negative differential resistance (NDR) regime of a plasma discharge possess unique self-pulsing characteristics where a DC driven discharge can be pulsed at a different frequency by varying the discharge current, feed gas, operating pressure as well as driving circuit parameters. In this work, the pulsing frequency of atmospheric pressure microplasma discharge is utilized for quantifying the ion number density over a range of discharge current. The ion number density is determined from measured discharge voltage, current, pulsing frequency and trace impurity that is injected into the system deliberately. Experiments are conducted in pure helium with nitrogen being introduced as the trace species. The ion number density is estimated over a range of discharge current and is compared with multi-dimensional simulation results. It should be noted that equation (1) is a widely accepted analytical expression of ion number density. As a result, we tested the ion number density from equation (1) with the current model (Eq. (8)). Whereas, the estimated ion number density from the model was in the ~10^{18} (1/m3) ranges, the ion number density based on equation (1) was found to be in the ~10^{12} (1/m3) ranges. The significantly lower estimation of ion number density based on eqn (1), i.e., Maxwell's equation, hinted that this equation poses a significant limitation on ion density calculation.

CHAPTER 7

STRIATIONS IN DIATOMIC DC GLOW DISCHARGES

7.1 BACKGROUND

Striations is an ionization wave characterized by a periodic glow and dark pattern in the positive column of glow discharge plasma. The phenomenon of striations has been explained in terms of electron kinetics, transport phenomenon and ionization processes. For the present study the role of vibrational kinetics on the simulation of striations in the positive column of diatomic gas N_2 is investigated. This study shows that instability causes oscillation and number of patterns which depend on the current and pressure condition. Detailed numerical simulation is carried out with a validation model to study the role of ion kinetics on the simulation of striations.

7.2 INTRODUCTION

The classical instability in positive column for molecular gases feature with a self –structured pattern in the positive column-referred as striations (Golubovskii, Nekuchaev, & Tsendin, 2000; Vladimir, 2006). Discharges in molecular gases are characterized by a high value of the electric field and an intense release of heat compared with atomic gases (Urbánková & Rohlena, 1980). The electron energy is fed predominantly into vibrationally

excited states of molecules. The internal energy is converted into gas heating via vibrational–translational relaxation. Intense gas heating and high values of the electric field determine specifics of wave processes in molecular plasmas (Mašek & Rohlena, 1991). In that case, the discharge shows an instability in the positive column which is a stratified state consisting of a periodic bright and dark space. The stratification of the positive column in glow discharge plasma is a very commonly observed phenomenon for diatomic gas molecules dated as early as 1830 by Michael Faraday. However, the research and articles related to this topic is not sufficient in the literature mostly due to its limited field of applications rather than the topic of pure scientific interests. The rapid progress in non-equilibrium and non-thermal plasma has made pure N_2 or N_2-O_2 mixture a standard fit due to the high atomic content and availability as a laser active medium and in a variety of new technologies (Chu & Lu, 2013; Hong, Uhm, & Yi, 2008). The application of those low temperature plasma includes material science, medical applications like sterilization of teeth and hands, voltage stabilizers (stabilitrons), rectifiers, gas discharge lasers and plasmas antennas (Bruggeman & Brandenburg, 2013; Mahamud & Farouk, 2016; Seiji et al., 2012). Positive column stratifications may defects the material under processing (Sobih, Crouse, & Li, 2008) or lowers the gas discharge laser efficiency (V. A. Lisovskiy, Koval, Artushenko, & Yegorenkov, 2012), therefore it is of considerable interest to the study the stratification of the positive column. However, the formation of the striation leads to few important questions. Such as, what is the actual mechanism behind the onset and self-sustainable condition of Striations, and what is the role of Ion kinetics, pressure and spacing on the striation process. These issues are primarily related with the discharge

mechanism and remain unexplored, and hence a strong interest to the study and simulation of striation process

The stratification of the positive column of a discharge in a gas is the most readily observed type of waves and instabilities in a plasma. This phenomenon of stratification of positive column can be observed both as standing (molecular gases) and moving (rare) called as ionization waves of positive column. Experimental study and description of standing striations started much earlier than that of moving ones, because it did not require special equipment for the observation. Production of stationary and moving striations is a good example of manifestation of a glow discharge. The self- sustaining moving ionization waves are presented by Wullner (Wullner;, 1843) in 1874 and Spottiswoode (Spottiswoode, 1876) in 1876. On the other hand standing type of striation were observed by Abria (Abria, 1843) in 1843. The experimental explanation of Ionization waves are performed by Pupps (Pupps, 1934). Who described that the oscillation wave does not happen due to the oscillation of the anode potential drop. Pekarek and Nedospasov in their review paper has described a detailed literature review and different theory of the ionization waves in noble end molecular gases (Nedospasov, 1968; Pekarek, 1968). It was clear that the behavior of ionization waves in molecular gases depends significantly on the specific processes, such as formation of negative ions, which change the electric field of the space charge, on the excitation of vibrational and rotational states of the molecules, which change strongly the form of the electron-energy distribution curve and their average kinetic energy.

Striae are observed over a broad range of current density, pressure and diameter of the tube. It is verified that the striations are the periodic changes in electron density and are caused not by redistribution of a fixed number of electrons, but by alternate regions of

predominant production and removal of electrons which can survive in a limited range of current values ($l0^{-4}$ A to 10 A), pressure ($l0^{-3}$ Torr to 10^{2} Torr), gas species (rare and molecular gases) and tube radius (V.A. Lisovskiy, Derevyanko, Kravchenko, Yegorenkov, & Lisovskiy, 2012; Pekarek, 1968). It has been established that the striations are due to ionization instability or manifestations of ionization oscillations and waves, which may be caused by step-wise ionization, the maximization of the electron distribution function, and by any agent causing enhancement in inhomogeneities in plasma (Abria, 1843; Pekarek, 1968; Pupps, 1934; Spottiswoode, 1876; Wullner;, 1843). Due to its complexity and lack of understanding of physics, the simulation of the stratification of positive column was not sufficient in the literature.

In this chapter a one-dimensional model will be studied to simulate striations in low pressure glow discharge. The simulation is performed with a N_2 chemistry as shown in Table 7.1 developed from the available data in the literature. In the model the electron energy distribution is treated kinetically to determine the electron energy distribution function (EEDF) and the electron induced reaction rates, electron species transport parameters; mobility and diffusivity as well as the electron energy mobility and diffusivity and the ions and neutrals are treated hydrodynamically. External driving circuit consisting of ballast resistance and parasitic is also taken into account. The chapter is organized as follows: section 2 of the paper provides a description of the discharge system modeled, a detailed description of the model is presented in section 3 and followed by results and discussions in section 4.

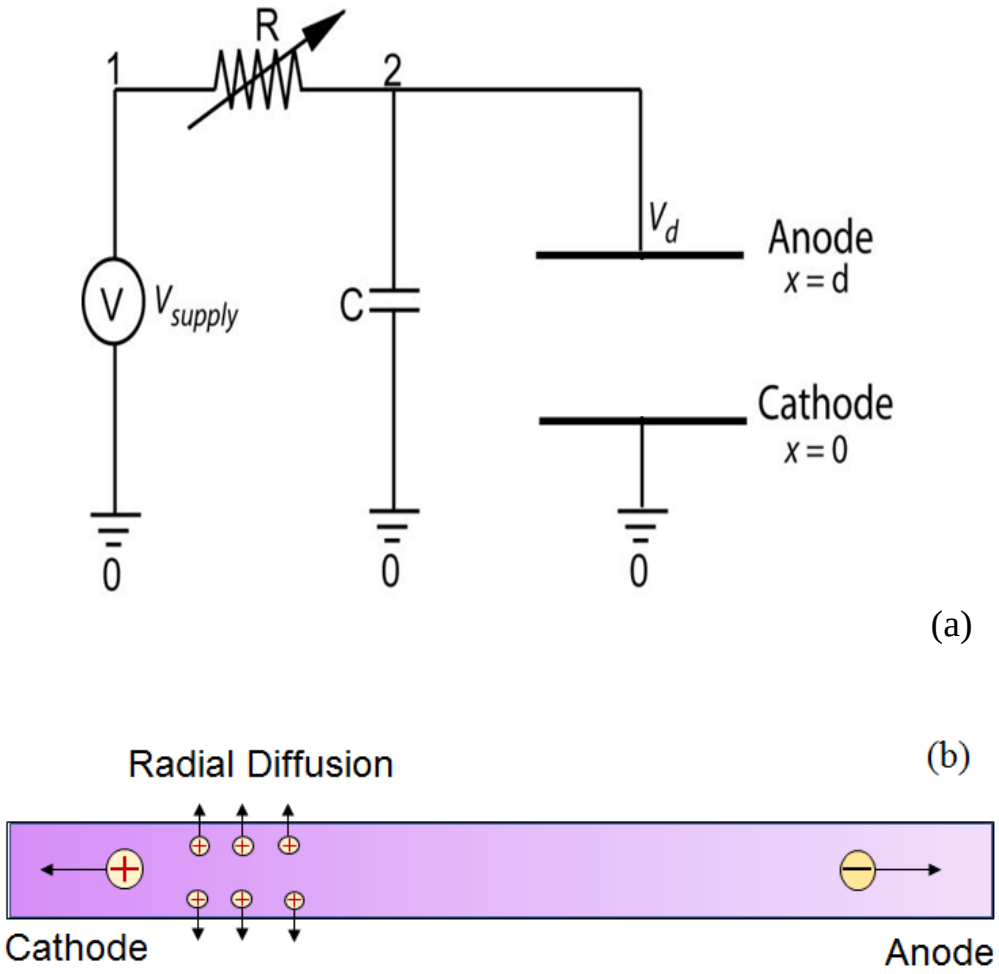

Figure 7.1 (a) Schematic of the problem geometry (b) Schematic of the geometry with 1D diffusion loss

7.3 SCHEMATIC OF THE PROBLEM GEOMETRY

The schematic of the discharge system with the external circuit is presented in Figure 7.1(a). The external power circuit consisted of a voltage source, a ballast resistance, R, a capacitor C. The capacitance C is present intrinsically due to the external cables and is known to be the parasitic capacitance. Due to the one dimensional model, it was necessary to specify the radial diffusion loss of the electrons and Ions coupled with the plasma model as shown in Figure 7.1(b). In these simulations the inter-electrode separation was fixed at d = 8.5 cm. The electrode surface area was prescribed to be 0.1 cm^2 resulting

in an electrode radius of ~ 1.8 cm. The discharge domain and electrode area were so chosen to be consistent with that of Lisovskiy et al. (V. A. Lisovskiy et al., 2012) and compared with their experimentally measured data.

7.4 MATHEMATICAL MODEL

A continuum based model is applied though the system is operating at low pressure and still satisfies the condition that the mean free path is lesser than the system dimension. The discharge physics model equations consider the temporal and spatial effects of the discharge in the direction perpendicular to the electrode plane. The 1D model also consider the radial diffusion losses. The self-consistent discharge model consists of coupled conservation equations for different species in the plasma (electrons, ions, vibrational species, metastable and neutrals). The conservation equations for the electrons and the ions are described by the species continuity equations with a drift-diffusion approximation for the fluxes. The model also accounts for the conservation of energy for the electrons, conservation of energy for the gas mixture and state relations. The electrostatic potential in the plasma model is obtained by solving the Poisson's equation and an external circuit model is coupled with the plasma model.

7.6 BOUNDARY CONDITIONS

Flux boundary conditions are provided for the electrons at the electrodes. The electron flux to the electrode is given by the sum of thermal flux and flux of secondary electron due to ion bombardment. The expression is as follows:

$$\vec{\Gamma}_e = \frac{1}{2} n_e u_{th} + + n_e(\mu_i \vec{E}) - \left(\sum_i \gamma_i (\vec{\Gamma}_i) + x D_e \nabla n_i \right) \quad [x = 1 \text{ at cathode, and } x = 0 \text{ at anode}] \qquad (6.1)$$

where, n_e is the electron number density, γ is the secondary electron emission coefficient, and u_{th} is the electron thermal velocity. The boundary conditions for the ions considering both the drift and thermal flux

$$\vec{\Gamma}_i = \frac{1}{2} v_{th,i} n_i + n_i(\mu_i \vec{E}) - x\, D_e \nabla n_i - x \sum_i \gamma_i \vec{\Gamma}_i \quad [x = 1 \text{ at cathode, and } x = 0 \text{ at anode}] \qquad (6.2)$$

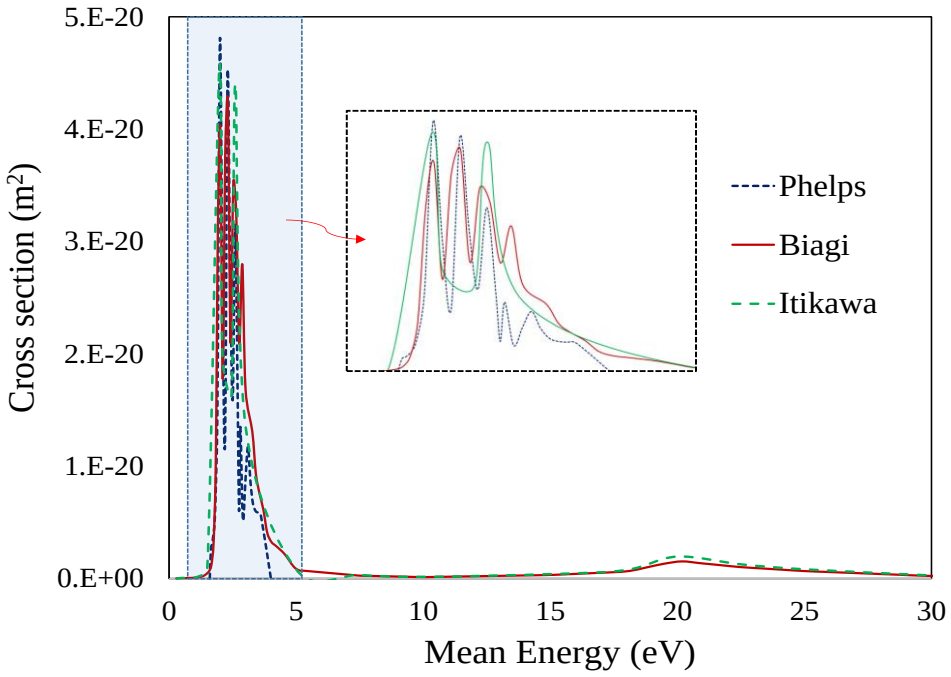

Figure 7.2 (a) A comparison of Cross sectional data (Biagi/Phelps/Itikawa) for the first level of excitation (R2:0.29 eV)

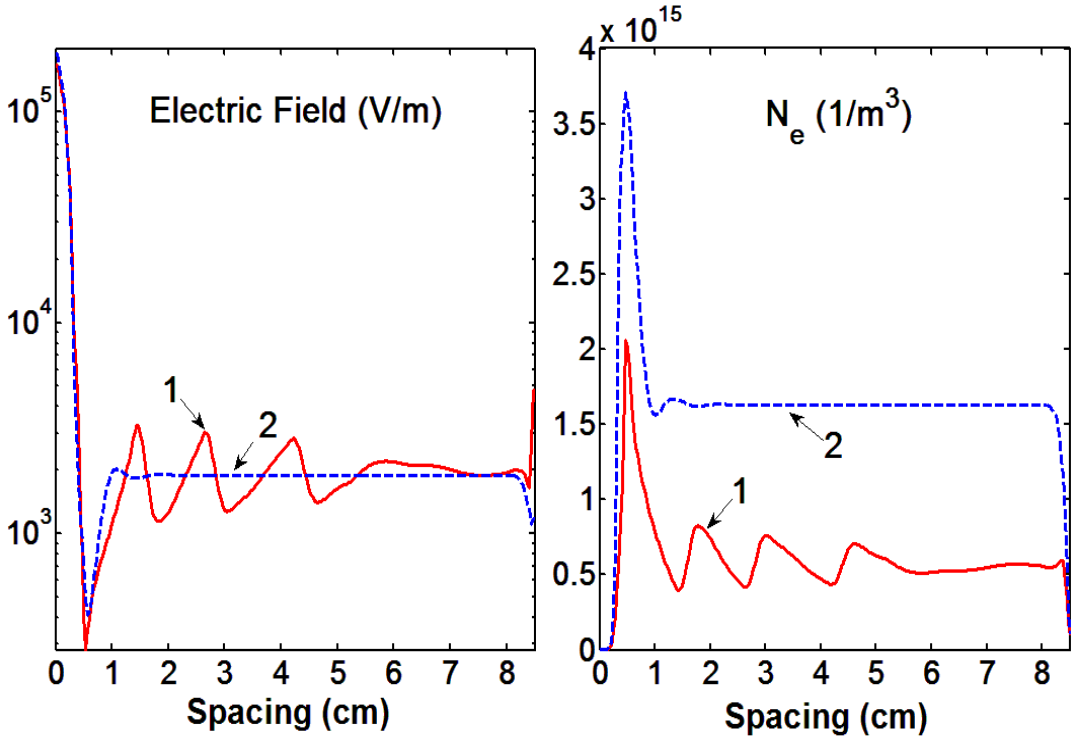

Figure 7.2 (b) The effect of vibrational kinetics on steady state (a) Electric field (b) electron number density. 1: With detailed vibrational reactions (0.29 eV~ 13 eV) 2: Without the initial vibrational reactions (2.98 eV ~ 13 eV).The current density 0.6 mA/cm^2.

The secondary electron emission coefficient was varied in the simulations. Best agreement with experimentally measured voltage-current characteristics was obtained for a $\gamma_i = 0.11$. Simulation results presented here are for $\gamma_i = 0.11$ unless mentioned otherwise.

The boundary condition for the electron energy is expressed as:

$$\vec{\Gamma}_\varepsilon = \frac{5}{6} n_\varepsilon u_{th} - \left(\sum_i \gamma_i \varepsilon_i (\vec{\Gamma}_i) + \varepsilon (D_e \nabla n_i) \right) \tag{6.3}$$

Where, n_e is the electron energy density, ε_i is the mean energy of ion, and D_e is the electron diffusion coefficient. The radial loss rate can be approximated by(Chaplin & Bellan, 2015)

$$\upsilon_{loss} = \frac{D_{eff}}{A^2} \tag{6.4}$$

Where A is the effective diffusion length and the Deff is the diffusion coefficient. For the boundary conditions of different ions and excited states a surface chemistry model is also implemented (Table 1) having a sticking coefficient of 1.0. The electrode surfaces are set to be isothermal walls with room temperature 300 K for solving the gas mixture temperature.

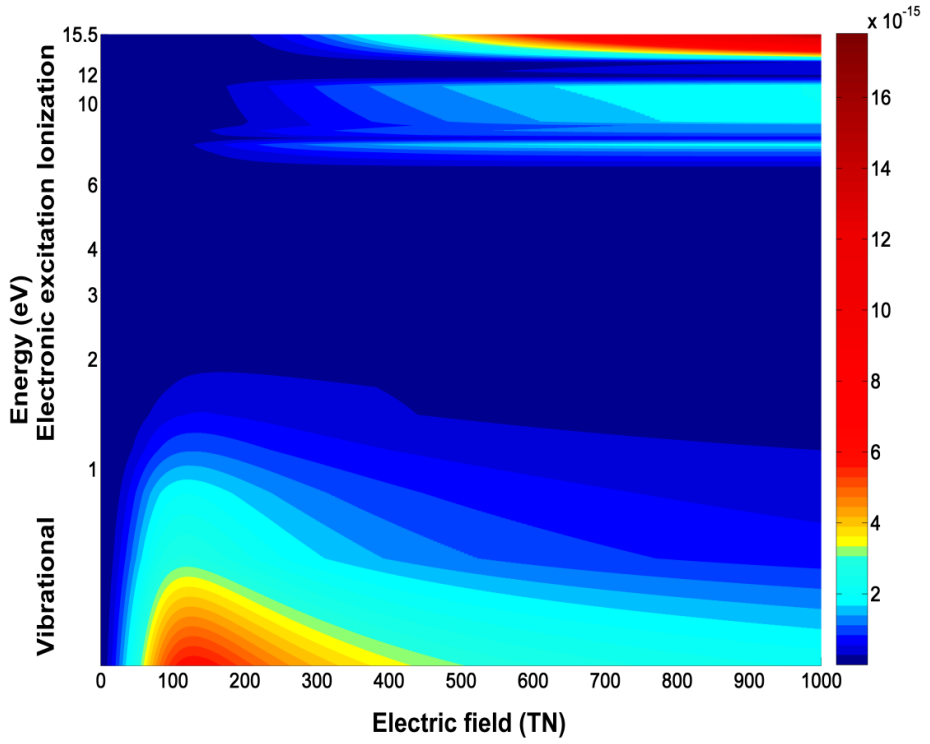

(a)

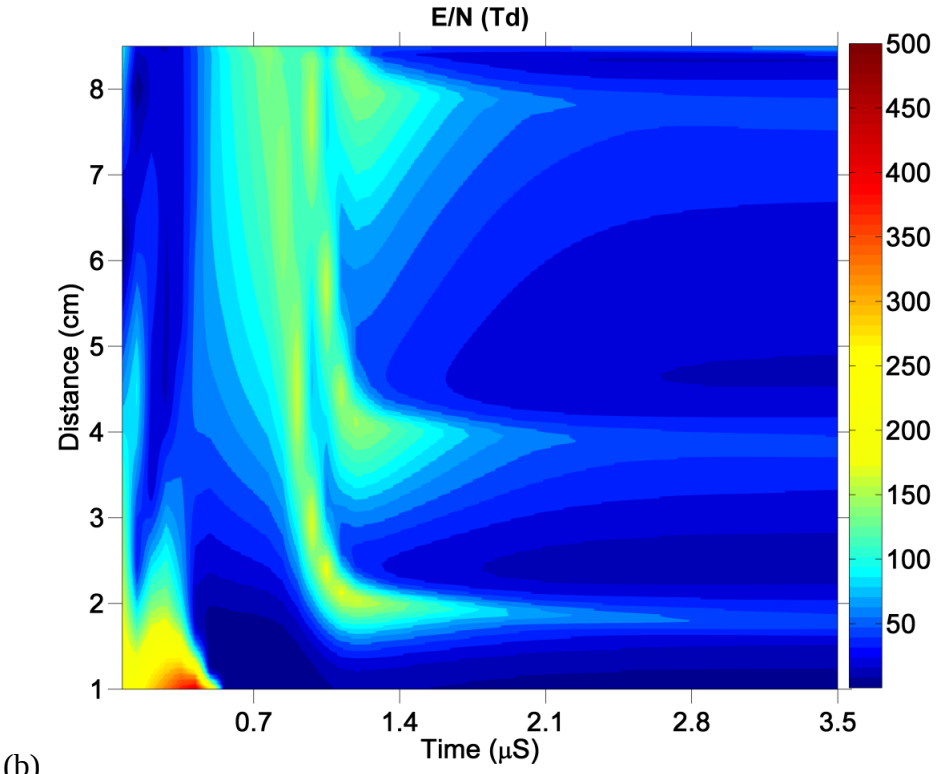

(b)

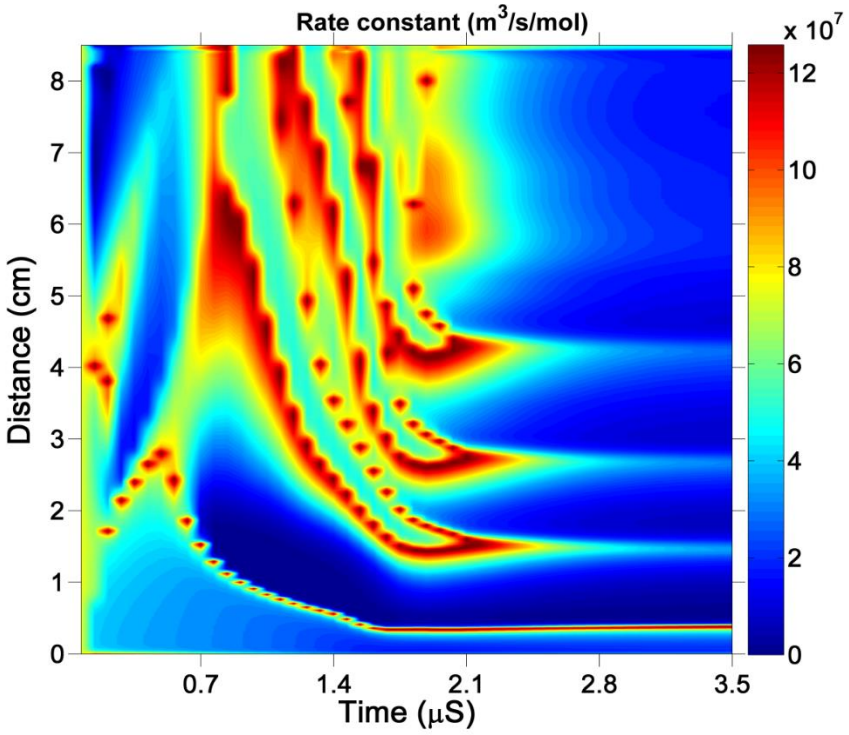

(c)

Figure 7.3: (a) Reaction rate constant from BOLSIG+ as a function of reduced electric field and energy (eV) (b) Transient variation of electric field from 1D simulation (c) Spatio-temporal profile of vibrational rate constant from 1D simulation

7.6 REACTION KINETICS

The mechanism contains N_2 kinetics with vibrational stage reactions, metastable reactions and heavy particle reactions. 25 species were considered in the simulations; electrons (e), monomer and dimer ions (N^+, N_2^+, N_4^+) electronically excited species, $N_2(v=1,2,....15)$, metastable $N_2(B^3\Pi)$, $N_2(a^{'1}\Sigma)$, $N_2(c^1 1)$ and neutrals (N_2, N). The chemical kinetics included in this study is summarized in Table 2. The reaction mechanism consists of elastic scattering, ionization, vibrational excitation and de-excitation, three body recombination, dissociative recombination, charge transfer, molecular ion conversion reactions etc. The electron transport coefficients (mobility μ_e , diffusivity D_e) and electron induced reaction rates (η) are calculated using the electron energy distribution function (EEDF) obtained as a solution of the Boltzmann equation employing the two term spherical harmonic expansion (SHE). BOLSIG+ (G. Hagelaar & L. Pitchford, 2005) is employed to calculate the EEDF for different values of reduced electric field (E/N) and generate lookup tables for the electron transport and electron energy transport coefficients. The lookup tables are generated as a function of the mean electron energy to take into account the non-local effects.

A detailed chemical kinetics model for Nitrogen is developed to conduct the kinetics coupled transport simulations. The source of the electron impact cross sectional data is obtained from Reference (Freund, Wetzel, & Shul, 1990; Kushner; "LXCAT Plasma Data Exchange Project,"). Striations are basically governed by the vibrational and metastable reactions, wherein the superelastic collision, heavy particle reactions and penning ionization collectively dictates the phenomenon in a more complex manner. A number of sources are available, such as Phelps, Biagi, Itikawa, Morgan and SIGLO data

base, with their own sets of reaction with a variation in number of reactions stages and in terms of order of precision ("LXCAT Plasma Data Exchange Project,"). In this study we examined the reliability of different database, with interest to the simulation of striations in the positive column. It was obtained that the Biagi or Itikawa dataset has the necessary level of consistency and completeness at lower to higher energy level. A comparative study of three different cross sectional dataset for the first excitation level, such as Biagi, Phelps and Itikawa, are shown in Figure 7.2 (a) and implicates important differences. Phelps dataset, whose reaction sets and values are based on the data of 70-80s, giving almost the similar values of the cross sectional data, however is inconsistent with no data at lower (< 1.6 eV) or higher energy level (> 4 eV). Due to the unavailability of data at lower and higher mean energy, the reaction rate based on the Phelps dataset will underpredict computational results. The cross-sectional dataset of Biagi, whose reactions mechanism and values are recent and are based on quasi theoretical cross section data, has two effective excitation level, one at lower energy level similar to Phelps, another at higher energy level of 20eV. This peak at 20eV happens to take place up to the 15th vibrational level (N2v=15) and fades with the increment of vibrational level. Moreover, BIAGI dataset are more precise and has a significant number of energy interval in comparison with any other dataset form the literature. The Itikawa dataset is hybrid in nature between Phelps and Biagi; which shown more Phelps like behavior at lower energy level and Biagi like behavior at high energy level. The Itikawa dataset is also coarser and has a less reaction mechanism. The similar trends are also obtained in other excitation levels. The reaction mechanism in the current study is presented for the combination database from of Biagi

(excitation, metastable), Kushner and Wetzel (Excitation to metastable and ionization) and is presented in Table 1.

In order to gain insight into the role of vibrational kinetics on the formation of striations, we tracked all the reactions and its consequence on the final simulation results. The vibrational kinetics of the lower energy level ($\varepsilon < 2.72$) was found to dominate the instability phenomenon in the positive column. Figure 7.2 (b) summarizes the importance of detailed kinetics to capture the modulation of electric field, triggering the fluctuation of electron number density in the positive column. Without the complete reaction, especially at the earliest vibrational level, a uniform glow discharge can only be observed with a higher electron number density.

7.7 NUMERICAL SCHEME

The system of equation is discretized on the basis of finite element method and is solved using a time-dependent solver in COMSOL ("COMSOL Multiphysics," 2013). A non-uniform mesh was employed with denser grids present closer to the electrodes. A total of '500' grids are used with a maximum and minimum grid size of '0.45' cm and the total number of degrees of freedom was '13529'. The time integration was performed using a fully implicit backward difference formula (BDF) and a constant time stepping. The numerical solution was obtained utilizing the Parallel-Sparse Direct Solver (PARADISO) (Schenk & Gartner, 2004).

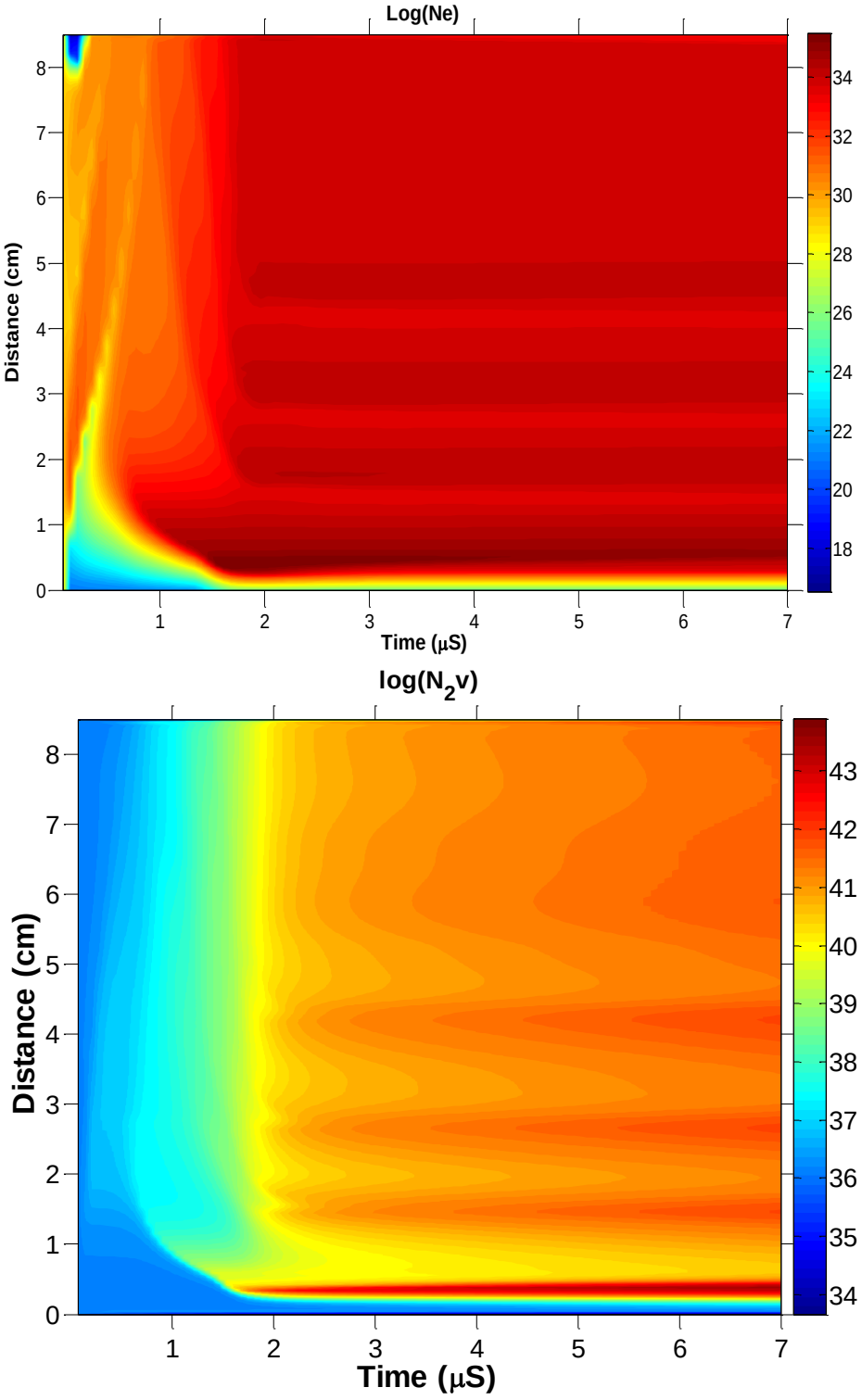

Figure 7.4: Spatio-temporal profile of electron and vibrational number density

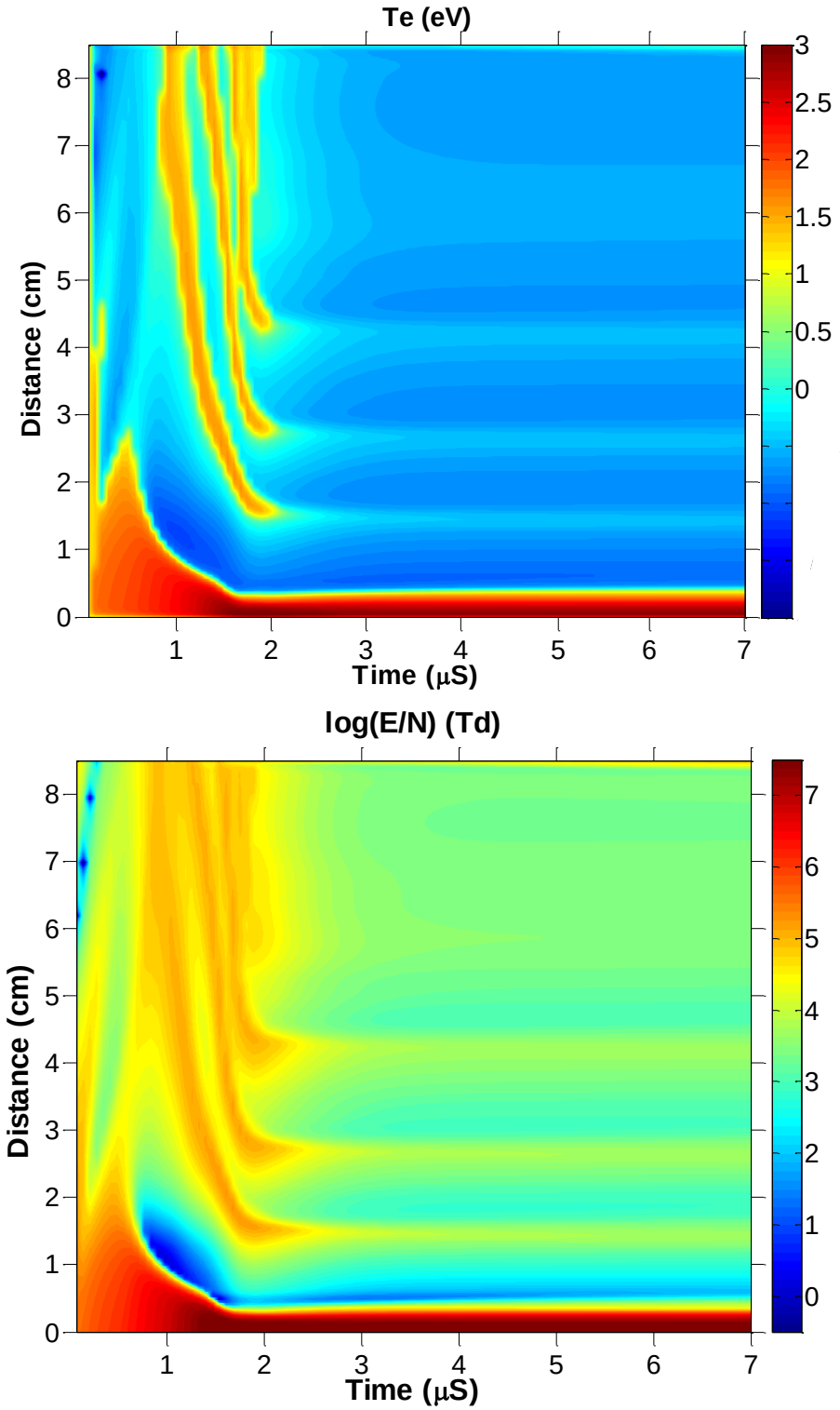

Figure 7.5: Reaction rate constant for the first few microseconds

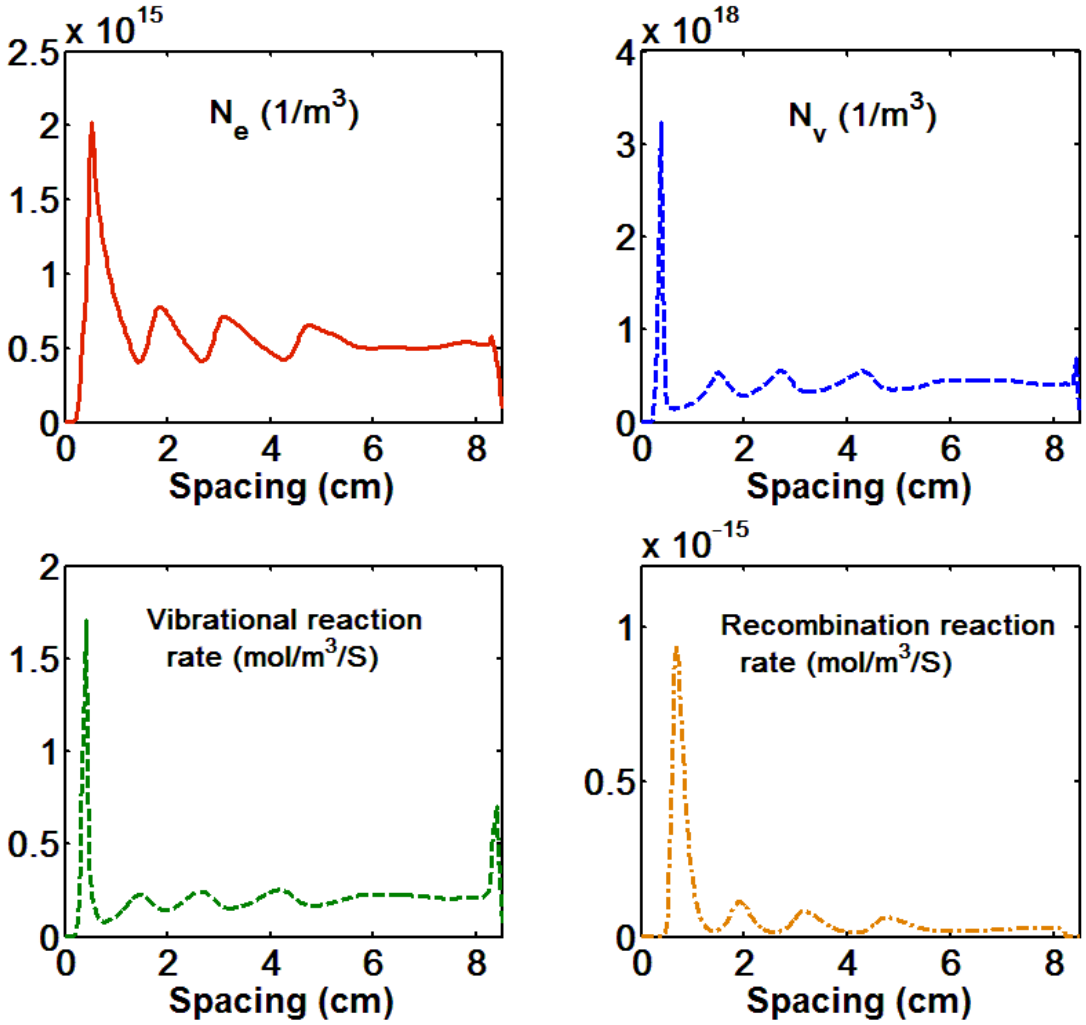

Figure 7.6 : Steady state profile of standing striations. Showing that the electron and vibrational number density are in opposite phase. The corresponding vibrational reaction rate and recombination rate are also presented which are dominat role in the positive column.

7.8 RESULTS AND DISCUSSION

The transient spatio temporal phenomenon happened during breakdown for electric field and reaction rate is explained in Figure 7.3 to 7.5 to explore the formation mechanism of positive column instability. The transient profile of electron density and vibrational number density replicates the effect of electric field and electron temperature on the spatio-temporal domain and their correlation with electron induced reaction rate constant. The

breakdown is observed to takes place at 0.5 μS for the baseline condition studied here when the electric field is sufficient enough and will cause an abrupt increase of electron temperature as well as the electron number density. However, the vibrational population density follows a different trend and generally requires much less electric field. The vibrational reaction rate does not increases exponentially with the electric field and rather it has a Gaussian distribution with a peak at ~150 Td as shown in Figure 7.3(a) based on the calculation of a Boltzmann equation solver (G. J. M. Hagelaar & L. C. Pitchford, 2005). The baseline simulation has three waves of striation starting at ~150 Td and consequently shows a very high vibrational reaction rates as observed in Figure 7.3(b) and 7.3(c). As the vibrational reaction requires much less electric field the surge in vibrational rate is observed at 0.3μs which is before the breakdown point. The breakdown causes a spatial redistribution of electric field with a higher electric field at the cathode side to a lower electric field at the anode side. At this lower electric filed vibrational reaction started to increase close to anode and reaches its peak at ~150 Td (0.7μs) when an abrupt increase of vibrational reaction is observed as shown in Figure 7.3(b) and 7.3(c). Due to the Gaussian distribution of rate constant and electric field, the reaction rate will falls with a further increment of electric field. The vibrational reaction as increases moves from anode to cathode followed by the electric field which takes about 1.5 μs. These short lived increases in vibrational reaction rate cause an increment of electron temperature. The electron temperature is constant in this region with a magnitude of 1.5 eV as the wave travels from anode to cathode. For the baseline condition studied here, three transient vibrational waves are observed to start from 1 μs, 1.5 μs, and 2 μs traveling from anode to the cathode side of the discharge.

Our reaction rate analyses from the numerical modeling found the following trend: $K_{vibrational} > K_{metastable} > K_{ionization}$. Hence, the energy is fed predominantly into vibrationally excited states of molecules for the diatomic gas discharges. During the steady state condition, three striations pattern are observed initiated from the anode side of the discharge during the breakdown.

The behavior of the strata pattern also significantly depends on the specific processes, such as formation of electrons, which change the electric field of the space charge which inversely varies with the electron temperature. The electron number density is found to vary between ~ $7x10^{14}$ m^{-3} and ~$4x10^{14}$ m^{-3} in one strata cycle. It can be also observed that the electric field in the positive column reaches its peak (~ 1×10^{3} V/m) where the formation of space charge is maximum, therefore, at the tail of each strata.

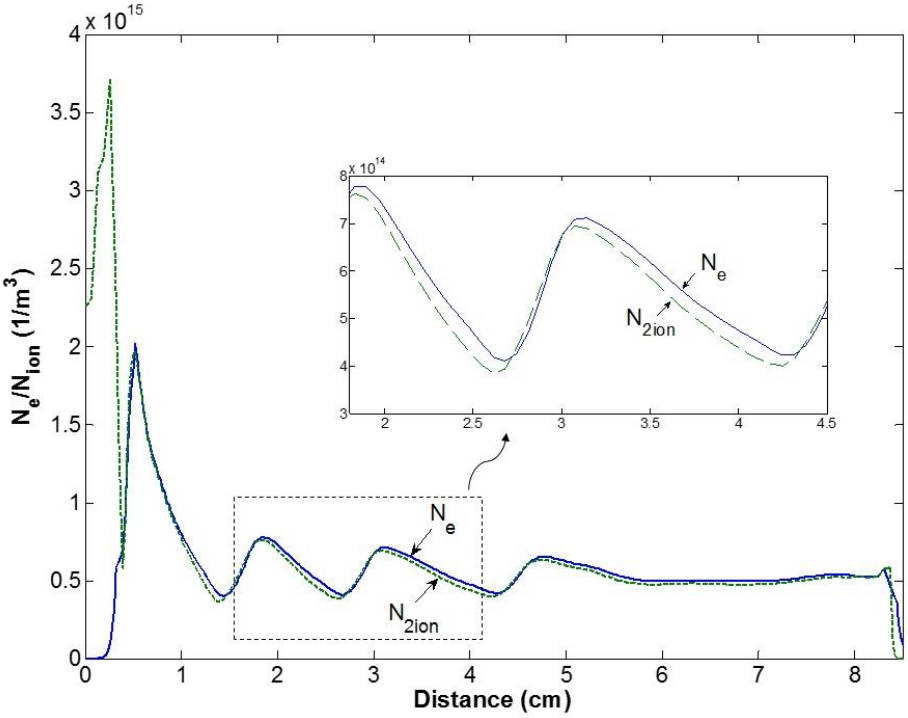

Figure 7.7: Spatial profile of electron/ion number density for the baseline condition (0.6 mA/cm^2).

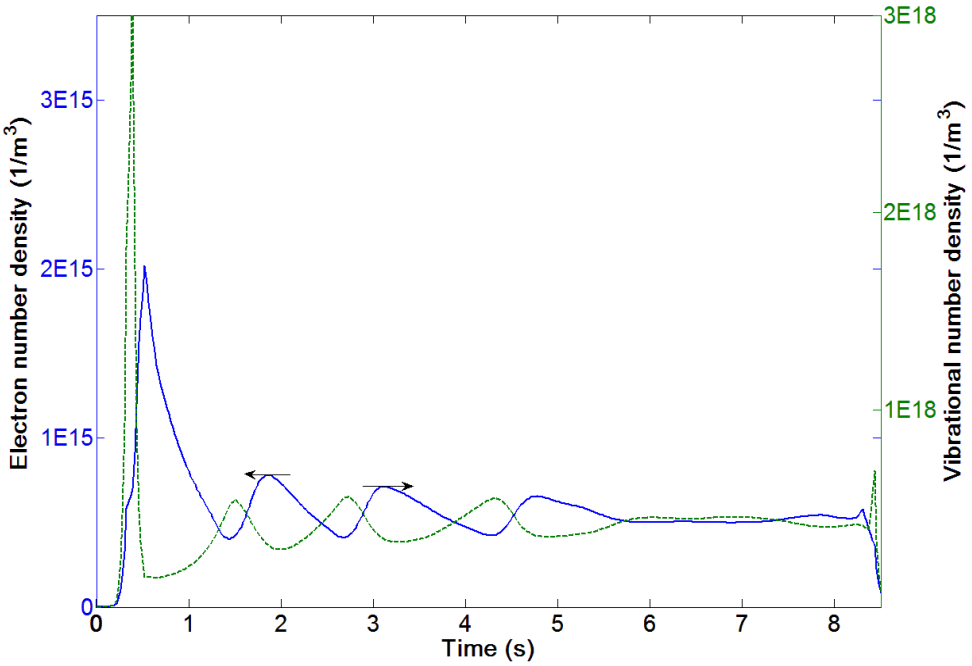

Figure 7.8: Spatial profile of electron and vibrational number density for the baseline condition (0.6 mA/cm^2).

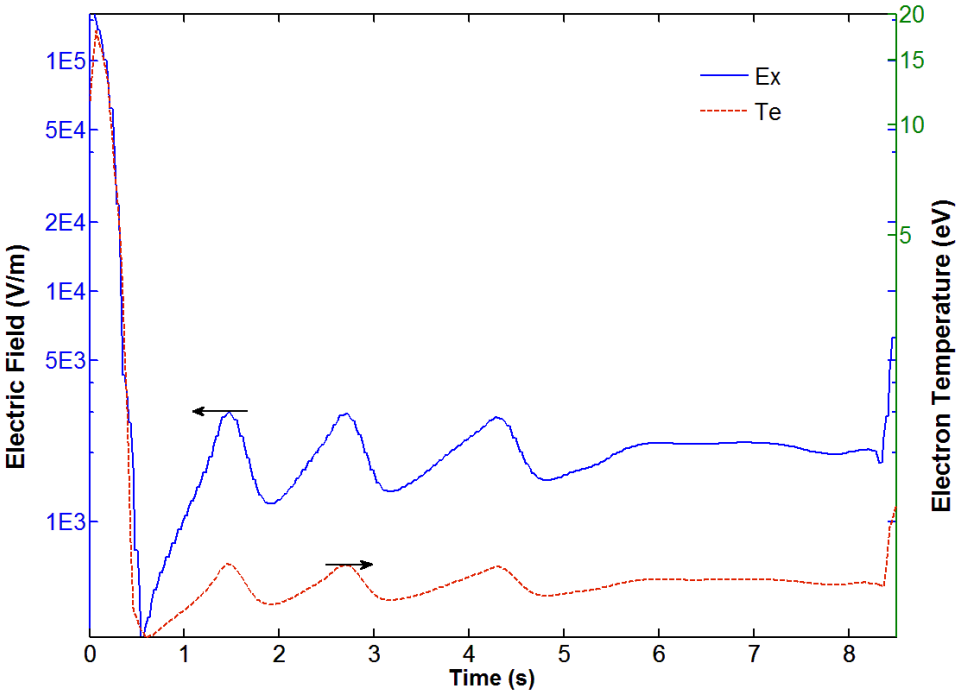

Figure 7.9: Spatial profile of electric field and electron temperature for the baseline condition (0.6 mA/cm^2).

The spatial distribution of electron and vibrational number density a steady state strata cycle is shown in Figure 7.6. The two most important reaction rates which varies significant in the modulated region, the vibrational reaction and recombination reactions, are also demonstrated. It was found that when the electron/Ion number density is maximum the vibrational number density is minimum and vice versa. The electrons attenuated from the peak of the strata due to inelastic collision and ionization is quite rare. The ions and electrons diminishes in this region due to the radial losses and volumetric recombination.

At the peak of the each strata, an intense ionization takes place by electrons accelerated towards the cathode side of the strata. Away from the peak all the values steadily diminishes to lower values which is observed in Figure 7.7 and 7.8. The positive ions and electron presents here due to the diffusion current from the peak of the strata. The ions and electrons diminish in this region due to the radial losses and volumetric recombination. The electrons lose their velocity due to inelastic collision and ionization rate starts to drop. At the tail of the strata formation, the discharge current is transferred by electron diffused through their high concentration electric field (Figure 7.9). This dark space of the striation or the tail of the strata is understood to have a depleted energy for any ionization. The diffusion rate is also high here (~ 27 m^2/s) as seen in Figure 7.10. So electron has to travel some distance to gain sufficient energy which will define the length of the strata. Therefore, the lower kinetic energy of electrons results in a reduced ions production in the tail of each strata. However, this will allow the increment of vibrational reactions which occurs at lower energy level. The vibrational number density peaks from the numerical results was obtained in the tail of the strata as shown in Figure 7.8. It was found that when the electron or Ion number density is maximum the vibrational number

density is minimum and the vibrational species concentration is maximum when the electron or Ion number density is minimum.

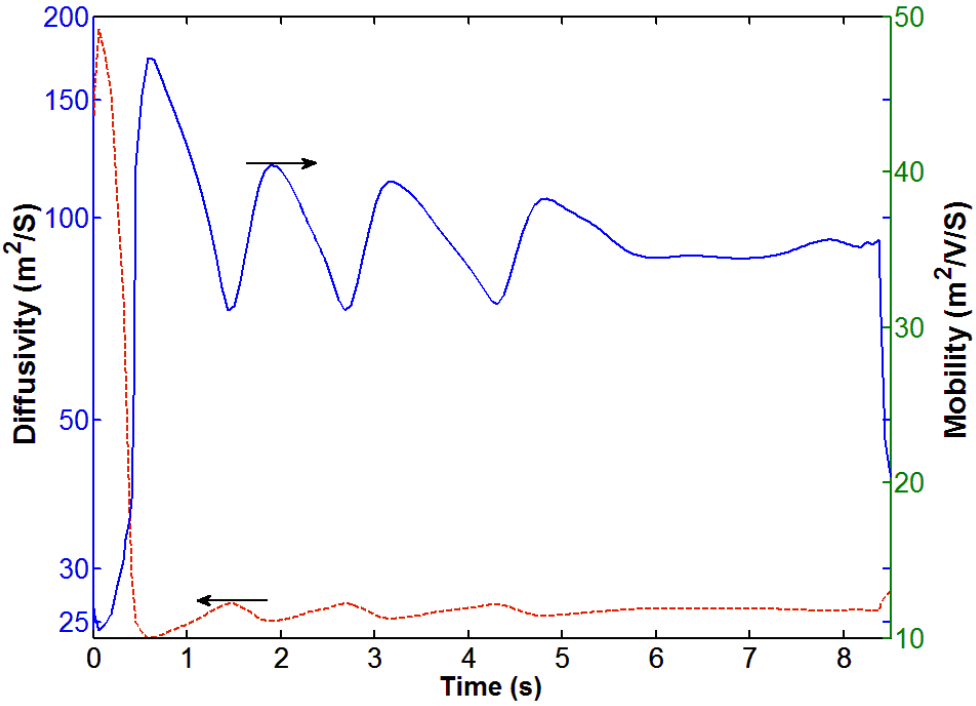

Figure 7.10: Steady state spatial distribution of Electron mobility and diffusivity for the baseline condition.

As observed earlier low energy electron triggers vibrational excited reaction which increases the vibrational reaction rate. It was also found that the vibrational peaks takes place (0.5 cm) before the ion peaks (0.8 cm) in the cathode sheath due to the low energy requirements of the vibrational species. As a result the location of the vibrational peak length falls inside the cathode sheath in Figure 7.8. In Figure 7.7 it is also note mentioning that the vibrational species reaches its maximum (5×1018 1/m3) in this dark discharge region. A number of study suggested Striations are attributed to the deviation of the quasineutrality of the plasma(Pekarek, 1968).

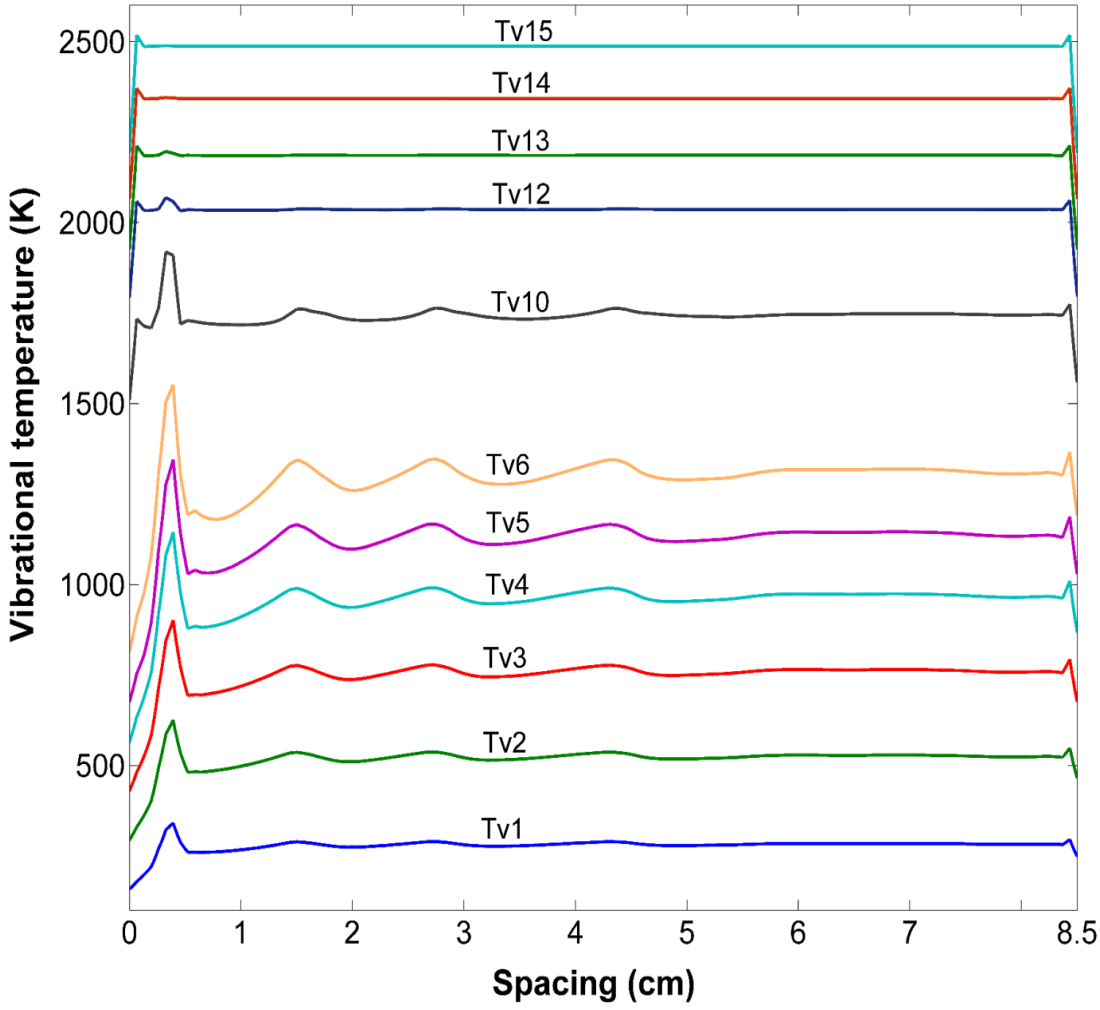

Figure 7.11: Vibrational temperature at different vibrational level for the baseline condition.

A deviation in electron and Ion distribution is also observed at steady state conditions which are not in a quasi-neutral state. The maximum deviation leads to the maximum electric field (4×10^3 V/m) at the darker region of the strata and minimum deviation leads to the minimum electric field condition (0.5×10^3 V/m). The electron temperature is directly related to the electric field strength and fluctuates between 0.6 eV (The bright one) to 0.3 eV (the darker one) in the striation region with a sharp increase in

the cathode sheath region. These values are within the range of experimental measurements (V. A. Lisovskiy et al., 2012).

As observed in Figure 7.3, 7.4 and 7.6, the stratification of the discharge also results in a spatial redistribution of electrons, ions and vibrational species. The vibrational species (~ 10^{18}) having a lower excitation energy (> 0.29 eV) significantly exceeds the electron or Ion number density (~ 10^{15}) and sharply increases in the dark discharge region, such as Faraday dark space in Figure 7.8. The vibrational temperature is a measurement of vibrational energy. In order to obtain a good approximation of vibrational temperature, we introduce spatial distribution of vibrational temperature assuming a Boltzmann distribution for vibrational level and by the formula $T_{vibr,x} = \frac{-\Delta\varepsilon}{\log(N_2 V_x / N_2)}$, where $\Delta\varepsilon$ is the excitation energy, N_2 is the neutral number density and $N_2 V_x$ is the species number density corresponding to the level x. The depiction of vibrational temperature (T_v = 250K ~ 2500K) at different vibrational level (v=1 ~ 15) in Figure 7.11 indicates the energy cascade of the vibrational energy states. The spatial wave features in the vibrational temperature is influenced by the vibrational excitation reaction rate which depends on the electron temperature. However, the wave are more prevalent at the lower energy states (v=1~10) which can be attributed to their dominant reaction kinetics. The temperature of the higher vibrational and metastable state is also significantly higher; however don't show any wave from the electron temperature incurring the minimal contribution on the waves. The population density of the vibrational state decreases with the increment of the vibrational states and significantly lowers at the higher energy states as shown in Figure 7.10. The comparison of vibrational population density at different vibrational level is an implication

of the distribution function. The vibrational population number density is plotted with respect to the vibrational temperature in various spatial location of the cathode sheath and positive column in Figure 7.8. The vibrational temperature increases from left to right with the increment of the vibrational level with a consequence of the decrement of the vibrational population density. The vibrational population density is the highest at vibrational cathode sheath and minimum at the Ion cathode sheath. It is also observed that the vibrational peak corresponds to the dark region in the striations and represents the minimum electrons/ion population density. Whereas, the maximum electron/ion concentration has the minimum vibrational population density.

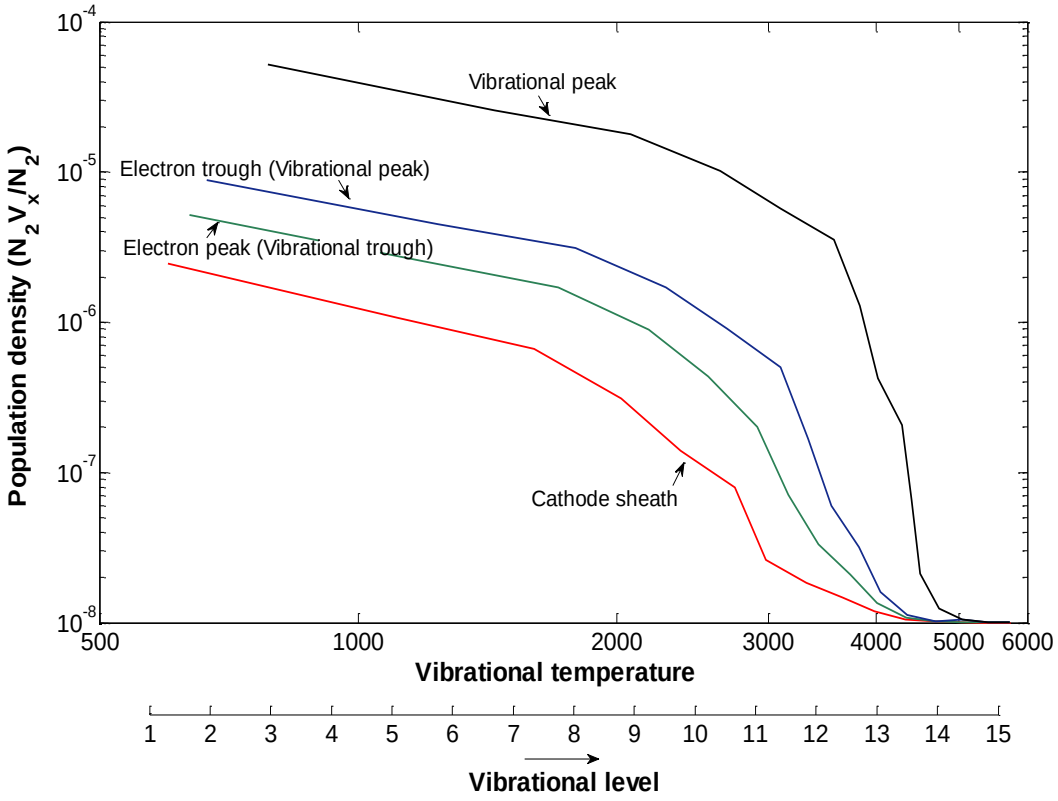

Figure 7.12: Vibrational population density with respect to vibrational temperature for the baseline condition 0.6 mA/cm^2.

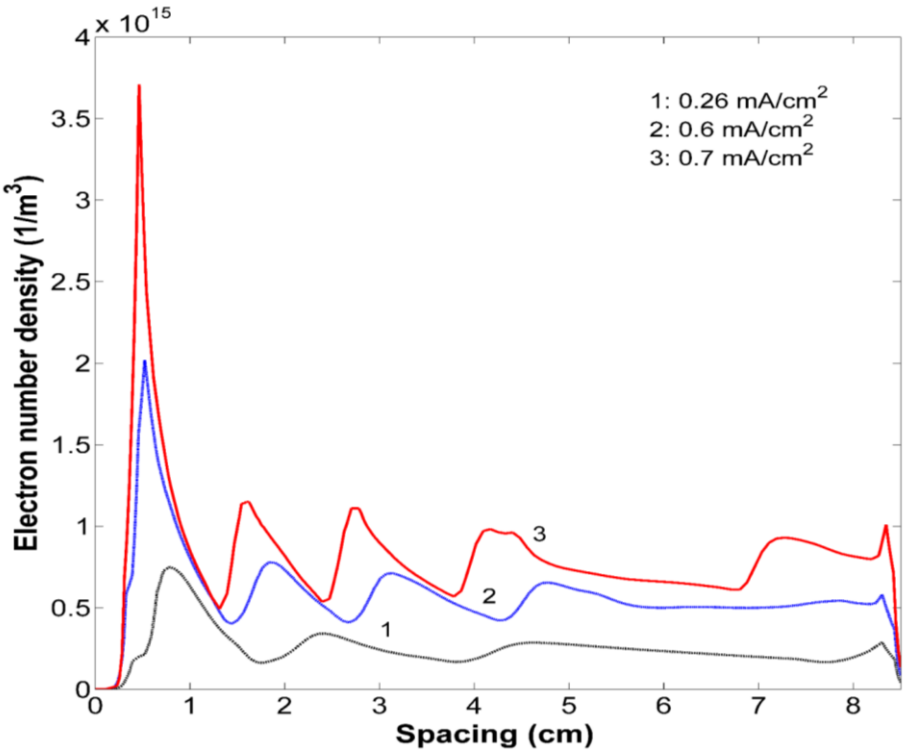

Figure 7.13: Steady state profile of electron number density at different discharge current.

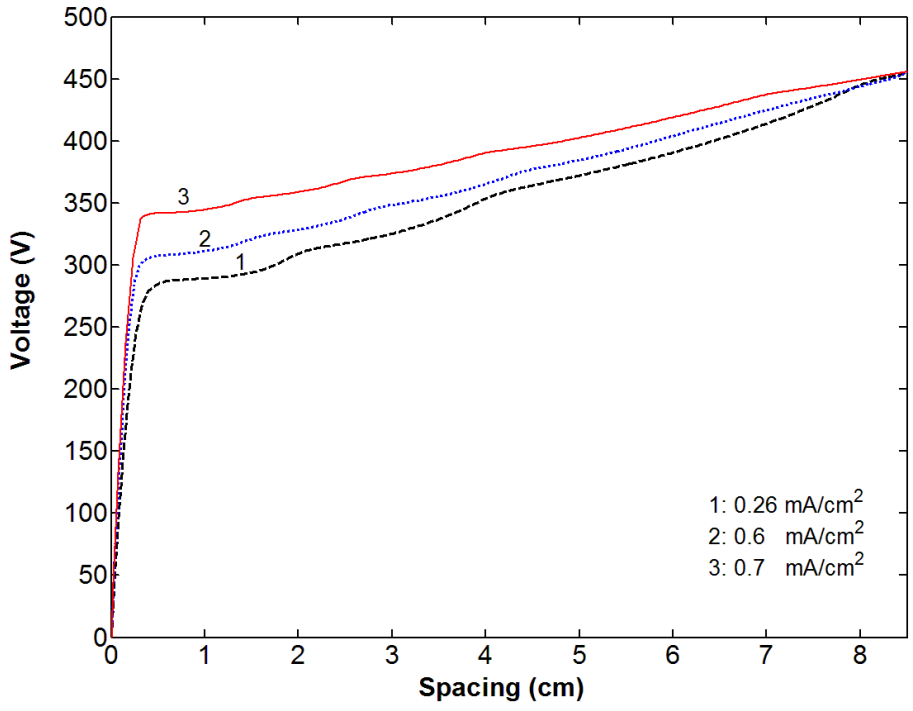

Figure 7.14: Steady state profile of potential at different discharge current.

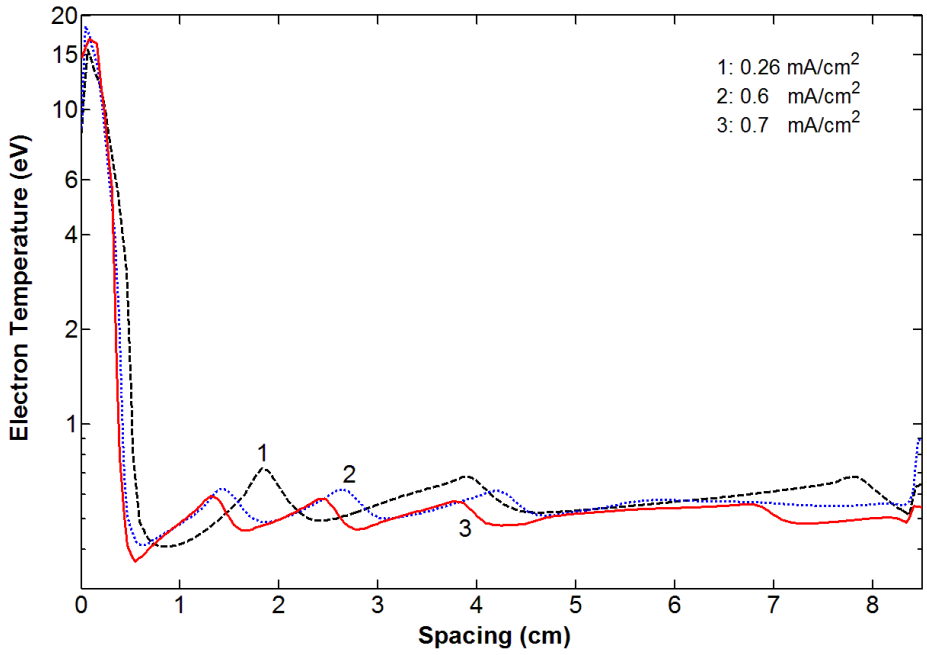

Figure 7.15: Steady state profile electron temperature at different discharge current.

Figure 7.13 to 7.15 presents a parametric study of electron number density, electric potential, and electron number density and electric field at different current condition where the current varies form 0.26 mA/cm^2 to 0.8 mA/cm^2. The parametric study shows that the number of wave pattern in the striations increases with current and with electron number density. The increment of strata pattern and electron number density with discharge current is depicted in Figure 7.13. The number of strata pattern is directly related to the duration of the discharge to reach its steady state condition that follows after breakdown. The duration of the fast fall of the discharge voltage depends on electron number density and discharge current. A longer fall time gives a higher probability of a higher electric field and a higher electron energy density. The discharge requires a reduced electric field of the order of 150 Td to initiates the vibrational reaction wave. Due to elongated fall time, say in about 1.5 μs, a higher reduced electric field (<150 Td) in the anode is maintained during

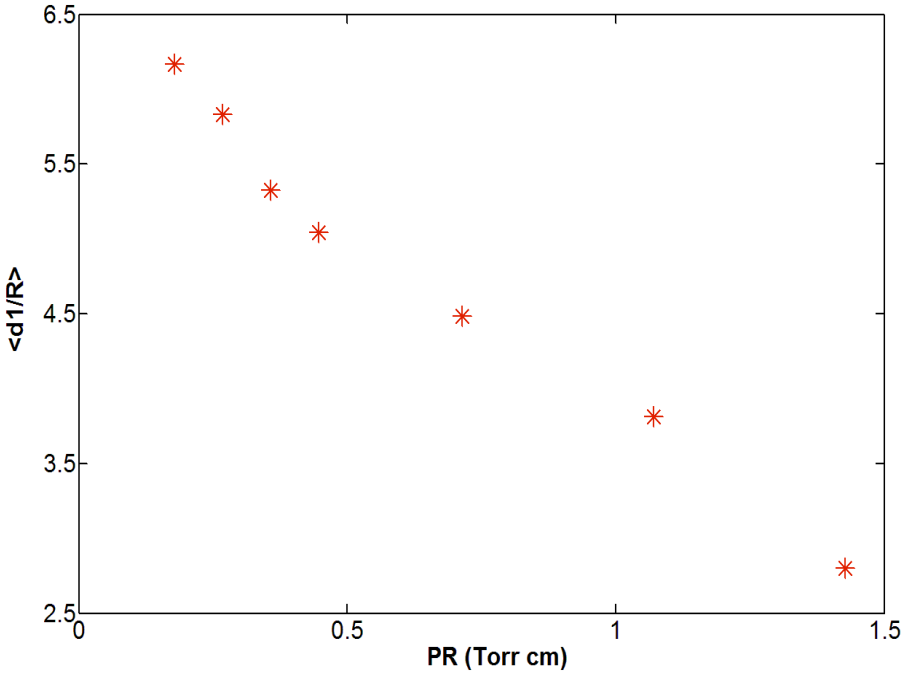

Figure 7.16: Verification of Goldstein-weinerlaw, <d1/R> vs PR for the baseline condition.

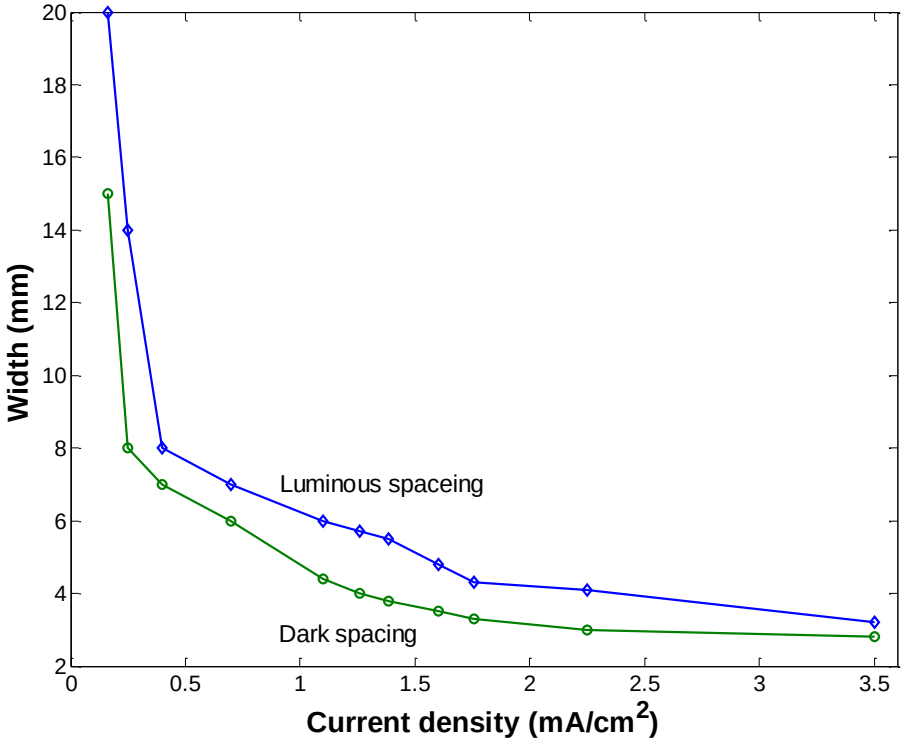

Figure 7.17: Luminous and dark spacing vs the current density with respect to discharge current.

-the break down to steady state discharge. During this short period a number of waves can generates and gives more vibrational waves in the steady state positive column. It should be noted that the study fall in the normal glow region which keep the discharge voltage constant regardless any change in current density as shown in Figure 7.14.

As the current increases, the formation of striations results in an incremental increase of cathode fall voltage with a constant discharge voltage so that the electric field on the positive column striations is lowered. This in turn has the effect of lowering the electron temperature for an increment of current as observed in Figure 7.15. The number of pattern increases with current density which will reduce the thickness of the luminous and dark region of the discharge as presented in Figure 7.16. The thickness values of the first striation measured for different discharge current values at the same gas pressure. It is also found that the thickness of the luminous region is higher than the thickness of the dark region. The experimental suggests that the striation thickness depends weakly on the discharge current as a constant pressure (V. A. Lisovskiy et al., 2012) and hence striation thickness is plotted with respect to pR for a constant discharge current density in Figure 7.16. The dimensionless thickness of the first striation <d1>/R, i.e. the obtained values of the thickness of the first striations (in cm) are divided by the tube radius (in cm). For the principal axis, the values of the gas pressure are multiplied by the tube radius, also in centimeters. From the correlation of <d1>/R= f(pR), as obtained in Figure 7.16, it can be found that the dimensionless thickness values of the first striations match a single straight line which indicates the linear dependency of <d1>/R on the product pR. The relation demonstrates a good relation of Goldstein Wehner law for the stratification process of the dc glow discharge in nitrogen.

7.9 CONCLUSION

A one dimensional, fluid based model is employed to investigate the kinetics of low pressure striations phenomenon in nitrogen which simulates the experimental conditions of a setup from the National University of Kharkiv. A reaction chemistry set for Nitrogen discharges is developed consisting 25 different species and 76 reactions. It is demonstrated that an adequate description of the vibrational kinetic is necessary for modeling of striations, where the reactions of the lower vibrational level ($\varepsilon < 2.72$) has the predominating influence. It is also observed that there exists a niche of variation in cross sectional area in these initial vibrational level among different datasets. The pattern of striations has also found to be a strong function of vibrational excitation reactions and the electron recombination reactions.

In summary, we simulated the formation of a self-sustained standing striations in the positive column. The development of the striations, which are observed only with a particular dataset in the literature, is dependent on the field dependent vibrational reaction rate. This study lays the foundation for a detailed understanding of striation in diatomic plasma discharges

Table

Kinetics

Electrons: e

Ions: N_2+, N+, N_4+

Vibrational: $N_2(v=1,2,3,4,....15)$

Metastable: $N_2(\mathrm{A}^3\Sigma)$, $N_2(B^3\Pi)$, $N_2(W^3\Delta)$, $N_2(a^1\Pi)$, $N_2(a'^1\Sigma)$, $N_2(w^1\Delta)$, $N_2(C^3\Pi)$, $N_2(E^3\Sigma)$, $N_2(c^1 1)$

Table 7.1. Gas phase kinetic processes taken into account in the Striations modeling

	Reactions		***Reaction Rate***
G1	$e+N_2 \rightarrow N_2+e$		$f(\varepsilon)$
G2	$e+N_2 \rightarrow N_2(v=1)+e$	*0.2889*	$f(\varepsilon)$
G3	$e+N_2 \rightarrow N_2(v=2)+e$	*0.5742*	$f(\varepsilon)$
G4	$e+N_2 \rightarrow N_2(v=3)+e$	*0.8559*	$f(\varepsilon)$
G5	$e+N_2 \rightarrow N_2(v=4)+e$	*1.1342*	$f(\varepsilon)$
G6	$e+N_2 \rightarrow N_2(v=5)+e$	*1.4088*	$f(\varepsilon)$
G7	$e+N_2 \rightarrow N_2(v=6)+e$	*1.68*	$f(\varepsilon)$
G8	$e+N_2 \rightarrow N_2(v=7)+e$	*1.9475*	$f(\varepsilon)$
G9	$e+N_2 \rightarrow N_2(v=8)+e$	2.2115	$f(\varepsilon)$
G10	$e+N_2 \rightarrow N_2(v=9)+e$	2.4718	$f(\varepsilon)$

G11	$e + N_2 \rightarrow N_2(v=10) + e$	2.7284	$f(\varepsilon)$
G12	$e + N_2 \rightarrow N_2(v=11) + e$	2.9815	$f(\varepsilon)$
G13	$e + N_2 \rightarrow N_2(v=12) + e$	3.231	$f(\varepsilon)$
G14	$e + N_2 \rightarrow N_2(v=13) + e$	3.4769	$f(\varepsilon)$
G15	$e + N_2 \rightarrow N_2(v=14) + e$	3.7149	$f(\varepsilon)$
G16	$e + N_2 \rightarrow N_2(v=15) + e$	3.9576	$f(\varepsilon)$
G17	$e + N_2 \rightarrow N_2(\mathrm{A}^3\Sigma) + e$	*6.17*	$f(\varepsilon)$
G18	$e + N_2 \rightarrow N_2(B^3\Pi) + e$	*7.35*	$f(\varepsilon)$
G19	$e + N_2 \rightarrow N_2(W^3\Delta) + e$	*7.36*	$f(\varepsilon)$
G20	$e + N_2 \rightarrow N_2(a^1\Pi) + e$	*8.4*	$f(\varepsilon)$
G21	$e + N_2 \rightarrow N_2(a'^1\Sigma) + e$	*8.55*	$f(\varepsilon)$
G22	$e + N_2 \rightarrow N_2(w^1\Delta) + e$	*8.89*	$f(\varepsilon)$
G23	$e + N_2 \rightarrow e + N + N$	*9.75*	$f(\varepsilon)$
G24	$e + N_2 \rightarrow N_2(C^3\Pi) + e$	*11.03*	$f(\varepsilon)$
G25	$e + N_2 \rightarrow N_2(E^3\Sigma) + e$	*11.87*	$f(\varepsilon)$
G26	$e + N_2 \rightarrow N_2(c^1 1) + e$	*12.94*	$f(\varepsilon)$
G27	$e + N_2 \rightarrow N_2 + +2e$	*15.6*	$f(\varepsilon)$
G28	$e + N_2(v=1) \rightarrow N_2(\mathrm{A}^3\Sigma) + e$	*6.17*	$f(\varepsilon)$
G29	$e + N_2(v=1) \rightarrow N_2 + 2e$	*15.5*	$f(\varepsilon)$

G30	$2\mathrm{e} + \mathrm{N}_2^+ \rightarrow \mathrm{N}_2 + \mathrm{e}$		A
G31	$e + N_2(v=1) \rightarrow N_2 + e$	-0.29	$f(\varepsilon)$
G32	$e + N_2(\mathrm{A}^3\Sigma) \rightarrow N_2 + e$	-6.17	$f(\varepsilon)$
G33	$e + N_2(\mathrm{A}^3\Sigma) \rightarrow N_2(v=1) + e$	-5.88	$f(\varepsilon)$
G34	$e + N \rightarrow N + e$		$f(\varepsilon)$
G35	$e + N \rightarrow 2e + N+$	8.54	A
G36	$2e + N+ \rightarrow N + e$		A
G37	$2N_2 + N_2+ \rightarrow N_2 + N_4+$		A
G38	$e + N_4+ \rightarrow N + N + N_2$		A
G39	$N + N_4+ \rightarrow 2N_2 + N+$		A
G40	$N_2(\mathrm{A}^3\Sigma) + N_2(a^1\Pi) \rightarrow e + N_4+$		A
G41	$2N_2(a^1\Pi) \rightarrow e + N_2 + N_2+$		A
G42	$N_2 + N_2 \rightarrow 2N + N_2$		A
G43	$N_2 + N_2(v=1) \rightarrow 2N + N_2$		A
G44	$N_2 + N_2(v=2) \rightarrow 2N + N_2$		A
G45	$N_2 + N_2(v=3) \rightarrow 2N + N_2$		A
G46	$N_2 + N_2(v=4) \rightarrow 2N + N_2$		A
G47	$N_2 + N_2(v=5) \rightarrow 2N + N_2$		A
G48	$N_2 + N_2(v=6) \rightarrow 2N + N_2$		A

G49	$N_2 + N_2(v=7) \rightarrow 2N + N_2$		A
G50	$N_2 + N_2(v=8) \rightarrow 2N + N_2$		A
G51	$N_2 + N_2(v=9) \rightarrow 2N + N_2$		A
G52	$N_2 + N_2(v=10) \rightarrow 2N + N_2$		A
G53	$N_2 + N_2(v=11) \rightarrow 2N + N_2$		A
G54	$N_2 + N_2(v=12) \rightarrow 2N + N_2$		A
G55	$N_2 + N_2(v=13) \rightarrow 2N + N_2$		A
G56	$N_2 + N_2(v=14) \rightarrow 2N + N_2$		A
G57	$N_2 + N_2(v=15) \rightarrow 2N + N_2$		A
G58	$N_2 + N_2(v=1) \rightarrow N_2 + N_2$		A
G58	$N_2 + N_2(v=2) \rightarrow N_2 + N_2$		A
G59	$N_2 + N_2(v=3) \rightarrow N_2 + N_2$		A
G60	$N_2 + N_2(v=4) \rightarrow N_2 + N_2$		A
G61	$N_2 + N_2(v=5) \rightarrow N_2 + N_2$		A
G62	$N_2 + N_2(v=6) \rightarrow N_2 + N_2$		A
G63	$N_2 + N_2(v=7) \rightarrow N_2 + N_2$		A
G64	$N_2 + N_2(v=8) \rightarrow N_2 + N_2$		A
G65	$N_2 + N_2(v=9) \rightarrow N_2 + N_2$		A
G66	$N_2 + N_2(v=10) \rightarrow N_2 + N_2$		A

G67	$N_2 + N_2(v=11) \rightarrow N_2 + N_2$		A
G68	$N_2 + N_2(v=12) \rightarrow N_2 + N_2$		A
G69	$N_2 + N_2(v=13) \rightarrow N_2 + N_2$		A
G69	$N_2 + N_2(v=14) \rightarrow N_2 + N_2$		A
G70	$N_2 + N_2(v=15) \rightarrow N_2 + N_2$		A
G71	$N_2 + N_2(\mathrm{A}^3\Sigma) \rightarrow N_2 + N_2$		A
G72	$N_2 + N_2(B^3\Pi) \rightarrow N_2 + N_2$		A
G73	$N_2 + N_2(W^3\Delta) \rightarrow N_2 + N_2$		A
G74	$N_2 + N_2(a^1\Pi) \rightarrow N_2 + N_2$		A
G75	$N_2 + N_2(a'^1\Sigma) \rightarrow N_2 + N_2$		A
G76	$N_2 + N_2(w^1\Delta) \rightarrow N_2 + N_2$		A
G77	$N_2 + N_2(C^3\Pi) \rightarrow N_2 + N_2$		A
G78	$N_2 + N_2(E^3\Sigma) \rightarrow N_2 + N_2$		A
G79	$N_2 + N_2(c^1 1) \rightarrow N_2 + N_2$		A

A: reaction rate in Arrhenius form; $f(\varepsilon)$: reaction rate obtained from EEDF (electron energy distribution function);

G30: $(N_A)^2 \times 10^{-31} \times (T_g / T_e)^{4.5}$

G36: $(N_A)^2 \times 10^{-26} \times (T_g / T_e)^{4.5}$

G37: $(N_A)^2 \times 5 \times 10^{-41} \times (1/T_g)$

G38: $(N_A) \times 3.13 \times 10^{-13} \times (T_e)^{-0.41}$

G39: $(N_A) \times 10^{-23}$

G40: $(N_A) \times 10^{-23}$

G41: $(N_A) \times 3.2 \times 10^{-18}$

G42~G57: $(N_A) \times 3.5 \times 10^{-15} \times (T_g/300)^{-1.6} \times \exp(-113000/T_g)$

G58: $(N_A) \times 3.5 \times 10^{-27}$

G59~G79: $(N_A) \times 1.5 \times 10^{-26}$

Table 7.2. Surface reactions considered in the Striations modeling

	Reactions
S1	$N_2^+ \rightarrow N_2$
S2	$N_2(v = 1 \sim 15) \rightarrow N_2$
S3	$N_2(metastable) \rightarrow N_2$

CHAPTER 8

SUMMARY AND CONCLUSION

8.1 SUMMARY

In this dissertation, four fundamental problems in microplasma science have been investigated based on mathematical analysis, numerical modeling, and experimental study. These problems are NDR instability in microplasma, Striations in a diatomic plasma discharge, suppression of NDR instability for low current operation, and Ion detection in microscale plasma discharges by leveraging the NDR instability in discharges. In addition, this study also focuses on reaction kinetics study as a part of the mathematical model and numerical simulation. To study the NDR instability, we developed a simplified reaction kinetics mechanism for pure helium discharges and pure helium with trace impurities. For the simulation of striations, we proposed a reduced a N_2 reaction kinetics mechanism which can predict striations at low or high pressure discharge systems.

For the mathematical modeling of nonequilibrium and nonthermal plasma instabilities, a multiscale and multiphysics modeling approach was considered which includes plasma discharge physics, plasma chemistry, surface reactions, energy equation, and an external circuit. The multiscale and multiphysics model is validated by the experimental measurement and also experimental data from the literature.

For the modeling of suppression of NDR instability and ion detection, the mathematical modeling approach was taken into consideration. Experimental measurements validate those mathematical models. The findings of this study will be presented in separate subsections.

8.1 CHARACTERIZATION OF NDR INSTABILITY

- An experimental setup is developed for the study of DC driven microplasma discharges and to characterize the NDR region of the voltage current characteristic curve. The experimental result represents that of parallel plate configuration. The setup captures the negative slope region of the voltage current characteristics curve along with the normal glow region. The transient voltage current profile in the NDR region predicts a self-pulsing relaxation oscillation which is similar to that of microhollow cathode discharges. Instead of a flat anode, a spherical shape cathode is used in this study to ease the visualization process.

- A multiscale and multiphysics model was developed for He-N_2 feed gas chemistry which incorporates plasma physics, gas phase reactions, surface reactions, energy equations, and external circuit equations. The multiphysics model was applied to both 1D and 2D geometrical configurations with appropriate boundary conditions. The interelectrode spacing was varied between 200 µm to 400 µm. The multiphysics model was able to capture the negative slope of the NDR region as observed in the experiment along with the flat normal glow mode. The transient

voltage profile predicts a sawtooth wave. However, the transient current profile from the 2D model was found to be a good match with the experimental results, where a multistage process generally takes place.

- The onset of oscillation takes place when the external circuit time is higher than the ion transit time.

- The multiphysics numerical model reveals that there ars different oscillatory modes inherited in the NDR region, which are hard to distinguish in the experimental study. We primarily distinguished two major oscillatory modes, such as relaxation oscillation and partial relaxation oscillation. During the complete relaxation, the discharge undergoes a complete ionization and recombination during each cycle of pulsing. This happens to take place at a low current where the external circuit time is significantly higher than the ion transit time. However, at a high discharge current, the external circuit time becomes comparable to ion transit time. In this case, a partial relaxation in the NDR region was observed. During the partial relaxation, the next cycle started before a complete ionization in the discharge took place. In this case, the frequency of oscillation was found to be significantly higher than the complete relaxation oscillation.

- The spatial temperature distribution shows that gas temperature does not vary significantly in the domain during the NDR pulsing. The spatial distribution of both 1D and 2D models can predict cathode fall region, faraday dark space region, and the positive column region.

- The dominant ion in the pure helium discharge was He_2^+ in the range of 10^{17} ~ 10^{19} ($1/m^3$) depending on the discharge current. However, with the addition of trace impurity, the ion distribution changed significantly. A trace amount of N_2 in the discharge, which has a lower ionization potential than the helium, can quickly saturate the region with N_2^+ ions. There was a critical limit of impurity, such 45 ppm of N_2 , after this limit, the majority of ions was found to be N_2^+ ,with a range of 10^{17} ~ 10^{19} ($1/m^3$) depending on the discharge current.

- Based on numerical simulation under different pressure (1 to 4 atm), a traditional scaling law was applied which normalized the current density with pressure squared (j_{rms}/p^2) and the pulsing frequency with pressure (f/p). It was found that (j_{rms}/p^2) vs. (f/p) collapse into a single trend line under different pressure conditions.

- On the basis of numerical simulation under different pressure (1 to 4 atm), a functional dependency of ion density to pulsing frequency and trace N2 concentration was found. The normalized ion number density (N_{ion}/N) vs. ($1/fX_{N2}$) also collapsed into a single line under different pressure. Despite being a numerical result, it is envisioned that one can utilize the dependence/variation in the plasma frequency to ion density as means of experimentally detecting trace impurities in feed gas as well as a method of indirect measurement of ion density by injecting a known amount of trace impurities.

8.2 SUPPRESSION OF SELF PULSING REGION OF DIRECT CURRENT DRIVEN DC MICROPLASMA DISCHARGES

- A method for the suppression of NDR instability is presented based on theoretical modeling on the external circuit and a subsequent experimental study. The suppression circuit of the current disclosure comprises an inductor connected in series with the ballast resistance and the discharge, which increases the combined response time of the plasma and the inductor, such that,

$$\tau_{L/R_{plasma}} > \tau_{RC} > \tau_{ion}$$

- The solution of the circuit model is based on the choice of the discharge resistance. It is a common norm to model the nonlinear NDR discharge resistance as a function of discharge current. The discharge resistance is expressed as:

$$R_{discharge} = C_1 \tanh(\frac{I - I_{\lim}}{p}) + C_2$$

Where, the constants, C_1= -1920 Ω, C_2= 2000 Ω, $I_{\lim}$= 0.317 mA, and p = 0.45 mA, were obtained from experimental fits.

- The transition from ‘subnormal’ to ‘normal’ glow occurs at 0.8 mA in the absence of an external inductor element. The transition point shifted to 0.65 mA and 0.40 mA for a 1H and 40H, respectively The NDR region is still retained with the different inductors, however the slope changes significantly. The slope of the NDR region varies from 440 kΩ, 305 kΩ, and 225 kΩ for an inductance value of 0 H, 1 H, and 40 H, respectively. It is interesting to note that as the

inductor decreases the NDR slope, it is also decreasing the positive static resistance of the system.

- It was observed that increasing the inductance decreased the pulsing frequency. For a discharge current of 0.25 mA the pulsing frequency was measured to be 21 Hz, 18 Hz and 16 Hz for inductance values of 0H, 1H, and 40H, respectively. In addition to the pulsing frequency, the phase lag between the voltage and current is substantially decreased, which was measured as ~ 13, 10 and 7 degrees for 0H, 1H and 40H, respectively, for the same discharge current of 0.25 mA. The role of the inductance on the static positive resistance can be summarized as:

$$L_x \uparrow \; V_L \uparrow \; f \downarrow \; V_{discharge\ \mathrm{RMS}} \downarrow \; R_{discharge\ \mathrm{RMS}} \downarrow$$

- A stability map in terms of external circuit parameter is introduced in this study to determine the stable region of operation in the presence of the inductor element. The 45-degree line in the stability plot represents the condition, where $\tau_{L_x/R_{discharge}} = \tau_{R_{ballast}C_p}$, and demarcates stable and unstable operation regimes. For conditions, where $\tau_{L_x/R_{discharge}} < \tau_{R_{ballast}C_p}$, a self-pulsing DC discharge that undergoes relaxation type oscillation is observed. Varying/incrementing the inductance value the combined time response of plasma with inductor can be increased to a value, where $\tau_{L_x/R_{discharge}} > \tau_{R_{ballast}C_p}$, making the driving circuit response time comparably shorter and establishing that a stable DC operation can be obtained.

8.3 ION NUMBER DENSITY QUANTIFICATION BASED ON NDR PULSING

- A methodology for quantifying ion number density from the pulsing frequency of plasma discharge is developed. The ion number density in the pure feed gas can be expressed in terms of the change in the current density, the pulsing frequency for the pure feed gas and in the presence of trace impurity, the discharge voltage, the inter-electrode separation distance and the ion mobility, such as

$$N_{i,p} = \frac{d\Delta J_i}{q\mu_{i,p}V_d\left(\sqrt{\frac{f_{p+imp}}{f_p}}-1\right)}$$

A model validation technique is also proposed to attain the availability of the model, such as

$$\frac{N_{i,p}}{N_{i,actual}} = \frac{\Delta J_i}{J_i\left(\sqrt{\frac{f_{p+imp}}{f_p}}-1\right)}$$

$$f_{p+imp} = f_p\left(\frac{\Delta J_i}{J_i}+1\right)^2 \quad [\text{for, } N_{i,p} \approx N_{i,actual}]$$

- The experimental setup is developed with mass flow controller to feed a known amount of trace impurity in the pure gas. The influence of impurity on the voltage current characteristic curve is also presented at two different concentrations - 160 and 500 ppm. The VI characteristics were found to shift to higher currents with an increase in the impurity level. For an identical discharge voltage of ~ 1600 V, the discharge current

increased by ~ 12.5 µA and 40.0 µA for a nitrogen level of 160 ppm and 500 ppm respectively.

- The pulsing frequency for the two different impurity levels, 160 ppm and 500 ppm of nitrogen as compared with pure helium case. The pulsing frequency for both the cases is found to increase with increasing discharge current. The frequency increased from ~ 5 kHz at ~ 0.03 mA to ~ 40 kHz at ~0.15 mA, increasing by a factor of ~ 8.

- If the frequency from the model validation equation match with the experimentally measured frequency, the ion number density equation can be applied. It was found that at a higher impurity level, such as 500 ppm, the experimental frequency does not match with the model frequency. Therefore the proposed model is not recommended. At a lower impurity level, ~160 ppm the model frequency matched well with the experimental data. Therefore, the ion number density formula can apply to this low impurity level.

8.5 RECOMMENDATIONS FOR FUTURE WORK

Microplasma technology is new and has the potential to some application due to its operating condition viability and low cost operation. Instabilities in a significant issue are this regard. This study aimed to developed mathematical model and experimental setup to characterize its instabilities. This study worked with He, He-N_2 chemistry, and N_2 chemistry. However ion kinetics of more gases can be considered to study in future.

8.4 STRIATIONS IN DIATOMIC PLASMA DISCHARGES

- A multiscale and multiphysics simulation was conducted for the simulation of striations in diatomic N_2 feed gas chemistry which incorporates plasma physics, gas phase reactions, surface reactions, and external circuit equations. To investigate the kinetics of striations phenomenon in nitrogen, the interelectrode spacing was considered to be 8.5 cm, which simulates the experimental conditions of a low pressure setup from the National University of Kharkiv. The operating pressure was varied between 0.5 Torr to 5 Torr. Both 1D and 2D models were capable of simulating the striations for low to high pressure microplasma discharges.

- In this study, the reliability of different databases were examined for N_2 discharges, with interest to the simulation of standing striations in the positive column. It was discovered that the Biagi or Itikawa dataset has the necessary level of resolution at lower and higher energy levels. A reaction chemistry set for Nitrogen discharges is developed consisting of 25 different species and 76 reactions. A comparative study of four different cross sectional datasets, such as Biagi, Phelps, Morgan, and Itikawa, was performed. The Phelps and Morgan dataset, whose reaction sets and values are based on the data of 70-80s, is incomplete with no data at lower (< 1.6 eV) or higher energy level (> 4 eV). Due to the unavailability of data at lower and higher energy levels, the simulation based on the Phelps or Morgan dataset cannot capture the positive column strata. However, the cross-sectional dataset of Biagi or Itikawa, whose reactions

mechanism and values are recent and are based on quasi-theoretical cross section data, can predict the striations pattern in the positive column. We determined that an adequate description of the vibrational kinetic is necessary for modeling the observed striations, where the reactions of the lower vibrational level ($\varepsilon < 2.72$) was found to have the predominating influence.

- The electron number density is found to vary between ~ $7x10^{14}$ m^{-3} and ~$4x10^{14}$ m^{-3} in one strata cycle. The electron temperature follows a similar trend (0.4 eV ~ 0.6 eV) in the positive column which inversely varies with the electron number density. It is also observed that the electric field in the positive column reaches its peak (~ 1×10^{3} V/m) at the trail of each stratum, where the formation of space charge is maximum.

- The spatial distribution of electron number density varies inversely with vibrational number density in one strata cycle. Therefore, the electron/Ion number density is the maximum where the vibrational number density is minimum and vice versa.

- Our reaction rate analyses from the numerical modeling found the following trend: $K_{vibrational} > K_{recombination} > K_{metastable} > K_{ionization}$. Hence, the applied energy is assumed to feed predominantly into vibrationally excited states of molecules for the diatomic gas discharges. The pattern of striations is found to be a strong function of vibrational excitation reactions and the electron recombination.

8.5.1. REACTION KINETICS OF HUMID AIR FOR THE SELF-PULSING NDR REGION

Reaction kinetics for air plasma and humid air plasma for the simulation of NDR instability in microplasma. Humid air, air with trace water quantities offers the possibilities of numerous applications and most cost effective to use. However, air chemistry is the most complicated as it is a diatomic gas and comprises both O_2 and N_2 with the addition of trace water quantities intrinsically. The reaction kinetics of air chemistry for NDR pulsing would provide a better understanding to attain the stable microplasma operation at lower current.

8.5.2. REACTION KINETICS STRIATIONS FOR AIR/HUMID AIR/H_2

In the present study, the mathematical model and simulation were carried out to simulate the striations in N_2. The same procedure can be applied to Air, Air with H_20, and H_2 discharges to better understand the mechanism of striations in other gases. Our experimental setup also predicts the striations in air discharges and humid air discharges. In this study, we also found that the importance of dataset and which dataset can be used to predict the striations for N_2 . The same approach can be taken into account to simulate striations in other gases which required rigorous simulation study.

8.5.3. INVESTIGATE A POSSIBLE MODES IN NDR REGION

This study predicts two different oscillatory modes in the NDR region. In addition, there are possibilities of multiples modes in the NDR region which can be investigated by

a further study. The high pressure system can predict more modes than the low pressure system as reaction kinetics is more complicated for high pressure system.

8.5.4. LEVERAGING THE NDR PULSING

In this study, the NDR pulsing is applied for ion detection with a proposal of trace impurity detection. Both the NDR pulsing and Striaiotns predict a special kind of waves which cannot be described by any known waveforms.

8.5.5. MODELING OF NONEQUILIBRIUM PLASMA ASSISTED COMBUSTION

The modeling of plasma assisted combustion is a topic of recent interests and is gaining popularity for a better combustion, uniform discharge, noise reduction, detonation. A turbulence based modeling is required in this regard which can assist in the development of better combustion system.

8.5.6. THERMALLY STABLE HIGH PRESSURE PLASMA SYSTEM

One of the major instability in high pressure plasma is it is intrinsic thermally unstable condition which leads to a breakdown and high temperature rise. A stable high pressure plasma system is highly desirable in this regard. The parallel plate, pin plate, and microhollow cathode configuration plasma system have been studied in this regard. In addition, high pressure microplasma jet is gaining popularity for some applications. A more fundamental study is required to attain high pressure and low power microplasma operation for some application. In this study, we have shown that the external circuit can enhance the

range of operation for the microplasma discharges. However, it asks the question if it is possible to suppress the thermal instability by using external circuit modification.

The nanosecond plasma is one more exciting plasm application, and by the Paschen law, it can be generated in a denser medium like liquid. The plasma generation in the high pressure dense liquid system is new, and the physics of it is still undiscovered. The nanosecond corona discharge is one of that application. Transient spark and corona discharges occur in a liquid medium which is initiated by the application of the high electric field. However, it is shown that a nonthermal plasma can be created with ultrasharp tips and nanotubes with a very low power and without any streamer. Time-resolved OES demonstrate narrow spectral lines that prove very useful for simple and sensitive multielement analysis, thus opening new possibilities for chemical detection, environmental monitoring, medicine and many other application

REFERENCES

Aleynik, A. N., Baykov, A. N., Baskakov, M. B., Dambaev, G. T., Deneko, O. I., Krasnozhenov, E. P., … Zhdanova, O. S. (2012). Application of non-equilibrium atmospheric pressure plasma for coagulation and sterilization. In *2012 7th International Forum on Strategic Technology (IFOST)* (pp. 1–4). IEEE. https://doi.org/10.1109/IFOST.2012.6357808

Almeida, P. G. C., Benilov, M. S., Cunha, M. D., & Gomes, J. G. L. (2017). Computing Different Modes on Cathodes of DC Glow and High-Pressure Arc Discharges: Time-Dependent Versus Stationary Solvers. *Plasma Processes and Polymers*, *14*(4–5), 1600122. https://doi.org/10.1002/ppap.201600122

Annemie Bogaerts, Erik Neyts, Renaat Gijbels, J. V. der M. (2002). Gas discharge plasmas and their applications. *Spectrochimica Acta Part B: Atomic Spectroscopy*, *57*(4), 609–658. https://doi.org/10.1016/S0584-8547(01)00406-2

Arslanbekov, R. R., & Kolobov, V. I. (2003). Two-dimensional simulations of the transition from Townsend to glow discharge and subnormal oscillations. *Journal of Physics D: Applied Physics*, *36*(23), 2986–2994. https://doi.org/10.1088/0022-3727/36/23/020

Arslanbekov, R. R., & Kolobov, V. I. (2005). 2-D simulations of striations in direct current glow discharges in argon. *IEEE Transactions on Plasma Science*, *33*(2), 354–355. https://doi.org/10.1109/TPS.2005.845123

Asadullin, T. Y., Galeyev, I. G., & Timerkayev, B. A. (2016). Way of stability increase of the glow discharge. *Journal of Physics: Conference Series*, *669*(1), 12001. https://doi.org/10.1088/1742-6596/669/1/012001

Aubert, X., Bauville, G., Guillon, J., Lacour, B., Puech, V., & Rousseau, A. (2007a). Analysis of the self-pulsing operating mode of a microdischarge. *Plasma Sources Science and Technology*, *16*(1), 23–32. https://doi.org/10.1088/0963-0252/16/1/004

Aubert, X., Bauville, G., Guillon, J., Lacour, B., Puech, V., & Rousseau, A. (2007b). Analysis of the self-pulsing operating mode of a microdischarge. *Plasma Sources Science and Technology*, *16*(1), 23–32. https://doi.org/10.1088/0963-0252/16/1/004

Babayan, S. E., Jeong, J. Y., Tu, V. J., Park, J., Selwyn, G. S., & Hicks, R. F. (1998). Deposition of silicon dioxide films with an atmospheric-pressure plasma jet. *Plasma Sources Science and Technology*, *7*(3), 286–288. https://doi.org/10.1088/0963-0252/7/3/006

Becker, K. H., Kersten, H., Hopwood, J., & Lopez, J. L. (2010). Microplasmas: scientific challenges & technological opportunities. *The European Physical Journal D*, *60*(3), 437–439. https://doi.org/10.1140/epjd/e2010-00231-4

Becker, K. H., Schoenbach, K. H., & Eden, J. G. (2006a). Microplasmas and applications. *Journal of Physics D: Applied Physics*, *39*(3), R55–R70. https://doi.org/10.1088/0022-3727/39/3/R01

Begum, A., Begum, A., Laroussi, M., & Pervez, M. R. (n.d.). Dielectric Probe: a New Electrical Diagnostic Tool for Atmospheric Pressure Non-Thermal Plasma Jet. Retrieved from http://citeseerx.ist.psu.edu/viewdoc/summary?doi=10.1.1.296.7761

Benedikt, J., Raballand, V., Yanguas-Gil, A., Focke, K., & von Keudell, A. (2007). Thin film deposition by means of atmospheric pressure microplasma jet. *Plasma Physics and Controlled Fusion*, *49*(12B), B419–B427. https://doi.org/10.1088/0741-3335/49/12B/S39

Bogaerts, A., & Gijbels, R. (1995). Modeling of metastable argon atoms in a direct-current glow discharge. *Physical Review A*, *52*(5), 3743–3751. https://doi.org/10.1103/PhysRevA.52.3743

Boyd, L. C. S. I. D. (2007). Numerical simulation of weakly ionized hypersonic flow over reentry capsules. Retrieved from https://dl.acm.org/citation.cfm?id=1369248

Bruggeman, P., & Brandenburg, R. (2013). Atmospheric pressure discharge filaments and microplasmas: physics, chemistry and diagnostics. *Journal of Physics D: Applied Physics*, *46*(46), 464001. Retrieved from http://stacks.iop.org/0022-3727/46/i=46/a=464001

Cathey, C., Wang, F., Tang, T., Kuthi, A., Gundersen, M., Sinibaldi, J., … Yu, J. (2007). Transient Plasma Ignition for Delay Reduction in Pulse Detonation Engines. In *45th*

AIAA Aerospace Sciences Meeting and Exhibit. Reston, Virigina: American Institute of Aeronautics and Astronautics. https://doi.org/10.2514/6.2007-443

Chabert, P., & Braithwaite, N. (Nicholas S. J. . (2011). *Physics of radio-frequency plasmas*. Cambridge University Press.

Chabert, P., Lazzaroni, C., & Rousseau, A. (2010). A model for the self-pulsing regime of microhollow cathode discharges. *Journal of Applied Physics*, *108*(11), 113307. https://doi.org/10.1063/1.3518533

Chirokov, A., Khot, S. N., Gangoli, S. P., Fridman, A., Henderson, P., Gutsol, A. F., & Dolgopolsky, A. (2009). Numerical and experimental investigation of the stability of radio-frequency (RF) discharges at atmospheric pressure. *Plasma Sources Science and Technology*, *18*(2), 25025. https://doi.org/10.1088/0963-0252/18/2/025025

Chirokov, A. V. (2005). *Stability of Atmospheric Pressure Glow Discharges*. Drexel University.

Choi, I., Yin, Z., Adamovich, I. V., & Lempert, W. R. (2011). Hydroxyl Radical Kinetics in Repetitively Pulsed Hydrogen–Air Nanosecond Plasmas. *IEEE Transactions on Plasma Science*, *39*(12), 3288–3299. https://doi.org/10.1109/TPS.2011.2163736

Chow, T. C. (1931). Oscillations and Travelling Striations in an Argon Discharge Tube. *Physical Review*, *37*(5), 574–581. https://doi.org/10.1103/PhysRev.37.574

COMSOL Multiphysics. (2013). *Multiphysics Reference Guide for COMSOL 4.3*. Burlington, MA, USA.

Deconinck, T., & Raja, L. L. (2009). Modeling of Mode Transition Behavior in Argon Microhollow Cathode Discharges. *Plasma Processes and Polymers*, *6*(5), 335–346. https://doi.org/10.1002/ppap.200800144

DeFilippo, A., Saxena, S., Rapp, V., Dibble, R., Chen, J.-Y., Nishiyama, A., & Ikeda, Y. (2011). Extending the Lean Stability Limits of Gasoline Using a Microwave-Assisted Spark Plug. https://doi.org/10.4271/2011-01-0663

Derzsi, A., Hartmann, P., Korolov, I., Karácsony, J., Bánó, G., & Donkó, Z. (2009). On the accuracy and limitations of fluid models of the cathode region of dc glow discharges. *Journal of Physics D: Applied Physics*, *42*(22), 225204.

https://doi.org/10.1088/0022-3727/42/22/225204

Donkó, Z. (1999). Modelling of low-current self-generated oscillations in a hollow cathode discharge. *Journal of Physics D: Applied Physics*, *32*(14), 1657–1664. https://doi.org/10.1088/0022-3727/32/14/318

Dorai, R., & Kushner, M. J. (2003). A model for plasma modification of polypropylene using atmospheric pressure discharges. *Journal of Physics D: Applied Physics*, *36*(6), 666–685. https://doi.org/10.1088/0022-3727/36/6/309

Druyvesteyn, M. J., & Penning, F. M. (1940). The Mechanism of Electrical Discharges in Gases of Low Pressure. *Reviews of Modern Physics*, *12*(2), 87–174. https://doi.org/10.1103/RevModPhys.12.87

Du, B., Aramaki, M., Mohr, S., Celik, Y., Luggenhölscher, D., & Czarnetzki, U. (2011). Spatially and temporally resolved optical spectroscopic investigations inside a self-pulsing micro thin-cathode discharge. *Journal of Physics D: Applied Physics*, *44*(25), 252001. https://doi.org/10.1088/0022-3727/44/25/252001

Du, B., Mohr, S., Luggenhölscher, D., & Czarnetzki, U. (2011). An atmospheric pressure self-pulsing micro thin-cathode discharge. *Journal of Physics D: Applied Physics*, *44*(12), 125204. https://doi.org/10.1088/0022-3727/44/12/125204

Dubrovin, D., Nijdam, S., van Veldhuizen, E. M., Ebert, U., Yair, Y., & Price, C. (2010). Sprite discharges on Venus and Jupiter-like planets: A laboratory investigation. *Journal of Geophysical Research: Space Physics*, *115*(A6), n/a-n/a. https://doi.org/10.1029/2009JA014851

Ecker, G. (1967). Negative Characteristic and Instability of the Collision-Dominated Helium Plasma Column. *Physics of Fluids*, *10*(5), 1037. https://doi.org/10.1063/1.1762218

Ecker, G., Kröll, W., & Zöller, O. (1964). Thermal Instability of the Plasma Column. *Physics of Fluids*, *7*(12), 2001. https://doi.org/10.1063/1.1711110

Eijkel, J. C. T., Stoeri, H., & Manz, A. (2000). A dc Microplasma on a Chip Employed as an Optical Emission Detector for Gas Chromatography. *Analytical Chemistry*, *72*(11), 2547–2552. https://doi.org/10.1021/ac991380d

Elkholy, A. H. E., Nijdam, S., van Oijen, J. A., & de Goey, L. P. H. (2017). A new DBD microplasma burner for measuring the effect of nanosecond discharge on burning velocity of CH4-Air flame at atmospheric pressure. Retrieved from http://repository.tue.nl/4dbad2bf-c048-4340-99a2-d004e03d0fd0

EMELEUS, K. G. (1975). Low-current striated Townsend and transitional discharges. *International Journal of Electronics*, *39*(2), 177–185. https://doi.org/10.1080/00207217508920475

Farouk, T., Antao, D. S., & Farouk, B. (2014a). Criticality of External Circuit in Simulating Atmospheric Pressure Direct Current Microglow Discharge. *IEEE Transactions on Plasma Science*, *42*(7), 1870–1879. https://doi.org/10.1109/TPS.2014.2327095

Farouk, T., Antao, D. S., & Farouk, B. (2014b). Criticality of External Circuit in Simulating Atmospheric Pressure Direct Current Microglow Discharge. *IEEE Transactions on Plasma Science*, *42*(7), 1870–1879. https://doi.org/10.1109/TPS.2014.2327095

Farouk, T., Farouk, B., & Fridman, A. (2010). Computational Studies of Atmospheric-Pressure Methane–Hydrogen DC Micro Glow Discharges. *IEEE Transactions on Plasma Science*, *38*(2), 73–85. https://doi.org/10.1109/TPS.2009.2036622

Farouk, T., Farouk, B., Staack, D., Gutsol, A., & Fridman, A. (2006). Simulation of dc atmospheric pressure argon micro glow-discharge. *Plasma Sources Science and Technology*, *15*(4), 676–688. https://doi.org/10.1088/0963-0252/15/4/012

Farouk, T., Farouk, B., Staack, D., Gutsol, A., & Fridman, A. (2007). Modeling of direct current micro-plasma discharges in atmospheric pressure hydrogen. *Plasma Sources Science and Technology*, *16*(3), 619–634. https://doi.org/10.1088/0963-0252/16/3/023

Felix, V., Lefaucheux, P., Aubry, O., Golda, J., Schulz-von der Gathen, V., Overzet, L. J., & Dussart, R. (2016). Origin of microplasma instabilities during DC operation of silicon based microhollow cathode devices. *Plasma Sources Science and Technology*, *25*(2), 25021. https://doi.org/10.1088/0963-0252/25/2/025021

FOULDS, K. W. H. (1956). XXVII. Moving Striations in Low Pressure Mercury Vapour. *Journal of Electronics and Control*, *2*(3), 270–278. https://doi.org/10.1080/00207215608937031

Fox, G. W. (1930). Oscillations in the Glow Discharge in Neon. *Physical Review*, *35*(9), 1066–1072. https://doi.org/10.1103/PhysRev.35.1066

Fox, G. W. (1931). Oscillations in the Glow Discharge in Argon. *Physical Review*, *37*(7), 815–820. https://doi.org/10.1103/PhysRev.37.815

Fridman, A., & Kennedy, L. A. (2004a). *Plasma Physics and Engineering*. Abingdon, UK: Taylor & Francis. https://doi.org/10.4324/9780203334874

Fridman, A., & Kennedy, L. A. (2004b). *Plasma Physics and Engineering*. Abingdon, UK: Taylor & Francis. https://doi.org/10.4324/9780203334874

Fridman, A., & Kennedy, L. A. (2004c). *Plasma Physics and Engineering*. Abingdon, UK: Taylor & Francis. https://doi.org/10.4324/9780203334874

Fu, Y., Verboncoeur, J. P., Christlieb, A. J., & Wang, X. (2017). Transition characteristics of low-pressure discharges in a hollow cathode. *Physics of Plasmas*, *24*(8), 83516. https://doi.org/10.1063/1.4997764

Fuh, C. A., Wu, W., & Wang, C. (2016). Microwave plasma-assisted ignition and flameholding in premixed ethylene/air mixtures. *Journal of Physics D: Applied Physics*, *49*(28), 285202. https://doi.org/10.1088/0022-3727/49/28/285202

Fujiwara, Y., Sakakita, H., Yamada, H., Yamagishi, Y., Itagaki, H., Kiyama, S., … Kim, J. (2016). Observations of multiple stationary striation phenomena in an atmospheric pressure neon plasma jet. *Japanese Journal of Applied Physics*, *55*(1), 10301. https://doi.org/10.7567/JJAP.55.010301

G. V. Gordeev. (1954). Low-frequency plasma oscillations. *Zh. Eksperim. I Teor. Fiz.*, *27*(1), 18.

Ganguly, B. N., & Parish, J. W. (2004). Absolute H atom density measurement in pure methane pulsed discharge. *Applied Physics Letters*, *84*(24), 4953–4955. https://doi.org/10.1063/1.1760888

Gentle, K. W. (1966). Moving Striations in the Argon Positive Column. I. Theory. *Physics of Fluids*, *9*(11), 2203. https://doi.org/10.1063/1.1761589

Gertsenshtein, M. E. (1952). No Title. *Zh. Eksp. Teor. Fiz.*, *22*.

Gnoffo, P. A., Gupta, R. N., & Shinn, J. L. (1989). Conservation Equations and Physical Models ’fOr Hypersonic Air Flows in Thermal and Chemical Nonequilibrium. Retrieved from https://ntrs.nasa.gov/archive/nasa/casi.ntrs.nasa.gov/19890006744.pdf

Go, D. B., Fisher, T. S., Garimella, S. V, & Bahadur, V. (2009). Planar microscale ionization devices in atmospheric air with diamond-based electrodes. *Plasma Sources Science and Technology*, *18*(3), 35004.

Go, D. B., & Venkattraman, A. (2014). Microscale gas breakdown: ion-enhanced field emission and the modified Paschen’s curve. *Journal of Physics D: Applied Physics*, *47*(50), 503001. https://doi.org/10.1088/0022-3727/47/50/503001

Gregório, J., Hoskinson, A. R., & Hopwood, J. (2015). Modeling of microplasmas from GHz to THz. *Journal of Applied Physics*, *118*(8), 83305. https://doi.org/10.1063/1.4928468

Haddad, G. I., East, J. R., & Eisele, H. (2003). Two-Terminal Active Devices for Terahertz Sources. *International Journal of High Speed Electronics and Systems*, *13*(2), 395–427. https://doi.org/10.1142/S0129156403001788

Hagelaar, G. J. M., & Pitchford, L. C. (2005). Solving the Boltzmann equation to obtain electron transport coefficients and rate coefficients for fluid models. *Plasma Sources Science and Technology*, *14*(4), 722–733. https://doi.org/10.1088/0963-0252/14/4/011

Han, J. (2013). Review of Major Directions in Non-Equilibrium Atmospheric Plasma Treatments in Medical, Biological, and Bioengineering Applications. *Plasma Medicine*, *3*(3), 175–243. https://doi.org/10.1615/PlasmaMed.2014012248

Hasan, N., Antao, D. S., & Farouk, B. (2014). DC negative corona discharge in atmospheric pressure helium: transition from the corona to the “normal” glow regime. *Plasma Sources Science and Technology*, *23*(3), 35013. https://doi.org/10.1088/0963-0252/23/3/035013

Hatori, S.; Shioda, S. (1974). Stabilization of Ionization Instability in an MHD Generator. *Journal of the Physical Society of Japan*, *36*(3).

He, S., Ouyang, J., He, F., & Jia, H. (2012). Self-pulsing operating mode of hollow cathode discharge in noble gas. *Physics of Plasmas*, *19*(2), 23504. https://doi.org/10.1063/1.3684222

Hong, J., Liu, Y., Zhang, B., Niu, X., & Han, L. (2015). A novel kind of TSV slurry with guanidine hydrochloride. *Journal of Semiconductors*, *36*(10), 106003. https://doi.org/10.1088/1674-4926/36/10/106003

Hsu, D. D., & Graves, D. B. (2003). Microhollow cathode discharge stability with flow and reaction. *Journal of Physics D: Applied Physics*, *36*(23), 2898–2907. https://doi.org/10.1088/0022-3727/36/23/006

I. D. Kaganovich, M. A. Fedotov, and L. D. T. (1994). Ionization instability of a Townsend discharge. *Zh. Tekh. Fiz.*, *64*(3).

I. M. Chapnik. (1957). No Title. *Zh. Tekhn. Fiz.*, *27*.

Ikeda, Y., Nishiyama, A., Katano, H., Kaneko, M., & Jeong, H. (2009). Research and Development of Microwave Plasma Combustion Engine (Part II: Engine Performance of Plasma Combustion Engine). https://doi.org/10.4271/2009-01-1049

Islam, T. (2012). THE MAGNETOVISCOUS-THERMAL INSTABILITY. *The Astrophysical Journal*, *746*(1), 8. https://doi.org/10.1088/0004-637X/746/1/8

Iza, F., & Hopwood, J. A. (2003). Low-power microwave plasma source based on a microstrip split-ring resonator. *IEEE Transactions on Plasma Science*, *31*(4), 782–787. https://doi.org/10.1109/TPS.2003.815470

Iza, F., & Hopwood, J. A. (2005). Self-organized filaments, striations and other nonuniformities in nonthermal atmospheric microwave excited microdischarges. *IEEE Transactions on Plasma Science*, *33*(2), 306–307. https://doi.org/10.1109/TPS.2005.845139

Iza, F., Kim, G. J., Lee, S. M., Lee, J. K., Walsh, J. L., Zhang, Y. T., & Kong, M. G. (2008). Microplasmas: Sources, Particle Kinetics, and Biomedical Applications. *Plasma Processes and Polymers*, *5*(4), 322–344. https://doi.org/10.1002/ppap.200700162

Jensen, K. F. (2005). Silicon-Based Microreactors. In *Microreactor Technology and*

Process Intensification ACS Symposium Series. American Chemical Society. https://doi.org/10.1021/bk-2005-0914.ch001

Ju, Y., Lefkowitz, J. K., Reuter, C. B., Won, S. H., Yang, X., Yang, S., … Chen, Q. (2016). Plasma Assisted Low Temperature Combustion. *Plasma Chemistry and Plasma Processing*, *36*(1), 85–105. https://doi.org/10.1007/s11090-015-9657-2

Kettner, M., Nauwerck, A., Spicher, U., Seidel, J., & Linkenheil, K. (2006). Microwave-based ignition principle for gasoline engines with direct injection and spray guided combustion system. *MTZ Worldwide*, *67*(6), 29–31. https://doi.org/10.1007/BF03227855

Kikuchi, T. (1921). On the Moving Striations in a Neon Tube. *Proceedings of the Royal Society A: Mathematical, Physical and Engineering Sciences*, *99*(698), 257–261. https://doi.org/10.1098/rspa.1921.0039

Kikuchi, T., Hasegawa, Y., & Shirai, H. (2004). Rf microplasma jet at atmospheric pressure: characterization and application to thin film processing. *Journal of Physics D: Applied Physics*, *37*(11), 1537–1543. https://doi.org/10.1088/0022-3727/37/11/005

Kim, W., Godfrey Mungal, M., & Cappelli, M. A. (2010). The role of in situ reforming in plasma enhanced ultra lean premixed methane/air flames. *Combustion and Flame*, *157*(2), 374–383. https://doi.org/10.1016/j.combustflame.2009.06.016

Kogelschatz, U. (2007). Applications of Microplasmas and Microreactor Technology. *Contributions to Plasma Physics*, *47*(1–2), 80–88. https://doi.org/10.1002/ctpp.200710012

Kolobov, V. I., & Fiala, A. (1994). Transition from a Townsend discharge to a normal discharge via two-dimensional modeling. *Physical Review E*, *50*(4), 3018–3032. https://doi.org/10.1103/PhysRevE.50.3018

Kolobov, V. I., & Tsendin, L. D. (1992). Analytic model of the cathode region of a short glow discharge in light gases. *Physical Review A*, *46*(12), 7837–7852. https://doi.org/10.1103/PhysRevA.46.7837

Kruger, C. H., Owano, T. G., Laux, C. O., & Zare, R. N. (1997). Nonequilibrium in Thermal Plasmas with Applications to Diamond Synthesis. *Le Journal de Physique IV*, *7*(C4), C4-67-C4-92. https://doi.org/10.1051/jp4:1997406

Kudryavtsev, A. A., & Tsendin, L. D. (2002). Townsend discharge instability on the right-hand branch of the Paschen curve. *Technical Physics Letters*, *28*(12), 1036–1039. https://doi.org/10.1134/1.1535495

Kukaev, E. N., Tsyganov, D. L., Zhukov, V. P., Starikovskaia, S. M., & Yu Starikovskii, A. (n.d.). DEFLAGRATION - TO - DETONATION CONTROL BY NON - EQUILIBRIUM GAS DISCHARGES AND ITS APPLICATIONS FOR PULSED DETONATION ENGINE. https://doi.org/10.2514/6.2004-870

Kushner, M. J. (2005). Modelling of microdischarge devices: plasma and gas dynamics. *Journal of Physics D: Applied Physics*, *38*(11), 1633–1643. https://doi.org/10.1088/0022-3727/38/11/001

Lazzaroni, C., & Chabert, P. (2011). Discharge resistance and power dissipation in the self-pulsing regime of micro-hollow cathode discharges. *Plasma Sources Science and Technology*, *20*(5), 55004. https://doi.org/10.1088/0963-0252/20/5/055004

Leo Esaki. (1960). A new device using the tunneling process in narrow p-n junctions. *Solid-State Electronics*, *1*(1), 13–21. https://doi.org/10.1016/0038-1101(60)90052-6

Li, C., Ebert, U., & Hundsdorfer, W. (2010). Spatially hybrid computations for streamer discharges with generic features of pulled fronts: I. Planar fronts. *Journal of Computational Physics*, *229*(1), 200–220. https://doi.org/10.1016/j.jcp.2009.09.027

Lieberman, D., Shepherd, J., Wang, F., & Gundersen, M. (2005). Characterization of a Corona Discharge Initiator Using Detonation Tube Impulse Measurements. In *43rd AIAA Aerospace Sciences Meeting and Exhibit*. Reston, Virigina: American Institute of Aeronautics and Astronautics. https://doi.org/10.2514/6.2005-1344

Lieberman, M. A., & Lichtenberg, A. J. (2005). *Principles of Plasma Discharges and Materials Processing*. Hoboken, NJ, USA: John Wiley & Sons, Inc. https://doi.org/10.1002/0471724254

Lin, L., & Wang, Q. (2015). Microplasma: A New Generation of Technology for Functional Nanomaterial Synthesis. *Plasma Chemistry and Plasma Processing*, *35*(6), 925–962. https://doi.org/10.1007/s11090-015-9640-y

Lindner, P. J., & Besser, R. S. (2012). A Microplasma Reactor for Chemical Process Intensification. *Chemical Engineering & Technology*, *35*(7), 1249–1256. https://doi.org/10.1002/ceat.201100684

Liu, D. X., Bruggeman, P., Iza, F., Rong, M. Z., & Kong, M. G. (2010). Global model of low-temperature atmospheric-pressure He + H_2O plasmas. *Plasma Sources Science and Technology*, *19*(2), 25018. https://doi.org/10.1088/0963-0252/19/2/025018

Loveless, A. M., & Garner, A. L. (2016). Generalization of scaling laws for gas breakdown to account for pressure. In *2016 IEEE International Conference on Plasma Science (ICOPS)* (pp. 1–1). IEEE. https://doi.org/10.1109/PLASMA.2016.7534000

Lymberopoulos, D. P., & Schieber, J. D. (1994). Stochastic dynamic simulation of the Boltzmann equation for electron swarms in glow discharges. *Physical Review E*, *50*(6), 4911–4919. https://doi.org/10.1103/PhysRevE.50.4911

M, A. (1843). No Title. *Ann. Chem. Phys.*, *7*(462).

Mahamud, R., & Farouk, T. (2014). Modeling of non-equilibrium and non-thermal plasma discharge in air: Three temperature modeling approach. *APS Gaseous Electronics Conference 2014, Abstract #MW1.044*. Retrieved from http://adsabs.harvard.edu/abs/2014APS..GECMW1044M

Mahamud, R., & Farouk, T. (2016). Suppression of self-pulsing regime of direct current driven microplasma discharges. *Applied Physics Letters*, *108*(20). https://doi.org/10.1063/1.4950730

Mahamud, R., & Farouk, T. I. (2013). Self-Pulsing Non-Equilibrium Plasma Discharge at Atmospheric and Higher Pressures. *APS Gaseous Electronics Conference 2013, Abstract #ET2.002*. Retrieved from http://adsabs.harvard.edu/abs/2013APS..GECET2002M

Mahamud, R., & Farouk, T. I. (2015). Modes of oscillation in dc driven high pressure microplasma discharges. In *ICOPS/BEAMS 2014 - 41st IEEE International Conference on Plasma Science and the 20th International Conference on High-Power Particle Beams*. https://doi.org/10.1109/PLASMA.2014.7012515

Mahamud, R., & Farouk, T. I. (2016). Ion kinetics and self pulsing in DC microplasma discharges at atmospheric and higher pressure. *Journal of Physics D: Applied Physics*, *49*(14), 145202. https://doi.org/10.1088/0022-3727/49/14/145202

Mahamud, R., Mobli, M., & Farouk, T. I. (2014). Modes of oscillation in a high pressure microplasma discharges. In *2014 IEEE 41st International Conference on Plasma*

Sciences (ICOPS) held with 2014 IEEE International Conference on High-Power Particle Beams (BEAMS) (pp. 1–6). IEEE. https://doi.org/10.1109/PLASMA.2014.7012760

Mani, S., Tharikaa, R., Ajith, S., Naveen, N., Vignesh, R., John, J., & Sanal Kumar, V. (2015). Influence of Starting Chamber Dynamics on Nozzle Flow Choking Time and the Liftoff Time of Dual-thrust Rockets. In *51st AIAA/SAE/ASEE Joint Propulsion Conference*. Reston, Virginia: American Institute of Aeronautics and Astronautics. https://doi.org/10.2514/6.2015-4178

Mariani, A., & Foucher, F. (2014). Radio frequency spark plug: An ignition system for modern internal combustion engines. *APPLIED ENERGY*, *122*, 151–161. https://doi.org/10.1016/j.apenergy.2014.02.009

Mcintyre, D. L., Thompson, G. J., & Smith, J. E. (2001). The Coaxial Cavity Resonator as a RF IC Engine Ignition Source. https://doi.org/10.4271/2001-01-0987

Mehran Keshe Tavakoli. (2005, October 20). Micro plasma reactor. Retrieved from https://www.google.com/patents/EP1770715A1

Mintoussov, E., Pancheshnyi, S., & Starikovskii, A. (2004). Propane-Air Flame Control by Non-Equilibrium Low-temperature Pulsed Nanosecond Barrier Discharge. In *42nd AIAA Aerospace Sciences Meeting and Exhibit*. Reston, Virigina: American Institute of Aeronautics and Astronautics. https://doi.org/10.2514/6.2004-1013

Miura, N., & Hopwood, J. (2012). Instability control in microwave-frequency microplasma. *The European Physical Journal D*, *66*(5), 143. https://doi.org/10.1140/epjd/e2012-20739-7

Mozetič, M., Primc, G., Vesel, A., Zaplotnik, R., Modic, M., Junkar, I., … Stana-Kleinschek, K. (2015). Application of extremely non-equilibrium plasmas in the processing of nano and biomedical materials. *Plasma Sources Science and Technology*, *24*(1), 15026. https://doi.org/10.1088/0963-0252/24/1/015026

Murakami, T., Okuno, Y., & Yamasaki, H. (2005). Suppression of ionization instability in a magnetohydrodynamic plasma by coupling with a radio-frequency electromagnetic field. *Applied Physics Letters*, *86*(19), 191502. https://doi.org/10.1063/1.1926410

Nedospasov, A. V. (1964). *Oscillations of a Positive-Column Plasma [in Russian]*.

Nedospasov, A. V. (1968). STRIATIONS. *Soviet Physics Uspekhi*, *11*(2), 174–187. https://doi.org/10.1070/PU1968v011n02ABEH003806

Nighan, W. L. (1977). Causes of thermal instability in externally sustained molecular discharges. *Physical Review A*, *15*(4), 1701–1720. https://doi.org/10.1103/PhysRevA.15.1701

Nijdam S, Bruggeman P, van V. E. M. and E. U. (2012). An Introduction to Nonequilibrium Plasmas at Atmospheric Pressure. In *Plasma chemistry and catalysis in gases and liquids*. Weinheim: Wiley.

O'Neill, W. J., Lee, D., Cofer, A. G., & Alexeenko, A. (2015). Dynamic Modeling and Experimental Validation of Thrust-stand for Micropropulsion Testing. In *51st AIAA/SAE/ASEE Joint Propulsion Conference*. Reston, Virginia: American Institute of Aeronautics and Astronautics. https://doi.org/10.2514/6.2015-4186

Oleson, N. L., & Cooper, A. W. (1968). Moving Striations (pp. 155–278). https://doi.org/10.1016/S0065-2539(08)60973-7

Pancheshnyi, S. V., Lacoste, D. A., Bourdon, A., & Laux, C. O. (2006). Ignition of Propane–Air Mixtures by a Repetitively Pulsed Nanosecond Discharge. *IEEE Transactions on Plasma Science*, *34*(6), 2478–2487. https://doi.org/10.1109/TPS.2006.876421

Park, S.-J., & Eden, J. G. (2002). 13–30 micron diameter microdischarge devices: Atomic ion and molecular emission at above atmospheric pressures. *Applied Physics Letters*, *81*(22), 4127–4129. https://doi.org/10.1063/1.1520707

Paschen, F. (1889). Ueber die zum Funkenübergang in Luft, Wasserstoff und Kohlensäure bei verschiedenen Drucken erforderliche Potentialdifferenz. *Annalen Der Physik*, *273*(5), 69–96. https://doi.org/10.1002/andp.18892730505

Pekarek, L. (1968). IONIZATION WAVES (STRIATIONS) IN A DISCHARGE PLASMA. *Soviet Physics Uspekhi*, *11*(2), 188–208. https://doi.org/10.1070/PU1968v011n02ABEH003809

Pekárek, L. (1957). Theory of Moving Striations. *Physical Review*, *108*(6), 1371–1372. https://doi.org/10.1103/PhysRev.108.1371

Peng, P., Cheng, Y., Hatzenbeller, R., Addy, M., Zhou, N., Schiappacasse, C., … Ruan, R. (2017). Ru-based multifunctional mesoporous catalyst for low-pressure and non-thermal plasma synthesis of ammonia. *International Journal of Hydrogen Energy*, *42*(30), 19056–19066. https://doi.org/10.1016/j.ijhydene.2017.06.118

Peřina, V., Rohlena, K., & Růžička, T. (1975). Ionization waves (moving striations) in a low pressure helium discharge — results of measurements compared with a direct solution of the electron Boltzmann equation. *Czechoslovak Journal of Physics*, *25*(6), 660–676. https://doi.org/10.1007/BF01591021

Pertl, F. A., Clarke, M. A., & Smith, J. E. (2011). Design of a compact quarter wave coaxial cavity resonator for plasma ignition applications. *International Journal of Microwave and Wireless Technologies*, *3*(4), 485–491. https://doi.org/10.1017/S1759078711000493

Petit, J.-P.; Billiotte, M. (1981). Method for suppressing the Velikhov instability. In *French Academy of Sciences.* (pp. 1115–1118).

Petit, J.-P.; Valensi, J. (1969). Growth rate of electrothermal instability and critical Hall parameter in closed-cycle MHD generators when the electron mobility is variable. In *French Academy of Sciences (269)* (pp. 365–367).

Petit, J.-P. (1969). Rate instability in a Hall generator with non-equilibrium ionization. In *Série A (in French). 268* (pp. 906–909).

Petrović, Z. L., & Phelps, A. V. (1993a). Oscillations of low-current electrical discharges between parallel-plane electrodes. I. dc discharges. *Physical Review E*, *47*(4), 2806–2815. https://doi.org/10.1103/PhysRevE.47.2806

Petrović, Z. L., & Phelps, A. V. (1993b). Oscillations of low-current electrical discharges between parallel-plane electrodes. I. dc discharges. *Physical Review E*, *47*(4), 2806–2815. https://doi.org/10.1103/PhysRevE.47.2806

Petrović, Z. L., & Phelps, A. V. (1993c). Oscillations of low-current electrical discharges between parallel-plane electrodes. I. dc discharges. *Physical Review E*, *47*(4), 2806–2815. https://doi.org/10.1103/PhysRevE.47.2806

Petrović, Z. L., & Phelps, A. V. (1997). Temporal and constriction behavior of low-pressure, cathode-dominated argon discharges. *Physical Review E*, *56*(5), 5920–5931. https://doi.org/10.1103/PhysRevE.56.5920

Petrovic, Z. L., Stefanovic, I., Vrhovac, S., & Zivkovic, J. (1997). Negative Differential Resistance, Oscillations and Constrictions of Low Pressure, Low Current Discharges. *Le Journal de Physique IV*, *7*(C4), C4-341-C4-352. https://doi.org/10.1051/jp4:1997428

Phelps, A. V., Petrović, Z. L., & Jelenković, B. M. (1993). Oscillations of low-current electrical discharges between parallel-plane electrodes. III. Models. *Physical Review E*, *47*(4), 2825–2838. https://doi.org/10.1103/PhysRevE.47.2825

Pilla, G., Galley, D., Lacoste, D. A., Lacas, F., Veynante, D., & Laux, C. O. (2006). Stabilization of a Turbulent Premixed Flame Using a Nanosecond Repetitively Pulsed Plasma. *IEEE Transactions on Plasma Science*, *34*(6), 2471–2477. https://doi.org/10.1109/TPS.2006.886081

Pineda, D. I., Wolk, B., Sennott, T., Chen, J.-Y., Dibble, R. W., & Singleton, D. (2015). Nanosecond Pulsed Discharge in a Lean Methane-Air Mixture. In *Laser Ignition Conference* (p. T5A.2). Washington, D.C.: OSA. https://doi.org/10.1364/LIC.2015.T5A.2

Qin, Y., He, F., Jiang, X. X., Xie, K., & Ouyang, J. T. (2014). Self-pulsing of hollow cathode discharge in various gases. *Physics of Plasmas*, *21*(7), 73501. https://doi.org/10.1063/1.4885640

Qin, Y., Xie, K., Zhang, Y., & Ouyang, J. (2016). Self-pulsing in a low-current hollow cathode discharge: From Townsend to glow discharge. *Physics of Plasmas*, *23*(2), 23501. https://doi.org/10.1063/1.4941281

Rafatov, I., Bogdanov, E. A., & Kudryavtsev, A. A. (2012). On the accuracy and reliability of different fluid models of the direct current glow discharge. *Physics of Plasmas*, *19*(3), 33502. https://doi.org/10.1063/1.3688875

Räisänen, A. V., & Lehto, A. (2003). *Radio engineering for wireless communication and sensor applications*. Artech House.

Raizer, Y. P. (1991). *Gas Discharge Physics*. (J. E. Allen, Ed.). Berlin, Heidelberg: Springer Berlin Heidelberg. https://doi.org/10.1007/978-3-642-61247-3

Raizer, Y. P., Gurevich, E. L., & Mokrov, M. S. (2006). Self-sustained oscillations in a low-current discharge with a semiconductor serving as a cathode and ballast resistor: II. Theory. *Technical Physics*, *51*(2), 185–197.

https://doi.org/10.1134/S1063784206020071

Ricci Castro, A. H., Kodaira, F. V. P., Prysiazhnyi, V., Mota, R. P., & Kostov, K. G. (2017). Deposition of thin films using argon/acetylene atmospheric pressure plasma jet. *Surface and Coatings Technology*, *312*, 13–18. https://doi.org/10.1016/j.surfcoat.2016.07.036

Rohlena, K., Růžička, T., & Pekárek, L. (1972). A theory of the low current ionization waves (striations) in inert gases. *Czechoslovak Journal of Physics*, *22*(10), 920–937. https://doi.org/10.1007/BF01690199

Roth, J. R. (1995). *Industrial plasma engineering*. Institute of Physics Pub. Retrieved from https://www.crcpress.com/Industrial-Plasma-Engineering-Volume-1-Principles/Reece-Roth/p/book/9780750303170

Rousseau, A., & Aubert, X. (2006). Self-pulsing microplasma at medium pressure range in argon. *Journal of Physics D: Applied Physics*, *39*(8), 1619–1622. https://doi.org/10.1088/0022-3727/39/8/021

Sakiyama, Y., & Graves, D. B. (2007a). Nonthermal atmospheric rf plasma in one-dimensional spherical coordinates: Asymmetric sheath structure and the discharge mechanism. *Journal of Applied Physics*, *101*(7), 73306. https://doi.org/10.1063/1.2715745

Sankaran, R. M., & Giapis, K. P. (2001). Maskless etching of silicon using patterned microdischarges. *Applied Physics Letters*, *79*(5), 593–595. https://doi.org/10.1063/1.1388867

Sankaran, R. M., & Giapis, K. P. (2003). High-pressure micro-discharges in etching and deposition applications. *Journal of Physics D: Applied Physics*, *36*(23), 2914–2921. https://doi.org/10.1088/0022-3727/36/23/008

Schenk, O., & Gartner, K. (2004). Solving unsymmetric sparse systems of linear equations with PARADISO. *Journal of Future Generation Computer Systems*, *20*(3), 475–487.

Schoenbach, K. H., El-Habachi, A., Moselhy, M. M., Shi, W., & Stark, R. H. (2000). Microhollow cathode discharge excimer lamps. *Physics of Plasmas*, *7*(5), 2186–2191. https://doi.org/10.1063/1.874039

Schoenbach, K. H., El-Habachi, A., Shi, W., & Ciocca, M. (1997). High-pressure hollow cathode discharges. *Plasma Sources Science and Technology*, *6*(4), 468–477. https://doi.org/10.1088/0963-0252/6/4/003

Schoenbach, K. H., Moselhy, M., Shi, W., & Bentley, R. (2003). Microhollow cathode discharges. *Journal of Vacuum Science & Technology A: Vacuum, Surfaces, and Films*, *21*(4), 1260–1265. https://doi.org/10.1116/1.1565154

Schutze, A., Jeong, J. Y., Babayan, S. E., Jaeyoung Park, Selwyn, G. S., & Hicks, R. F. (1998). The atmospheric-pressure plasma jet: a review and comparison to other plasma sources. *IEEE Transactions on Plasma Science*, *26*(6), 1685–1694. https://doi.org/10.1109/27.747887

Shapiro, G. I.; Nelson, A. H. (n.d.). Stabilization of ionization instability in a variable electric field. *Pis'ma v Zhurnal Tekhnischeskoi Fiziki. Akademiia Nauk SSSR*, *4*(12), 393–396.

Shneider, M. N., Mokrov, M. S., & Milikh, G. M. (2012). Dynamic contraction of the positive column of a self-sustained glow discharge in molecular gas. *Physics of Plasmas*, *19*(3), 33512. https://doi.org/10.1063/1.3694913

Šijačić, D. D., & Ebert, U. (2002). Transition from Townsend to glow discharge: Subcritical, mixed, or supercritical characteristics. *Physical Review E*, *66*(6), 66410. https://doi.org/10.1103/PhysRevE.66.066410

Šijačić, D. D., Ebert, U., & Rafatov, I. (2005). Oscillations in dc driven barrier discharges: Numerical solutions, stability analysis, and phase diagram. *Physical Review E*, *71*(6), 66402. https://doi.org/10.1103/PhysRevE.71.066402

Smirnov, B. M. (Boris M. (2001). *Physics of ionized gases*. John Wiley.

Solbes, A. (1968). A quasi linear plane wave study of electrothermal instabilities. In *Electricity from MHD: Proceedings of a Symposium on magnetohydrodynamic electrical power generation. Vol. I. Warsaw, Poland: International Atomic Energy Agency*.

Spottiswoode, W. (1874). Experiments on Stratification in Electrical Discharges through Rarefied Gases. *Proceedings of the Royal Society of London*, *23*(156–163), 455–462. https://doi.org/10.1098/rspl.1874.0069

Spottiswoode, W. (1876). On Stratified Discharges.--II. Observations with a Revolving Mirror. *Proceedings of the Royal Society of London*, *25*(171–178), 73–82. https://doi.org/10.1098/rspl.1876.0017

Staack, D., Farouk, B., Gutsol, A., & Fridman, A. (2005a). Characterization of a dc atmospheric pressure normal glow discharge. *Plasma Sources Science and Technology*, *14*(4), 700–711. https://doi.org/10.1088/0963-0252/14/4/009

Staack, D., Farouk, B., Gutsol, A., & Fridman, A. (2007). Thin Film Deposition using Atmospheric Pressure Microplasmas. In *2007 IEEE Pulsed Power Plasma Science Conference* (pp. 833–833). IEEE. https://doi.org/10.1109/PPPS.2007.4346139

Staack, D., Farouk, B., Gutsol, A., & Fridman, A. (2009a). Stabilization of the ionization overheating thermal instability in atmospheric pressure microplasmas. *Journal of Applied Physics*, *106*(1), 13303. https://doi.org/10.1063/1.3143781

Starikovskaia, S. M., & Starikovskii, A. Y. (2010). Plasma-Assisted Ignition and Combustion. In *Handbook of Combustion*. Weinheim, Germany: Wiley-VCH Verlag GmbH & Co. KGaA. https://doi.org/10.1002/9783527628148.hoc075

Starikovskiy, A., Aleksandrov, N., & Rakitin, A. (n.d.). Plasma-assisted ignition and deflagration-to-detonation transition. *Philosophical Transactions: Mathematical, Physical and Engineering Sciences*. Royal Society. https://doi.org/10.2307/41348287

Stefanović, I., Kuschel, T., Škoro, N., Marić, D., Petrović, Z. L., & Winter, J. (2011a). Oscillation modes of direct current microdischarges with parallel-plate geometry. *Journal of Applied Physics*, *110*(8), 83310. https://doi.org/10.1063/1.3656449

Stefanović, I., Kuschel, T., Škoro, N., Marić, D., Petrović, Z. L., & Winter, J. (2011b). Oscillation modes of direct current microdischarges with parallel-plate geometry. *Journal of Applied Physics*, *110*(8), 83310. https://doi.org/10.1063/1.3656449

Stefanović, I., Kuschel, T., Škoro, N., Marić, D., Petrović, Z. L., & Winter, J. (2011c). Oscillation modes of direct current microdischarges with parallel-plate geometry. *Journal of Applied Physics*, *110*(8), 83310. https://doi.org/10.1063/1.3656449

Stefanović, I., & Petrović, Z. L. (1997). Volt Ampere Characteristics of Low Current DC Discharges in Ar, H_2, CH_4 and SF_6. *Japanese Journal of Applied Physics*, *36*(Part 1, No. 7B), 4728–4732. https://doi.org/10.1143/JJAP.36.4728

Stevens, C. A., Pertl, F. A., Hoke, J. L., Schauer, F. R., & Smith, J. E. (n.d.). Comparative testing of a novel microwave ignition source, the quarter wave coaxial cavity igniter. https://doi.org/10.1177/0954407011411389

Stoffels, E., Flikweert, A. J., Stoffels, W. W., & Kroesen, G. M. W. (2002). Plasma needle: a non-destructive atmospheric plasma source for fine surface treatment of (bio)materials. *Plasma Sources Science and Technology*, *11*(4), 383–388. https://doi.org/10.1088/0963-0252/11/4/304

Suhr, H. (1989). Applications and trends of nonequilibrium plasma chemistry with organic and organometallic compounds. *Plasma Chemistry and Plasma Processing*, *9*(S1), 7S–28S. https://doi.org/10.1007/BF01015871

Surendra, M., Graves, D. B., & Jellum, G. M. (1990). Self-consistent model of a direct-current glow discharge: Treatment of fast electrons. *Physical Review A*, *41*(2), 1112–1125. https://doi.org/10.1103/PhysRevA.41.1112

Swain, D. W. (1971). Moving Striations in a Low-Pressure Argon Discharge. *Physics of Fluids*, *14*(7), 1383. https://doi.org/10.1063/1.1693618

Tachibana, K. (2006). Current status of microplasma research. *IEEJ Transactions on Electrical and Electronic Engineering*, *1*(2), 145–155. https://doi.org/10.1002/tee.20031

Takashima, K., Yin, Z., & Adamovich, I. V. (2012). Measurements and kinetic modeling of energy coupling in volume and surface nanosecond pulse discharges. *Plasma Sources Science and Technology*, *22*(1), 15013. https://doi.org/10.1088/0963-0252/22/1/015013

Taylan, O., & Berberoglu, H. (2014). Electrical characterization and an equivalent circuit model of a microhollow cathode discharge reactor. *Journal of Applied Physics*, *116*(4), 43302. https://doi.org/10.1063/1.4891250

Tholeti, S. S., Shivkumar, G., & Alexeenko, A. A. (2016). Field emission microplasma actuation for microchannel flows. *Journal of Physics D: Applied Physics*, *49*(21), 215203. https://doi.org/10.1088/0022-3727/49/21/215203

Thomson, J. J. (1909). LII. *On striations in the electric discharge*. *Philosophical Magazine Series 6*, *18*(106), 441–451. https://doi.org/10.1080/14786441008636720

Thomson, J. J. (1929). I. *On striations, the cathode dark space, and the negative glow in the electric discharge. The London, Edinburgh, and Dublin Philosophical Magazine and Journal of Science, 8*(48), 1–29. https://doi.org/10.1080/14786440708564852

Tochikubo, F., Shirai, N., & Uchida, S. (2011). Simulation of Atmospheric Pressure Direct Current Glow Discharge along a Miniature Helium Flow in Nitrogen. *Applied Physics Express, 4*(5), 56001. https://doi.org/10.1143/APEX.4.056001

Togai, K. (2015). *KINETIC MODELING AND SENSITIVITY ANALYSIS OF PLASMA-ASSISTED COMBUSTION*. Retrieved from https://search.proquest.com/openview/43777dea2e6ec59e1c2019e384a81d5e/1?pq-origsite=gscholar&cbl=18750&diss=y

Togai, K., Tsolas, N., & Yetter, R. A. (2016). Kinetics of plasma-assisted oxidation of methane. In *54th AIAA Aerospace Sciences Meeting*. Reston, Virginia: American Institute of Aeronautics and Astronautics. https://doi.org/10.2514/6.2016-0192

Tropina, A. A., Kuzmenko, A. P., Marasov, S. V., & Vilchinsky, D. V. (2014). Ignition System Based on the Nanosecond Pulsed Discharge. *IEEE Transactions on Plasma Science, 42*(12), 3881–3885. https://doi.org/10.1109/TPS.2014.2339654

U Ebert, F Brau, G Derks, W Hundsdorfer, C-Y Kao, C Li, A Luque, B Meulenbroek, S Nijdam, V. R. (2010). Density models for streamer discharges: beyond cylindrical symmetry and homogeneous media. https://doi.org/10.1016/j.jcp.2011.04.019

U Ebert1, 2, F Brau3, G Derks4, W Hundsdorfer1, C-Y Kao5, C Li2, A Luque6, B Meulenbroek7, S Nijdam2, V. R. (2008). Numerical simulation of filamentary discharges with parallel adaptive mesh refinement. *Journal of Computational Physics, 227*(13), 6574–6590. https://doi.org/10.1016/J.JCP.2008.03.020

Velikhov, E. P.; Dykhne, A. M.; Shipuk, I. Y. (1965). Ionization instability of a plasma with hot electrons. In *7th International Conference on Ionization Phenomena in Gases. Belgrade, Yugoslavia*.

Velikhov, E. P.; Dykhne, A. M. (1963). Plasma turbulence due to the ionization instability in a strong magnetic field. In *6th International Conference on Phenomena in Ionized Gases,Paris, France* (p. 511).

Velikhov, E. P., Kovalev, A. S., & Rakhimov, A. T. (1987). Physical phenomena in a gas-discharge plasma. *Moscow, Izdatel'stvo Nauka, 1987, 160 P. In Russian.*

Retrieved from http://adsabs.harvard.edu/abs/1987MoIzN....Q....V

Vitruk, P. P., Baker, H. J., & Hall, D. R. (1992). The characteristics and stability of high power transverse radio frequency discharges for waveguide CO_2 slab laser excitation. *Journal of Physics D: Applied Physics*, *25*(12), 1767–1776. https://doi.org/10.1088/0022-3727/25/12/012

Vlasov, A. A. (1968). THE VIBRATIONAL PROPERTIES OF AN ELECTRON GAS. *Soviet Physics Uspekhi*, *10*(6), 721–733. https://doi.org/10.1070/PU1968v010n06ABEH003709

Walsh, J. L., Iza, F., Janson, N. B., Law, V. J., & Kong, M. G. (2010). Three distinct modes in a cold atmospheric pressure plasma jet. *Journal of Physics D: Applied Physics*, *43*(7), 75201. https://doi.org/10.1088/0022-3727/43/7/075201

Wang, F., Jiang, C., Kuthi, A., Gundersen, M., Sinibaldi, J., Brophy, C., & Lee, L. (2004). Transient Plasma Ignition of Hydrocarbon-Air Mixtures in Pulse Detonation Engines. In *42nd AIAA Aerospace Sciences Meeting and Exhibit*. Reston, Virigina: American Institute of Aeronautics and Astronautics. https://doi.org/10.2514/6.2004-834

Wang, Q., Economou, D. J., & Donnelly, V. M. (2006). Simulation of a direct current microplasma discharge in helium at atmospheric pressure. *Journal of Applied Physics*, *100*(2), 23301. https://doi.org/10.1063/1.2214591

Wang, Q., Sun, J., Zhang, J., Liu, L., & Wang, D. (2013). Improving the homogeneity of alternating current-drive atmospheric pressure dielectric barrier discharges in helium with an additional low-amplitude radio frequency power source: A numerical study. *Physics of Plasmas*, *20*(4), 43511. https://doi.org/10.1063/1.4799824

Watanabe, S., & Oleson, N. L. (1955). Traveling Density Waves in Positive Columns. *Physical Review*, *99*(6), 1701–1704. https://doi.org/10.1103/PhysRev.99.1701

Wester, R., Seiwert, S., & Wagner, R. (1991). Theoretical and experimental investigations of the filamentation of high-frequency excited CO_2 laser discharges. *Journal of Physics D: Applied Physics*, *24*(10), 1796–1802. https://doi.org/10.1088/0022-3727/24/10/013

Wirz, R., Mueller, J., Gale, M., & Marrese, C. (2004). Miniature Ion Thruster for Precision Formation Flying. In *40th AIAA/ASME/SAE/ASEE Joint Propulsion*

Conference and Exhibit. Reston, Virigina: American Institute of Aeronautics and Astronautics. https://doi.org/10.2514/6.2004-4115

Wolk, B., DeFilippo, A., Chen, J.-Y., Dibble, R., Nishiyama, A., & Ikeda, Y. (2013). Enhancement of flame development by microwave-assisted spark ignition in constant volume combustion chamber. *Combustion and Flame*, *160*(7), 1225–1234. https://doi.org/10.1016/j.combustflame.2013.02.004

Wormeester, G., Nijdam, S., & Ebert, U. (2011). Feather-Like Structures in Positive Streamers Interpreted as Electron Avalanches. *Japanese Journal of Applied Physics*, *50*(8S1), 08JA01. https://doi.org/10.7567/JJAP.50.08JA01

Wu, Y., & Lieberman, M. A. (1998). A traveling wave-driven, inductively coupled large area plasma source. *Applied Physics Letters*, *72*(7), 777–779. https://doi.org/10.1063/1.120890

Wullner A. (1874). No Title. *Prog. Ann. Phys.*, *32*.

Xu, L., Garner, A. L., Tao, B., & Keener, K. M. (2017). Microbial Inactivation and Quality Changes in Orange Juice Treated by High Voltage Atmospheric Cold Plasma. *Food and Bioprocess Technology*, *10*(10), 1778–1791. https://doi.org/10.1007/s11947-017-1947-7

Xu, R., & Kunz, M. W. (2016). Linear Vlasov theory of a magnetised, thermally stratified atmosphere. https://doi.org/10.1017/S0022377816000908

Xu, X. "Peter," & Kushner, M. J. (1998). Multiple microdischarge dynamics in dielectric barrier discharges. *Journal of Applied Physics*, *84*(8), 4153–4160. https://doi.org/10.1063/1.368629

Yoshiki, H., & Horiike, Y. (2001). Capacitively Coupled Microplasma Source on a Chip at Atmospheric Pressure. *Japanese Journal of Applied Physics*, *40*(Part 2, No. 4A), L360–L362. https://doi.org/10.1143/JJAP.40.L360

Zeleny, J., Physics Labqratqry, S., & Univfrsity, Y. (n.d.). ON THE POTENTIAL RELATIONS IN THE STRIATED POSITIUE COLUMN OF ELECTRICAL DISCHARGES THROUGH HYDROGEN. Retrieved from https://journals.aps.org/pr/pdf/10.1103/PhysRev.35.699

Zhang, C., Shao, T., Ren, C., Yan, P., & Niu, Z. (2016). Mode transition in microsecond-pulse gliding discharges at atmospheric pressure. In *2016 IEEE International Power Modulator and High Voltage Conference (IPMHVC)* (pp. 572–575). IEEE. https://doi.org/10.1109/IPMHVC.2016.8012890

Zhang, Z., Petersen, J., & Shneider, M. (2010). Microplasma Electron Number Density Measurement by Resonant Coherent Microwave Rayleigh Scattering. In *48th AIAA Aerospace Sciences Meeting Including the New Horizons Forum and Aerospace Exposition*. Reston, Virigina: American Institute of Aeronautics and Astronautics. https://doi.org/10.2514/6.2010-858

Zhu, W., & Lopez, J. L. (2012). A dc non-thermal atmospheric-pressure plasma microjet. *Plasma Sources Science and Technology*, *21*(3), 34018. https://doi.org/10.1088/0963-0252/21/3/034018

APPENDIX A

THREE TEMPERATURE MODELING APPROACH FOR DIATOMIC PLASMA DISCHARGES MODELING

BACKGROUND

The rapid progress in atmospheric pressure non-thermal plasma discharge has made air to be a preferable choice for feed gas. Despite the ease of operation of such discharges in air, the preference of air provides added complexity to modeling and simulations in terms of kinetics and different temperature modes. In addition, the energy cascade in classical low temperature plasma is simpler. However, high pressure nonthermal plasma discharges have a much different cascade involving the vibrational states in transferring the electron energy to the translational model. The diatomic molecules have three distinctive partition function, these as rotational, vibrational, and translational temperature. In this section a simplified method to model three temperature in diatomic gas discharges in proposed based on three energy conservation equation and energy transferring mechanism between them. This approach is often used in modeling air flows in thermal and chemical nonequilibrium in hypersonic reentry configuration (Boyd, 2007; Gnoffo, Gupta, & Shinn, 1989).

MODELING APPROACH

The three-temperature model assumes that three temperatures can describe the partitioning of energy among the translational, rotational, vibrational, and electronic modes in all species. This section describes a brief description of the three temperature modeling approach which can be useful to obtain the three temperature in diatomic gas plasma discharges, such as air or N_2. One of the primary assumption of our three temperature model is to assume a one temperature T, which characterize heavy particle translational and molecular rotational energies. This is in accordance with the Park two temperature model which is based on the knowledge that the energy exchange between translational and the rotational mode is very fast. The primary modeling assumption of our three temperature modeling are as follows:

- Continuum-based modeling approach was taken into account
- Neutral particles and ions defined by a single translational temperature, vibrationally excited species defined by a single vibrational temperature, and electron with an electronic temperature
- The species continuity equations describe the conservation equations for different species in the plasma (electrons, ions, radicals, and neutrals) with a drift-diffusion approximation for the fluxes
- The electrostatic potential in the plasma model is obtained by solving the Poisson's equation, and an external circuit model is coupled with the plasma model to vary the supply of the plasma discharge

GOVERNING EQUATIONS

A multiphysics modeling approach was undertaken which similar to other model comprises plasma dynamics model, circuit model, gas phase reaction kinetics, surface reaction, and energy equation. Plasma dynamics model solve the species transport (electrons, ions and neutral), electric field, and electron energy equations. The conservation equation for the electrons and the ions and the neutrals are defined by the continuity equation. The drift diffusion approximation was used for flux definition. The detailed of those equation are described in Chapter 2. In this chapter only the energy equation part will be discussed which is the major part of this study.

The basic of energy equation is to solve the three separate energy conservation equation with the appropriate mode coupling option.

The first energy equation to solve is the electron energy equation as shown below:

$$\frac{\partial}{\partial t}(n_e\varepsilon)+\nabla.\left[n_e\varepsilon\mu_\varepsilon\vec{E}-D_\varepsilon\nabla(n_e\varepsilon)\right]=\vec{j}_e.\vec{E}-\sum_j\Delta E_j K_i-3\frac{m_e}{m_{neutral}}K_{el}k_B(T_e-T) \qquad \text{(A1)}$$

ΔE_j The energy loss due to inelastic collision. The first term in the right hand side represents the energy gain due to electron joule heating and the second and third term represents the energy loss due to inelastic and elastic collisions respectively.

In this model the rotational mode of temperature was assumed to be in thermal equilibrium with the translational temperature. Therefore, a single energy equation was solved to obtain the translational temperature.

$$\frac{\partial(\rho c_p T_g)}{\partial t} = \nabla \cdot (\kappa_g \nabla T_g) + Q_k + \sum_i \vec{j}_i \cdot \vec{E} + 3\frac{m_e}{m_{neutral}} K_{el} k_B (T_e - T) + [\text{vibrational} - \text{neutral} - \text{relaxation}] \quad \text{(A2)}$$

The vibrational to translational relaxation term can be expressed as

$$[\text{vibrational} - \text{neutral} - \text{relaxation}] = \sum \frac{\rho_s}{\langle \tau_s \rangle} C_v^s (T - T_v) \quad \text{(A3)}$$

Here τ_s is the characteristic relaxation time for vibrational neutral energy, C_V^S is the specific heat at constant volume for species s for translational energy, T and T_v are the translational and vibrational temperature respectively.

The simplified vibrational energy equation considered for the modeling is similar to the translational energy equation. In addition it comprises the relaxation energy exchange between vibrational and translational mode, the relaxation energy exchange between vibrational and electronic modes, and the vibrational energy lost or gained due to molecular depletion (dissociation) or production (recombination).

$$\frac{\partial(\rho c_p T_v)}{\partial t} = \nabla \cdot (\kappa_v \nabla T_v) + \dot{Q}_k + \sum \frac{\rho_s}{\langle \tau_{es} \rangle} C_v^s (T_e - T_v) + [\text{vibrational} - \textit{translational} - \text{relaxation}] \quad \text{(A4)}$$

Where,

η_v: Thermal conductivity for vibrational energy due to collisions between molecules and other particles

τ_{es}: Characteristic relaxation time for electron vibrational energy exchange

Q_k : Energy loss or gain due to molecular depletion (dissociation or production (recombination)

The vibrational to electronic relaxation term can be expressed as

$$[\text{Vibrational} - \textit{Electronic} - \text{relaxation}] = \sum \frac{\rho_s}{\langle \tau_{es} \rangle} C_v^s (T_e - T_v) \quad \text{(A5)}$$

Here τ_{es} is the characteristic relaxation time for electronic-vibrational (e - V) process, C_V^S is the specific heat at constant volume for species s for vibrational energy, T_e is the electronic temperature.

η_v : Thermal conductivity for vibrational energy due to collisions between molecules and other particles

The source term in the neutral energy balance equation

$$S_{en} = \sum_n (E_n + FC_n + GP_n) \quad \text{(A6)}$$

E_n : Energy exchange due to elastic collision

FC_n : Heating due to Frank Condon effect

GP_n : Heating due to gas phase thermochemistry

$$FC_n = \sum_r k_r N_e N_n \Delta E_r \quad \text{(A7)}$$

The source term in the electron energy balance equation

$$S_{en} = \sum_{n} (E_n + FC_n + IE_n + GP_n) \quad \text{(A8)}$$

E_n : Energy exchange due to elastic collision

FC_n : Heating due to Frank Condon effect

IE_n : Electron impact vibrational excitation of neutral molecules

GP_n : Heating due to gas phase thermochemistry

BOUNDARY CONDITION

To solve the continuity and mass conservation equation, the flux boundary condition are provided for the electron and the ions. The flux boundary condition comprises both the drift and the thermal flux. The detailed of the equation is described in Chapter 3 in the numerical modeling part. For the boundary condition of the vibration ally excited species the Boltzmann distribution of the vibrational excited species was employed, such as

$$T_{vibrational} = -h\omega / \log(N_{2v} / N_2) \quad \text{(A9)}$$

Where N_{2v} and N_2 are the vibrational and neutral number densities, respectively. $-hw$ is the excitation energy for the level of excitation of N_{2v}. It was taken as 0.29 eV which corresponds to the first level of excitation of N_{2v} particle.

REACTION KINETICS AND NEOMERICAL MODELING

The reaction kinetics of the study is similar to the one that was developed in Chapter 6. However, instead of Biagi based dataset, Phelps based cross sectional data was used for the three temperature modeling. The simulation was performed in an attempt to verify the three temperature model and not to capture the striations in the positive column. The simulation of striations required a precise description of the cross sectional data and computationally expensive process.

A one dimensional model is developed based on finite element method (FEM) to study the three temperature mathematical model which is coupled with the plasma discharge model and the external circuit model.

RESULTS & DISCUSSION

The numerical model was first used to capture the normal glow discharge mode which shows cathode fall region, faraday dark space, and the positive column region. A representation of normal glow discharge is shown in Figure A.1. The maximum electron number density in cathode fall region was 2.5×10^{19} ($1/m^3$), and the number density in the positive column region was obtained as 1.8×10^{19} ($1/m^3$).

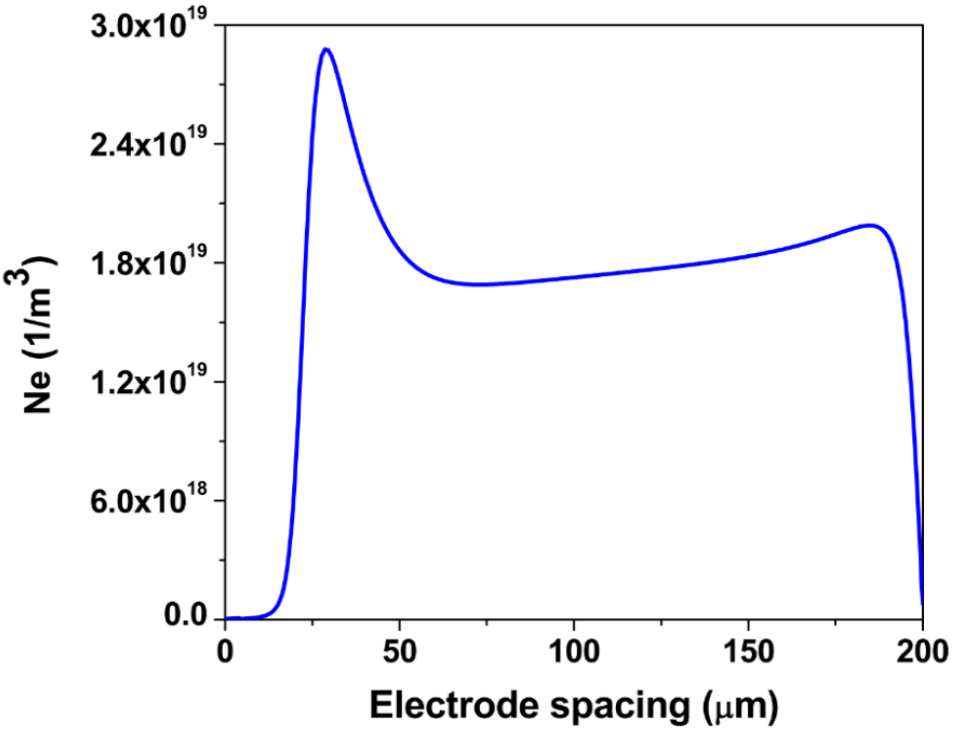

Figure A.1 Quasi steady electron number density (j_d = 8 A/cm^2 V_d= 195 V)

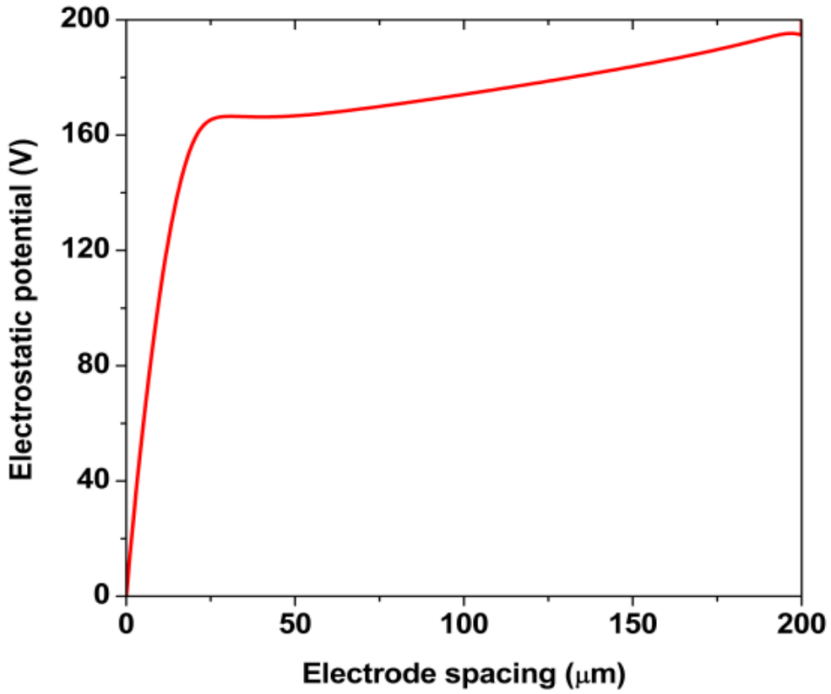

Figure A.2 Quasi steady electro static potential distribution (j_d = 8 A/cm^2 V_d = 195 V)

The electric potential for the baseline condition is presented in Figure A.2 with almost flat voltage line in the positive column. The voltage drop in the positive column is in the range of ~40 V which represents a almost constant voltage drop in the positive column and stronger secondary emission coefficient dependent cathode voltage drop. Similarly, the vibrational number density for the first two vibrational level is presented in Figure A.3, where the vibrational number density at the first level is higher than the vibrational number density at the second stage. This is due a lower level of excitation energy of the first vibrational level. Therefore, the population number densities of the vibrational level decreases with the increment of vibrational stages.

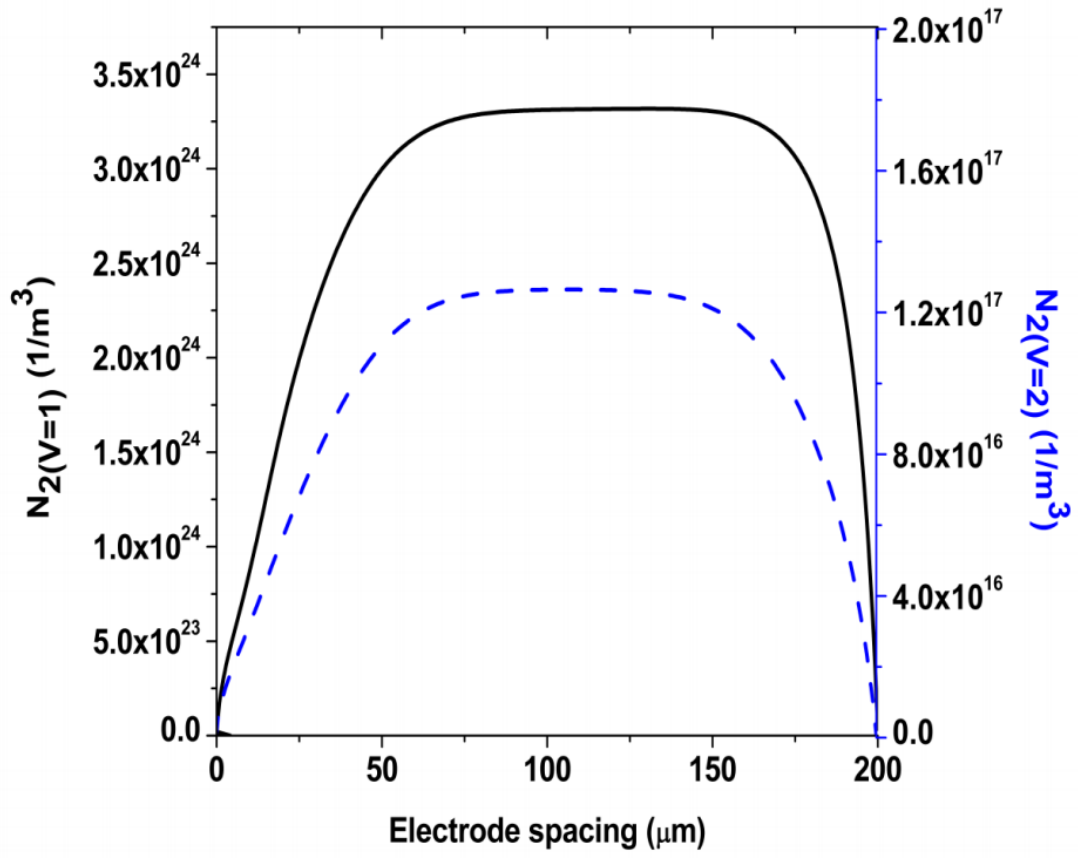

Figure A.3 Quasi steady number density distribution of vibrationally excited species (j_d = 8 A/cm^2 195 V)

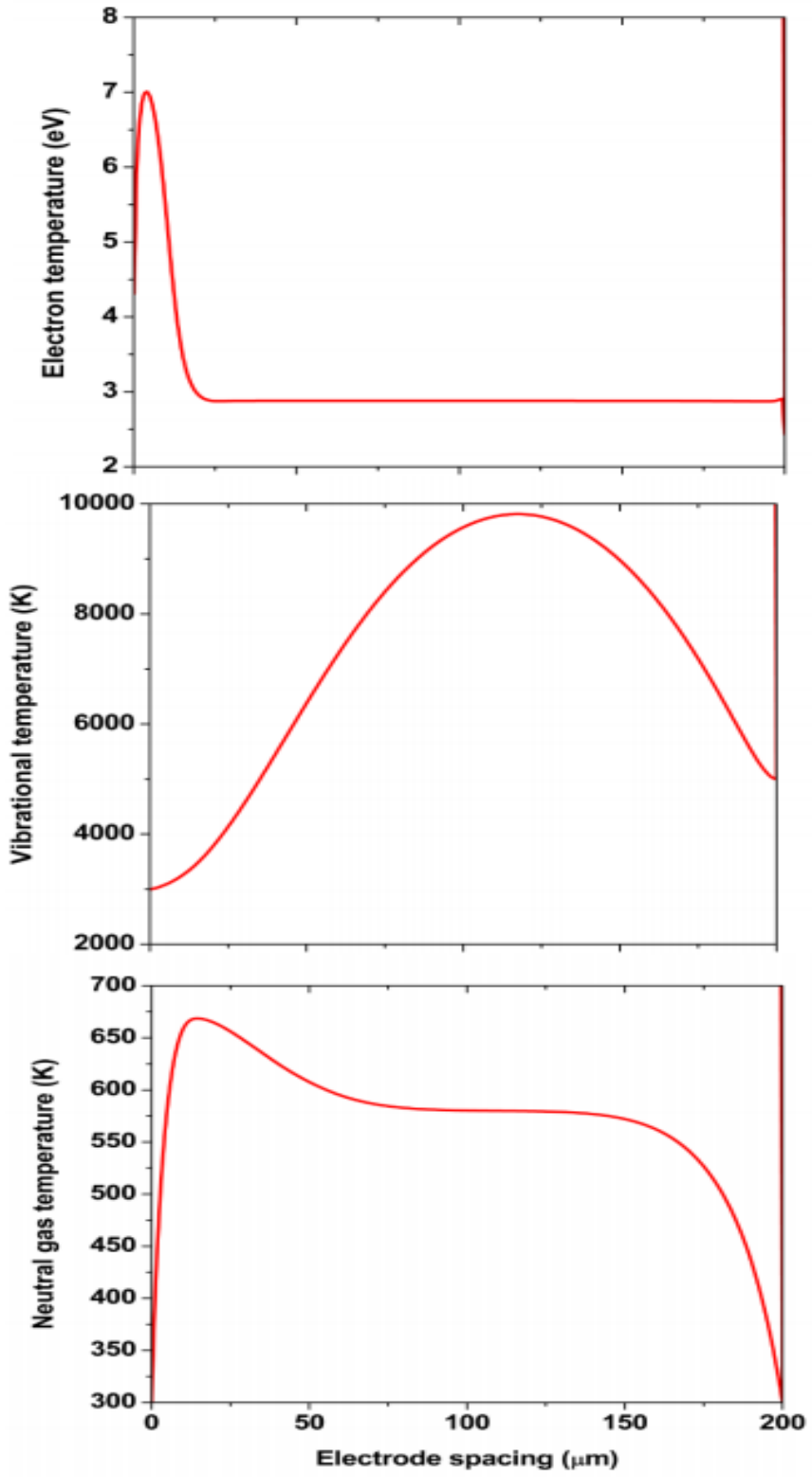

Figure A.4 Quasi steady spatial profile of electron, vibrational and translational/neutral gas temperature along the interelectrode distance (j_d = 8 A/cm^2 195 V)

Three different temperature such as electron, vibrational, and neutral gas temperature from the three representative energy equation are presented in Figure I (4). The maximum electron temperature was obtained in the cathode sheath region as ~7 eV and the electron temperature in the positive column was obtained as ~ 3 eV. The maximum vibrational temperature was 10000 K in the positive column and 3000k and 4000k in the cathode and anode respectively. The maximum neutral gas temperature/rotational temperature was found to be 650K in the cathode sheath.

APPENDIX B

CORONA TREATMENT ON PVDF FIBER

Plasma treated nanocomposite textile fiber offers the possibility of better morphological and piezoelectric property by shifting PVDF crystalline phase from α to β. To investigate this possibility, in this study atmospheric pressure corona was applied on PVDF fiber during the electrospinning process.

This study investigates the effect of corona application on piezoelectric PVDF nanofiber membrane. Corona glow was produced by high voltage power source, with 0.01 mA current, 1-3 mm distance between the anode and cathode, and 3-7 kV voltage in the air gap. Electrospinning process was used to generate thin nanofiber membrane with a flow rate of 0.7-1 ml/hr and 25-26 kV voltage to get the nanofiber with large area of sensitivity, high degree of alignment and uniformity in a continuous fabrication process. To get the piezo-electric properties the nanofiber membrane was heat treated above glass transition temperature (80-120ºC) to get piezoelectric properties and corona was applied to enhance the property. Corona treated nanocomposite fiber offers improved morphological and piezoelectric properties.

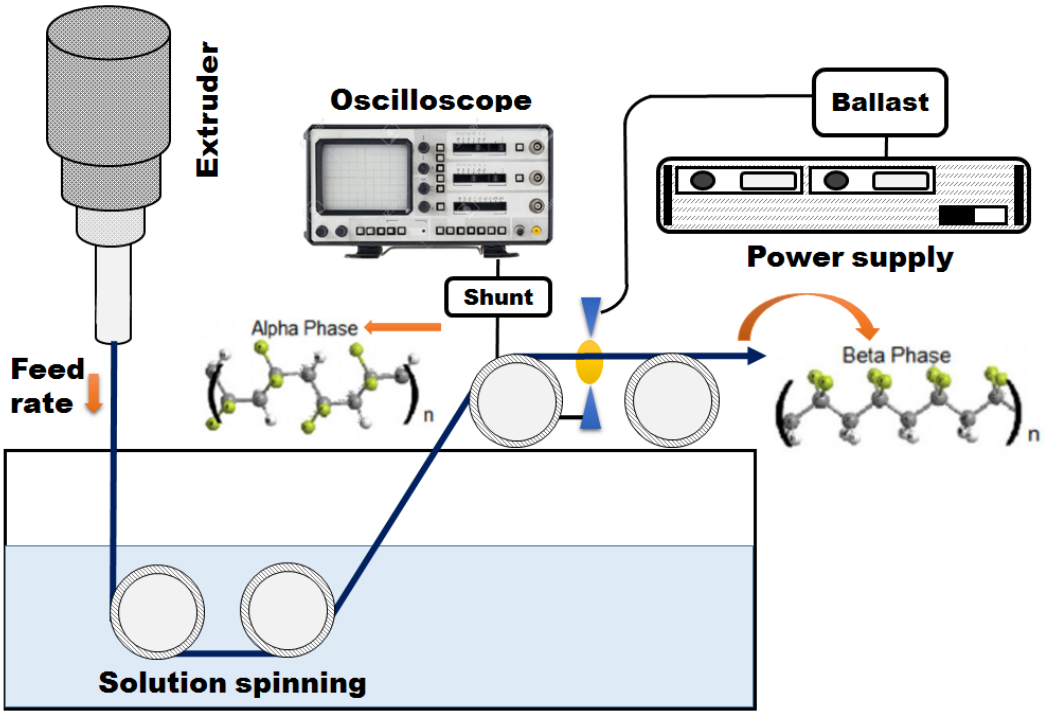

Figure B. 1 The experimental setup of and procedure of plasma assisted solution spinning process

EXPERIMENTAL SETUP

The experiments were performed using a MECC NF-500 electrospinning system. Two feed pumps are provided in the unit for controlled feeding (0.2-10.0 ml/hr) of polymer solutions through the nozzle of a spinneret. The spinneret assembly can be modified to include either a single-nozzle or coaxial nozzle spinneret. The metallic body of the spinneret is connected to the positive terminal of a high voltage DC power supply with a capacity up to 60 kV. The ground terminal of the power supply is connected to the collector plate placed at a distance below the spinneret. The distance between the spinneret nozzle tip and the collector plate can be adjusted to modify the electric field strength between the terminals. An Aluminum foil was used to cover the grounded plate collector, which

functioned as a conductive substrate for deposition of the nanofibers during electrospinning. The process parameters – voltage, spinneret tip-to-collector distance (TCD) and feed rates were adjusted by using the control unit of the NF-500 system. The inner chamber of the NF-500 unit is connected to a dehumidifier unit which maintains constant humidity level during electrospinning. The plasma treatment were conducted using a Spellman SL20P2000 DC power supply setup connected in series to a 3 MΩ ballast resistor. It should be noted that a high value of ballast resistor is necessary for the corona generation at a very low discharge current. For time dependent current measurements a current shunt (10 kΩ) was placed between one electrode of the discharge and the ground. The current shunt are connected to an oscilloscope for DC or time dependent measurements.

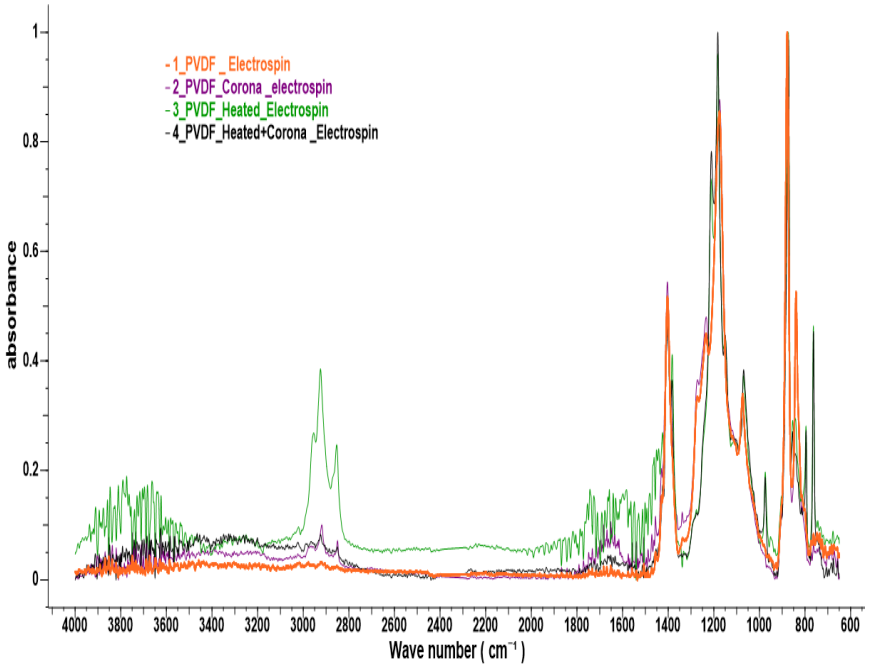

Figure B.2: Different FTIR for different PVDF Electro-spun fiber with different treated samples

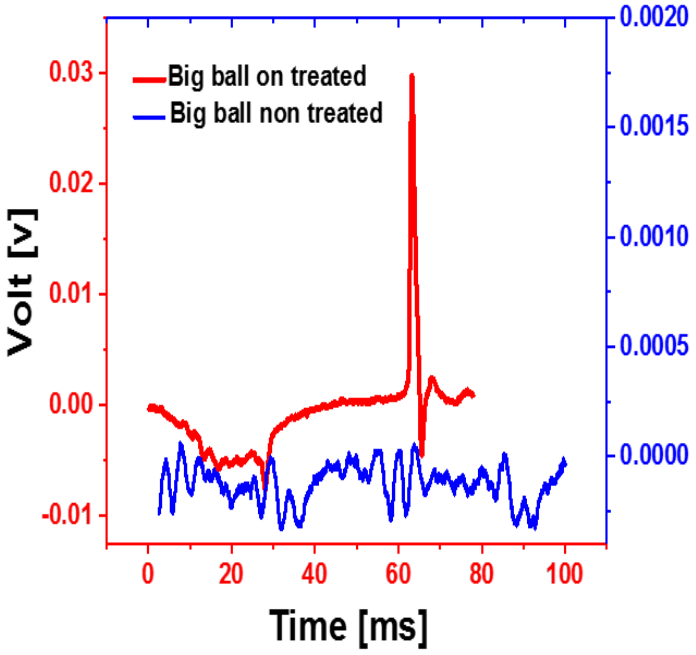

(I)

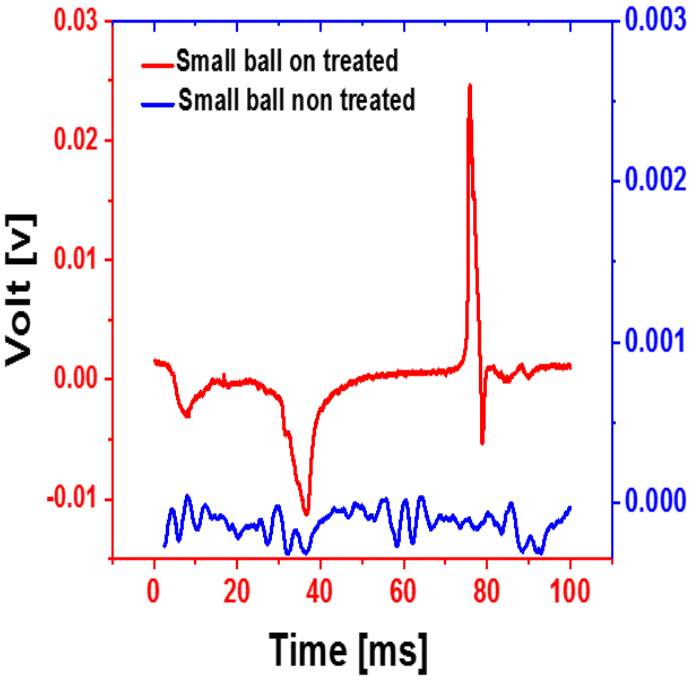

(II)

Figure B.3 : Average of 10 experiments with (I) Big Impactor (II) Small Impactor

Table B.1: Crystallization point, enthalpy and Percentage crystallization of pure and plasma treated PVDF fibers

Type	***Crystallization point (ºC)***	***Enthalpy (J/g)***	***Percent Crystallization (%)***
PVDF fiber	*161.69*	*40.73*	*38.79*
PVDF+ Plasma	*160.12*	*49.55*	*47.19*

RESULTS AND DISCUSSION

Pure PVDF electro-spun fibers were processed by electro-spinning process and hat and corona was applied on the fiber surface. From the DSC test results, pure PVDF fiber has the crystallinity of 38.79% and the melting endotherms 40.73 J/g and for plasma treated PVDF had crystallinity of 47.19% and the melting endotherms 49.55 J/g. So, the formation of the β phase crystalline structure in the PVDF fiber with plasma is more than pure solution spun PVDF fiber.

In order to distinguish the crystalline phase for pure, corona poled, heated, and corona poled with heating electro-spun PVDF fiber was analyzed by FTIR spectra. For electro-spun pure PVDF fiber few peaks were found. Application of corona without heat no major wave number shift happened. But after heating the fibers, wave number shifted and some new peaks were found and some were disappeared. When the heated fiber treat with corona, no shift in wave number was found but the area under the curve changed, which signifies some effect of corona poling of the fiber. The voltage test results for corona poling fiber can testify it. By heating the fiber, area under the curve of β phase for wave number 840,

and 1272 cm-1 decreased from 53 to 21 and 33 to 23. and by application of corona, the area increased from 21 to 25 for the peak 840 cm^{-1} and the area was decreased from 23 to 20 for the peak 1272 cm^{-1}.

The voltage response was increased 0.03 V for heated corona treated fiber than not corona treated nanofiber membrane. This FTIR results indicate that corona application improves the voltage response for PVDF fiber.